# Entanglement and Thermalization in Many Body Quantum Systems

Philip Crowley

University College London


A dissertation submitted for the degree of

Doctor of Philosophy

February 2017

To Basil Crowley
1950 — 2016

# Declaration

I, Philip Crowley, confirm that the work presented in this thesis is my own. Where information has been derived from other sources, I confirm that this has been indicated in the thesis. The work contains nothing which is the outcome of work done in collaboration except where specifically indicated in the text.

Parts of this dissertation have been published, or submitted for publication, as follows.

**Chapter 2**: V Stojevic, PJD Crowley, T Đurić, C Grey, and AG Green. Time Evolution and Deterministic Optimisation of Correlator Product States. Physical Review B. 2016 Oct 17; 94(16):165135.

**Chapter 2**: T Đurić, N Chancellor, PJD Crowley, P Di Cintio , and AG Green. Pfaffian-like ground states for bosonic atoms and molecules in one-dimensional optical lattices. Physical Review B. 2016 Feb 29; 93(8):085143.

**Chapter 3**: PJD Crowley, and AG Green. Anisotropic Landau-Lifshitz-Gilbert models of dissipation in qubits. Physical Review A. 2016 Dec 9;94(6):062106.

**Chapter 4**: PJD Crowley, V Oganesyan, and AG Green. The Suppression of Entanglement, Emergence of Chaos, and Failure of Quantum Adiabatic Computation. In preparation.

**Chapter 5**: PJD Crowley, T Đurić, W Vinci, PA Warburton, AG Green. Quantum and classical dynamics in adiabatic computation. Physical Review A. 2014 Oct 15; 90(4):042317.

**Chapter 6**: PJD Crowley. Many body localisation in the Quantum East Model. In preparation

Philip Crowley
February 2017

# Abstract

In this thesis we study problems relating the the structure and simulation of entangled many body quantum systems, their utility in adiabatic quantum computation, and the influence of the environment in thermalizing the system and degrading the usefulness of quantum dynamics in this setting. We then study a particular strongly coupled many body quantum system in order to better understand when quantum systems do not thermalize in this manner.

In chapter 2 of this thesis we study the properties of quantum dynamics restricted to an efficiently representable sub-manifold of quantum states both the finite and infinite chain of spin-1/2 subsystems. We investigate the trade-off between gains in efficiency due to this restriction against losses in fidelity. We find the integration to be very stable and shows significant gains in efficiency compared to the naively related matrix product states. However, much of this advantage is offset by a significant reduction in fidelity. We investigate the effect of explicit symmetry breaking in the ansatz and formulate the principles for determining when correlator product states may be a useful tool. We find that scaling with overlap/bond order may be more stable with correlator product states allowing a more efficient extraction of critical exponents and present an example in which the use of correlator product states is orders of magnitude quicker than matrix product states.

In chapters 3, 4 and 5 we extend this picture to allow for the study of the dissipative and decohering dynamics of a quantum system interacting with a bath, and pay particular reference to its effect on adiabatic quantum computation. In chapter 3 we consider a system of mutually interacting superconducting flux qubits coupled to a thermal bath that generalises the dissipative model of Landau-Lifschitz-Gilbert to the case of anisotropic bath couplings. We show that the dissipation acts to bias the quantum trajectories towards a reduced phase space. We study the model in the context of the D-Wave computing device and recover dynamics closely related to several models proposed on phenomenological grounds. In chapter 4 we extend this analysis to study explicitly the influence of dissipative dynamics on the lifetime of entanglement. In chapter 5 we apply this understanding to develop a methodology for benchmarking the quantum correlations harnessed by an adiabatic computation and apply this process to the D-Wave Vesuvius machine.

Further developing this interest in the effect of thermalisation of quantum dynamics in chapter 6 we consider systems which fail to thermalise even in the presence of strong coupling to their surroundings. This many body localised behaviour has been recently established to be a robust phase of matter in the presence of strong disorder in one dimension. Here we show the the low lying energy states of a many body system contain immobile excitations, this immobility results in an transition in the character of low lying eigenstates at arbitrarily weak disorder. This represents a novel appearance of localising behaviour in many body systems.

Finally we consider possible avenues for future work stemming from this thesis.

# Acknowledgements

First I'd like to thank my supervisor Andrew Green, without whose effort, guidance and support, this thesis would certainly not have been possible. I'd also like to thank Vadim Oganesyan with whom discussions have been a great source of inspiration in the last year. I am additionally grateful to both Vadim and Andrew for the guidance and support with taking the next steps in physics.

I owe a great deal of thanks to all of the other disciples of condensed matter who I have encountered along the way, to all of whom I am grateful for being able to share in their understanding. In particular those at UCL who regularly provided insight and understanding: Chris Pedder, Gregor Hannappel, Eliott Christou, Tom Kirk, Luke Yeo, Tanja Duric, Nick Chancellor, and Felix Nissen whose legacy of code was particularly useful in Chapter 5.

Friends at UCL, for providing an escape to Gordon square, or to the Bree Louise, and lunch time discussions on how to right the wrongs of the world. I am grateful to you all: Toby Gill, Rodolfo Hermans, Byron Villis, Guy Matmon, Izzy Bennett, TT, Johnny Nguyen, Chris Perry, Nairi Usher, Michael Faulkner, Ben Warner, and in particular both to Alice Pyne for wisdom and tea (both equally key in my eventual survival), and to Sam Aoudjane for being a GR8 M8. In addition to those who were friends I am grateful to all the support staff and others at UCL who helped me at different points along my journey.

I owe an huge amount of thanks to Elena Sabatini for not only tolerating this process with good humour, but for providing me with the energy to continue, and for a great, great deal more. Similarly to all my remaining friends who have given cheer to my years in London: Jack Munneley, Tom Scrivin, Justin Alsing, Till Hackler, Alex Shen, Geraldine Geux, Coline Jumeaux, Hollie Tu, Theo Clarke, Ted Cook, and especially Brigette Manion. To Tom Scrivin I owe a special thanks for taking the time to have a look at a draft of this thesis, and to help expunge some of the more hilarious typographical errors.

I am greatly indebted to all members of my family who have provided so much for me, especially to my mother, stepfather and stepmother and siblings. In particular I owe an enormous debt to my father, whose patience and thoughtful, nurturing, parenting encouraged me to develop and interest in the physical sciences. I cannot overstate the degree to these efforts of his have influenced my direction in life. I'm sure he would have been proud to see this thesis.

Cheers you lot.

# Contents

# List of Figures

# List of Tables

# 1 | Introduction

We introduce and relate the main themes of this thesis: simulation of many body systems, adiabatic quantum computation, open system dynamics and the thermalization of quantum systems.

The advent of quantum mechanics constituted the major paradigm shift of physics in the twentieth century. It introduced a framework of physical possibilities without analogue in classical physics. Quantum mechanics often makes surprising predictions counter to our real world intuition, with Einstein famously decrying entanglement in particular as "spukhafte Fernwirkung" or "spooky action at a distance" [1,2]. Despite such protestations, the seminal work of Bell [3,4] cemented the idea that no local realistic picture could capture the predictions of quantum theory.

The effort to understand and harness the implications of this has given rise to the field of quantum information science. But with progress we have come to understand that the peculiar nature of quantum dynamics has consequences across wide range of fields of physics.

Of relevance to this thesis this has lead to an emergence of a field of study which is focussed on understanding the role of entanglement in condensed matter systems. This active field, which sits at the interface of quantum information science, condensed matter theory, statistical physics, quantum field theory, and the study of many-body entangled states has lead to a rapid development in our appreciation of the role of entanglement in strongly correlated many body quantum systems.

## 1.1 Quantum entanglement

A pure quantum state of a spin-1/2 degree of freedom is generically described by $|\psi\rangle = \alpha_\uparrow |\uparrow\rangle + \alpha_\downarrow |\downarrow\rangle$. We begin be considering the articular case of the singlet state

$$|\psi_1\rangle = \frac{1}{\sqrt{2}} \left( |\uparrow\downarrow\rangle - |\downarrow\uparrow\rangle \right). \tag{1.1}$$

Consider an investigation in which two experimenters perform local projective measurements on the two constituent spin-1/2 degrees of freedom, projecting onto the $|\uparrow\rangle$, $|\downarrow\rangle$ basis. It is easily seen that the two experimenters will always find their measurements on the two subsystems to be anti-aligned. Recording the outcomes $\uparrow\downarrow$ and $\downarrow\uparrow$ both with a probability 1/2. This is despite the case that neither of the two subsystems is in a definite state, i.e. that neither subsystem can be said to have been up or down prior to the measurement. This hints at the possibility of non-classical statistics, but is in this case not experimentally distinguishable from the alternative state

$$|\psi_2\rangle = \begin{cases} |\uparrow\downarrow\rangle & \text{with probability } p = \frac{1}{2} \\ |\downarrow\uparrow\rangle & \text{with probability } p = \frac{1}{2} \end{cases}. \tag{1.2}$$

In the second case the system does have a definite state prior to measurement, to which the experimenters are ignorant. These states can be seen to be indistinguishable as the corresponding

density matrices

$$\rho_1 = \frac{1}{2}\begin{pmatrix} 0 & 0 & 0 & 0 \\ 0 & 1 & -1 & 0 \\ 0 & -1 & 1 & 0 \\ 0 & 0 & 0 & 0 \end{pmatrix} \quad \text{and} \quad \rho_2 = \frac{1}{2}\begin{pmatrix} 0 & 0 & 0 & 0 \\ 0 & 1 & 0 & 0 \\ 0 & 0 & 1 & 0 \\ 0 & 0 & 0 & 0 \end{pmatrix} \tag{1.3}$$

have the same diagonal elements in the measurement basis. Where we have used a convention $(|\uparrow\uparrow\rangle, |\uparrow\downarrow\rangle, |\downarrow\uparrow\rangle, |\downarrow\downarrow\rangle)$ for ordering the rows and columns. Both of these states $\rho_1$ and $\rho_2$ measure the spins to be anti-aligned in the $z$-direction with certainty.

To determine whether this is the case our experimenters now agree instead to measure along the $x$-axis, by performing projective measurements onto the basis $|\leftarrow\rangle = (|\uparrow\rangle + |\downarrow\rangle)/\sqrt{2}$, $|\rightarrow\rangle = (|\uparrow\rangle - |\downarrow\rangle)/\sqrt{2}$, the spins of $\rho_1$ are still measured to be anti-aligned with certainty, whereas for $\rho_2$ they will be measured to be aligned or anti-aligned with probability $p = 1/2$. However in the new measurement basis there are a different set of states which ape the quantum measurement statistics which we now cannot rule out. Just as in equation (1.2) these states mimic the quantum measurement statistics but along the new axis of measurement. Thus the experimenters observation of anti-alignement still cannot rule out a classical origin of the observed statistics.

To attempt to get around this our experimenters contrive a new protocol: they will randomly choose an axis along which to measure on the fly. It is important that this measurement axis is randomly determined in such a manner that there is no possible causal influence between the state preparation and the choice of measurement axis. This then rules out the possibility that our choice of measurement basis could influence the state preparation. Without prior knowledge there is a limit to how frequently two spins can be anti-aligned. We compare the quantum singlet state $\rho_1$ with the non-entangled state $\rho_3$ that attempts to mimic the singlet as best it can by anti-aligning the two spins along a randomly chosen axis. These two states are given by

$$\rho_1 = \frac{1}{2}\begin{pmatrix} 0 & 0 & 0 & 0 \\ 0 & 1 & -1 & 0 \\ 0 & -1 & 1 & 0 \\ 0 & 0 & 0 & 0 \end{pmatrix} \quad \text{and} \quad \rho_3 = \frac{1}{6}\begin{pmatrix} 1 & 0 & 0 & 0 \\ 0 & 2 & -1 & 0 \\ 0 & -1 & 2 & 0 \\ 0 & 0 & 0 & 1 \end{pmatrix} \tag{1.4}$$

and are now discernibly different. Measuring along a randomly chosen axis, we still find the spins of $\rho_1$ to be randomly anti-aligned with certainty whilst in $\rho_3$ which has purely classical correlations, in which the spins are not entangled, they are only anti-aligned with probability 2/3.

This ability of quantum mechanics to produce measurement statistics not consistent with any underlying distribution of classical states is the essence of quantum entanglement.

### 1.1.1 Bell's theorem

These notions were made rigorous by John Stewart Bell. Bell's work responded to an earlier paper by Einstein, Podolsky and Rosen (EPR) [5]. In this paper Einstein *et al* sought to show that quantum mechanics was an incomplete theory, and contained within it inconsistent or paradoxical results. Taking issue with the phenomenon of entanglement in particular Einstein aim was to show that taking it at face value led to contradictions. He preferred to believe that there was an explanation for the seeming probabilistic results in terms of hidden local variables, and aimed to work towards a more complete theory which would supersede quantum mechanics, and remove the necessity for a probabilistic theory of measurement.

The basic principle was to argue that by spatially separating entangled particles we have an opportunity to measure non-commuting operators with a greater precision than is allowed by Heisenberg's uncertainty principle. This set-up discussed in their paper is shown in Figure 1.1.

Bell's work [3], later generalised by Clauser, Horne, Shimony, and Holt [6], formalised the notion that there were two resolutions to the EPR paradox:


Figure 1.1: *The EPR thought experiment*: Two particles interact before moving off in opposite directions. Heisenberg's undertainty principle does not permit the identification of simultaneously meaningful definite values of position and momentum with any one particle. Einstein Podolsky and Rosen claimed by measuring the position of one particle and the momentum of the other that a meaningful position and momentum of both particles could be inferred.

- **Quantum mechanics contains hidden local variables**, as was Einstein's preferred resolution.
- **Quantum mechanics is not a local-realistic theory**. This approach is simply to reject the premise from which EPR argued. It resolves the paradox by relaxing the need for a physical theory that can be understood in terms of an underlying state of locally acting degrees of freedom.

Furthermore Bell showed that the former resolution could potentially be ruled out by a suitable experimental observation. This became known as Bell's theorem which stated the conditions under which bipartite correlations could be explained by a hidden variable theory. At the time of writing there has recently been the first observed loophole-free violation of the Bell inequality [7] establishing experimentally that locally-realistic theories, rather than quantum dynamics, are incompatible with experimental observations.

Turning to problems of condensed matter this establishes that even at a microscopic level a system of interacting quantum particles cannot be described by local coordinates, but instead requires the system to be considered as a whole, and described in terms of non-local pan-system variables which cannot all be meaningfully assigned a position within the system.

## 1.2 Many body quantum systems

In the case of the classical system of two magnetic moments, a definite state of the system is described by 4 coordinates, the polar and azimuthal angles of the each vector. By contrast the spin half system described in the previous section has 6 degrees of freedom. The four complex numbers, of the state

$$|\psi\rangle = \alpha_{\uparrow\uparrow}|\uparrow\uparrow\rangle + \alpha_{\uparrow\downarrow}|\uparrow\downarrow\rangle + \alpha_{\downarrow\uparrow}|\downarrow\uparrow\rangle + \alpha_{\downarrow\downarrow}|\downarrow\downarrow\rangle\,. \tag{1.5}$$

less the two gauge degrees of freedom corresponding to the norm and global phase of $|\psi\rangle$. The two additional degrees of freedom in the quantum state over the classical state characterise the entanglement in the system.

When we go to larger quantum systems, composed of $N$ subsystems, the number of degrees of freedom in the quantum state grows exponentially with $N$, far faster than in a classical description of the same system, in which they grow linearly with $N$.

### 1.2.1 The many body Hilbert space and the curse of dimensionality

Once we have included these extra non-local quantum degrees of freedom, we find that the space of possible many body quantum states, the many-body Hilbert space, is very large. As mentioned,

| $N$ | $2^N$ | Memory volume of $2^N$ complex floats | Approximate information capacity of... |
|---|---|---|---|
| 1 | 2 | 32 bytes | |
| 10 | $1,024$ | 16.4 kilobytes | |
| 20 | $1,048,576$ | 16.8 megabytes | 1 large fold-out map |
| 30 | $1,073,741,824$ | 17.2 gigabytes | 2 double-layer DVDs |
| 40 | $1,099,511,627,776$ | 17.6 terabytes | 10 copies of Wikipedia |
| 50 | $1,125,899,906,842,624$ | 18.0 petabytes | 9 months data output of the Large Hadron Collider |
| 60 | $1,152,921,504,606,846,976$ | 18.4 exabytes | Combined capacity of all Google data centres |
| ⋮ | ⋮ | ⋮ | ⋮ |
| 399 | $10^{120}$ | $1.60 \times 10^{121}$ bytes | The observable universe [9] |
| ⋮ | ⋮ | ⋮ | ⋮ |
| $6.02 \times 10^{23}$ | $10^{2.00 \times 10^{24}}$ | $10^{3.20 \times 10^{25}}$ bytes | ??? |

Table 1.1: A table of the different information volumes of a fully represented representations of a generic state of a system of $N$ two-level systems. Such a state is represented computationally by $2^N$ complex floats, each of which is 16 bytes (i.e. two doubles of 8 bytes each).

to specify a generic state of $N$ interacting quantum subsystems requires $\mathrm{O}(\exp(N))$ complex numbers. This exponential scaling is both a blessing and a curse:

If the ability to manipulate exponentially large amounts of data with linear resources can be meaningfully harnessed, this resource will provide computational power far in excess of what is possible within classical computation. This implies that any worthwhile scheme for quantum computation will violate the Extended Church Turing thesis [8], a tenet of complexity theory which states that all 'reasonable' forms of computation require resources that differ by at most a polynomial rescaling. Developing tools for understanding and leveraging the possibility that quantum computers may be significantly more powerful than classical ones has led to the field of quantum information science.

However, if we aim to simulate many body quantum systems, and therefore want to represent and manipulate such quantum states of exponentially many complex numbers on a classical computer, this exponential scaling is problematic. As shown in table 1.1 we require a data capacity far beyond that of the known universe before we are able to represent even thousands of interacting subsystems. This is a serious problem for the study of many body systems where we are interested in systems composed of between $\mathrm{O}(10^5)$ and $\mathrm{O}(10^{23})$ interacting unit subsystems.

The only hope is that the Hilbert space is not just 'too big'[①] but *ludicrously* oversized. It seems unpalatable that the state of a system of 400 two-level systems has hidden in it the information capacity of the known universe.[②③] Particularly as we know that the known universe contains more than 400 two-level systems. This was most tersely noted by Van Vleck [13] who dismissed the idea of generic many-body wavefunction on a system of electrons saying "In general the many-electron wave function for a system of $N$ electrons is not a legitimate scientific concept".

### 1.2.2 The structure of physical quantum states

This hope leads us to ask, what further physical constraints specify the kinds of quantum states are typically permitted in many body systems? To answer this we must first clarify the physics at which we intend to look: problems of many body quantum simulation mostly consist of finding

[①]The Hilbert space is often said to be 'too big' in reference to the gauge freedom $|\psi\rangle \sim a|\psi\rangle$ for $a \in \mathbb{C}$. But here we are discussing a much larger and physically motivated discrepancy.

[②]This is after all a strict upper bound, due to Bekenstein [10, 11], and not just an estimated value.

[③]A similar claim could be made about data volume of a probability distribution of the classical system, however there is some distinction since we believe that classical probability only describes the observers lack of 'true knowledge', while we believe that the quantum state actually exists [12].

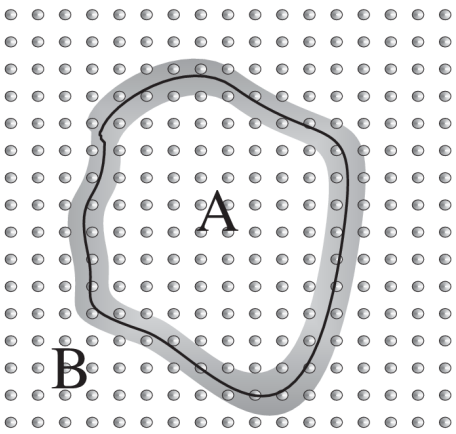


Figure 1.2: Toy picture of the area law of entanglement: Given a quantum state on a system which is divided into two contiguous disjoint regions $A$ and $B$, with the boundary $\partial A$ (solid black line) between $A$ and $B$. If there exists a correlation length $\xi$ in the underlying state $\psi$ then the only degrees of freedom (denoted here by lattice sites) which contribute to the entanglement $S_A$ between $A$ and $B$ are, those within distance $\xi$ of $\partial A$ (grey shaded region). Image source ref [14]

ground states of, or simulating dynamics of, local Hamiltonians.[①] In the case of studying these problems we are in luck, the states we are interested in have non-generic properties:

- The first of these is the *entanglement area law*. This states that for a system in a low energy state of a local, gapped Hamiltonian, the entropy of entanglement $S_A$ between a finite sub-region $A$ of the full system, and its complement $B$ scales with the area of the boundary between the $A$ and $B$. That is: $S_A \sim |\partial A|$ [14–17]. This is most intuitively understood as due to a finite correlation length scale $\xi$ in the quantum state: only degrees of freedom within a distance $\xi$ of the boundary $\partial A$ will contribute to correlations between $A$ and its complement $B$. The volume of this boundary region, and hence the total correlation and entanglement between $A$ and $B$, scale as $S_A \sim \xi|\partial A|$[②]. However a typical state drawn from the Hilbert space will have volume law entanglement [20], characterised by $S_A \sim |A|$. The result is that any state with a finite correlation length, including any low lying energy state of a 'realistic' (i.e. gapped local Hamiltonian), is highly atypical of the Hilbert space. Such states correspond to an exponentially small corner of the many body Hilbert space. Generalising this to a broader classes of systems, we find that the corresponding ground states of fermionic systems [21, 22] and critical systems [23–25] are still highly atypical with only multiplicative logarithmic corrections to the area law. For a more complete discussion the topic of entanglement area laws is reviewed in ref [17].

- Secondly we know that wherever we start in the Hilbert space we can only visit an exponentially small subset of quantum states in a reasonable time [26]. More formally, the trajectory of a many body quantum state evolving under a local Hamiltonian for a time $t \sim \mathrm{O}(\mathrm{poly}(N))$ visits a fraction of the Hilbert space that is exponentially small in $N$, and that the evolution time to come close to a generic quantum state is typically $t \sim \mathrm{O}(\exp(N))$. These are unphysically long time-scales.

These properties tell us that for any typical low energy quantum state, or for an evolution for any reasonable amount of time, the state of the system is confined to an exponentially small corner of the Hilbert space. The many body Hilbert space is nothing more than 'a convenient illusion'. How can we use this insight to simplify the problem? The most immediate way is to pre-empt the

[①] Local Hamiltonians are ones with finite range or sufficiently-fast decaying interactions
[②] We note the reverse is also true, that area law implies finite correlation length [18, 19]

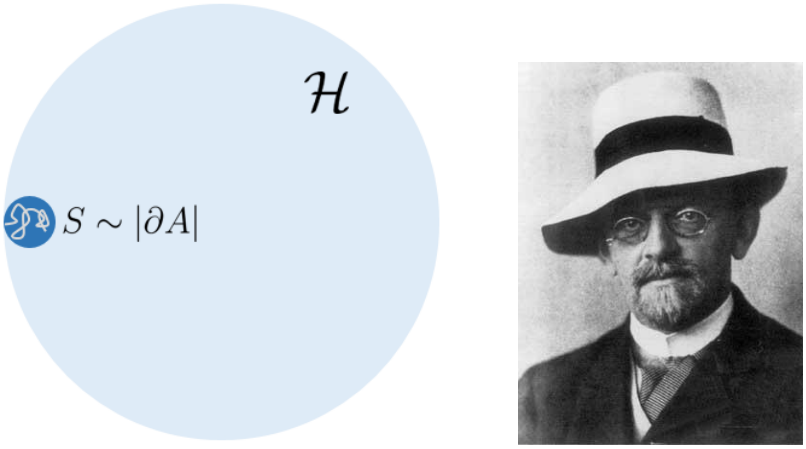


(a) (b)

Figure 1.3: *The physical parts of the Hilbert space* (a) Area laws in the many body Hilbert space (light shaded area). The sub-manifold of states which obey entanglement area laws corresponds to an exponentially small corner of the full Hilbert space (dark shaded area). Furthermore a typical dynamical trajectory (solid grey line) only covers an exponentially small fraction of the full Hilbert space in a reasonable time. (b) Mathematician and hotelier David Hilbert, who proposed this very large space

answer, and work explicitly with wavefunction ansätze which have these physical features built in. These states will therefore not suffer from the curse of exponential dimensionality.

In the following sections we review briefly some background on working with ansatz wavefunctions. In Chapter 2 we then go on to discuss the correlator product ansatz in detail and develop a method for ground-state optimisation and time evolution for this family of wavefunctions.

## 1.3 Numerical simulation of many body quantum systems

### 1.3.1 Tensor networks

The development of quantum state ansätze with area laws, (or, where applicable, logarithmically corrected area laws) which provide faithful representations of quantum states has been a major area of recent development. These contributions have come to be known as 'tensor network theory', we will cover some relevant results, but a more complete pedagogical review can be found in refs [27, 28].

Stated most tersely, tensor network theory is about identifying wavefunction ansätze $|\psi(\boldsymbol{x})\rangle$ for $\boldsymbol{x} \in X$, which live in some judiciously chosen sub-manifold of the Hilbert space $|\psi(X)\rangle = \mathcal{M} \subset \mathcal{H}$. For versatility we desire that this manifold $\mathcal{M}$ covers as much as possible of the 'area law' region in Figure 1.3, and for efficiency, as little as possible of the rest of $\mathcal{H}$. Formally we require that these ansätze admit efficient (i.e. poly$(N)$) algorithms for representing and time evolving these quantum states, and for calculating local expectation values. Before covering details of how useful results are obtained with such seemingly extreme approximations, we review some of the tools we need to work with these ansätze, and discuss of what they are capable.

#### Approximating quantum states and the Schmidt decomposition

The state of a quantum system whose Hilbert space $\mathcal{H}$ is of dimension $d$, and spanned by the set of basis vectors $\{|i\rangle\}$, is written

$$|\psi\rangle = \sum_{i=1}^{d} \psi_i |i\rangle \,. \tag{1.6}$$

for complex numbers $\psi_i$. Extending this picture to a state defined on a global system composed of two subsystems, $A$ and $B$ (as depicted in Figure 1.2). The Hilbert space is now composed $\mathcal{H} = \mathcal{H}_A \otimes \mathcal{H}_B$ which is spanned by the basis set $\{|i\rangle_A |j\rangle_B\}$, and a generic state of the system is written

$$|\psi\rangle = \sum_{i=1}^{d_A} \sum_{j=1}^{d_B} \psi_{ij} |i\rangle_A |j\rangle_B \tag{1.7}$$

where the $\psi_{ij}$ constitute a $d_A \times d_B$ matrix of complex numbers. In many body physics this product $d_A d_B$ is exponentially large in the physical size of the system. If we want to represent $\psi$ in a computation, we will generally not have the means to store all of the data of such a large matrix as $\psi_{ij}$, We ask then how we might approximate $|\psi\rangle$ in such a way that we are able to 'capture the physics' without being dominated by artefacts of the approximation.

One reasonable approach is to find the best approximation to $\psi_{ij}$ of a lower rank $\chi$

$$\psi_{ij} \approx \sum_{n=1}^{\chi} A_{in} B_{nj} \tag{1.8}$$

this reduces us from $d_A d_B$ variables to $\chi(d_A + d_B)$. Since $d_A$ and $d_B$ are exponentially large and providing $\chi$ (which we are free to choose) is not, this constitutes a significant improvement. The Eckart-Young-Mirsky theorem tells us the optimal approximation of a matrix of lower rank approximation is given by the truncated singular value decomposition [29]

$$\sum_{n=1}^{\chi} A_{in} B_{nj} = \sum_{n=1}^{\chi} U_{in} S_n V_{nj} \tag{1.9}$$

where $U$, $S$ and $V$ are found by singular value decomposition (SVD) of $\psi_{ij}$, and the $S_n$ are the $\chi$ leading singular values. An SVD performed in this context is known as a Schmidt decomposition. This allows the identification of $A$ and $B$, as, for example $A_{in} = U_{in}\sqrt{S_n}/\mathcal{N}$ and $B_{nj} = \sqrt{S_n} V_{nj}/\mathcal{N}$ where $\mathcal{N}$ is a normalisation factor. This approximation is optimal in the sense that the approximated state

$$|\phi\rangle = \sum_{i=1}^{d_A} \sum_{j=1}^{d_B} \sum_{n=1}^{\chi} A_{in} B_{nj} |i\rangle_A |j\rangle_B \tag{1.10}$$

maximises the fidelity $F = |\langle\phi|\psi\rangle|^2$ over states of the same reduced rank $\chi$, which is known in many contexts in many body physics as the 'bond order'. This scheme provides a process for throwing away a huge amount of data, but what kind of error have we introduced in doing this?

### Properties of the Schmidt decomposition

To understand the quality of the approximation made in the previous sections we consider the trace distance $D(\phi, \psi) = ||\psi\rangle\langle\psi| - |\phi\rangle\langle\phi||_1$ between the original state and its approximation. This quantity bounds the error on any projective measurement [30] $|\langle\phi|\Pi|\phi\rangle - \langle\psi|\Pi|\psi\rangle| \leq D(\phi, \psi)$ and hence expectation value $|\langle\phi|O|\phi\rangle - \langle\psi|O|\psi\rangle| \leq |O|_1 D(\phi, \psi)$. For the Schmidt composition we find that

$$D(\phi, \psi) = \sqrt{1 - F} = \sqrt{\sum_{n>\chi} S_n^2}. \tag{1.11}$$

We might also ask what are the physics of this approximation? What kind of states have we restricted ourselves to? We find the restriction is to weakly entangled states. Writing

$$|\phi\rangle = \sum_{n=1}^{\chi} S_n |u_n\rangle |v_n\rangle \tag{1.12}$$

where $|u_n\rangle = \sum_{i=1}^{d_A} U_{in} |i\rangle_A$, $|v_n\rangle = \sum_{i=1}^{d_B} V_{ni} |i\rangle_B$ and $S_n$ are the Schmidt values of $\phi$,[1] and studying the reduced density matrix on $A$, we find it is given by

$$\rho_A = \mathrm{tr}_B \left[ |\phi\rangle \langle\phi| \right] = \sum_{n=1}^{\chi} S_n^2 |u_n\rangle \langle u_n| . \tag{1.13}$$

Given the orthogonality of the $|u_n\rangle$, we can write down the entropy of entanglement between $A$ and $B$. This quantity is given by $\mathcal{E}_{AB} = S(\rho_A) = -\mathrm{tr} \left[ \rho_A \log \rho_A \right] = -\sum_{n=1}^{\chi} S_n^2 \log S_n^2 \leq \log \chi$ where the inequality is saturated for $S_n = 1/\sqrt{\chi}$.

So we see that we have restricted to low entanglement states, which is what the physical arguments of Section 1.2.2 led us to seek. Whether or not the error in equation (1.11) is tolerable depends on the incidental values of the Schmidt spectrum $S_n$. Fortunately in the cases of physical interest we introduced earlier the $S_n$ are often found to be decay exponentially with $n$[2].

### Graphical tensor notation

To study anything but the most trivial tensor product state decompositions will involve large numbers of indices. To aid clarity we will provide some equations in a graphical tensor notation. This notation is common in physics, e.g. in Feynman diagrams where it is used to represent field integrals. Here it is adapted for a different usage with different rules, resulting in diagrams which may seem alien to those familiar with this previous context. To avoid confusion we reintroduce the notation from the ground up.

In graphical notation each scalar, vector, matrix, tensor or function is represented by a solid shape, and each unsummed index or argument is represented by a dangling line. Thus we depict the vector $V_i$, the matrix $M_{ij}$, and the arbitrary rank tensor $T_{ijk\cdots l}$ as the objects

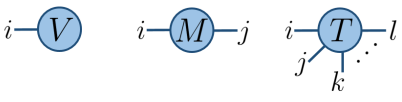


. (1.14)

Index summation/contraction is denoted by joining dangling lines, thus $U_i = \sum_j M_{ij} V_j$ becomes

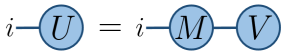


. (1.15)

The composite object on the right hand side has one dangling index, consistent with our knowledge that the product of a matrix and a vector is a vector.

We will discuss the context where the indices are finite, but the notation does not require this. The objects in equation 1.14 can equally well be used to represent the function $V(x_i)$, $M(x_i, x_j)$ and $T(x_i, x_j, x_k, \cdots, x_l)$, the contraction in equation 1.15 would then describe the integral $U(x_i) = \int \mathrm{d}x_j M(x_i, x_j) V(x_j)$.

Similarly to equation (1.15) $M_{ij} = \sum_k A_{ik} B_{kj}$ is denoted

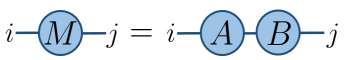


. (1.16)

The trace of this object can be found by contracting the remaining to indices to arrive at

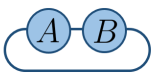


, (1.17)

[1] these differ from the leading $\chi$ Schmidt values of $\psi$ by a normalisation constant.

[2] This can in fact be related back to the spectrum of the Hamiltonian by entanglement thermalization hypothesis

this object has no remaining indices (legs) since this composite object is a scalar. This notation can also denote more complex objects, such as the partial trace $\rho_B = \mathrm{tr}_A[\rho]$

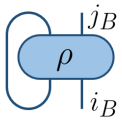


, (1.18)

and the singular value decomposition, which was used in the previous section:

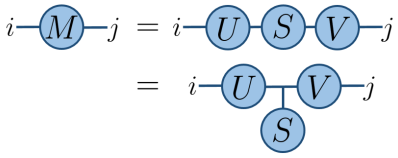


(1.19)

where in the second line we have used that since the matrix $S$ is diagonal there is a common index between all three matrices in the decomposition. In this picture the aforementioned Schmidt decomposition in equation (1.10) appears as

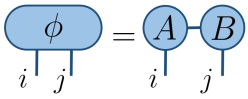


(1.20)

where we have contracted the Schmidt values onto the unitaries $U$ and $V$ to yield the matrices $A$ and $B$ which are in general no longer unitary.

### Matrix product States

We have seen how to use the Schmidt decomposition to make a controlled approximation for a quantum state by keeping only the strongest correlations across a bipartition.

In one dimension there is a natural ordering of all contiguous bipartitions of the system. This allows us to use the Schmidt decomposition to construct a special class of states known as matrix product states or MPS [27,31–38]. This is done by repeatedly applying the Schmidt decomposition on successive 'bonds' (i.e. between successive sites) and truncating the bond order as follows

$$\begin{aligned} |\psi\rangle = \sum_{i_1 i_2 \cdots i_N} \psi^{i_1 i_2 \cdots i_N} |i_1 i_2 \cdots i_N\rangle &= \sum_{i_1 i_2 \cdots i_N} \sum_{\alpha_1} A^{i_1}_{\alpha_1} B^{i_2 \cdots i_N}_{\alpha_1} |i_1 i_2 \cdots i_N\rangle \\ &= \sum_{i_1 i_2 \cdots i_N} \sum_{\alpha_1} A^{i_1}_{\alpha_1} A^{i_2}_{\alpha_1 \alpha_2} \cdots A^{i_N}_{\alpha_{N-1}} |i_1 i_2 \cdots i_N\rangle \end{aligned} \tag{1.21}$$

or depicted in graphical notation

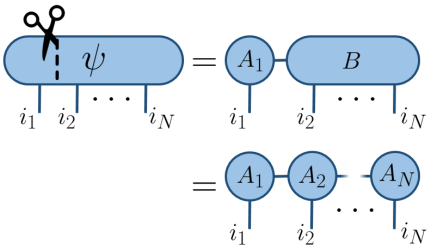


(1.22)

### Tensor network states

MPS constitute an example of what has become a menagerie tensor network wavefunction ansätze, a few instances of which are shown in Figure 1.4. The characteristic feature of tensor network

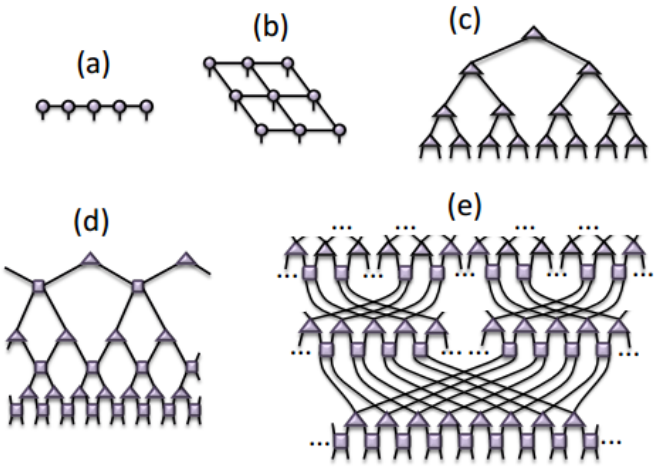


Figure 1.4: *Examples of tensor networks*: (a) Matrix product states (MPS) (b) Projected entangled pair states (PEPS) (c) Tree tensor network (TTN) (d) Multiscale entanglement renormalization ansatz (MERA) (e) Branching MERA. These are a selection of commonly used tensor network states, in all of these tensors indices are bipartite. CPS state which we introduce later, have multipartite indices. Figure from ref [28].

.

states is that the wavefunction is represented by a network of locally acting tensors. This network has a fixed number of external (i.e. dangling) indices, set by the physical system it is representing, and any number of internal indices.

The entanglement structure quantum state represented by a tensor network ansatz is inherited from the geometry of the network. Most commonly these geometries are either: the same geometry as the physical lattice, resulting in $S \sim L^{d-1}$ area law entanglement (as with e.g. matrix product states, correlator product states, and projected entangled pair states, string bond states); or holographic geometry, which is endowed with an additional renormalisation direction, and which results in $S \sim L^{d-1} \log L$ entanglement [39, 40] (as in tree tensor networks, multi-scale entanglement renormalization ansatz (MERA), and branching MERA) characteristic of fermionic and critical states.

In addition to the correct entanglement structure for the problem of interest, these networks are constructed to have other useful properties which make their usage computationally tractable. A tensor network is said to perform a given task efficiently if there exist routines for performing this task with the tensor network, and these routines require resources (e.g. CPU time, computer memory) which grow at most polynomially with the size of the system represented. Desirable properties include:

- **Efficiently representable:** The total number of tensor elements in the network scales polynomially. This allows the tensor network to be stored in computer memory.
- **Efficiently sampleable:** There exist polynomial time routines for calculating the overlap with a useful computational basis — often classical (i.e. zero-entanglement) configurations $\langle C|\psi\rangle$. This property allows for the Monte-Carlo evaluation of wavefunction overlaps and local operator expectation values.
- **Efficiently contractable:** There exist efficient routines for the exact calculation of wavefunction overlaps $\langle\phi|\psi\rangle$ and local expectation values $\langle\psi|O|\psi\rangle$ when both $|\phi\rangle$ and $|\psi\rangle$ are of the ansatz form in question, and .
- **Efficiently simulable:** There exist efficient routines for approximating time evolvin the quantum state via the Schrödinger equation.

There is a hierarchy of these properties

$$\begin{matrix}\text{Efficiently}\\ \text{simulable}\end{matrix} \subset \begin{matrix}\text{Efficiently}\\ \text{contractable}\end{matrix} \subset \begin{matrix}\text{Efficiently}\\ \text{sampleable}\end{matrix} \subset \begin{matrix}\text{Efficiently}\\ \text{representable}\end{matrix} \tag{1.23}$$

In chapter 2 we investigate a novel wavefunction ansatz, correlator product states (CPS), which has these features designed into it. We develop an efficient process for dynamically evolving these wavefunctions and discuss the accuracy and efficiency of the ansatz as a tool for investigating many-body dynamics with reference to the well-known matrix product state (MPS) ansatz, a comparable tool. Returning to this topic later, we first go on to discuss how this relates to other work presented in this thesis.

## 1.4 Many body physics and quantum computation

In the previous sections we have discussed some of the understanding that has been developed in simulating many-body quantum systems on a classical computer. But what if our simulation were not constrained by the limits of classical computation? Feynman was one of the first to discuss how the exponentially large number of degrees of freedom present in quantum mechanics might be harnessed to computational ends. He noted that his conception of a 'universal quantum simulator' would be capable of performing exponentially better than a classical computer *at simulating generic quantum systems* [41]. As it is automatically afforded the exponentially large state space that is so hard to simulate.

Emboldened by this we can go further. Returning to the exponentially large number of degrees of freedom in a typical quantum state, one can ask: can this exponentially large state space be harnessed for solving other problems? The idea that quantum systems are automatically endowed with an 'exponential parallelism' by the many-body Hilbert space [42] has been frequently cited in further work into the development of quantum computing. These efforts have further sought to extend beyond the simulation of quantum systems, into universal quantum computation [8, 43]. This would yield a powerful tool which could be turned to any problem, rather than just physical simulation.

### 1.4.1 The relationship of physical law and computational complexity

However harnessing quantum mechanics in this way has proven surprisingly difficult, with the 35 years having provided relatively small number of quantum algorithms that offer speed-up over their classical counterparts. The nature of physically realisable quantum states—those produced by reasonable numbers of few-body operations, the basic building blocks of the quantum algorithm—are highly atypical of the Hilbert space, this coupled with the slowness of quantum dynamics to explore the Hilbert space under local operations (as discussed in section 1.2.2) might give some intuition as to why this might be the case.

A notable example of how physical constraints dramatically reduce the computational complexity of quantum dynamics is that the case of one dimensional dynamics many body systems. The special properties of physical states have been harnessed to develop efficient routines for numerical simulation of quantum systems in one dimension for both critical [44–46] and non-critical [33,36,38] systems. From the Extended Church Turing thesis [8] we know that this relationship is reciprocal. The classical simulability of one dimensional dynamics tells us that physical realisation of a *one-dimensional* quantum simulator cannot provide enhancement over classical computation. Only if dynamics of interest can be found which cannot be captured by these ansätze will a one-dimensional simulator be of interest.

By the same token the absence of classical computational routines to efficiently simulate higher

dimensional systems hints at the possibility that simulation in such systems might provide quantum speed-up. In a return to Feynman's original suggestion the development of methods for quantum simulation [47, 48] in such systems has been an interesting avenue of development.

### 1.4.2 The D-Wave machine

One such realised system, the D-Wave machine performs quantum simulation of the transverse-field Ising model with an array of flux qubits. This capability is used to implement 'quantum annealing' a heuristic procedure for finding the ground states on a two-dimensional Ising spin glass. Efficiently providing solutions to this NP-complete problem [49]. NP-complete problems constitute a class of polynomially equivalent problems which includes some relevant and computationally challenging problems. Such a source of efficient (polynomial time) solutions to any NP-complete problem would represent a significant advance over any known method, or anticipated, tools in classical computation.[①] However, currently no quantum speed-up is detected in the D-Wave machine [50].

This lack of quantum speed-up appears to be due to the thermalizing effect of the environment. Investigations into the power adiabatic quantum computation, in particular in open systems forms the second theme of this thesis. In chapter 3 we study the influence of the environment of an array of flux qubits, and show that this can recover heuristic dynamics that were shown to reproduce the behaviour of an interesting heuristic model of the D-Wave machines behaviour [51–53], providing theoretical underpinning to this observation. Following this in chapters 4 and 5 we apply this understanding to examine adiabatic quantum computation in more detail.

## 1.5 Thermalization and quantum statistical mechanics

In the final theme of this these we investigate the process of thermalization in quantum systems. Thermalization is the process by which a system converges on a thermodynamic equilibrium state via mutual interaction with its environment. It presents a major hurdle for harnessing the potential power of quantum mechanics for information processing.

The physical process of thermalization is easily observed: for example a hot cup of tea seemingly over-readily becomes tepid when one is distracted for some time. However, at first glance this kind of observation does not sit easily with the time-reversible microscopic dynamics which we understand to underpin both classical and quantum mechanics.

To highlight further this apparent paradox we will consider a system isolated from its environment. A simple example is that of an ideal gas in an isolated box. We can contrive to prepare this gas in any kind of absurd initial state, we could for example prepare all the particles to be moving in unison together across the box. However, regardless of this initial state, after a sufficiently long period for transient effects to pass, we expect the physics of this system to be well captured by statistical mechanics, in which the outcomes of measurements of the trajectories and positions of the systems constituent parts are modelled as random variables. How do the deterministic and time reversible dynamics of an isolated system evolve to a state of thermal equilibrium given a generic initial condition? How, despite the explicit time symmetric underlying dynamics, do we see the emergence of an arrow of time?

We see that apart from holding the key to further development in quantum information processing, understanding this process also sheds light on some of the deeper questions in physics as we investigate: how do quantum systems thermalize themselves?

[①] It is expected, but not proven, that $P \neq NP$

### 1.5.1 Classical chaos, ergodicity and integrability

Chaotic dynamics provides one picture by which we can try to resolve this apparent paradox in the classical case. Chaos describes a situation in which errors, or uncertainty, grow exponentially. The presence of such chaotic dynamics provides some scope for any uncertainty in the initial state to grow until it consumes all vestiges of the initial configuration. This divergence of trajectories allows chaotic systems to rapidly explore their phase space, e.g. in Figure 1.5, and to converge quickly on the behaviour posited by the assumptions of statistical mechanics. The ability of a system to explore its full phase space in this way is known as ergodicity.

Not all classical systems are chaotic though, a simple example being a collection of harmonic oscillators. Such a system provides an example of a classically integrable system. A characteristic feature of many body integrable systems is the existence of an extensive set of integrals of motion. These follow from a set of canonical coordinates $(J_i, \theta_i)$ known as action-angle variables. These evolve as

$$\frac{\mathrm{d}J_i}{\mathrm{d}t} = 0 \qquad \frac{\mathrm{d}\theta_i}{\mathrm{d}t} = \omega_i. \tag{1.24}$$

For example, in the case of the harmonic oscillators these are related to the more familiar coordinates $(p, q)$ by

$$\begin{aligned} J_i &= \frac{p_i^2}{2m\omega_i} + \frac{m\omega_i q_i^2}{2} \\ \theta_i &= \omega_i t \end{aligned} \qquad \Longleftrightarrow \qquad \begin{aligned} p_i &= \sqrt{2m\omega_i J_i}\cos\theta_i \\ q_i &= \sqrt{\frac{2J_i}{m\omega_i}}\sin\theta_i, \end{aligned} \tag{1.25}$$

whereas for the aforementioned free particle, the $J_i$ are proportional to the orthogonal components of linear momentum and the $\theta_i$ are the corresponding position coordinates. The $J_i$ are conserved quantities or integrals of motion (IOM). A fully integrable system has so many IOM that specifying the $(J_i, \theta_i)$ is sufficient to uniquely specify a microstate of the system. The evolution of the system is then characterised by simple orbits on an $N$-dimensional torus in phase space, where $N$, the number of pairs of canonical coordinate $(p_i, q_i)$ is also hence the number of integrals of motion $J_i$.

The Hamiltonian of an integrable system takes a simple linear form $H = \sum_i J_i\omega_i$. Integrability clearly refers to a very special dynamical situation. One might assume that if this linearity, requisite for integrability, is broken by the presence of any non-linearity in the system, that the conserved quantities $J_i$ become dynamic, and the special structure is lost. However the result of Kolmogorov, Arnol'd and Moser (KAM theorem) showed that many of the integrals of motion (depending on the nature of the integrability breaking) are in fact stable to the presence of many such perturbations provided they are sufficiently weak [54–56].

Integrals of motion act as a memory of the system's initial conditions. A system is only fully ergodic if the energy $E$ is the only integral of motion. In the presence of further integrals of motion the system is unable to explore much of its phase space, analogous to how the billiard bouncing in a circle cannot reach the centre of the circle in Figure 1.5. This establishes that a system's ability to thermalize is strongly affected by its integrability, or vicinity to an integrable point, as clearly a collection of particles following the trajectories in Figure 1.5b will not converge on the predictions of statistical mechanics.

### 1.5.2 Berry-Tabor conjecture

The possibility of an analogous dichotomy to chaos vs integrability in quantum systems was studied by Michael Berry. It is clear the linearity of the Schrödinger equation presents a challenge to defining integrability in a similar way. Not only does the unitarity of the time evolution operator mean there is never any divergence of trajectories in the Hilbert space, but every quantum system

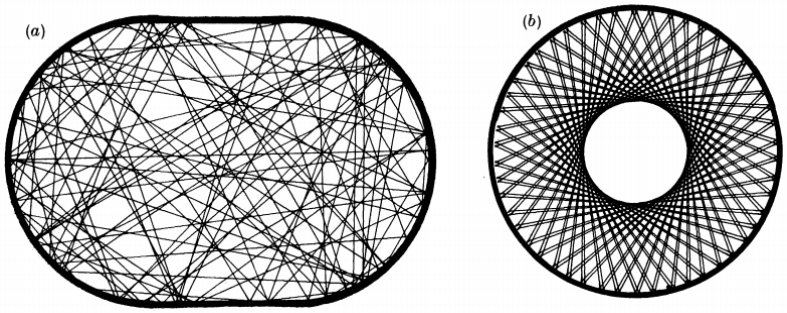


Figure 1.5: *The configuration space trajectories of Chaotic and integrable systems*: (a) Bouncing billiard trajectories in the Bunimovich stadium are (almost all) chaotic and ergodic [57]. (b) Those in the circle are neither. Figure from ref [58].

.

supports an extensive set of integrals of motion: it can be seen that

$$|\psi(t)\rangle = \sum_i \sqrt{J_i} \mathrm{e}^{-\mathrm{i}\theta_i(t)} |E_i\rangle \,, \qquad \theta_i(t) = E_i t, \tag{1.26}$$

where $|E_i\rangle$ are the eigenstates of the Hamiltonian, constitute a solution to the Schrödinger equation,

$$\mathrm{i}\frac{\mathrm{d}\,|\psi\rangle}{\mathrm{d}t} = H\,|\psi\rangle \,, \tag{1.27}$$

in terms of action angle variables (1.24). Berry's work showed that despite this there was a behaviour in quantum systems which corresponded to classical chaos. Berry and Tabor conjectured [60] that quantum systems corresponding to (i) classically chaotic/ergodic and (ii) classically integrable systems fall into distinct universality classes. These universality classes are readily distinguishable by the statistical properties of their spectra and eigenstates. We will discuss the underlying theory of this transition in more detail in Section 6.1.3. Just as integrability is broken by a sufficiently strong perturbation in classical systems, quantum systems undergo a similar transition, an example is given in Figure 1.6 which shows the electronic level spacing distribution of a Rydberg atom transform from a characteristically integrable form to an ergodic form under the influence of an external perturbation which breaks integrability.

### 1.5.3 Thermalization in isolated quantum systems

We have argued in previous sections how, in the correct circumstances, a system prepared in an arbitrary initial state evolves to a state that agrees with the predictions of statistical mechanics. This is provided we do not simultaneously measure so many degrees of freedom that we are outside the purview of statistical mechanics. For the minority of degrees of freedom that we interrogate, the wider system is acting as a bath. In this sense the system is said to act as its own bath. This division of a system into a minor part which is interrogated and a major part which is not disturbed is reminiscent of the usual system-environment division in the study of open systems.

It is in this sense that we find the quantum systems identified as ergodic by the Berry-Tabor conjecture thermalize. If we consider a closed quantum system composed of a subsystem $A$ and its complement $B$ in the limit of $|A| \ll |B|$ we find that any observable on the subsystem $A$ relaxes to its thermal value. i.e. that

$$\langle O_A(t)\rangle = \langle\psi(t)|\hat{O}_A|\psi(t)\rangle \xrightarrow{t\to\infty} \mathrm{tr}\left[\hat{O}_A\rho_{\mathrm{th}}\right] \tag{1.28}$$

where $\rho_{\mathrm{th.}}$ is the correct statistical ensemble state. This is only satisfied for sufficiently local

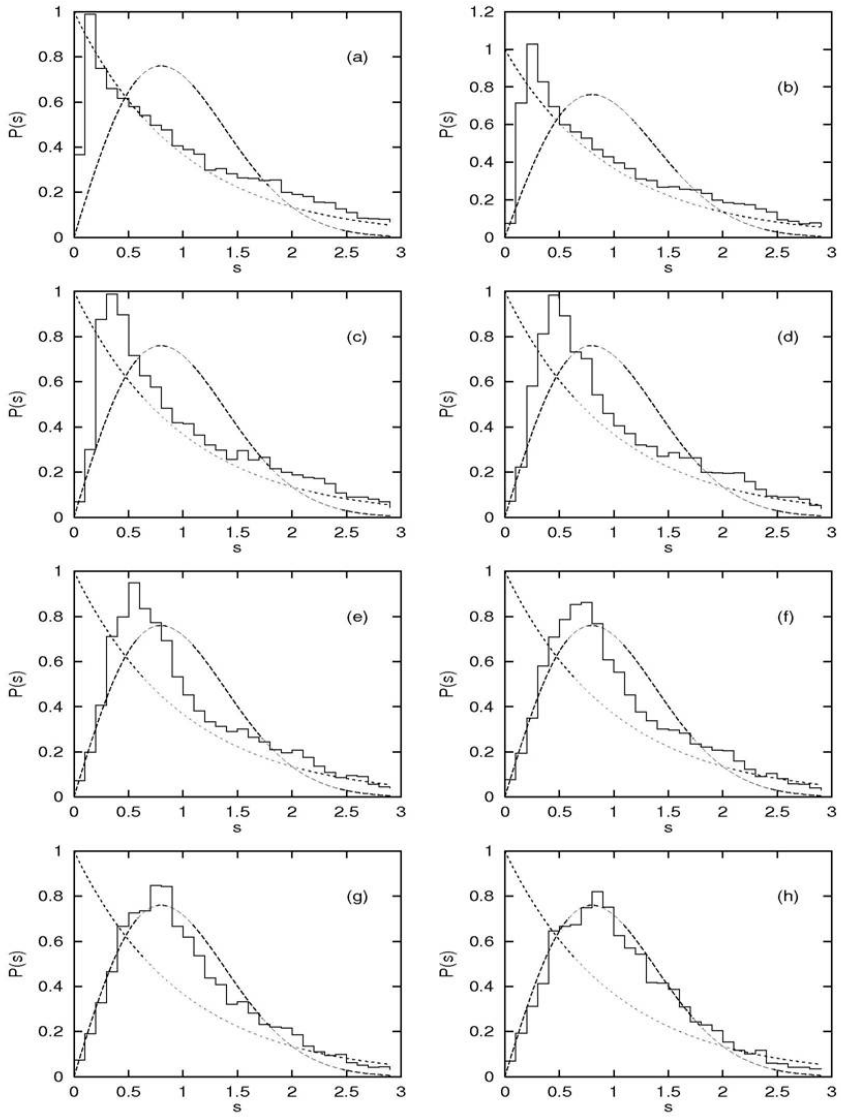


Figure 1.6: *Transition from integrable (Poisson) statistics to ergodic (GOE) statistic*: Calculated distributions (dashed) compared with histograms of level spacings (solid) of the Rydberg atom electronic energy level spectra. The spectra is altered by the presence of an electric field. This alteration is quantified by the quantum defect $\delta$ which increases from 0.04 (a) to 0.32 (h). The system becomes more chaotic as dynamical symmetries are broken by increasing the quantum defect, consequently, the level spacing distribution evolves from an initially Poisson form (a) to the GOE form (h). Figure from ref [59].

operators that only interrogate a minority of the degrees of freedom of system. These are the physically relevant observables and it is only such local operators which can be interrogated in any experimentally realisable protocol. This notion of thermalization proceeds so long as

$$\mathrm{tr}_B\left[|\psi\rangle\langle\psi|\right] \xrightarrow{t\to\infty} \mathrm{tr}_B\left[\rho_{\mathrm{th}}\right] \tag{1.29}$$

without requiring the much stronger condition that the global state thermalizes, i.e. $|\psi\rangle\langle\psi| \neq \rho_{\mathrm{th.}}$. The restrictions that this places on the statistics of the spectra and eigenstates is immediately clear: in particular if we prepare the system in a static solution of the dynamical equations, given by an eigenstate $|\psi\rangle = |E_\alpha\rangle$, we have that

$$\mathrm{tr}_B\left[|E_\alpha\rangle\langle E_\alpha|\right] = \mathrm{tr}_B\left[\rho_{\mathrm{th}}\right] \tag{1.30}$$

i.e. that local observables are thermal for single eigenstate ensembles. This is a statement of eigenstate thermalization hypothesis (ETH) [61–64]. It is found that a large majority of the types of systems studied in many body quantum physics appear to behave in a way consistent with ETH. We will discuss ETH in more detail in Section 6.1.4, but for now we move on to briefly introduce an interesting class of systems which do not behave in this way.

### 1.5.4 Localization

The other class of quantum systems are those which correspond to classically integrable systems. Like their classical counterparts these do not thermalize, instead maintaining vestiges of their initial conditions after arbitrarily long times. Such systems thus have zero conductivity and can be imagined as perfect insulators. The failure to thermalize follows directly from the absence of any kind of transport.

Understanding the conditions in which this thermalization fails is an active area of research [65]. Though most many-body quantum systems studied in physics are ergodic, it is now well established that sufficiently strong quenched disorder is capable of driving one-dimensional quantum systems into a non-ergodic phase. For historical reasons [66] and consistent with the locality of the integrals of motion in such a phase, this non-thermalizing phase is known as the localized phase.

The existence of such a phase is attractive from the point of view of quantum information processing. The non-diffusion of information within an interacting many-body quantum system hints at the possibility of there existing ways to contrive dynamics which maintain quantum coherence in the presence of external interactions. In chapter 6 we will investigate interesting novel circumstances in which this behaviour can occur.

## 1.6 Outline of thesis

The remainder of this thesis will proceed follows:

In chapter 2 we begin our investigation into many body quantum systems by considering an interesting many body wavefunction ansatz. We discuss the properties of this ansatz, and show that it has explicitly finite range quantum correlations. We develop an efficient process for numerical optimization and dynamical evolution with such states. We then consider the discuss the accuracy and efficiency of working with this ansatz as a tool for investigating many-body dynamics, and make direct comparison the well-known matrix product state (MPS) ansatz.

In chapter 3 we consider the influence of exchange of energy with an environment on a quantum system. We extend tools developed in chapter 2 to include the effects of the environment using results from the Keldysh theory of non-equilibrium systems. We apply this perspective and consider the dynamics of flux qubits which have a highly anisotropic coupling to the environment. We find

that this anisotropy is reflected in the dynamics and results in dynamical behaviour that is highly reminiscent of recently proposed heuristic dynamics which were able to reproduce many of the features of a well-known array of flux qubits produced by D-Wave, built with the aim of performing a specific adiabatic quantum computation.

In chapter 4 we extend this picture consider the dynamics of entanglement in open systems, and comment on the implications of open system dynamics for the efficacy of adiabatic quantum computation.

In chapter 5 we extend the insights of chapters 3 and 4 to develop a heuristic picture of adiabatic quantum computation in many body open systems. We use this understanding to inform a procedure for benchmarking adiabatic quantum computers that allows for a more nuanced understanding than the 'quantum' vs 'classical' dichotomy. We apply this procedure to the D-Wave machine in order to determine its quantum information processing capability. However ultimately we find that strong coupling to environmental degrees of freedom confounds the possibility of quantum computation in this device.

In chapter 6 we discuss an interesting paradigm for preserving the locality of quantum information in the presence of strong many-body interactions. This is the aforementioned localized phase. We consider a different method for inducing localized dynamics in many body systems that is alternative to the well-known approach of strong disorder. We study a system with kinetically constrained dynamics and show that there exist low lying localized states in the spectrum in the presence of arbitrarily weak disorder.

In chapter 7 we make some closing remarks and discuss possibilities for future work.

# 2 | Efficient dynamics with finite range entanglement states

We study a restricted class of correlator product states (CPS) for a spin-half chain in which each spin is contained in just two overlapping plaquettes. This class is also a restriction on matrix product states (MPS) with local dimension $2^n$ ($n$ being the size of the overlapping regions of plaquettes) equal to the bond dimension. We investigate the trade-off between gains in efficiency due to this restriction against losses in fidelity.

The time-dependent variational principle formulated for these states is numerically very stable. Moreover, it shows significant gains in efficiency compared to the naively related matrix product states—the evolution or optimisation scales as $2^{3n}$ for the correlator product states versus $2^{4n}$ for the unrestricted matrix product state. However, much of this advantage is offset by a significant reduction in fidelity.

Correlator product states break the local Hilbert space symmetry by the explicit selection of a local basis. We investigate this dependence in detail and formulate the broad principles under which correlator product states may be a useful tool. In particular, we find that scaling with overlap/bond order may be more stable with correlator product states allowing a more efficient extraction of critical exponents—we present an example in which the use of correlator product states is several orders of magnitude quicker than matrix product states.

The original work in this chapter, beginning in Section 2.2, was done in collaboration with V Stojevic, T Đurić, C Grey, and A Green, and published as ref [67].

The study of many body quantum systems is fraught by the curse of dimensionality. Tensor networks offer a pragmatic approach to the numerical study of quantum systems by providing a variational ansatz that allows one to throw away unimportant degrees of freedom whilst keeping those that 'really matter'. In 1D the matrix product state (MPS) ansatz has been a major workhorse. This is because there are efficient (polynomial) routines for the representation, contraction, and evolution of these quantum states [33, 36, 38]. The higher dimensional generalisation of MPS, projected entangled pair states (PEPS) also provides efficient representations of quantum states. However there is a hierarchy of efficiencies, and the ability to represent a state does not imply the existence of efficient routines for calculating expectation values or for simulating dynamics with such states. Indeed it has been demonstrated that the problems of evaluating and evolving PEPS are in the challenging complexity class #P-complete [68]. In practice, in higher dimensions to evaluate even local properties of the state, such as operator expectation values, it is necessary to introduce further approximation schemes.

One approach for addressing these complexities is to work with an more restricted variational ansatz than PEPS which has properties that make such calculations tractable. Such further restrictions on the form of the ansatz will inevitably lead to a further loss of simulation accuracy via increased approximation error. However, to pursue this line of investigation, one must hope that this loss will be counterbalanced by a gain in the efficiency of calculation.

Here we consider correlator product states (CPS). These states introduced and characterised in Section 2.2. CPS are defined in any spatial dimension, and constitute and efficiently sample-able subset of PEPS states. A variety of physically interesting states are captured by CPS states [69] including stabiliser states [70], the toric code [71], the Huse-Elser ansatz [72], the Laughlin wavefunction [73], and resonating valence bond states [74]. CPS have been used in various numerical studies to approximate the ground states of strongly correlated systems [69, 72, 75–85].

However, the CPS exhibits a dependence on the basis in which it is defined. Furthermore, unlike MPS and PEPS states, which are frequently used to study dynamics as well as ground state properties, there are no previous studies on the capabilities of using CPS states for capturing time evolution.

We have motivated the use of tensor network ansätze in Section 1.2. We first build on this by discussing methods for dynamically evolving such states in Section 2.1, after which we focus on the properties of the CPS state. Our aims in this study are two-fold:

1. *To develop deterministic methods for optimising and evolving CPS states.* Using the time dependent variational principle outlined Section 2.1 we will then develop an algorithm for evolving this class of states in Section 2.2. The TDVP algorithm is robust and deterministic, bringing advantages over stochastic methods; allows the straightforward access to time evolution information; and permits easy calculation of local expectation values. However there are also disadvantages, principally that the algorithm can only be performed deterministically in one dimension. Nevertheless our characterisation offers some understanding of the CPS ansatz applicable to higher dimensions.

2. *To study the basis dependence of CPS and its interplay with computational error and computational speed-up* CPS states offer a speed-up over MPS states by harnessing some of the special properties of this smaller, more restricted, manifold of states. We find however that this is offset by a reduced capacity for capturing certain correlations. Furthermore we explore the subtle dependency of both this speed up, and this capacity for representing quantum dynamics and ground state properties on the choice of local basis.

## 2.1 The time dependent variational principle (TDVP)

In this section we will define time evolution for quantum states restricted to a variational manifold $\mathcal{M} \subset \mathcal{H}$, such as those introduced in Section 1.2, and discuss some of the structural similarities between classical mechanics and both the TDVP [86], and quantum mechanics itself [87]. These methods, reviewed in [88], were originally proposed by Dirac [89, 90] and Frenkel [91]. Other formalisms which were also developed at that time [92] are also equivalent [93].

We begin with a wavefunction ansatz $|\psi(x)\rangle$ defined by a vector of parameters $x = \{x^i\}_{i=1}^n \in X \subseteq \mathbb{R}^n$. The submanifold $\mathcal{M}$ is then defined by the image $|\psi(X)\rangle = \mathcal{M} \subset \mathcal{H}$. In general the Schrödinger equation

$$\mathrm{i}|\dot{\psi}\rangle = \mathrm{i}\,|\partial_i\psi\rangle\,\dot{x}^i = H\,|\psi\rangle \tag{2.1}$$

will have no solutions, since the left hand side has been restricted by our choice of ansatz, whereas the right hand side remains arbitrary, i.e. we require that $|\psi(t+\delta t)\rangle \in \mathcal{M}$ however the exact infinitesimal update $(1 - \mathrm{i}H\delta t)\,|\psi\rangle \in \mathcal{H}$ is generally not in $\mathcal{M}$. In order to rectify this we define projected dynamics, which do not leave the variational manifold, by the optimisation

$$\dot{x} = \underset{\dot{x}}{\operatorname{argmin}} \left\| \mathrm{i}\dot{x}^i\,|\partial_i\psi\rangle - H\,|\psi\rangle \right\|. \tag{2.2}$$

As shown in Figure 2.1 it can be seen that the solution to this gives a dynamical equation which

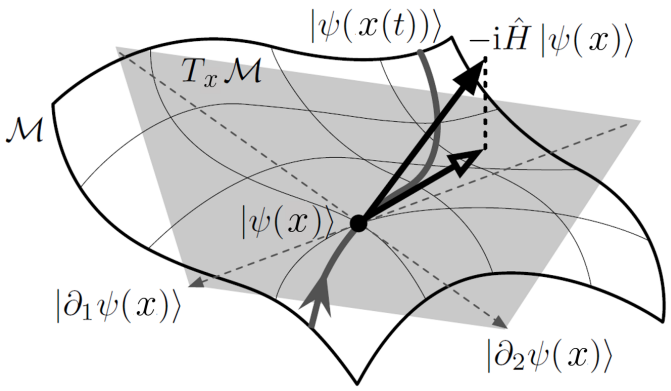


Figure 2.1: The geometry of an infinitesimal update in the time dependent variational principle. The state (black circle) follows a trajectory (solid grey curve) which is confined to the manifold $\mathcal{M}$ (curved grid surface). An exact infinitesimal update moves the state in the direction $-iH\,|\psi(x)\rangle$ (solid arrow) but will in general point out of the manifold $\mathcal{M}$. An infinitesimal update in a direction which lies within the tangent space $T_x\mathcal{M}$ (shaded polygon), made up of the linear span of $\{|\partial_i\psi(x)\rangle\}$ (dashed grey arrows), will not cause the state to leave $\mathcal{M}$. Thus the best permissible approximation to $-iH\,|\psi(x)\rangle$ is found by projecting this vector onto $T_x\mathcal{M}$, yielding the projected update direction (hollow arrow) to which the trajectory is parallel by definition. Figure adapted from ref [94]

.

is projected onto the tangent space

$$\mathrm{i}|\dot{\psi}\rangle = \mathrm{i}\,|\partial_i\psi\rangle\,\dot{x}^i = P_{T_\mathcal{M}} H\,|\psi\rangle\,. \tag{2.3}$$

where $P_{T_\mathcal{M}}$ is the projector onto the tangent space $T_x\mathcal{M}$ made up of directions of evolution that are permitted by the ansatz. $T_x\mathcal{M}$ is given by the linear span of the derivatives of $|\psi\rangle$ with respect to the manifold coordinates $T_x\mathcal{M} = \mathrm{span}\,(\{|\partial_i\psi(x)\rangle\})$.[①] The projected dynamics are then given by solving equation (2.3)

### 2.1.1 Gauge freedoms

Before going further we address the possibility of gauge freedoms: Gauge freedoms occur when there exists a possible shift in coordinates $x \to x' = x + \delta x$ which leaves the physics unaltered. Some gauge freedoms are intrinsic to quantum mechanics, others are artefacts of a given choice of coordinates $x$. These entail that there is a sub-manifold of coordinates in $X$ which all correspond to the same physical state of the system.

A simple example of a gauge freedom is the global phase of $|\psi\rangle$. A change of gauge of this $U(1)$ freedom $|\psi\rangle \to |\psi'\rangle = \mathrm{e}^{-i\alpha(t)}\,|\psi\rangle$ alters the Schrödinger equation as follows

$$\mathrm{i}|\dot{\psi}\rangle = H\,|\psi\rangle + \partial_t\alpha(t)\,|\psi\rangle\,. \tag{2.4}$$

The existence of gauge freedoms may entail that equation (2.2) does not have a unique solution.

This can be resolved by making a choice of gauge which allows us to deterministically integrate the equations of motion. A useful gauge choice we will make is requiring that gauge degrees of freedom do not evolve, i.e. by projecting out any components in $\delta x$ which correspond to gauge freedoms.

In the case of the U(1) gauge freedom this is achieved by projecting out the component of the

[①] Where, in the usual way, for a set $S = \{|n\rangle\}$ the linear span is defined by $\mathrm{span}\,(S) = \{\sum_n \beta_n\,|n\rangle\,|\beta_n \in \mathbb{C}\}$

Schrödinger equation along $|\psi\rangle$.[1] This is puts is in the covariant gauge

$$\mathrm{i}\,|\mathrm{D}_t\psi\rangle = H\,|\psi\rangle - |\psi\rangle\,\frac{\langle\psi|H|\psi\rangle}{\langle\psi|\psi\rangle} \tag{2.5}$$

where the gauge covariant derivative $\mathrm{D}_t$ is defined by

$$|\mathrm{D}_t\psi\rangle = |\dot{\psi}\rangle - |\psi\rangle\,\frac{\langle\psi|\dot{\psi}\rangle}{\langle\psi|\psi\rangle}. \tag{2.6}$$

this yields the projected dynamical equation

$$\mathrm{i}\,|\mathrm{D}_i\psi\rangle\,\dot{x}^i = P_{T\mathcal{M}}H\,|\psi\rangle - P_{T\mathcal{M}}\,|\psi\rangle\,\frac{\langle\psi|H|\psi\rangle}{\langle\psi|\psi\rangle} \tag{2.7}$$

where $|\mathrm{D}_i\psi\rangle$ is defined analogously.

### 2.1.2 Dynamics of TDVP coordinates

We can now find the dynamical equations for $x \in X$ corresponding to the projected Schrödinger dynamics. Taking equation (2.7) and resolving over $\langle\mathrm{D}_j\psi|$, which constitute a basis of vectors that spans the (similarly corrected) tangent space $T_x\mathcal{M} = \mathrm{span}(\{|\mathrm{D}_i\psi\rangle\})$, we obtain

$$\mathrm{i}\langle\mathrm{D}_i\psi|\mathrm{D}_j\psi\rangle\dot{x}^j = \langle\mathrm{D}_i\psi|\,H\,|\psi\rangle \tag{2.8}$$

where we have used $\langle\psi|\mathrm{D}_i\psi\rangle = 0$ and that $P_{T\mathcal{M}}\,|\mathrm{D}_i\psi\rangle = |\mathrm{D}_i\psi\rangle$ by construction. We have here a system of $n$ complex equations defining the behaviour of $n$ real variables, the $x^i$. This tells us there exists a large redundancy in our equations of motion (2.8). This can be resolved in multiple ways, e.g. by taking the real, or imaginary part, and it turns out not to matter how we resolve this[2] [93]. Here we take the real part which yields

$$\begin{aligned}\Omega_{ij}\dot{x}^j &= \frac{\langle\mathrm{D}_i\psi|\,H\,|\psi\rangle + \langle\psi|\,H\,|\mathrm{D}_i\psi\rangle}{\langle\psi|\psi\rangle} \\ &= \partial_i\left(\frac{\langle\psi|H|\psi\rangle}{\langle\psi|\psi\rangle}\right) \\ &= h_i.\end{aligned} \tag{2.9}$$

where we have defined $h_i = \partial_i h$, where

$$h(x) = \langle\psi(x)|H|\psi(x)\rangle/\langle\psi(x)|\psi(x)\rangle \tag{2.10}$$

and the antisymmetric curvature[3] tensor $\Omega_{ij}(x)$ by

$$\Omega_{ij} = \frac{\mathrm{i}\langle\mathrm{D}_i\psi|\mathrm{D}_j\psi\rangle - \mathrm{i}\langle\mathrm{D}_j\psi|\mathrm{D}_i\psi\rangle}{\langle\psi|\psi\rangle}. \tag{2.12}$$

To give a physical meaning to equation (2.9), it is essentially newtons law for the manifold $\mathcal{M}$, defining the dynamics of the system with a force, the first derivative of energtics. It is first order

[1] Though we must be careful not to fix the U(1) gauge freedom if we later choose an ansatz which breaks this gauge symmetry, e.g.by using real valued tensor networks

[2] This is true so long as we satisfy the reasonable condition that for every $|\phi\rangle \in T_x\mathcal{M}$ that $i\,|\phi\rangle \in T_x\mathcal{M}$, i.e. that we do not break the U(1) gauge symmetry [93]

[3] We refer to $\Omega$ as a curvature tensor for its similarity to the Berry curvature, which is most easily seen by writing it as

$$\Omega_{ij} = \mathrm{i}\partial_i\left(\frac{\langle\psi|\partial_j\psi\rangle}{\langle\psi|\psi\rangle}\right) - \mathrm{i}\partial_j\left(\frac{\langle\psi|\partial_i\psi\rangle}{\langle\psi|\psi\rangle}\right) = \partial_i A_j - \partial_j A_i. \tag{2.11}$$

This analogy also makes explicit the structure of the gauge covariant derivative $|\mathrm{D}_i\psi\rangle = (\partial_i + \mathrm{i}A_i)\,|\psi\rangle$

rather than second order simply because the vector $\dot{x}^i$ includes the derivatives of *all* canonical coordinates *and* momenta of the manifold $\mathcal{M}$.[①] In reality this leads to a closer relationship with Hamiltonian classical mechanics a connection we substantiate shortly.

### 2.1.3 Dynamics observable expectation values

For any hermitian operator $K$ we can ask how the expectation value evolves. We can explore this by the chain rule

$$\frac{\mathrm{d}\langle K\rangle}{\mathrm{d}t} = \dot{k} = \partial_i k \dot{x}^i = k_i \dot{x}^i. \tag{2.13}$$

where we use a notation

$$\begin{aligned} k &= \frac{\langle\psi|K|\psi\rangle}{\langle\psi|\psi\rangle} \\ k_i &= \partial_i k \end{aligned} \tag{2.14}$$

To proceed we introduce the contravariant companion $\Omega^{ij}$ to the covariant curvature tensor $\Omega_{ij}$, related by $\Omega^{ij} = \left[\Omega^{-1}\right]_{ij}$. In general gauge symmetries will lead to zeros in the spectrum of $\Omega_{ij}$, our choice of gauge entails that we resolve this problem with the convention $0^{-1} = 0$ for the purposes of calculating $\Omega^{-1}$ (i.e. $\Omega^{-1}$ is the pseudoinverse of $\Omega$ and $\Omega\Omega^{-1}\Omega = \Omega$ as expected). The metric like behaviour of $\Omega^{ij}$ and $\Omega_{ij}$ means we can raise and lower indices in the usual way: $k^i = \Omega^{ij}k_j$ and $k_i = \Omega_{ij}k^j$ [②] Thus from equation (2.9) we have

$$\dot{k} = k_i \dot{x}^i = k_i \Omega^{ij} h_i. \tag{2.15}$$

### 2.1.4 Geometry of the TDVP and quantum mechanics

As an interlude we briefly review some of the observations of refs [86,87,95–97] regarding properties of the TDVP. Some of these properties are surprising, and allow for some interesting insights into quantum mechanics.

#### Time reversible

The TDVP provides a time reversible approximation to full quantum dynamics. This may come as a surprise, as, shown in Figure 2.1, it was explicitly formulated via a projection on a subspace, and since we typically associate projection we the loss of information, one might expect that projecting the Schrödinger equation onto the tangent manifold would have destroyed some information — namely that about the history of components of the full quantum evolution that our manifold could not support. This would lead to time evolution $x(t) \to x(t + \delta t)$ that was many-to-one, i.e. that multiple trajectories which were only differentiated by information in the components which were projected out, would coalesce.

This is not the case and we can see that the process is still well defined under the transformation $t \to -t$, and is in fact completely invariant under $t \to -t$ and $H \to -H$.

#### Conservation of energy

Having arbitrarily deformed the dynamics to suit ourselves, it might seem overly optimistic to expect a notion of conservation of energy at all. However, by equation (2.15) and the antisymmetry of $\Omega$ we have $\dot{h} = h_i\Omega^{ij}h_j = h^i\Omega_{ij}h^j = \dot{x}^i\Omega_{ij}\dot{x}^j = 0$.

[①] much how the classical equation $m\ddot{x} = -\partial_x V(x)$ is recast as the two equations $\dot{p} = -\partial_x V(x)$ and $\dot{x} = \partial_p(p^2/2m)$ by promoting $p = m\dot{x}$ to the level of coordinate

[②] Although in general $\Omega_{ij}\Omega^{jn} \neq \delta_i^n$ we do not encounter inconsistencies as this deviation from the identity is only in directions corresponding to gauge freedoms. No physical observables $k_i = \partial_i k$ have components in gauge directions by definition, and by our gauge choice neither does $\dot{x}_i$. Thus we maintain $\Omega_{ij}\Omega^{jn}k_n = k_i$ and $\Omega_{ij}\Omega^{jn}\dot{x}_n = \dot{x}_i$

**Preservation of other conservation laws**

Let $K$ be a hermitian operator. We can write down a unitary shift operator $S_\lambda = \mathrm{e}^{i\lambda K}$. If for every $|\psi\rangle \in \mathcal{M}$ we have $S_\lambda |\psi\rangle \in \mathcal{M}$ then for every trajectory $x(t) \in X$ there is a partner trajectory $s_\lambda(x(t)) \in X$ related by the action of $S_\lambda$:

$$S_\lambda |\psi(x)\rangle = |\psi(s_\lambda(x))\rangle . \tag{2.16}$$

Expanding to linear order in $\lambda$ and making cancellations this becomes

$$i\lambda K |\psi(x)\rangle = \lambda \partial_\lambda s^i_{\lambda=0} |\partial_i \psi(x)\rangle . \tag{2.17}$$

By closing with $\langle \mathrm{D}_i \psi(x)|$ and comparing with equation (2.14) we see that $\partial_\lambda s^j_{\lambda=0}(x) = k^j(x)$, where $k^j = \Omega^{ji}\partial_i k$ and $k = \langle K \rangle$. Thus to linear order

$$S_\lambda |\psi(x)\rangle = (1 - i\lambda K) |\psi(x)\rangle = |\psi(x)\rangle + \lambda k^i |\partial_i \psi(x)\rangle = |\psi(x + \lambda k)\rangle . \tag{2.18}$$

showing that, for small $\lambda$, the action of $S_\lambda$ in $\mathcal{H}$ is to shift the coordinates $x_i \to x_i + \lambda k_i$.

Now let $K$ be symmetry of $H$, i.e. that $[K, H] = 0$. From this we know that $S_\lambda H S^\dagger_\lambda = H$, and equivalently by taking expectation values and expanding to linear order we find

$$h(x) = h(x + \lambda k) = h(x) + \lambda k^i h_i. \tag{2.19}$$

Cancelling $h$ from both sides we have $k^i h_i = 0$, and thus, from equation (2.15), that $\dot{k} = 0$.

This shows that even in the projected dynamics $[K, H] = 0$ implies that $\langle \dot{K} \rangle = 0$. This is provided that the operation of $K$ is supported by $\mathcal{M}$, a sufficient condition is $K |\psi\rangle = k |\psi\rangle + k^i |\partial_i \psi\rangle$.

**Poisson bracket**

The dynamics of equation (2.9) are generated by the antisymmetric form $\Omega$ correspondingly have the same Poisson structure as classical mechanics. Defining an antisymmetric bracket

$$\{f, g\} = f_i \Omega^{ij} g_j \tag{2.20}$$

and allowing operators to take explicit time dependence, we find that the dynamical equation (2.15) becomes

$$\dot{f} = \{f, h\} + \partial_t f. \tag{2.21}$$

Note that this is *not* Dirac's correspondence principle—the dynamics of on observable $f$ is generated by Hamilton's equation with a quantum Poisson bracket.

**Symplectic structure, canonical coordinates and Hamilton's equations**

It is furthermore possible to show for any choice of manifold $\mathcal{M}$ one can choose coordinates a set of coordinates such that $x = \{q_1, q_2, \cdots, p_1, p_2, \cdots\}$ with

$$\Omega_{p_i q_j} = -\Omega_{q_j p_i} = \delta_{ij} \qquad \text{and} \qquad \Omega_{p_i p_j} = \Omega_{q_i q_j} = 0 \tag{2.22}$$

The steps for finding these coordinates are explicitly shown in ref [96]. This makes the symplectic structure of the dynamics explicit. In these coordinates the dynamical equations (2.9) become the familiar equations

$$\dot{p_i} = \{p_i, h\} = -\frac{\partial h}{\partial q_i} \qquad \text{and} \qquad \dot{q_i} = \{q_i, h\} = \frac{\partial h}{\partial p_i}. \tag{2.23}$$

We do not recount this proof here, but we do show a choice of coordinates that do satisfy equations (2.22): noting that by simply rearranging the definition of $\Omega$ in equation (2.12) we can recast the tensor in the appealing form of a curvature tensor

$$\Omega_{ij} = (\partial_i A_j - \partial_j A_i) \tag{2.24}$$

where $A_i = \mathrm{i}\langle\psi|\partial_i\psi\rangle/\langle\psi|\psi\rangle$. From this we see that the above conditions for $\Omega$ to be in canonical form (equation (2.22)) are automatically satisfied if we assert a condition such as[①]

$$\mathrm{i}\frac{\langle\psi|\partial_{q_i}\psi\rangle}{\langle\psi|\psi\rangle} = p_i \qquad \text{and} \qquad \mathrm{i}\frac{\langle\psi|\partial_{p_i}\psi\rangle}{\langle\psi|\psi\rangle} = 0. \tag{2.26}$$

As a corollary of this it is easily seen that dynamics on the full Hilbert space $\mathcal{H}$ can be written in terms of canonical coordinates, as in equation (1.26). However in that case the canonical coordinates are defined with respect to the eigenbasis and hence identifying the canonical coordinates is tantamount to solving the many-body problem.

### Parent Lagrangian and relation to the path integral

Following the familiar form of equation (2.23) we can reconstruct the corresponding Lagrangian

$$L = \sum_i p_i\dot{q}_i - h = \frac{\langle\psi|i\partial_t - H|\psi\rangle}{\langle\psi|\psi\rangle} \tag{2.27}$$

where we have substituted in the identifications of equation (2.26) to put it in a coordinate-free form. As expected, it can be shown that the Euler-Lagrange dynamical equations of these Lagrangians are indeed equations (2.23) and (2.9).

This result is more well-known, and can be taking as the starting point for deriving the TDVP, which is obtained the variation $\delta\mathcal{S} = 0$ of the action

$$\mathcal{S} = \int_{t_0}^{t_1} \mathrm{d}t \frac{\langle\psi|i\partial_t - H|\psi\rangle}{\langle\psi|\psi\rangle}. \tag{2.28}$$

This action is indeed precisely the action that one obtains from a path integral resolved over the family of states $|\psi(x)\rangle$ [98] (as we will later discuss in more detail in Section 3.2.1).

We thus find the same equations of motion from both (i) projecting the Schrödinger equation directly onto the manifold $\mathcal{M}$ and (ii) resolving the path integral over the states of $\mathcal{M}$[②] and taking the saddle points of this path integral to obtian the TDVP dynamics. That we are able to obtain the same dynamics from two different approaches gives us faith that their form does not not depend on choices we have made along the way.

### Bohr-Sommerfeld quantisation and excited states

As a remark we note that interestingly the utility of the TDVP is not just restricted to the study of ground states and dynamics, and that imposing Bohr-Sommerfeld quantisation condition

$$2\pi n = \sum_i \oint p_i \mathrm{d}q_i = i\int \mathrm{d}t \frac{\langle\psi|\partial_t\psi\rangle}{\langle\psi|\psi\rangle}, \quad n \in \mathbb{Z} \tag{2.29}$$

[①] We find there are many such conditions related by transformations between different canonical coordinates for example

$$\mathrm{i}\frac{\langle\psi|\partial_{q_i}\psi\rangle}{\langle\psi|\psi\rangle} = 0 \qquad \text{and} \qquad \mathrm{i}\frac{\langle\psi|\partial_{p_i}\psi\rangle}{\langle\psi|\psi\rangle} = -q_i. \tag{2.25}$$

would serve equally well

[②] This is achieved in the usual way by inserting resolutions of the identity over $\mathcal{M}$ at each interval $\mathrm{d}t$. The path integral, as usual, also exact provided any state in $\mathcal{H}$ can be expressed as a linear combination of states in $\mathcal{M}$.

it is possible, in certain cases, to use the TDVP to pick out exact eigenstates and their energies [95, 97]. Indicating the possibility of physical relevance to the Fourier spectra of observables in the TDVP.

**A geometric formulation quantum mechanics**

The interesting properties noted here are not specific to the time dependent variational principle and of course are present in quantum mechanics more generally, which is recovered by choosing a manifold that fills the Hilbert space, i.e. $\mathcal{M} = \mathcal{H}$.

These properties of quantum mechanics have been explored in attempts by other authors to frame quantum theory in its entirety in geometrical terms. For more complete discussion of this topic see ref [87] and references therein. Some of the structures of quantum mechanics are very natural in this approach, whereas others, such as projective measurement, are not.[①] The different perspective does however allow us to view quantum theory in a new light.

## 2.2 Correlator product states

In this section we motivate and discuss a special class of tensor network states known as correlator product states (CPS). We then adapt these states to the study of translationally invariant (i.e. uniform) systems to allow us to investigate the thermodynamic limit, this yields uniform correlator product states (uCPS) which will be the focus of the remaining part of the chapter.

### 2.2.1 The CPS ansatz

In this section we introduce the CPS wavefunction and discuss both what kinds of physics it is capable of capturing, and how it relates to other tensor network ansätze.

The CPS ansatz if formed by dividing the lattice into small non-disjoint sets of lattice sites $P$. Each of these is associated with a (generally complex valued) tensor (or plaquette) $C_P^{i_1\cdots i_p}$ which carries an index for every site in $P$ and no sites outside of $P$. The amplitude corresponding to a given lattice configuration $i_1 i_2 \cdots i_N$ is then given by the product $\prod_P C_P^{i_1\cdots i_p}$. This results in the wavefunction ansatz

$$|\psi\rangle = \sum_{i_1\cdots i_N} \prod_P C_P^{i_1\cdots i_p} |i_1 i_2 \cdots i_N\rangle \,. \tag{2.30}$$

The physical site indices carried by each plaquette $C_P$ can be freely chosen. For example a simple CPS ansatz defined on a one dimensional lattice in which plaquettes carry only the indices of nearest neighbours (i.e. the sites $n$ and $n+1$) is denoted

$$\begin{aligned} |\psi\rangle &= \sum_{i_1\cdots i_N} \prod_{n=1}^{N-1} C_n^{i_n i_{n+1}} |i_1 i_2 \cdots i_N\rangle \\ &= \end{aligned} \tag{2.31}$$

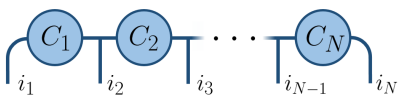


where in the second line we have used the graphical notation introduced in Section 1.3.1. Those familiar with MPS and PEPS will notice that, unlike with those tensor network ansätze, in CPS not all index contractions are bipartite, this is due to the fact that each physical index is generally carried by more than one of the plaquette tensors.[②] In general the sites $i_P$ that a plaquette $P$ covers may be freely chosen and any site can be on any number of plaquettes. However, in

[①] It has been noted that the structure of quantum measurement is incompatible with relativity, hinting that maybe this will have to be revised if quantum mechanics and relativity are to be reconciled. For more see refs [2, 99].

[②] In the graphical representation this leads to some degeneracy of representation as we can join edges corresponding to the same index in any way without changing their meaning, e.g. see equation (2.55)

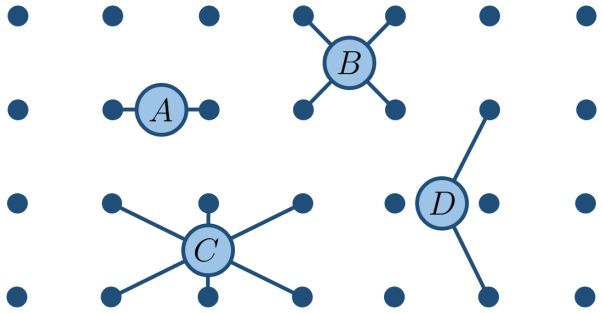


Figure 2.2: A selection of different possible plaquettes defined on a two dimensional square lattice including: a nearest neighbour plaquette $A$, a four-site square plaquette $B$, a six-site rectangular plaquette $C$, and a next-nearest-neighbour plaquette $D$. A CPS wavefunction, as defined in equation (2.30), is then produced by tiling the entire lattice with one or more types of plaquette.

.

order to maintain computational efficiency it is necessary that either; the number of sites on any given plaquette does not grow with the system size, and that the number of plaquettes is at most polynomial in the system size; or that a further approximation scheme is employed to compress that data stored in the plaquette tensors.

Though in this work we address the properties of the CPS ansatz in one-dimension, CPS are in principle readily generalisable to higher dimensions, as shown in Figure 2.2.

### 2.2.2 Correlations in CPS wavefunctions

Here we address the question of what kinds of correlations can be captured using the CPS ansatz, and how we might understand the CPS manifold.

The CPS is able to easily capture local correlations in a known basis, for example if we consider a 1D anti-ferromagnetic chain, the ground state $|\psi\rangle \sim |\uparrow\downarrow\uparrow\downarrow\cdots\rangle + |\downarrow\uparrow\downarrow\uparrow\ldots\rangle$ is easily captured by equation (2.31) with

$$C_n = \begin{pmatrix} 0 & 1 \\ 1 & 0 \end{pmatrix}. \tag{2.32}$$

Some small, locally varying, density $\rho_n$ of excitations (i.e. domain walls such as $|\cdots\uparrow\downarrow\uparrow\downarrow\downarrow\uparrow\downarrow\uparrow\cdots\rangle$) can be included in this ansatz by relaxing the zeros of the on diagonal elements

$$C_n = \begin{pmatrix} \sqrt{\rho_n} & \sqrt{1-\rho_n} \\ \sqrt{1-\rho_n} & \sqrt{\rho_n} \end{pmatrix}. \tag{2.33}$$

where $\rho_n = \langle\psi|P_n|\psi\rangle$ and where $P_n = |\uparrow\uparrow\rangle_{n,n+1}\langle\uparrow\uparrow| + |\downarrow\downarrow\rangle_{n,n+1}\langle\downarrow\downarrow| = (1+\sigma_n^z\sigma_{n+1}^z)/2$ measures for presence of an excitation. However the positions of these excitation are entirely uncorrelated, and it is easily shown that the excitation position correlation function

$$\mathrm{Corr}(n,m) = \langle\psi|P_nP_m|\psi\rangle - \langle\psi|P_n|\psi\rangle\langle\psi|P_m|\psi\rangle = 0 \tag{2.34}$$

for all $n \neq m$. These correlations cannot be non-zero without extending the ansatz to include longer range plaquettes. This hints at the limitations of the CPS ansatz, in its explicit inability to properly capture certain kinds of correlations between regions which do not feature on the same plaquette.

To develop a formal statement from this intuition we consider a generic CPS state defined on a lattice. We then partition the system into 3 regions, $A$, $B$ and $C$ such that there are no plaquettes which have support in both $A$ and $B$. We can then enumerate the states of the regions $A$, $B$ and $C$ with $|i_A\rangle$, $|i_B\rangle$ and $|i_C\rangle$ respectively, and write $C_A$ and $C_B$ as the product of all plaquettes which have support in $A$ or $B$, and $C_C$ as the product of all remaining plaquettes. This proceeds as

follows

$$\begin{aligned}|\psi\rangle &= \sum_{i_1\cdots i_N}\prod_P C_P^{i_1\cdots i_p}|i_1 i_2\cdots i_N\rangle \\ &= \sum_{i_1\cdots i_N}\underbrace{\left(\prod_{P\in A}C_P^{i_1\cdots i_p}\right)}_{C_A}\underbrace{\left(\prod_{P\in B}C_P^{i_1\cdots i_p}\right)}_{C_B}\underbrace{\left(\prod_{P\notin(A\cup B)}C_P^{i_1\cdots i_p}\right)}_{C_C}|i_1 i_2\cdots i_N\rangle \\ &= \sum_{i_A i_B i_C} C_A^{i_A i_C}C_B^{i_C i_B}C_C^{i_C}|i_A i_B i_C\rangle\end{aligned} \tag{2.35}$$

where a plaquette is said to be in a region if *any* of the sites on which has support are in that region. The reduced density matrix on $A, B$ is then given by the separable state

$$\begin{aligned}\rho_{AB} &= \sum_{i_A i_B j_A j_B \alpha} C_A^{i_A\alpha}C_B^{\alpha i_B}\bar{C}_A^{j_A\alpha}\bar{C}_B^{\alpha j_B}|C_C^\alpha|^2|i_A i_B\rangle\langle j_A j_B| \\ &= \sum_\alpha p_\alpha \rho_\alpha^A\otimes\rho_\alpha^B\end{aligned} \tag{2.36}$$

where $\alpha$ enumerates the states of $C$ and the $\rho_\alpha^A$ are rank-1 projectors given by

$$\rho_\alpha^A = \frac{1}{\sum_{i_A}\left|C_A^{i_A\alpha}\right|^2}\left(\sum_{i_A}C_A^{i_A\alpha}|i_A\rangle\right)\left(\sum_{j_A}\bar{C}_A^{j_A\alpha}\langle j_A|\right) \tag{2.37}$$

and similarly for $\rho_\alpha^B$, and the probabilities are given by

$$p_\alpha = |C_C^\alpha|^2\sum_{i_A}\left|C_A^{i_A\alpha}\right|^2\sum_{i_B}\left|C_B^{i_B\alpha}\right|^2. \tag{2.38}$$

Furthermore if instead of tracing out $i_C$, we projected it onto a definite state $|\alpha\rangle\in\{|i_C\rangle\}$ our final state would be the purification of equation 2.36

$$\rho = \rho_\alpha^A\otimes\rho_\alpha^B\otimes|\alpha\rangle_C\langle\alpha|. \tag{2.39}$$

which is both a product state and a pure state.

Thus we arrive at the following two characteristics properties of the CPS manifold:

1. Let $A$ and $B$ be any two disjoint regions such that there are no plaquettes with support in both of these regions $A$ and $B$. It follows that the reduced density matrix $\rho_{AB}$ (obtained by tracing out their complement $C = (A\cup B)^c$) is a separable state on $AB$ and there is no *quantum entanglement* between $A$ and $B$.

2. Let $A$ be any subregion of the full system. Let $\partial\subset A^c$ be the boundary region into which plaquettes with support in $A$ extend, and let $\bar{A} = (A\cup\partial)^c$ denote the rest of the system. It follows that there exists a set of projective measurements which acts only on the boundary region $\partial$ such that, regardless of the outcome of the measurement, the post-measurment state is a product state between $A$, $\bar{A}$ and $\partial$. Hence in this post measurement state there are no *classical or quantum* correlations between $A$, $\bar{A}$ or $\partial$.

These arrangements are depicted in Figure 2.3. Contrasting these statements with the observation that arbitrary quantum correlations can be represented within a plaquette, we see that CPS states are ones in which quantum correlations are restricted to the support of plaquettes.

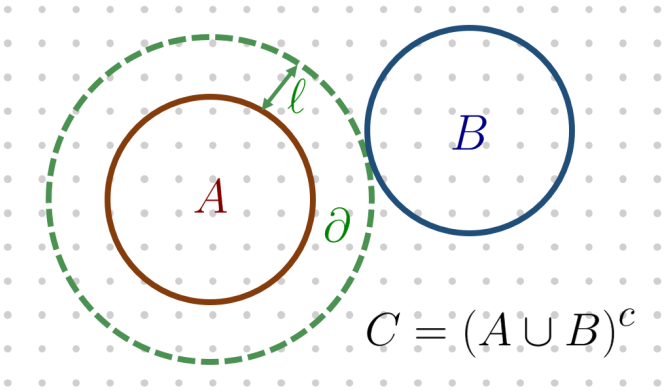


Figure 2.3: *Correlations in CPS states.* For two regions $A$ and $B$ separated by a distance greater than the plaquette size $\ell$ correlations are always classical. This is in the sense that the reduced density matrix $\rho_{AB}$ is a separable state. Furthermore if a projective measurement in the CPS basis is made over a buffer region $\partial$ (i) divides the system in two (ii) has a minimum thickness of $\ell$, then the post measurement $\rho_{AB}$ state is a product state. In planar geometry the smallest such region $\partial$ is a buffer region which is tight to either $A$ or $B$ as shown.

### 2.2.3 Relationship of CPS states to other tensor networks

Here we discuss the relationships between correlator product states and other tensor network states.

#### Matrix product states

We note that by substituting equation (2.32) into equation (2.31) the wavefunction for the anti-ferromagnetic cat state can be recast as

$$\begin{aligned} |\psi\rangle &= (|\uparrow\rangle \quad |\downarrow\rangle) \begin{pmatrix} 0 & 1 \\ 1 & 0 \end{pmatrix} \begin{pmatrix} |\uparrow\rangle & 0 \\ 0 & |\downarrow\rangle \end{pmatrix} \begin{pmatrix} 0 & 1 \\ 1 & 0 \end{pmatrix} \begin{pmatrix} |\uparrow\rangle & 0 \\ 0 & |\downarrow\rangle \end{pmatrix} \cdots \begin{pmatrix} 0 & 1 \\ 1 & 0 \end{pmatrix} \begin{pmatrix} |\uparrow\rangle \\ |\downarrow\rangle \end{pmatrix} \\ &= (|\uparrow\rangle \quad |\downarrow\rangle) \begin{pmatrix} 0 & |\downarrow\rangle \\ |\uparrow\rangle & 0 \end{pmatrix} \begin{pmatrix} 0 & |\downarrow\rangle \\ |\uparrow\rangle & 0 \end{pmatrix} \cdots \begin{pmatrix} |\downarrow\rangle \\ |\uparrow\rangle \end{pmatrix} \end{aligned} \tag{2.40}$$

making explicit the matrix-product state form of this CPS state. This is an example of slightly more general relationship: consider a generic 1D CPS state defined on a lattice with local Hilbert space dimension $d$. We say that two sites $i$ and $j$ are connected if there is a plaquette with support on both $i$ and $j$. For a CPS state in which each each plaquette connects a contiguous series of $n$ sites, the CPS state can be written in a matrix product form with a bond dimension

$$\chi_{\text{CPS}} \leq d^{n-1}. \tag{2.41}$$

However this CPS ansatz does not cover the space of MPS states of bond dimension $d^n$, but is a further restriction on them.

As an example of this relationship if we consider a CPS state with 4-site plaquette with local Hilbert space dimension $d$ denoted by

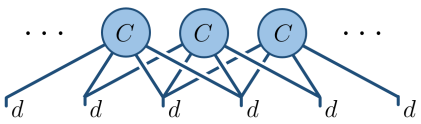


(2.42)

where the $\cdots$ indicate continuation of the motif. Purely by deformation of the graphical notation

we can rearrange this into the form

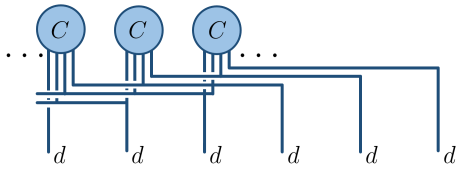


(2.43)

from which it is clear that making the identification

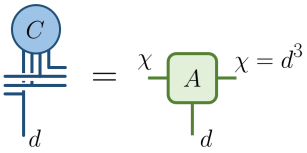


(2.44)

puts us into the MPS form with, given equation (2.41) the plaquette size of $n = 4$, the expected bond order of $\chi = d^3$

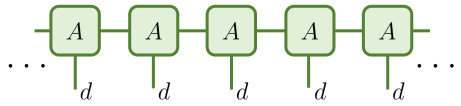


(2.45)

This mapping however is not unique, and by deforming equation 2.43 in a different manner, we can make other identifications analogous to equation 2.44 which also bring us into MPS form. Similar arguments can be made to relate CPS to PEPS in higher spatial dimensions.

CPS states can only be efficiently represented by PEPS (or MPS in one dimension) when the plaquettes act only locally. If the plaquettes are non-local, the CPS representation may remain efficient, even though the bond order of the equivalent PEPS manifold diverges. This is the case for example for a CPS state in which there are two site plaquettes connecting every possible pair $i, j$. This state is represented by $N(N-1)/2$ two-site correlators, but the bond dimension of the smallest MPS manifold in which it can be embedded is $\chi \sim d^{N^2/4}$. The Laughlin wavefunction, an well-known ansatz for the ground state of a two-dimensional electron gas in a magnetic field, is an example of such a CPS state [69].

#### String bond states

As mentioned previously in passing, the plaquettes need not be explicitly stored, but may themselves calculated using a another ansatz which further compresses the information stored in plaquettes. One example of this is string bond states [100], in which the plaquettes are one dimensional strings on a higher dimensional lattice. The plaquette tensors $C_P^{i_1 i_2 \cdots i_p}$ are then stored as matrix product states, this arrangement is depicted in Figure 2.4.

### 2.2.4 Uniform correlator product state (uCPS)

In what follows of this chapter we are mostly concerned with a subclass of uniform (translationally invariant), CPS in one spatial dimension, in the thermodynamics limit. The sub-class we consider has the further restriction that each lattice site is on at most two plaquettes. These states will be refereed to as uniform correlator product states.

A simple two-site plaquette uCPS is thus represented given by

$|\psi_2\rangle =$ 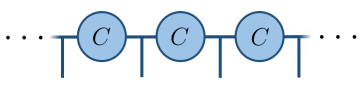


(2.46)

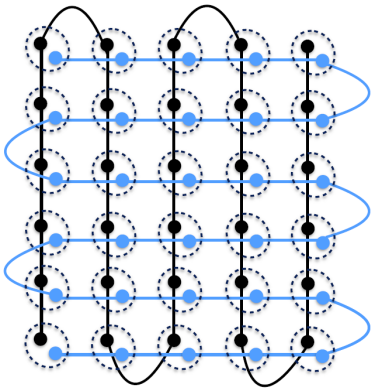

Figure 2.4: A string bond states on a two dimensional lattice. This is a CPS with two one dimensional plaquettes which snake over the lattice. The solid circles indicate the indices of the string bond state, and the dashed circles physical sites, (which are connected to multiple indices).

.

However, with the definition above, it is also possible to bring any uCPS into this form, for example consider the four-site plaquette uCPS

$$|\psi_4\rangle = \quad \cdots \; C \; C \; C \; \cdots \quad d \; d \; d \; d \; d \; d \; d \; d \tag{2.47}$$

where $d$ is the local Hilbert space dimension. By deformation of the graphical notation this becomes

$$|\psi_4\rangle = \quad \cdots \; C \; C \; C \; \cdots \quad d \; d \; d \; d \; d \; d \; d \; d \quad . \tag{2.48}$$

And finally by a simple redefinition in which the local Hilbert space dimension is expanded $d \to d^2$ we obtain the same uCPS form as in equation (2.46)

$$|\psi_4\rangle = \quad \cdots \; C \; C \; C \; \cdots \quad d^2 \; d^2 \; d^2 \; d^2 \quad . \tag{2.49}$$

### Relationship to uMPS

Here we ascertain the parameters of the uMPS with which uCPS can be meaningfully compared.

We showed in Section 2.2.3 that a generic CPS with $n$-site plaquettes can be written as an MPS with bond order $\chi = d^{n-1}$. However the further restriction we have made that in uCPS each physical index is carried by at most two plaquettes makes possible a better identification, in which each plaquette is identified with $n/2$ uMPS, e.g. for $n = 6$ we have

$$C \quad d^3 \quad = \quad C \quad d \quad d \quad d \quad . \tag{2.50}$$

where each dotted box is identified with a tensor of a uMPS with $n/2$-site translational invariance bond order

$$\chi_{\text{uCPS}} = d^{n/2}. \tag{2.51}$$

### Boundary conditions and gauge freedoms in uCPS

The translationally invariant uCPS wavefunction

$$|\psi\rangle = \sum_{i_1 i_2 \cdots i_{N-1} i_N} C^{i_1 i_2} C^{i_2 i_3} \cdots C^{i_{N-1} i_N} |i_1 i_2 i_3 \cdots i_{N-1} i_N\rangle$$

$$= \quad \text{  } \quad (2.52)$$



has a near gauge freedom $C^{ij} \to C^{ij} z^j / z^i$ where the $z^i$ tensors generated by neighbouring plaquettes cancel everywhere except on the ends of the system. In order to promote this to a full gauge freedom, as will prove useful when study the dynamics, we include additional single-site plaquettes $v_L$ and $v_R$ at the boundaries of the system giving

$$|\psi\rangle = \sum_{i_1 i_2 \cdots i_{N-1} i_N} v_L^{i_1} C^{i_1 i_2} C^{i_2 i_3} \cdots C^{i_{N-1} i_N} v_R^{i_N} |i_1 i_2 i_3 \cdots i_{N-1} i_N\rangle$$

$$= \quad \text{ 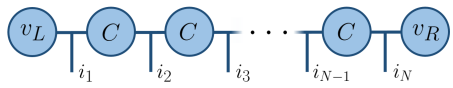 } \quad (2.53)$$



### Expectation values and the uCPS transfer matrix

Here we compare the costs of contracting comparable uCPS and uMPS tensor networks. The expectation value of a local operator $O$ is given by

$$\langle\psi|O|\psi\rangle = \quad \text{ 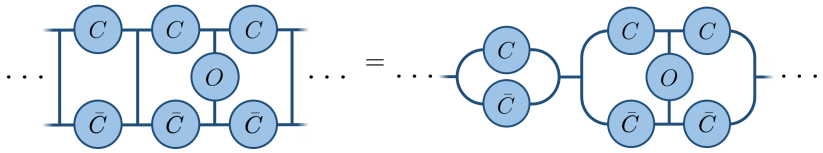 } \quad (2.54)$$



where we have used that networks composed purely of edges can be freely deformed without changing their meaning. An example of this is the identity

$$\quad \text{  } \quad (2.55)$$

Thus it is clear that expectation values of local operators include infinite chains of the $\chi \times \chi$ transfer matrix $E$ (where as before $\chi = d^{n/2}$) which is defined element-wise by $E^{ij} = |C^{ij}|^2$, or equivalently

$$\quad \text{ 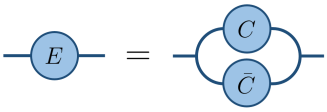 } \quad (2.56)$$



### Computational costs in uCPS

The $\chi \times \chi$ transfer matrix $E$ defined in equation (2.56) allows for a favourable comparison with uMPS, in which the corresponding transfer matrix is $\chi^2 \times \chi^2$. This is leads to a computational advantage specific to the uCPS submanifold of the uMPS state space: since a uCPS maps to an $n/2$-site uMPS [①] with physical dimension $d$ and bond dimension $\chi = d^{n/2}$ (see equation (2.51)), and the cost of calculating local uMPS expectation values is $\mathrm{O}(nd\chi^3) \sim \mathrm{O}(d\chi^3 \log \chi)$. Given the efficiency of these routines, one might naively anticipate that the cost of evaluating local expectation values in uCPS will scale in this way too. However the smaller uCPS transfer matrix makes possible an evaluation with cost $\mathrm{O}(\chi^3)$. The details of how this efficient contraction is computed are given in appendix C.1

[①] an $m$-site uMPS is an infinite MPS state which is invariant under translation by $m$ sites

### 2.2.5 TDVP with uCPS

As discussed is Section 2.1, when restricted to a variational wavefunction $|\psi(x)\rangle$ on a sub-manifold $\mathcal{M}$ of the full Hilbert space $\mathcal{H}$, there is in general no solution to the exact Schrödinger equation, and instead we define dynamics via equation (2.2). Making trivial generalisations to the prescription of Section 2.1 on account of the fact that our variational parameters $C^{ij}$ are complex[①] we obtain the dynamical equation

$$\Omega_{ij,kl}\dot{C}^{kl} = h_{ij} \tag{2.57}$$

where $\Omega_{ij,kl} = \mathrm{i}\langle\partial_{ij}\psi|\partial_{kl}\psi\rangle - \mathrm{i}\langle\partial_{ij}\psi|\psi\rangle\langle\psi|\partial_{kl}\psi\rangle$, $h_{ij} = \langle\partial_{ij}\psi|\,H\,|\psi\rangle - \langle\partial_{ij}\psi|\psi\rangle\,\langle\psi|\,H\,|\psi\rangle$, and we note use of the conventions $|\partial_{ij}\psi\rangle = \dfrac{\partial\,|\psi\rangle}{\partial C^{ij}}$ is the derivative with respect to $C^{ij}$, $\langle\partial_{ij}\psi| = \dfrac{\partial\,\langle\psi|}{\partial \bar{C}^{ij}}$ is the derivative with respect to the complex conjugate $\bar{C}^{ij}$, and we take $\langle\psi|\psi\rangle = 1$ (which is achieved by rescaling the $C^{ij}$ such that the transfer matrix $E$ has a principal eigenvalue $\lambda_1 = 1$).

#### Gauge fixing

Following Section 2.1.1 we then fix the gauge degrees of freedom. The most prominent gauge freedom of the uCPS state is the transformation $C^{ij} \to C^{ij}z^j/z^i$. This freedom is fixed by requiring $\langle\psi|\partial_{ij}\psi\rangle \mathrm{d}C^{ij} = 0$: for which, with uCPS, it is sufficient to require that

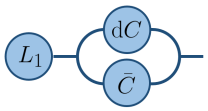


$$= 0 \tag{2.58}$$

or symbolically, that $\sum_i L_1^i \mathrm{d}C^{ij}\bar{C}^{ij} = 0$, where $L_1$ is the principal eigenvector of the transfer matrix $E$. This gauge fixing has the added desirable property that $\Omega_{ij,kl}$ becomes the entirely local object

$$\Omega_{ij,kl} = \mathrm{i}\langle\partial_{ij}\psi|\partial_{kl}\psi\rangle = \mathrm{i}$$

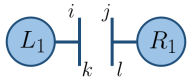


$$. \tag{2.59}$$

To see how to impose this condition we change coordinates to the basis of left and right eigenvector $L_\alpha$ and $R_\alpha$ of the transfer matrix by writing

$$\mathrm{d}C^{ij}\bar{C}^{ij} = \sum_{\alpha\beta} \mathrm{d}B^{\alpha\beta} R^i_\alpha L^j_\beta \tag{2.60}$$

where $B$ is a $\chi \times \chi$ matrix, and the transfer matrix is given by

$$E^{ij} = \sum_{\alpha=1}^{\chi} \lambda_\alpha R^i_\alpha L^j_\alpha \tag{2.61}$$

with $\lambda_1 = 1$, and $|\lambda_\alpha| < 1$ otherwise. We see that the gauge condition in 2.58 now becomes $\mathrm{d}B^{\alpha\beta} = 0$ for $\alpha = 1$. Thus we define $B^{\tilde{\alpha}\beta}$, a $(\chi - 1) \times \chi$ matrix in which $\tilde{\alpha}$ runs over $2 \ldots \chi$. With this condition in place, we can then work entirely in the $B$ coordinates by making use of the chain rule with equation 2.60. Thus the analogue of equation (2.57) is given by

$$\Omega_{\tilde{\alpha}\beta\tilde{\gamma}\delta}\dot{B}^{\tilde{\gamma}\delta} = h_{\tilde{\alpha}\beta} = \langle\partial_{\tilde{\alpha}\beta}\psi|\,H\,|\psi\rangle \tag{2.62}$$

where as before we use the conventions $|\partial_{\tilde{\alpha}\beta}\psi\rangle = \frac{\partial|\psi\rangle}{\partial B^{\tilde{\alpha}\beta}}$ is the derivative with respect to $B^{\tilde{\alpha}\beta}$, $\langle\partial_{\tilde{\alpha}\beta}\psi| = \frac{\partial\langle\psi|}{\partial \bar{B}^{\tilde{\alpha}\beta}}$ is the derivative with respect to the complex conjugate $\bar{B}^{\tilde{\alpha}\beta}$ . Thus by inverting

[①] We could equally well follow Section 2.1 and work with a doubled space of real parameters (which we did there as it makes some interesting structures very apparent) using e.g. $z_i = x_i + \mathrm{i}y$ or $z_i = r_i e^{i\theta_i}$ but it turns out to be marginally simpler in this instance to work in a space of complex parameters.

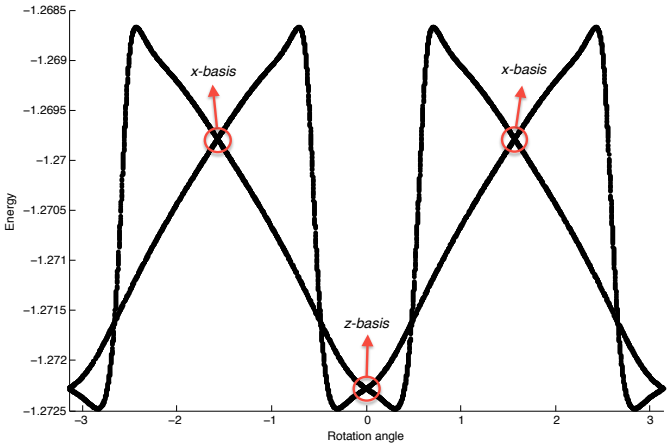


Figure 2.5: *The behaviour of 2-site overlap uCPS ground state energy approximations for the quantum Ising model at criticality:* the calculated energies are given as a function of the angle $\theta$ which defines the local basis used in the CPS ansatz $|\pm\rangle = \cos\theta\,|\uparrow\rangle \pm \sin\theta\,|\downarrow\rangle$. The TDVP algorithm exhibits unique convergence to the global minimum only at the points marked by the red circles, which denote the $z$- and $x$- basis choices, and at an intermediate point. In general, depending on the details of the initial random state, imaginary time TDVP will converge to one of the minima associated with the splitting of otherwise degenerate energy levels, which occurs due to the lack of rotation invariance of the uCPS Ansatz.

$\Omega$ in equation 2.62 the gauge fixed uCPS TDVP time derivative $\dot{C}$ allowing for numerically stable and deterministic integration of the equations of motion.

#### Efficient implementation of uCPS TDVP

The integration of the equations of motion 2.62 and evaluation of local expectation values can be performed with computational costs $\mathrm{O}(\chi^3)$. We elaborate how this high efficiency is achieved at the two key bottlenecks in appendix C.

## 2.3 Ground state approximations with CPS

In this section uCPS is used to approximate the ground states of several canonical models. Approximated ground states are obtained by imaginary time evolution, using a trivial extension of the dynamical equations of Section 2.2.5.

The investigate the capacity of the uCPS ansatz to capture ground state properties both near and far from criticality. We are also able to study the sensitivity of this capacity to the choice of basis in which the uCPS is defined.

### 2.3.1 Basis dependence

In this section we review the effect of choice of local basis on the capacity of the CPS ansatz to capture ground state properties. We first consider the transverse field Ising model

$$H = -\sum_i \sigma_i^z \sigma_{i+1}^z + h \sum_i \sigma_i^x \tag{2.63}$$

which is critical for $h = \pm 1$. In Figure 2.5 we show the ground state energies of the critical $h = 1$ Hamiltonian approximated using 4-site plaquette uCPS ansätze (as in equation (2.47)) defined in a range of bases related by on-site rotations. From this some observations are immediate:

- *Existence of local minima:* the two branches in Figure 2.5 correspond to different fixed points of the imaginary time evolution reached from different initial conditions. This multiplicity

implies the existence of local minima. Our analysis did not uncover a way of knowing *a priori* to which minima an initial configuration will converge.

The exact ground state at $h = 1$ is quantum critical but both uMPS and uCPS are unable to capture this[①] and the system is effectively in the ferromagnetic phase (this behaviour is apparent in Figure 2.13 and ref [101]). The double branch is found to be related to the doubly degenerate ground state of this phase. This symmetry is explicitly broken by the CPS ansatz except when the local basis is aligned to the $x$ or $z$ axes. Consistent with this understanding the branching is not observed in the paramagnetic phase.

The symmetry of the problem is respected when the basis is $x$ or $z$. At these points, as well as at one intermediate point, the TDVP converges to a unique global minimum. The intermediate points correspond approximately to the mean field theory solutions to the model.

- *Dependency on entanglement generating terms:* Roughly speaking the approximated ground state energy is improved when the basis is aligned closer to the entanglement generating $\sigma_i^z\sigma_{i+1}^z$ term: notably the $z$ basis is better than the $x$ basis. However it is interesting that the best energy estimate is *not* obtained for the $z$ basis, but for an intermediate orientation, though at this optimal point convergence to the global minimum is not guaranteed.

A simple generalisation of the transverse Ising model in equation 2.63 is the XY model

$$H = -\sum_i \left( \frac{1+\gamma}{2}\sigma_i^x\sigma_{i+1}^x + \frac{1-\gamma}{2}\sigma_i^y\sigma_{i+1}^y \right) + h\sum_i \sigma_i^z \tag{2.64}$$

for which the transverse field Ising model is recovered for $\gamma = \pm 1$. In the range $0 < h < 1$ and $0 \leq \gamma \leq 1$ the ground state is doubly degenerate. However at $\gamma = 0$ this symmetry increases from $\mathrm{Z}_2$ to $U(1)$. We use this to test the relation between the multiplicity of local minima in the variational manifold and the dimension of the ground state manifold of the full quantum problem. We find that, consistent with our understanding, at $\gamma = 0$ the multiplicity of local minima appears to be correspondingly infinite (i.e. that the number of local minima increases without bound as $n$ increases), that there is no local basis for which the optimization converges to a unique fixed point, and that the $\mathrm{O}(\chi^4) \to \mathrm{O}(\chi^3)$ speed-up is lost.

One resolution to this is to sample local basis choices when finding ground states of models, such as the XY model, for which the deterministic optimisation of CPS has many fixed points. With this strategy it becomes questionable whether the deterministic optimisation algorithm is better than Monte Carlo. A better solution is to promote the local unitary rotation to a variational parameter, a possibility for future study.

When the ground state symmetry is further increased to SU(2), as in the Heisenberg model

$$H = -\sum_i \boldsymbol{\sigma_i} \cdot \boldsymbol{\sigma_{i+1}} \tag{2.65}$$

the branches are no longer observed, as the invariance of the Hamiltonian implies that the uCPS approximations must be similarly invariant, and convergence is always to the global minimum.

The issue of basis dependence is certainly one of concern for the CPS anstaz, whether optimizing with imaginary time evolution, or other deterministic or Monte Carlo methods. It appears that what constitutes an optimal basis is both model and goal dependent. However we note that aligning the local bases to entanglement generating terms (where possible) is a justifiable heuristic.

[①] One would anticipate that any variational ansätze with finite range correlations will be similarly unable to correctly capture the position of the critical point. In an attempt to address this failure other authors have investigated variational ansätze, such as tree-tensor-networks [37] and MERA [45], with structures designed to capture long range correlations and critical phenomena.

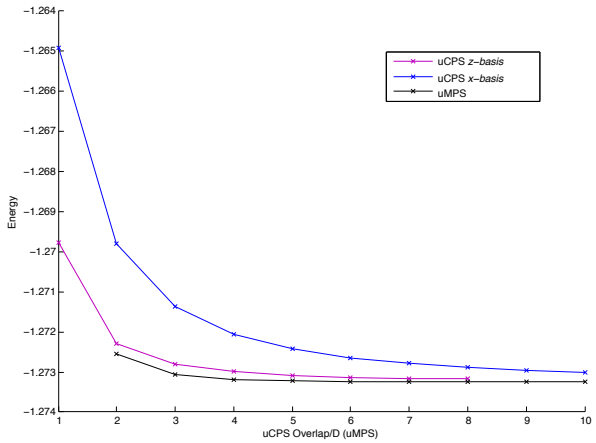


Figure 2.6: *Convergence of uCPS and uMPS ground state energies for the transverse Quantum Ising model at criticality:* The horizontal axis denotes the bond dimension $\chi$ for uMPS data and overlap size $n/2$ where $n$ is the plaquette size for uCPS data. Data is shown for $x$-basis uCPS (blue) $z$-basis uCPS (red) and MPS (black).

### 2.3.2 Ground state convergence at Criticality

Next we investigate the ground state convergence properties of the transverse field quantum Ising model at criticality, comparing uCPS in the $z$ and $x$ bases with uMPS. As noted, TDVP always converges to the global minimum for these basis choices.

Figure 2.6 demonstrates that the uCPS ground state energy estimates are better for the $z$ than for the $x$-basis choice (this is also evidenced for 2-site uCPS overlap in Figure 2.5). Surprisingly we find that, while the uMPS energy converges roughly polynomially as a function of bond dimension $\chi_{(\text{uMPS})}$ (since the model is critical), the uCPS energy converges instead polynomially *with the size of the uCPS overlap* $n/2$. Thus, since $\chi_{(\text{uCPS})} = 2^{n/2}$, to achieve the same order of accuracy in the energy estimates uCPS requires an exponentially larger bond dimension than uMPS.

Complementing this result is another surprising observation, depicted in the plot in Figure 2.7: the total time needed to reach convergence to same accuracy scales similarly for uMPS with respect to bond dimension and for uCPS with respect to overlap size.

Thus, the indications from this example are that, even though the *computer memory* costs are exponentially larger for uCPS than for uMPS, the *computer time* needed to reach some desired accuracy for the ground state energy approximation scales in the same way for both uCPS and uMPS. This result seems to be generic, and is observed to hold for all the models studied in this chapter.

In this context it is also useful to consider the $SU(2)$ invariant Heisenberg model, so that it is impossible to pick out some preferred basis choice. This allows one to avoid the complications associated with basis dependence. However, the result of using an orientation dependent ansatz on a rotation invariant Hamiltonian manifests in extremely slow convergence of the ground state energy approximations, as a function of uCPS overlap. This is compared to what is observed for models whose entanglement generating terms point in a definite direction, such as e.g. the quantum Ising model. This is illustrated by the plot in Figure 2.8. In addition, the computational time required for TDVP to converge are much longer, at equal uCPS overlap, than for the quantum Ising model. For example, the maximal bond dimension that we could achieve in reasonable time is $\chi_{\text{uCPS}} = 2^6$, and the corresponding energy density reproduces the correct result only to three digits. This slowdown originates in the iterative subroutine for inverting $\Omega$ in the TDVP algorithm, which requires a much larger number of iterations to converge to the required accuracy.

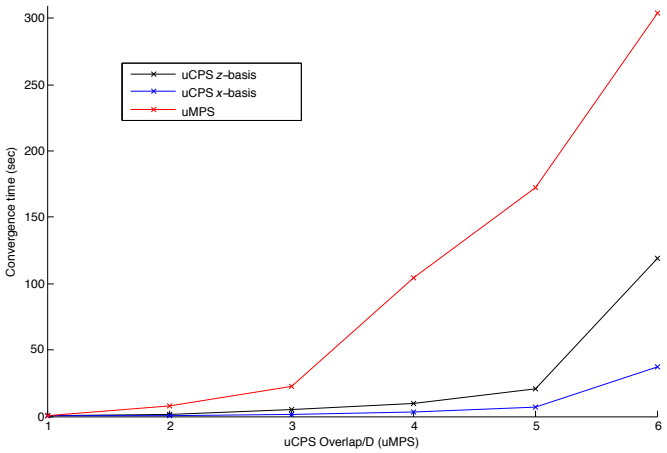


Figure 2.7: *Convergence times for uCPS and uMPS approximations for the ground state of the quantum Ising model at criticality:* The hotizontal axis denotes overlap size for uCPS data, and bond dimension for uMPS data.

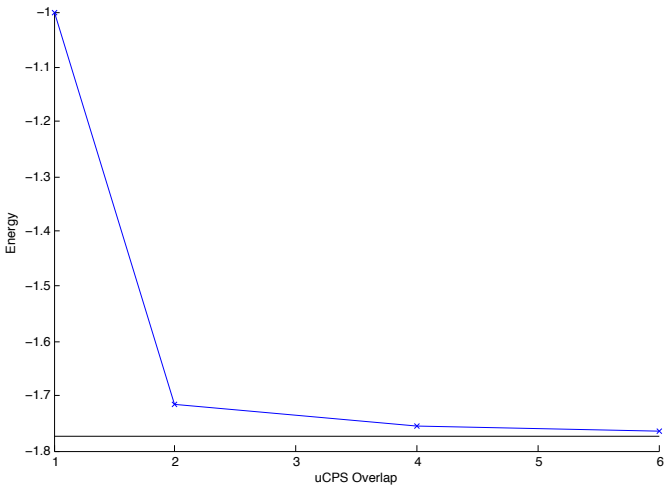


Figure 2.8: *Convergence of uCPS ground state energies for the Heisenberg model.* The black horizontal line denotes the exact energy. Whilst the uCPS approximations are not basis dependent, convergence turns out to be very slow.

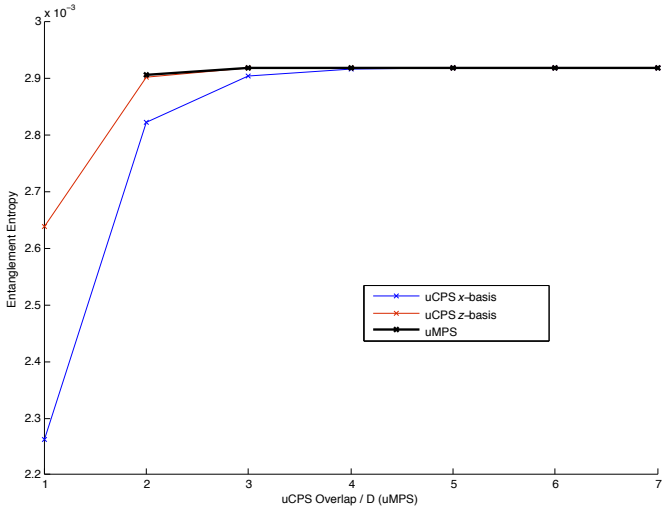


Figure 2.9: *Entanglement entropy $S$ as function of uCPS overlap/uMPS bond dimension $\chi$*: Data plotted for the quantum Ising model in the ordered gapped phase ($J = 1$, $h = 0.5$).

### 2.3.3 Ground state convergence in the gapped phase

Next we examine the ground state convergence of uCPS deep in the gapped phase. The observations made above, regarding the computational time and memory costs of uCPS vs. that of uMPS, remain true away from criticality. Here we shall demonstrate that the analogous observations also hold for two rather different types of physical quantities, namely the correlation length $\mu$ and the entanglement entropy $S$. The correlation length is obtained from the largest eigenvalue $\lambda_2$ of the transfer matrix smaller than 1 as:

$$\mu_{\mathrm{uMPS}} = -\frac{1}{\log(\lambda_2^{(\mathrm{uMPS})})} \quad , \quad \mu_{\mathrm{uCPS}}(n) = -\frac{n}{2\log(\lambda_2^{(\mathrm{uCPS})})} \ , \tag{2.66}$$

for uMPS and uCPS, respectively, where $n/2$ is the uCPS overlap. The entanglement entropy $S$ is the simplest measure, for pure quantum states defined on a region $R$, of entanglement between a sub-region $A \subset R$ and the rest of the system. It is defined as:

$$S = -\mathrm{tr}\left[\rho_A \log \rho_A\right] = -\sum_i \lambda_i^2 \log \lambda_i^2 \ , \tag{2.67}$$

where $\lambda_i$ are the Schmidt coefficients corresponding to the density matrix $\rho_A$ associated with the sub-region $A$. One can show that the Schmidt coefficients corresponding to a cut of the infinite spin chain into two semi-infinite sub-chains are given by the singular values of $\rho_l^{\frac{1}{2}} \rho_r^{\frac{1}{2}}$, where $\rho_l$ and $\rho_r$ are the left and right uMPS environment matrices defined in Appendix B; for uCPS left and right environment eigenvectors see equations (2.58), (2.59) and (2.60).

The convergence of $S$ for a half-infinite chain, for the quantum Ising model in the paramagnetic phase (specifically for $J = 1$, $h = 0.5$), is depicted in the plot in Figure 2.9. We note that for the $z$-basis choice convergence of $S$ approaches that of uMPS. This is not surprising, given that in the limit $h \to 0$ the ground state approaches a product state aligned along the $z$-basis, and so one would expect uCPS in this basis to be capable of capturing the exact state accurately already at small overlap.

The present example also demonstrates that uCPS is able to reproduce ground state energies to machine precision both for $z$- and $x$-basis choices. Due to the exponentially higher memory cost of uCPS compared to uMPS, in practice it is necessary to be far in the gapped phase to observe such convergence; for example, for $J = 1$, $h = 0.5$, machine precision is achieved for both basis

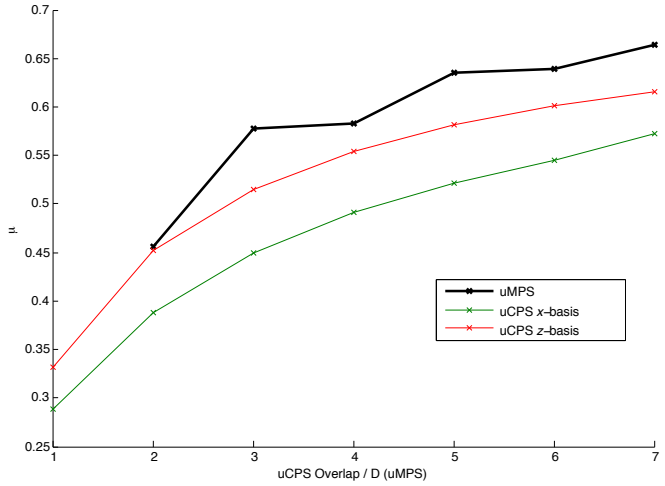


Figure 2.10: *Correlation length $\mu$ as function of uCPS overlap/uMPS bond dimension $\chi$*: Data plotted for the quantum Ising model in the ordered gapped phase ($J = 1$, $h = 0.5$).

choices with a 7-site uCPS overlap (which already corresponds to $\chi_{\mathrm{uCPS}} = 128$), while for $J = 1$, $h = 0.7$, the necessary overlap size is out of reach for a desktop with 16 GB of RAM. Remarkably, a naive first-order implementation of uCPS TDVP is sufficient to achieve this; despite the fact that most of the eigenvalues of $\Omega$ are zero in this regime, no numerical instabilities are encountered. This behaviour depends crucially on implementing an appropriate pre-conditioner in the iterative subroutine step responsible for applying the inverse of $\Omega$ to a vector, as is described in Appendix C.3.

The convergence of the correlation length with uMPS bond dimension/uCPS overlap is depicted in the plot in Figure 2.10. A notable feature is that, for both $x$ and $z$-basis choices, uCPS convergence is much smoother than for uMPS. Such behaviour is also observed at criticality, as is discussed later in this section (see Figure 2.12).

Finally let us also note that tor the XY model with $|\gamma|$ close to one, both at and away from criticality, convergence properties are similar to those of the quantum Ising model. As $\gamma$ approaches zero convergence becomes slower, and the TDVP algorithm more sensitive to integration errors.

### Finite entanglement scaling

Next we study the scaling properties of the correlation length (2.66) and entanglement entropy (2.67) for uCPS at criticality. At criticality the area law no longer holds, these quantities, will be finite for any finite bond dimension $\chi$, but will grow indefinitely as $\chi \to \infty$. Since a finite $\chi$ bounds the amount of entanglement that can be encoded in a CPS/MPS. The scaling of the entanglement entropy with respect to $\chi$ is referred to as *finite entanglement scaling*. This has been extensively studied in the uMPS setting [101–104].

In what follows, we show that at criticality overlap size $n/2$ plays the same role for uCPS as the bond dimension does for uMPS, and furthermore show how universal quantities can be calculated using uCPS finite entanglement scaling.

### Scaling at criticality I: $\mu$ vs $\chi$

Let us first consider the scaling of the correlation length $\mu$ (2.66) with uCPS overlap. Ref [101] provides numerical evidence that for a critical system uMPS scales with bond dimension as $(\chi_{\mathrm{uMPS}})^{\kappa}$ in the limit of large $\chi_{\mathrm{uMPS}}$, where $\kappa$ is a universal constant. In ref [102] it was further-

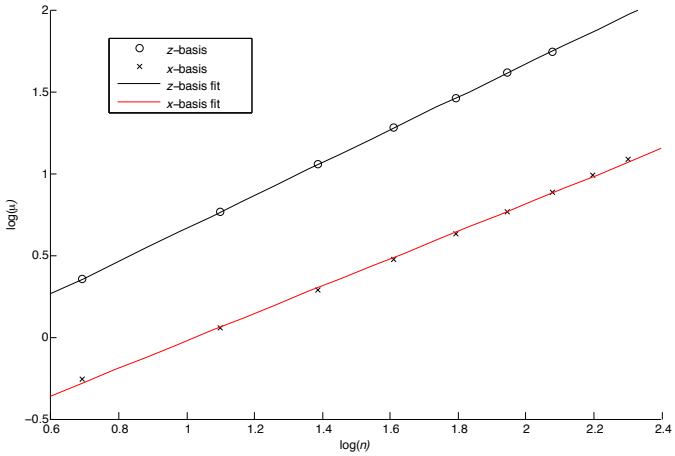


Figure 2.11: *The logarithm of the correlation length $\mu$ versus the logarithm of uCPS overlap for uCPS ground state approximations for the quantum Ising model at criticality*: Data plotted for both the $x$- and $z$- basis choices. In the $z$-basis the linear fit is particularly accurate, with slope equal to one to good approximation.

more argued that $\kappa$ only depends on the central charge $c$ of the critical system via the relation:

$$\kappa = \frac{6}{c\left(\sqrt{\frac{12}{c}}+1\right)} \ . \tag{2.68}$$

Figure 2.11 demonstrates that, to high accuracy, for uCPS $\mu$ is instead proportional to $n^{\tilde{\kappa}}$, where $n$ is the uCPS overlap, and $\tilde{\kappa}$ a constant. For the critical quantum Ising model, a linear fit of $\log\mu$ vs. $\log n$ for uCPS in the $z$-basis yields $\tilde{\kappa} = 1.004 \pm 0.006$. It seems plausible that the exact value of $\tilde{\kappa}$ is equal to one in the limit $n \to \infty$, i.e. that the correlation length is exactly proportional to uCPS overlap size, as indicated by a naive interpretation of equation (2.66). This would be consistent with the result of Section 2.2.2 that the CPS state has a range of entanglement limited to the plaquette size.

Returning to Figure 2.11 we see in the $x$-basis there is a much more significant oscillation over the whole range of available overlap sizes, making any conclusion regarding the value of $\tilde{\kappa}$ in the limit $n \to \infty$ difficult. Based on the available data we were not able to determine whether or not $\tilde{\kappa}$ is basis dependent in this limit. This in turn means that at this stage it is not possible to comment on the possible universality of $\tilde{\kappa}$.

At present we can therefore not see any manner in which, in the uCPS context, something akin to (2.68) could be used to estimate the central charge $c$.

### Scaling at criticality II: $S$ vs $\mu$

Nevertheless, uCPS can be used to calculate universal quantities along the lines of [103,104], where it has been demonstrated that a particularly powerful way to calculate critical exponents and the central charge is to scale not directly with respect to $\chi$, as in Figure 2.9, but with respect to the uMPS correlation length $\mu(\chi)$. The central charge, for example, can be estimated from the scaling of the entanglement entropy (2.70) with the correlation length (2.66) as follows. For a $(1+1)$ critical system it has been shown [23, 25, 105] that the entanglement entropy corresponding to an interval $A$ of length $l_A$ grows as:

$$S_A = \frac{c}{3}\log l_A + k \ , \tag{2.69}$$

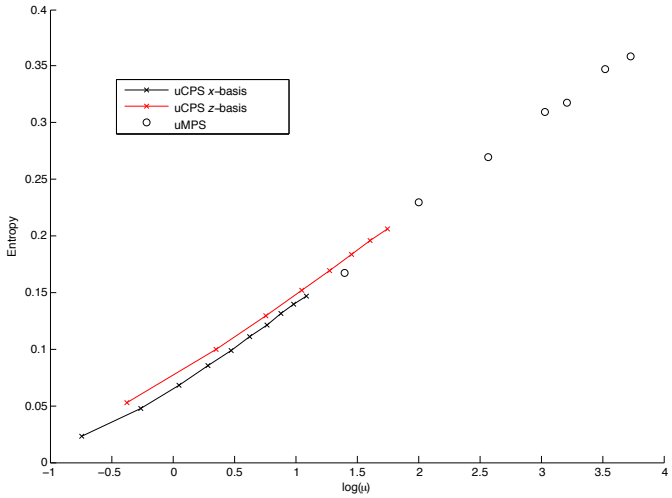


Figure 2.12: *The scaling of uCPS/uMPS entanglement entropy $S$ with correlation length $\mu$*: The entanglement entropy $S$ is plotted vs $\log \mu$. The slope approaches a constant value, which is theoretically predicted to be $\frac{c}{6}$, where $c$ is the central charge.

where $c$ is the central charge of the system, and $k$ a constant. The entanglement entropy of the half-infinite line then scales as:

$$S = \frac{c}{6} \log \mu + \tilde{k} \ , \tag{2.70}$$

where $\mu$ is some length scale introduced in the system. In our case this is precisely the correlation length associated with finite bond dimension (2.66), and $\tilde{k}$ is again some constant. Relation (2.70) in conjunction with (2.66) can thus be used to obtain an estimate of the central charge.

The scaling of $S$ with $\log \mu(n)$ for the quantum Ising model at criticality is depicted in the plot in Figure 2.12. As one can see, oscillations in the entanglement entropy as a function of $\log \mu$ observed for uMPS are absent from uCPS in a fixed basis. Performing a simple $1/n$, $n \to \infty$ extrapolation for the slope of this curve, with $z$-basis data up to $n = 10$, yields the estimate $c = 0.50142...$ for the central charge. This agrees with the exact value of $c = \frac{1}{2}$ to 0.3% error, and provides better accuracy than the result obtained via finite uMPS entanglement scaling using all bond dimensions from $\chi = 2$ to $\chi = 64$ in ref [104].

### Computational costs at criticality

The time needed to generate this uMPS data on a typical desktop, (even when using techniques more advanced than the simple first-order implementation of imaginary time TDVP, such as the conjugated gradients method or iDMRG), is of the order of a week. On a comparably powerful computer the uCPS data used here was generated in a few hours. It should be noted, however, that uMPS finite entanglement methods are much more accurate for critical exponent than for the central charge estimates. Furthermore the exponentially larger memory cost of uCPS means that uMPS is capable of accessing states with a lot more entanglement (as Figure 2.12 clearly demonstrates). Nevertheless, for the range of bond dimensions for which uCPS has a sufficient amount of RAM, the lack of oscillations means that uCPS can in practice be useful for making accurate estimates much more quickly than is possible with uMPS.

It is also interesting that uMPS and uCPS data points in Figure 2.12 lie roughly on the same line, and while uMPS data is significantly noisier, it seems to be bounded by the optimal $z$ and the suboptimal $x$ uCPS basis choices. This gives an indication that there may be some relationship between the oscillations in the uMPS data and the rotation invariance of the uMPS ansatz.

### 2.3.4 Remarks on ground state approximations with CPS

While the cost of performing a single TDVP step scales better with bond dimension for uCPS than for uMPS, an exponentially larger amount of computer memory is needed to achieve the same accuracy with uCPS as with uMPS. However, the computational time required to obtain the same accuracy, surprisingly, scales in a similar manner for both. The precise nature of the scaling is sensitively dependent on both the model under investigation and the choice of basis. For models with degenerate ground states, convergence to the global minimum is in general only achieved for a certain fraction of TDVP runs.

The uCPS algorithm exhibits certain advantages over uMPS when calculating universal quantities using finite entanglement scaling; oscillations found in uMPS are not present for uCPS, so scaling can be deduced more accurately with comparable computer time (but larger computer memory) cost. This seems to occur precisely *because* of the fixing of the basis. It would be particularly useful if oscillations are eliminated for CPS/string bond states in a similar manner beyond one dimension, where obtaining large numbers of points for a range of bond dimensions, as may be necessary with oscillations present, can be prohibitively expensive.

## 2.4 Quenches with uCPS

In this section we use real time TDVP applied to uCPS to study quenches across the critical point in the quantum Ising model 2.63 which exhibit *dynamical phase transitions*. Dynamical phase transitions can occur whenever the return amplitude,

$$G(t) = \langle \psi_0 | \, e^{-iHt} \, | \psi_0 \rangle \ , \tag{2.71}$$

also referred to as the Loschmidt amplitude, has zeros [106]. The rate function for the return probability (referred to from here on just as the rate function):

$$l(t) = -\lim_{L\to\infty} \frac{1}{L} \log |G(t)|^2 \ , \tag{2.72}$$

where $L$ is the length of the system, can acquire non-analyticities, analogous to those present in the free energy in a thermodynamic setting. For a uCPS/uMPS, this quantity corresponds simply to the logarithm of the second largest eigenvalue of the transfer matrix of the infinitely chain tensor network corresponding to the overlap $\langle \psi_0 | \psi_t \rangle$.

The thermodynamic equivalent of (2.71) is obtained from purely imaginary time evolution, i.e. $t = -i\tau$ with $\tau \in \mathbb{R}$. In this case $G(\tau)$ corresponds to the canonical partition function of a system with finite length in the $\tau$ direction, and with boundaries described by $|\psi_0\rangle$. Equilibrium phase transitions of the system are in correspondence with the zeros of $G(\tau)$ that occur as one takes the thermodynamic limit $L \to \infty$, which, if present, result non-analyticities in the free-energy $-\log |G(\tau)|^2$. It should be noted that, while the thermodynamic partition function can acquire zeros only in the thermodynamic limit, for the return amplitude (2.71) this can also happen also at finite system size. In general no simple correspondence between equilibrium and dynamical phase transitions exists [107].

The rate function (2.72) can be calculated exactly for the quantum Ising model, and a dynamical phase transition occurs for quenches across the critical point [108, 109], so in this setting a simple correspondence between the dynamical and equilibrium cases does exists. The ground state of the quantum Ising model (2.63) undergoes an equilibrium phase transition from a ferromagnetic phase for $h < 1$ to a paramagnetic phase for $h > 1$. This transition is captured accurately by uMPS even at small bond dimension, with the expectation value of order parameter operator $\langle \sigma^z \rangle$ going

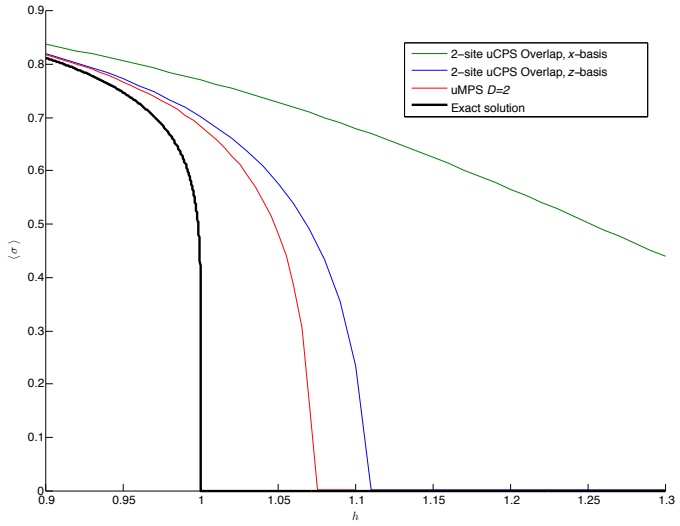


Figure 2.13: *Comparison of quantum phase transition as approximated with different ansätze*: Both uCPS and uMPS are capable of capturing the quantum Ising model equilibrium phase transition, from the ferromagnetic phase, $h < 1$, characterised by a non-zero value for the order parameter operator expectation value $\langle \sigma^z \rangle$, to the paramagnetic phase $h > 1$ when $\langle \sigma^z \rangle = 0$. The accuracy of the uCPS approximation for the critical point, $h = 1$, degrades as a function of the rotation angle away from the $z$-basis. In the $x$-basis the phase transition is entirely missed.

from a positive value for $h < h_c$, to zero (to machine precision) for $h > h_c$, with $h_c$ approaching the exact value $h_c = 1$ from above with increasing bond dimension. The uCPS behaviour is highly basis-dependent, as is demonstrated by the plot in Figure 2.13. The critical point is approximated with comparable accuracy by uMPS and uCPS in the $z$-basis, at bond dimension equal to uCPS overlap, but the uCPS approximation gets increasingly less accurate for choices of basis away from $z$, and completely misses the phase transition in the $x$-basis.

In the following, we concentrate on a quench initiated in the paramagnetic phase, with $h = 1.5$ in the quantum Ising Hamiltonian (2.63), with the time evolution performed according to a Hamiltonian with the magnetic field (instantaneously) changed to $h = 0.1$; the post-quench Hamiltonian is therefore deep in the ferromagnetic phase. The reversed quench, from the ferromagnetic to the paramagnetic phase, also exhibits a dynamical phase transition, but is more unwieldy to analyse [109]. As it yields very similar conclusions regarding the properties of uCPS, it will not be explicitly discussed here.

In the $z$-basis uCPS captures the dynamical phase transition very accurately, as demonstrated in the plot in Figure 2.14. In addition to capturing non-analyticities, simulations with uCPS in this basis exhibit approximate recurrences at large times, i.e. beyond the point at which the exact rate function is captured correctly, for all values of uCPS overlap. For single-site overlap recurrences are exact. Plots of uCPS approximations for both single- and 3-site overlap in the $z$-basis are depicted in the two top plots of Figure 2.16 and clearly show recurrences.

In contrast, uCPS in the $x$-basis (Figure 2.15) is unable to capture the non-analyticities of the rate function at all. For times prior to the first non-analyticity, the accuracy of the uCPS approximation of the rate function increases with increasing overlap, however the non-analyticity is never actually captured. Beyond the point at which the non-analyticity occurs in the exact function, the behaviour of the uCPS approximation completely misses the correct behaviour and is chaotic, not converging to any definite function with increasing uCPS overlap size. It should be noted that non-analytic behaviour is not observed at any time in the $x$-basis uCPS approximation. This is very different to the large time behaviour of uCPS in the $z$-basis.

The behaviour of the uMPS approximation of the quench, at large times, exhibits a combination

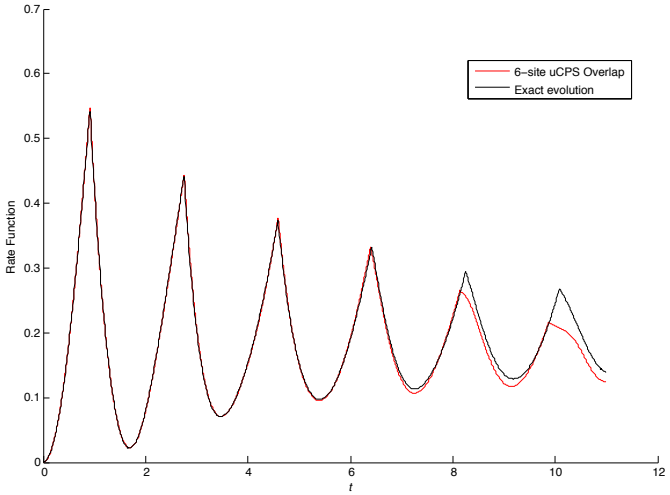


Figure 2.14: *The rate function vs. time in the z-basis for 6-site uCPS overlap compared with the exact evolution*: The quench corresponds to the ground state of the quantum Ising Hamiltonian with $h = 1.5$ (paramagnetic phase) evolved with the $h = 0.1$ Hamiltonian (ferromagnetic phase).

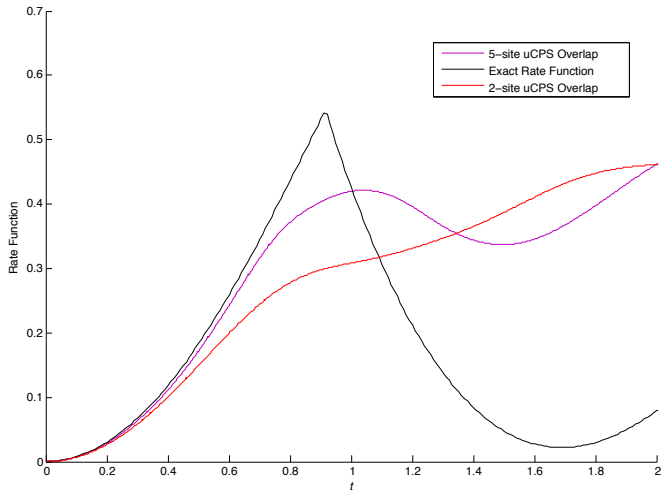


Figure 2.15: The uCPS approximation, for 2- and 5-site uCPS overlap in the $x$-basis, of the rate function for the $h = 1.5 \to h = 0.1$ quench in the quantum Ising model. In this basis uCPS completely misses the dynamical phase transition. The behaviour of the uCPS approximation is analytical even at large times (not displayed).

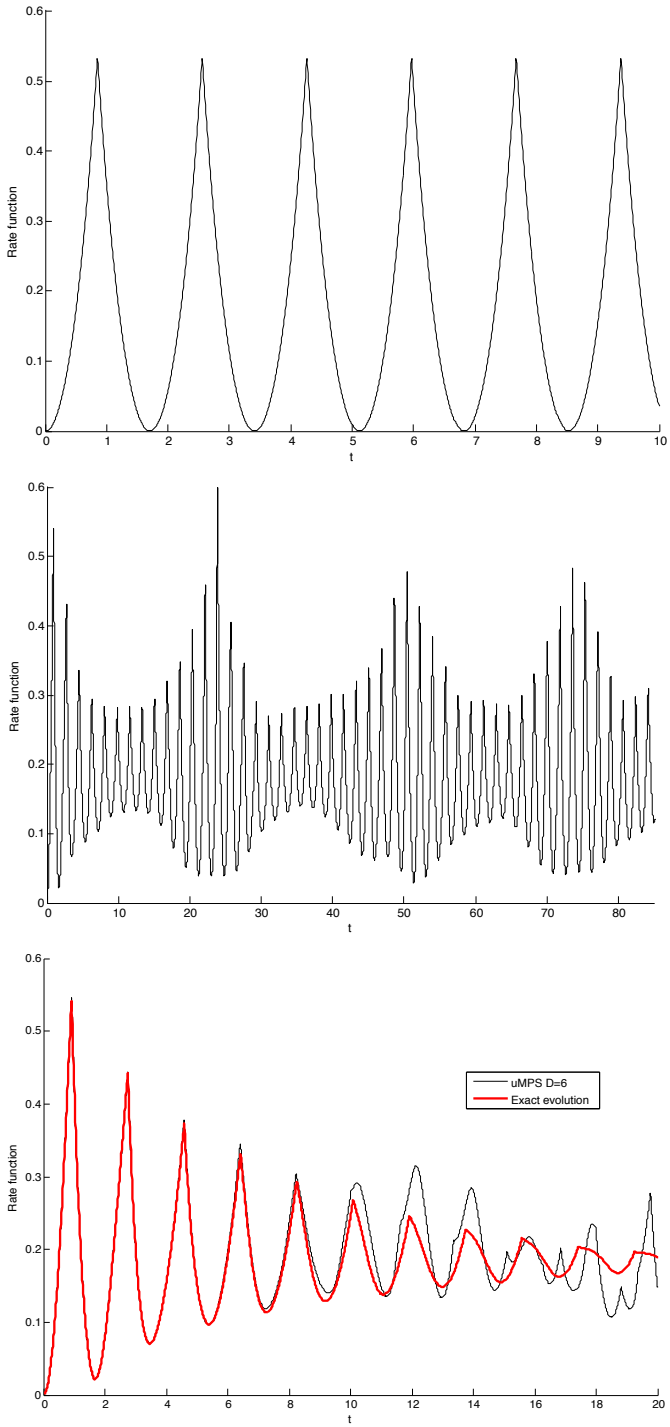


Figure 2.16: *Rate function vs. time in z-basis exhibits recurrence when projected to the uCPS manifold*: Recurrence is exact for 1-site CPS overlap (top), and approximate when the overlap is larger than one, as demonstrated for the 3-site uCPS overlap case (middle). The uMPS approximation does not exhibit recurrences at large times; beyond the point at which the rate function is accurately captured, the behaviour is chaotic (bottom), and the precise behaviour is also highly bond-dimension dependent.

of that observed for $z$- and $x$-basis uCPS approximations in the following sense: as can be seen in lowermost plot in Figure 2.16, beyond the point at which the exact rate function is captured accurately (for a given bond order), the uMPS behaviour is chaotic, as is the case for uCPS in the $x$-basis, but it does exhibit non-analyticities at arbitrarily large times, a feature observed for uCPS in the $z$-basis.

Comparing the $\chi = 6$ uMPS approximation in Figure 2.16 with the 6-site uCPS overlap approximation in the $z$-basis in Figure 2.14 demonstrates that the quality of the uCPS and uMPS approximations is comparable. This is another example—here in the context of real time evolution—of the general observation that the capacity of uCPS and uMPS to capture the properties of spin systems is roughly the same, in an optimal basis, for uCPS overlap equal to the uMPS bond dimension. In addition, we observe that, for the examples studied in this section, the time needed to run uMPS and uCPS approximations of the same quench at uCPS overlap size equal to uMPS bond dimension is roughly the same. This demonstrates that also in the context of quenches it is only the computer memory cost, and not the computer time cost, that scales exponentially worse for uCPS.

## 2.5 Discussion

This chapter has centred around developing the deterministic TDVP algorithm to study a restricted class of uCPS states. Such an algorithm is itself a departure as CPS states are usually optimised stochastically and—as far as we are aware—not used to study real time Hamiltonian evolution. Our analysis has revealed several interesting features of the numerical cost of using uCPS and their sensitivity to choice of basis.

### 2.5.1 Computational cost of uCPS TDVP algorithm

Implementation of the TDVP algorithm shows interesting efficiency gains, aspects of which may be extendible to higher dimensions. In Section 2.3 it has been demonstrated that the cost of a single uCPS TDVP step scales, optimally, as $O(\chi^3)$. Since uCPS maps to an uMPS with bond dimension equal to the physical spin dimension, and the cost of one uMPS TDVP step is $O(d\chi^3)$, one naively expect the cost of each uCPS TDVP step to scale as $O(\chi^4)$, but the special structure of uCPS enables this naive scaling to be improved. This special structure is most effectively analysed by considering the uCPS $\rightarrow$ uMPS mapping, which necessitates the introduction of the copier tensor, and the fact that a singe $n$-site coper factorises into a product of $n$ single-site copiers already hints at the reduction to $O(\log(\chi)\chi^3)$. The mapping of a generic CPS to PEPS involves copiers that factorise in a similar manner, so it is likely that an increase in efficiency is possible also in more than one dimensions for deterministic algorithms that respect the CPS structure.

However, the efficiency with which a uCPS represents a state to a given degree of accuracy is not as great as one might naively anticipate. As discussed in Section 2.2, we have considered a restricted set of CPS that are equivalent to MPS with bond and local Hilbert space dimension equal. One might expect then that uCPS with an optimally chosen basis are of comparable accuracy to uMPS of this bond order. This is not the case. Both deep in the gapped phase and also at criticality, quantities of interest, such as the ground state energy, converge with size of the uCPS overlap $n$ in roughly the same manner as they converge with bond dimensions for uMPS. The implication is that, as far as physical observables are concerned, uCPS scaling is exponentially worse than uMPS, since $\chi_{\text{uCPS}} = d^n$, where $d$ is the dimension of the spin of a single site. For critical systems one can make a particularly precise statement: while for uMPS the correlation length $\mu$ increases with bond dimension $\chi$ as $\mu \propto \chi^{\kappa}$, in the limit $\chi \rightarrow \infty$, for uCPS the correlation length scales instead as $\mu \propto n^{\tilde{\kappa}}$, where $\kappa$ and $\tilde{\kappa}$ are constants. It is not possible to determine, from the accessible range

of uCPS overlap sizes, whether or not $\tilde{\kappa}$ is basis dependent, and thus, whether or not it encodes universal behaviour. Interestingly for the quantum Ising model in the $z$-basis $\tilde{\kappa}$ seems to be one to good accuracy, and so the correlation length is precisely proportional to the uCPS overlap.

Surprisingly, while the *memory* cost is exponentially worse for uCPS than for uMPS, the computer *time* needed to fully converge to the optimal uCPS ground state approximation, using imaginary time TDVP initiated from a random state, scales in the same way for uCPS with respect to overlap, as it does for uMPS with respect to bond dimension. Combined with the above result, that uCPS achieves roughly the same accuracy as uMPS for overlap equal to uMPS bond dimension, this observation implies that uCPS in the optimal basis matches uMPS accuracy with the same computer time cost, but an exponentially worse memory cost. This does not contradict the statement that the cost of a single step in the imaginary time TDVP is exponentially worse for uCPS, both in time and memory cost (since at each step exponentially larger matrices need to be multiplied). The speed-up observed with uCPS, over the course of the whole imaginary time TDVP run, reflects the fact that for uCPS much larger time steps can be taken than for uMPS before instability sets in. In addition, while for imaginary time TDVP integration errors due to excessively large time steps can conspire to actually aid convergence, both for uCPS and uMPS —and of course as long as these time steps are not too large—this effect aids convergence more efficiently in the case of uCPS. The net result is that the exponentially higher cost of a single step for uCPS in the TDVP algorithm is counteracted by these two effects to bring the computer time cost of the whole TDVP run down, so that it actually scales exponentially better than would be expected when considering the costs of a single step of the algorithm; clearly, none of this improves the memory requirements.

The computational costs are observed to have the same properties in the context of real-time TDVP, which has been used to simulate quantum quenches in Section 2.4. The only caveat is that in the analysis, in place of considering the time necessary for imaginary time TDVP to converge, one must compare the uCPS vs. uMPS cost of simulating the evolution of a quench over some reasonably long time. Given that integration errors are not of great concern for imaginary time TDVP, only a simple Euler-step integrator was used to generate the ground state approximations, and one may object that some of the conclusions made above regarding the cost of imaginary time TDVP are merely artefacts of the particularly simple type of integration scheme. This is not the case, as can be checked by employing a more sophisticated integration algorithm. Moreover, our real time uCPS quench simulations were computed using the adaptive step Runge-Kutta-Fehlberg 4(5) method, with the same conclusions regarding uCPS vs. uMPS computational costs.

### 2.5.2 Basis dependence

In addition to the above, basis dependence has a major impact on the behaviour of the uCPS TDVP algorithm. In Section 2.4 it was demonstrated that with a sub-optimal choice of basis important physics can be missed, as demonstrated by the fact that both dynamical and static phase transitions in the quantum Ising model are not observed if one chooses to work in the $x$-basis. Clearly, this is a cautionary lesson when working with higher dimensional CPS/string bond states.

In the imaginary time context, it is observed that the uCPS TDVP algorithm converges to the global minimum irrespective of the choice of the initial random state in general only when the ground state is not degenerate. For degenerate vacua the algorithm converges to the global minimum only for a certain fraction of runs initiated from a random state, except possibly for very special choices of basis for which convergence is unique. If there is a finite number of degenerate vacua, the number of possible minima is in general equal to the degeneracy and does not increase with bond dimension. For a continuous symmetry group uCPS TDVP seems to converge—as far

as our numerical analysis is capable of ascertaining—to a number of local minima that increases without bound with uCPS overlap. The statements concerning the scaling and cost of obtaining a ground state made above still hold, but when convergence is not unique the algorithm acquires a probabilistic ingredient, and for continuous symmetries the scaling of the computational cost can increase by more than a constant factor.

In reference to models examined in Section 2.3, for the quantum Ising Hamiltonian entanglement is generated by the $\sum_i \sigma_i^z \sigma_{i+1}^z$ term, and a number of suitable basis choices exist that yield unique convergence; for the XY model with $\gamma = 0$, which has $U(1)$ symmetry, no such choice exists. At the other extreme convergence is observed to be unique, irrespective of basis choice, for the Heisenberg model, which is described by a rotation invariant Hamiltonian. Here all basis choices are clearly equivalent, and imaginary time TDVP always converges to a unique minimum. However, energy converges extremely slowly compared to the other models studied (see Figure 2.8) which demonstrates that uCPS is best suited to the study of Hamiltonians maximally aligned with the uCPS basis.

In conclusion, a good basis choice is one for which the entanglement generating terms are 'optimally aligned', in some sense, with the uCPS basis. The problem of what precisely is meant by 'optimal' is encountered for all CPS/string bond state approaches, and is a difficult one to tackle with any generality—not only due to technical challenges, but also because the answer depends on what precisely one wishes to achieve. We have illustrated how this pans out in detail in the context of uCPS in Section 2.3. In this case, convergence properties, probabilistic aspects of the algorithm, and the accuracy of estimates for physical observables are all basis dependent, yet can not in general be optimised simultaneously; the choice depends on which of these properties one wishes to prioritise.

## 2.6 Conclusions

Although quantum states in dimensions higher than one can be represented efficiently by tensor networks, physical properties may not in general be calculated efficiently without further approximations. One way around this is to place additional restrictions on the tensor network so that its properties are easier to calculate. Such restrictions inevitably involve compromises and a balance between efficiency gains and accuracy. We have investigated this balance in the controlled context of a restricted class of uniform one-dimensional Correlator Product States that may also be considered a restriction on uniform matrix product states. Similar restrictions may be applied in higher dimensions—Correlator Product States with small, double overlaps can be mapped to small bond order PEPS.

Our main results are:

- **The application of the time dependent variational principle to uCPS**: Usually CPS—as well as the more general class of string bond states—are optimised using a stochastic Monte-Carlo type approach. They are well-suited to this because of their efficient sampleability. By considering the mapping of uCPS into uMPS, one naively expects a single uCPS TDVP step to scale as $O(\chi^4)$. Utilising the special structure uCPS, we have shown that the cost of a single uCPS TDVP step can be reduced to $O(\chi^3)$. Since this is based on the properties of the copier tensor whose properties generalise to higher dimensional CPS $\rightarrow$ PEPS mappings, our analysis indicates that a similar reduction should be possible for higher dimensional deterministic algorithms that respect the CPS structure.

- **The capacity of uCPS to capture physical information about a system scales exponentially worse with bond dimension than uMPS**: In order to capture the ground state energy, or a quantum quench, to the same accuracy as a $\chi$ dimensional uMPS, one has to

work with uCPS with overlap size of the order $n \approx \chi$, which is exponentially more expensive since $\chi_{\text{uCPS}} = d^n$, where $d$ is the dimension of a single spin. This is, surprisingly, only reflected in computer memory usage, not in the computer time needed to obtain the ground state via imaginary time TDVP, or to run quantum quenches, which for a uCPS with overlap of size $n$ is of the same order as for uMPS with $\chi = n$.

- **The choice of uCPS basis has a strong effect on the behaviour of the TDVP algorithm**: In particular this is seen in the capacity of uCPS to accurately approximate the physical system under consideration, as well as on the behaviour of uCPS under scaling. A good basis choice, generally speaking, has the property that it is closely aligned with the entanglement generating terms in the Hamiltonian. With an optimal choice of basis uCPS will generally capture the physics as well as uMPS, for uCPS overlap equal to the uMPS bond dimension. On the other hand, with a suboptimal choice uCPS can completely fail to capture important physics such as equilibrium or dynamical phase transitions. We also observe that, being an Ansatz that is not rotation invariant, except for special basis choices uCPS will in general break any degeneracy present in the exact ground state (or in the related uMPS approximation): depending on details of the random initial state, imaginary time TDVP will converge to local minima associated with this separation of otherwise degenerate energy levels.

- **Given a fixed basis, the scaling of physical quantities with bond dimension is much smoother for uCPS than for uMPS**: In particular, the scaling of quantities such as entanglement entropy or the correlation length often has strong oscillations at lower bond dimensions in the case of uMPS, and these almost entirely disappear for uCPS in a fixed basis.

- **Some properties of uMPS exhibit a combination of features that can be isolated by making judicious choices of uCPS basis**: For example, the oscillations seen in the scaling behaviour of uMPS seem to be bounded by the smooth behaviour of uCPS scalings, at one end by the uCPS in the optimal basis and the other by the least optimal choice of basis (see Figure 2.12). Similarly the behaviour of uMPS at large times for the quench exhibiting dynamical phase transitions is a combination of the recurring non-analyticities seen for the optimal uCPS choice of basis, and the chaotic but analytic behaviour observed in the least optimal basis (see Figures 2.15 and 2.16).

The analysis in this paper has mostly been geared towards bettering our theoretical understanding of uCPS compared to standard uMPS, with a view to identifying characteristic properties of the uCPS variational manifold that may be of use when studying CPS/string bond states in general, and in particular in higher dimensions. It should be stressed that uCPS has potential practical advantages already in one dimension. A general observation made at various points in this chapter is that the uCPS TDVP algorithm, applied to a suitable Hamiltonian and in an optimal basis, is very robust—both in its imaginary and real time variants (see e.g. Figures 2.9 and 2.16)— under the right circumstances more so than a comparably costly uMPS TDVP run. A further advantage of uCPS is described at the end of Section 2.3, where it is shown that one can utilise the superior scaling properties of uCPS compared to uMPS in order to generate estimates of universal quantities in critical theories, with accuracies not achievable with comparable computational time cost using uMPS. Finally, an aspect of our analysis that has not been emphasised in the course of this chapter is that, while uCPS yields similarly accurate estimates of physical quantities for overlap sizes equal to uMPS bond dimension, the actual bond dimensions accessed by uCPS are exponentially larger than what is accessible with uMPS at comparable computational time cost. For example, for the critical quantum Ising model the bond dimension $2^{10} = 1024$ uCPS ground state estimate in the

$x$-basis is reached with roughly the same computer time cost needed to generate the uMPS $\chi = 10$ ground state approximation (see Figure 2.6). This is a direct result of our very conservative choice of CPS tensors in which we represent *all* quantum correlations on a given length scale set by the plaquette size $n$. With prior knowledge of the relevant correlations in a quantum state a better choice of CPS ansatz may be possible which does not exhibit the $\sim \exp(n)$ memory cost scaling. Investigation of this possibility is an interesting avenue for future study. Another interesting question is whether CPS can provide better pre-conditioning for other tools: for example, whether the uCPS $\rightarrow$ uMPS mapping described in Section 2.2 could provide a more efficient way of initialising a $\chi = 1024$ iDMRG run, than e.g. by building it up from a $\chi = 10$ uMPS state.

# 3 | Influence of thermal processes in Open Quantum Systems

We derive a microscopic model for dissipative dynamics in a system of mutually interacting qubits coupled to a thermal bath that generalizes the dissipative model of Landau-Lifshitz-Gilbert to the case of anisotropic bath couplings. We show that the dissipation acts to bias the quantum trajectories towards a reduced phase space. This model applies to a system of superconducting flux qubits whose coupling to the environment is necessarily anisotropic. We study the model in the context of the D-Wave computing device and show that the form of environmental coupling in this case produces dynamics that are closely related to several models proposed on phenomenological grounds.

The original work in this chapter, beginning with Section 3.2, was done in collaboration with A Green, and published as ref [110].

In this chapter we study the dynamics of a system, which is in contact with the thermalizing influence of an external bath. We study these open systems dynamics using a well-known Keldysh path integral approach [111], from this we obtain a stochastic Schrödinger-Langevin description of the dynamics. Like many other open systems treatments, this approach neglects the possibility of long lasting quantum correlations, such as entanglement, between the system and the bath, however this approach does capture classical correlations between the system and the bath.[②]

We use this to study the open systems dynamics of superconducting flux qubits. Due to the physical geometry of the flux qubit, the influence of environmental effects on the system dynamics is highly anisotropic. The anisotropy of this environmental coupling introduces qualitatively new features into the system dynamics. We show the existence of a regime where the qubit dynamics are typically confined to a low dimensional sub-manifold of the full Hilbert space.

The flux qubit is a two level system, which in turn is well-known to map onto the dynamics of O(3) classical spins via the Hopf map $s^\alpha = z_i^* \sigma_{ij}^\alpha z_j$. The dissipative dynamics of both the two level system [112] (and references therein) and classical spins [113–122] have been studied extensively. Our approach, which uses a Keldysh path integral to obtain a Langevin [123–125] description of the flux qubit dynamics, and which accounts for the anisotropic coupling to the environment, extends the previous work on dissipative spin models.

An accurate model for the dissipative dynamics of a flux qubit can be used to assess the capabilities of putative quantum technologies. We apply our model to the D-Wave computing machine, which consists of a large array of controllable flux qubits. Extensive analysis has sought to correlate the behaviour of this machine with various quantum and classical models [51–53,126–130]. Since classical dynamics correspond to a particular restriction on fully quantum dynamics, the effectiveness of this comparative approach is dependent on identifying the appropriate restrictions that correspond to the classical limit. We show in an appropriate strong coupling limit the biasing

[②] Classical correlations are often neglected in open systems treatments where the Markovian approximation $\rho \approx \rho_{\text{system}} \otimes \rho_{\text{bath}}$ is commonplace.

of trajectories in the anisotropic Langevin equation allows one to obtain dynamics which closely resemble the heuristic models of the D-Wave dynamics of refs [51–53].

## 3.1 Background

In Section 3.1.1 we introduce the flux qubit and its analogy to the dynamics of a magnetic moment, i.e. a spin. In Section 3.1.2 we then consider previous studies of the dissipative dynamics of magnetic moments, and consider the implications of this for the dissipative dynamics of flux qubits. In Section 3.1.5 we then briefly consider some thermodynamic principles that will dictate the structure of any dissipative qubit dynamics, before, in Section 3.2 we go on to derive them.

### 3.1.1 The flux qubits and spin dynamics

The most basic flux qubit consists of the simple SQUID (superconducting quantum interference device) shown in Figure 3.1a, this consists of a superconducting current loop with a Josephson junction and an inductor.[①] The flux through the loop is $\phi_{\text{ext}}$. This system is described by the Hamiltonian

$$H = \underbrace{\frac{q^2}{2C} - \frac{\Phi_0^2}{2L}\cos\left(2\pi\frac{\phi-\phi_{\text{ext}}}{\Phi_0}\right)}_{\text{Josephson Junction}} + \underbrace{\frac{\phi^2}{2L}}_{\text{Inductor}} \tag{3.1}$$

where $\Phi_0$ is the flux quantum and the coordinates satisfy the commutation relation $[\phi, q] = \mathrm{i}\hbar$ it is clear that this is a single particle problem. There is no exact solution to equation (3.1), but from study of Figure 3.1b and from the harmonic approximation we expect, by analogy with ground-state of the quantum harmonic oscillator, that each of the lowest well(s) of the sinusoidal potential, if sufficiently deep and wide, to support approximately Gaussian low lying bound state(s).

In a flux qubit we are interested in the situation where, furthermore, $\phi_{\text{ext}}$ is sufficiently close to $\pm\Phi_0/2$ that there are two low lying wells. Thus the low energy space is approximately a double well potential as in Figure 3.1b. In this situation there is a low lying doublet, made up of the lowest lying state of each well. When this doublet is well separated from further excited states we can and consider this low energy subspace in isolation to good approximation. The effective Hamiltonian, being a $2\times 2$ matrix, can then be written as a sum of Pauli matrices $H = -\boldsymbol{B}\cdot\boldsymbol{\sigma}/2$. Since both of the low lying wells all have the same curvature, we need only consider the offset in the wells minima to find the energy difference in their low lying energy levels. The energy splitting $B_{\text{z}}$ between the left-localized and right-localized state is given by the difference of the two low lying minima, and hence is approximately

$$B_{\text{z}} \approx \frac{\Phi_0\phi_{\text{ext}}}{L}. \tag{3.2}$$

A general state on this low energy subspace can be identified with an O(3) vector using the usual Hopf map to the Bloch sphere

$$|\psi\rangle = \cos\left(\frac{\theta}{2}\right)\mathrm{e}^{-\mathrm{i}\varphi/2}\,|0\rangle + \sin\left(\frac{\theta}{2}\right)\mathrm{e}^{\mathrm{i}\varphi/2}\,|1\rangle \quad\Longleftrightarrow\quad \boldsymbol{s} = \langle\psi|\boldsymbol{\sigma}|\psi\rangle = \begin{pmatrix}\sin\theta\cos\varphi\\ \sin\theta\sin\varphi\\ \cos\theta\end{pmatrix}. \tag{3.3}$$

Establishing the link between the dynamics of qubits and magnetic moments, both of which are then captured by

$$\dot{\boldsymbol{s}} = \boldsymbol{s}\times\boldsymbol{B}. \tag{3.4}$$

But how do we incorporate the effects of environmental coupling into this equation? Flux noise,

[①] Developments in flux qubit technology has lead to designs with increased substructure e.g.ref [131], with the aim of increasing tunability or decreasing susceptibility to noise. Despite this the picture outlined in this section remains roughly the same.

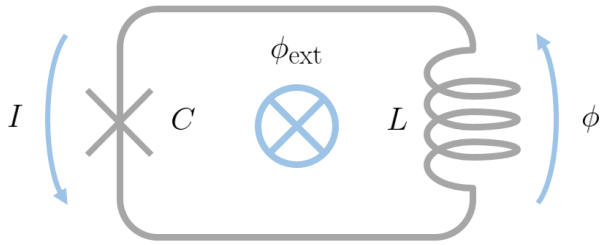


(a)

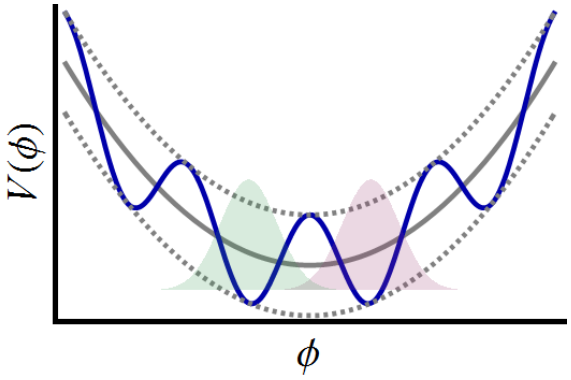


(b)

Figure 3.1: *The RF squid flux qubit* (a) A basic RF-squid flux qubit. In its most basic form the flux qubit consists of a Josephson junction, characterised by capacitance $C$, and inductor $L$ connected in a loop through which there is a flux $\phi_{\text{ext}}$. (b) The overall potential (solid blue), composed of a sinusoidal part due to the Josephson junction, and a parabolic part due to the inductance loop (solid grey), can be tuned to provide a potential which at low energies approximates a double well. Each of the lowest two wells will support an approximately Gaussian bound state shown in red and green.

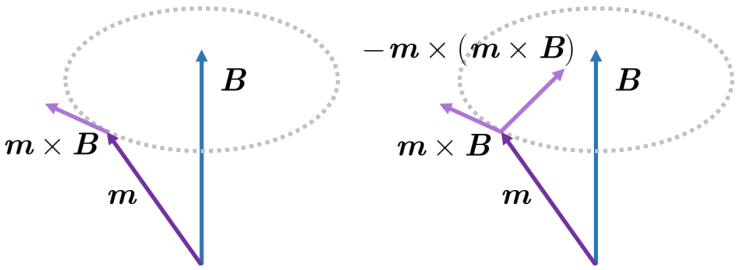


Figure 3.2: Undamped magnetic precession (left) and damped magnetic precession (right). Both dynamical terms are perpendicular to $\boldsymbol{m}$, thus the norm $|\boldsymbol{m}|$ is a constant of motion, and the dynamics are traced over a sphere.

.

i.e. small fluctuations in $\phi_{\text{ext}}$ due to environmental coupling, are the often dominant source of environmental interaction in these systems. To leading order this causes variation only in the energy separation of the two low lying Gaussian states, and does not significantly effect their coupling. Using these as a basis, the result is that fluctuations in this setting are predominantly along $B_z$. However noise alone will lead to infinite heating, so there is necessarily also dissipation, but of what form? Answering this is a more involved question which we will come to shortly.

### 3.1.2 The dynamics of dissipative magnetic systems

Due to the analogy in the previous section we look to how dissipation is treated in magnetic systems in order to gain insight into how it might be treated in qubits. It is easily shown that the free dynamics of a magnetic moment in the presence of an external field $\boldsymbol{B}$ are described by

$$\dot{\boldsymbol{m}} = \boldsymbol{m} \times \boldsymbol{B}. \tag{3.5}$$

There is a model due to Landau and Lifshitz which describes the open system dynamics of magnetisation [132]. The dynamics consists of two terms corresponding to precessing, Hamiltonian evolution, and relaxing, dissipative evolution

$$\dot{\boldsymbol{m}} = \boldsymbol{m} \times \boldsymbol{B} - \gamma \boldsymbol{m} \times (\boldsymbol{m} \times \boldsymbol{B}) \tag{3.6}$$

where $\gamma$ is a damping factor. Later analysis by Gilbert [133] showed that, contrary to the predictions of Landau and Lifshitz, in experiments the highly damped magnetic systems were found to evolve according to

$$\dot{\boldsymbol{m}} = \boldsymbol{m} \times \boldsymbol{B} - \gamma \boldsymbol{m} \times \dot{\boldsymbol{m}}. \tag{3.7}$$

This phenomenological model is related to the model of Landau and Lifshitz via a simple substitution which shows that these form are equivalent up to a prefactor, with Gilbert's form, equation (3.7), becoming

$$\dot{\boldsymbol{m}} = \frac{1}{1 + m^2\gamma^2}\Big(\boldsymbol{m} \times \boldsymbol{B} - \gamma \boldsymbol{m} \times (\boldsymbol{m} \times \boldsymbol{B})\Big). \tag{3.8}$$

The pre-factor might seem unimportant, amounting to a choice of units of time, and furthermore the dynamics are equivalent up to $\mathrm{O}(\gamma)$. However, as was pointed out [134, 135], these dynamics suggest qualitatively different behaviour in the limit of strong damping: equation (3.6) tends to instantaneous relaxation to $\boldsymbol{m} \parallel \boldsymbol{B}$, i.e. $\dot{\boldsymbol{m}} \to \infty$,[①] whereas the experimentally motivated alternative form of Gilbert in equations (3.7) and (3.8) tends towards over-damped slowed motion $\dot{\boldsymbol{m}} \to 0$. The freezing behaviour of equation (3.7) constitutes the physically expected behaviour of

[①]This misbehaviour is reminiscent of the unphysical renormalisation of the potential in the Caldeira-Leggett model which occurs if one fails to include the appropriate counter term, hinting at the potential pitfalls which we should anticipate when including dissipation in magnetic systems.

an over-damped system, and so we conclude that Gilbert's correction gives us the correct model. Moreover, in addition to its success as a model for the dynamics of bulk magnetisation, this dynamical equation has used as a model for interacting magnetic moments, where quantisation effects become relevant [116, 117].

This discussion suggests that when we turn calculate the dissipative dynamics of quantum spin spin systems that we should expect dynamics of the form of equation 3.7. Though this equation includes dissipation, it fails to include noise.

### 3.1.3 The dissipative dynamics of individual spins

It is found that within the Markovian approximation the dissipative dynamics of individual spins are governed by the well-known Landau-Lifshitz-Gilbert (LLG) equation. We later recover this in Section 3.2 from a Keldysh path integral, but it is also shown with method of operators Langevin equations as in appendix E.1. In two equivalent forms these dynamics are described by

$$\dot{\boldsymbol{s}} = \boldsymbol{s} \times (\boldsymbol{B} + \boldsymbol{\eta} - \gamma \dot{\boldsymbol{s}}) \,, \tag{3.9a}$$

$$\dot{\boldsymbol{s}} = \frac{1}{1 + s^2\gamma^2} \boldsymbol{s} \times (\boldsymbol{B} + \boldsymbol{\eta} - \gamma\, \boldsymbol{s} \times [\boldsymbol{B} + \boldsymbol{\eta}]) \,. \tag{3.9b}$$

where $\langle \eta_i(t)\eta_j(t')\rangle = 2T\gamma\delta(t-t')$. As shown in Section E.1 this equation describes the dynamics of a quantum spin-1/2 degree of freedom when each of the $\sigma_x$, $\sigma_y$, and $\sigma_z$ operators are each coupled independently to a bath of harmonic oscillators. In this case the neglect of the possibility of entanglement between the system and environment, together with the Markovian approximation amounts to a classical treatment of the environment.

This model captures the dissipative dynamics of the system, has the phenomenologically correct strong coupling limit (as discussed in Section 3.1.2), and obeys the fluctuation dissipation theorem, but does not allow for the possibility of entanglement between the system and bath degrees of freedom.

### 3.1.4 Flux qubits and dissipation

As we saw earlier the low energy dynamics of the RF squid map on to those of a spin-1/2 magnetic moment yielding the flux qubit. This similarity of spins and qubits is suggestive that they may display the same dissipative behaviour of equation (3.9). Indeed this model has been used to model an extended array of superconducting qubits in ref [128] whilst related vector models have been used in refs [51, 52, 127]. However, the LLG equation describes the dissipative dynamics of a two-level system that is isotropically coupled to its environment, i.e. with identical baths coupled to the $\sigma_x$, $\sigma_y$, and $\sigma_z$ operators. For qubits, these operators may have different physical origins and hence will couple differently to noise. Thus, the dissipation will also be anisotropic, as the stochastic noise and dissipative terms are related by the fluctuation dissipation relation. As a result, systems, such as flux qubits, with anisotropic couplings have corresponding anisotropies in the dissipation and noise.

As mentioned previously, due to the physical geometry of the superconducting flux qubit, stray flux and other environmental effects couple to the $\hat{s}_z$ operator. The anisotropy of this environmental coupling introduces qualitatively new features into the system's dynamics. We show the existence of a regime where the qubit dynamics are typically confined to a low dimensional sub-manifold of the full Hilbert space.

### 3.1.5 Fluctuation dissipation relation

Some basic principles dynamics constrain the dynamics of dissipative systems in interesting ways.

The fluctuation dissipation theorem (FDT) is often stated in terse terms as a relationship between the power spectrum of any random fluctuations in the system, characterised by certain correlators, and the response of the system, characterised susceptibilities. In field theories this is further obscured as these objects are known as the time-ordered and retarded correlators, named for their mathematical structure rather than their physical significance. As shown in appendix D, this formal statement requires that the relation (stated here for Bosonic systems)

$$\operatorname{Im} G^{\mathrm{T}}(\omega) = \operatorname{Im} G^{\mathrm{R}}(\omega) \coth\left(\frac{\beta\omega}{2}\right). \tag{3.10}$$

is satisfied by the time-ordered and retarded correlators. However stating the principle in these terms does not elucidate the underlying physics which can be understood as the following simple statement: *for every process the converts heat into work there is corresponding, and closely related, inverse process that turns work into heat.* The former are known as fluctuations, and the latter as dissipation. To give just a handful of examples:

- **Einstein's theory of Brownian movement** [136]: An object immersed in fluid experiences drag when in motion, dissipating its kinetic energy and heating the fluid. In the reverse process the object is stochastically buffeted around by molecules in the fluid converting heat of the fluid into kinetic energy of the particle.
- **Kirchhoff's law of thermal radiation** [137]: Some fraction of light incident on an object will be absorbed, heating the object. In a reverse process the heat of object is converted into thermal radiation
- **Johnson-Nyquist noise** [138,139]: Electrical resistors dissipate the energy of charge carriers as heat, and correspondingly the inverse process generates current fluctuations from heat.

The necessity for a relationship between between these mutually inverse processes follows from micro-reversibility. This principle requires that *corresponding to every individual process there is a reverse process, and in a state of equilibrium the average rate of every process is equal to the average rate of its reverse process* [140]. This enforces the necessary cancellation of dynamics at the equilibrium Gibb's distribution, through a condition that relates the forms of any process and its inverse. As a result, for open system dynamics, the inverse processes of fluctuations and dissipation do not take independent forms, but one is defined by the other via the fluctuation dissipation theorem.

## 3.2 A stochastic Schrödinger evolution for open systems

Here we develop a dynamical equation for a quantum system interacting with its environment. We introduce the Keldysh formalism and obtain the open system dynamics from the saddle points of a Keldysh contour. There are many ways the these dynamics could be obtained, but the Keldysh approach is attractive due to the ease of enforcing identities such as the fluctuation dissipation relation in this picture.

We begin by introducing the Feynman path integral, generalising this slightly from the usual $x, p$ coordinates, and using taking the saddle points of the Keldysh path integral to obtain out of equilibrium open system dynamics.

### 3.2.1 The Feynman path integral

We begin by introducing the usual Feynman path integral. Consider a single particle system described by a Hamiltonian $H = T + V$ where the kinetic energy $T = p^2/2m$ and the potential

$V = V(x)$. We can discretise the time evolution operator by simply writing

$$U(t) = \mathrm{e}^{-\mathrm{i}Ht} = \left(\mathrm{e}^{-\mathrm{i}H\delta t}\right)^N \tag{3.11}$$

where $N\delta t = t$. By resolving the identity $\mathbf{1} = \int \mathrm{d}x \, |x\rangle \langle x|$ between successive time steps we obtain

$$\langle x_N | \, \mathrm{e}^{-\mathrm{i}Ht} \, | x_0 \rangle = \int \mathrm{d}x_{N-1} \cdots \int \mathrm{d}x_1 \, \langle x_N | \, \mathrm{e}^{-\mathrm{i}H\delta t} \, | x_{N-1} \rangle \cdots \langle x_2 | \, \mathrm{e}^{-\mathrm{i}H\delta t} \, | x_1 \rangle \, \langle x_1 | \, \mathrm{e}^{-\mathrm{i}H\delta t} \, | x_0 \rangle \, . \tag{3.12}$$

This is further simplified by use of the Zassenhaus formula[①] from which we know

$$\mathrm{e}^{-\mathrm{i}H\delta t} = \mathrm{e}^{-\mathrm{i}T\delta t} \mathrm{e}^{-\mathrm{i}V\delta t} + \mathrm{O}(\delta t)^2 \tag{3.13}$$

and hence by further resolving the identity $\mathbf{1} = \int \mathrm{d}p \, |p\rangle \langle p|$ we find that

$$\begin{aligned} \langle x_{n+1} | \, \mathrm{e}^{-\mathrm{i}H\delta t} \, | x_n \rangle &= \langle x_{n+1} | \, \mathrm{e}^{-\mathrm{i}T\delta t} \mathrm{e}^{-\mathrm{i}V\delta t} \, | x_n \rangle \\ &= \int \mathrm{d}p_n \, \langle x_{n+1} | \, \mathrm{e}^{-\mathrm{i}T\delta t} \, | p_n \rangle \, \langle p_n | \, \mathrm{e}^{-\mathrm{i}V\delta t} \, | x_n \rangle \\ &= \int \mathrm{d}p_n \mathrm{e}^{-\mathrm{i}\frac{p_n^2}{2m}\delta t} \mathrm{e}^{-\mathrm{i}V(x_n)\delta t} \langle x_{n+1} | p_n \rangle \langle p_n | x_n \rangle \\ &= \exp\left[ i\delta t \left( \frac{m}{2} \left[ \frac{x_{n+1} - x_n}{\delta t} \right]^2 - V(x_n) \right) \right] \end{aligned} \tag{3.14}$$

where in the last line we have used that $\langle x | p \rangle \sim \mathrm{e}^{\mathrm{i}px}$ and performed integrated out the newly introduced momentum variable. The familiar path integral formulation of the quantum harmonic oscillator is then obtained by defining a functional integral by writing $\int \mathrm{D}x(t) \sim \int \mathrm{d}x_{N-1} \cdots \int \mathrm{d}x_2 \int \mathrm{d}x_1$ and taking the limit $\delta t \to 0$ yielding

$$\langle x_\mathrm{f} | \, \mathrm{e}^{-\mathrm{i}Ht} \, | x_\mathrm{i} \rangle = \int \mathrm{D}x(t') \mathrm{e}^{\mathrm{i} \int \mathrm{d}t' L}. \tag{3.15}$$

where the Lagrangian is given by

$$L = \frac{m}{2} \dot{x}^2 - V(x). \tag{3.16}$$

This is the path integral formulation of quantum mechanics due to Feynman. This provides an interesting alternative picture of quantum mechanics to the complementary Schrödinger equation.

### 3.2.2 Generic path integral approaches

We could equally well have made the same approach using a resolution of the identity over any manifold of states. Given an unbiased measure $\mathrm{D}\psi$ over the states $|\psi\rangle$ we write[②]

$$\mathbf{1} = \int \mathrm{d}\psi \frac{|\psi\rangle \langle \psi|}{\langle \psi | \psi \rangle}. \tag{3.17}$$

[①] To jog memories, the Zassenhaus formula [141] is the expansion

$$\mathrm{e}^{t(X+Y)} = e^{tX} \, e^{tY} \, e^{-\frac{t^2}{2}[X,Y]} \mathrm{e}^{\frac{t^3}{6}(2[Y,[X,Y]]+[X,[X,Y]])} \mathrm{e}^{\frac{-t^4}{24}([[[X,Y],X],X]+3[[[X,Y],X],Y]+3[[[X,Y],Y],Y])} \ldots$$

[②] We are being very generous to ourselves here as $\mathrm{D}\psi$ is not known except in some very simple cases.

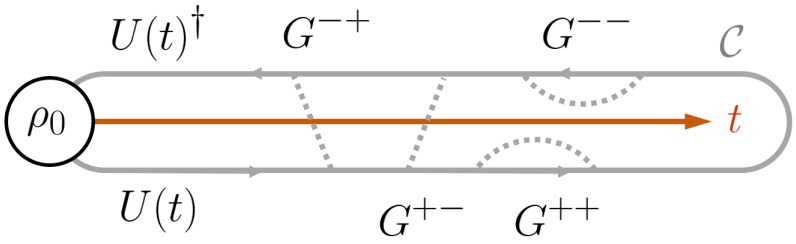


Figure 3.3: The Keldysh Contour (solid grey) goes along the time-axis before returning to the initial state. The two branches are labelled as the + outwards branch and the − return branch. The correspoding fields $\phi_+$ and $\phi_-$ live on these branches. The four correlators are depicted. $\rho_0$ is left general here and depicted as a two index object $\rho(\phi^+, \phi^-)$. When $\rho_0$ is the equilibrium state $\mathrm{e}^{-\beta H}/Z$ it can be included as an extension of the contour in the vertical (imaginary) direction using the usual relation of quantum dynamics and equilibrium statistical mechanics via a Wick rotation.

Using this we follow the same procedure as previously, except now we write

$$\begin{aligned}
\langle\psi_n|\,\mathrm{e}^{-\mathrm{i}H\delta t}\,|\psi_{n-1}\rangle &= \langle\psi_n|\,\mathrm{e}^{-\mathrm{i}H\delta t}\,|\psi_n\rangle - \langle\psi_n|\,\mathrm{e}^{-\mathrm{i}H\delta t}\,|\delta\psi_n\rangle \\
&= \langle\psi_n|\,(1-\mathrm{i}H\delta t)\,|\psi_n\rangle - \langle\psi_n|\delta\psi_n\rangle + \mathrm{O}(\delta t^2) \\
&= \langle\psi_n|\psi_n\rangle - \mathrm{i}\,\langle\psi_n|\,H\,|\psi_n\rangle\,\delta t - \langle\psi_n|\,\partial_t\,|\psi_n\rangle\,\delta t + \mathrm{O}(\delta t^2) \\
&= \langle\psi_n|\psi_n\rangle\exp\left(\mathrm{i}\delta t\frac{\langle\psi_n|\,\mathrm{i}\partial_t - H\,|\psi_n\rangle}{\langle\psi_n|\psi_n\rangle}\right) + \mathrm{O}(\delta t^2)
\end{aligned} \tag{3.18}$$

and similarly writing $\int \mathrm{D}\psi(t) \sim \int \mathrm{d}\psi_{N-1}\cdots\int \mathrm{d}\psi_2\int \mathrm{d}\psi_1$ yields the path integral

$$\langle\psi_\mathrm{f}|\,\mathrm{e}^{-\mathrm{i}Ht}\,|\psi_\mathrm{i}\rangle = \int \mathrm{D}\psi(t')\mathrm{e}^{\mathrm{i}\int \mathrm{d}t' L_0} \tag{3.19}$$

where the Lagrangian

$$L_0 = \frac{\langle\psi|\mathrm{i}\partial_t - H|\psi\rangle}{\langle\psi|\psi\rangle}. \tag{3.20}$$

corresponds precisely to that used in equation (2.28) to obtain the TDVP. Indeed, allowing full variation over the Hilbert space, taking saddle points of equation (3.19) via the Euler Lagrange equation

$$\frac{\delta L}{\delta\langle\psi|} - \frac{\mathrm{d}}{\mathrm{d}t}\frac{\delta L}{\delta\langle\dot{\psi}|} = \mathrm{i}|\dot{\psi}\rangle - H\,|\psi\rangle - \alpha\,|\psi\rangle = 0 \tag{3.21}$$

we recover the Schrödinger equation (up to a gauge symmetry transformation of equation 2.4 of $\alpha = \langle\psi|\mathrm{i}\partial_t - H|\psi\rangle/\langle\psi|\psi\rangle^2$), encouraging that we have not lost anything in this process.[①]

### 3.2.3 Path integrals out of equilibrium dynamics and their saddle point dynamics

A state vector is sufficient to define the behaviour of a closed system, for which equations (3.15) and (3.19) characterise the system. A Non-equilibrium, open quantum system requires an ensemble of state vectors, or a density matrix, due to the exchange of information with the bath of information to the bath. Evolving a density matrix $\rho$ requires both pre- and post-multiplication by the time evolution operator $U(t) = \mathcal{T}\exp\left[i\int \mathrm{d}t'\,H(t')\right]$. Thus $\rho_t = U(t)\rho_0 U^\dagger(t)$ in contrast to the time evolution of a state vector which requires only one time evolution operator $|\psi_t\rangle = U(t,0)\,|\psi_0\rangle$.

It is still possible to move a path integral picture, as previously outlined, using the Keldysh

[①]In reality a word of warning is due, and the path integral formulation needs to be treated with care. We have restricted ourselves to trajectories which are linear sums of *continuous* trajectories of our reference state $|\psi\rangle$. This requirement of continuity can cause the path integral to fail to capture physics [142].

theory which provides a framework for moving to the path integral picture, as outlined in the previous section, in such non-equilibrium systems.

As a result the path integral degrees of freedom $\phi$ (e.g.the $x$ coordinate of the Feynman path integral, or $\psi$ in the second example) are doubled $\phi \to (\phi^+(t), \phi^-(t))$. These doubled degrees of freedom arise from the pre-multiplied and post-multiplied time evolution operators $U$ and $U^\dagger$. These are associated with forward $(+)$ and backward $(-)$ branches of a closed path integral contour, the Keldysh contour $\mathcal{C}$, over which the action integral is performed. This is shown in Figure 3.3.

**A simple example: A system with a single coupling to a Markovian bath**

We start by considering the simple system

$$H = H_0 + F\sum_\alpha g_\alpha x + \frac{1}{2}\sum_\alpha \left(p_\alpha^2 + \omega_\alpha^2 x_\alpha^2\right) \tag{3.22}$$

where $H_0$ is the system Hamiltonian, and is left unspecified, $F$ is an operator on the system Hilbert space which is similarly left unspecified, and $F$ couples the operator to a bath of oscillators.

We then move to a path integral picture, where the natural choice is that of a Feynman path integral over the oscillator degrees of the bath, as in Section 3.2.1 and a more generic path integral over the system degrees of freedom, as in Section 3.2.2. This yields a partition function

$$Z = \int \mathrm{D}\phi \prod_\alpha \mathrm{D}x_\alpha \mathrm{e}^{i\mathcal{S}} \tag{3.23}$$

where the functional integral is over $\phi$, the degrees of freedom of the system, and $x_\alpha$, those of the bath. The action integral, performed over the Keldysh contour, is then

$$\mathcal{S}\left[\phi, x_\alpha\right] = \int_{\mathcal{C}} \mathrm{d}t\, L = \int_{\mathcal{C}} \mathrm{d}t\, \left(L_0\left(\phi\right) + F(\phi)\sum_\alpha g_\alpha x_\alpha + \frac{1}{2}\sum_\alpha \left(\dot{x}_\alpha^2 - \omega_\alpha^2 x_\alpha^2\right)\right) \tag{3.24}$$

where $L_0$ is given by equation (3.20) and $F(\phi) = \langle\psi|F|\psi\rangle/\langle\psi|\psi\rangle$. The contour is comprised of two principal components, the interval $\int_{-\infty}^{\infty}\mathrm{d}t$ and the reverse leg $\int_{\infty}^{-\infty}\mathrm{d}t$ together with some bits at the boundary to stitch them together. Expanding this explicitly we obtain

$$\mathcal{S}\left[\phi, x_\alpha\right] = \int_{-\infty}^{\infty} \mathrm{d}t L(\phi^+, x_\alpha^+) - \int_{-\infty}^{\infty} \mathrm{d}t L(\phi^-, x_\alpha^-) \tag{3.25}$$

subject to the aforementioned boundary conditions. A Keldysh rotation consists the coordinate change $\phi^\pm = \phi \pm \phi^{\mathrm{q}}$, and similarly for $x_\alpha^\pm$. The fields $\phi$ and $\phi^{\mathrm{q}}$ are referred to as the *classical* and *quantum* fields which can be identified with the diagonal and off diagonal terms in the density matrix $\rho(t) = \rho(\phi^+(t), \phi^-(t))$. Performing this transformation and expanding to quadratic order in the quantum fields $\phi^{\mathrm{q}}, x_\alpha^{\mathrm{q}}$ we obtain

$$\begin{aligned}\mathcal{S}\left[\phi, x_\alpha\right] = \int_{-\infty}^{\infty} \mathrm{d}t \Bigg[ & 2\sum_i \phi_i^{\mathrm{q}}\left(\frac{\partial L_0}{\partial \phi_i} - \frac{\mathrm{d}}{\mathrm{d}t}\frac{\partial L_0}{\partial \dot{\phi}_i}\right) + 2F\sum_{i,\alpha} g_\alpha x_\alpha^{\mathrm{q}} + 2\sum_\alpha \frac{\partial F}{\partial \phi_i}\phi_i^{\mathrm{q}} g_\alpha x_\alpha \\ & + \sum_\alpha \begin{pmatrix} x_\alpha & x_\alpha^{\mathrm{q}}\end{pmatrix}\begin{pmatrix} 0 & [G_\alpha^{\mathrm{A}}]^{-1} \\ [G_\alpha^{\mathrm{R}}]^{-1} & [G_\alpha^{-1}]^{\mathrm{K}}\end{pmatrix}\begin{pmatrix} x_\alpha \\ x_\alpha^{\mathrm{q}}\end{pmatrix}\Bigg].\end{aligned} \tag{3.26}$$

Naively we do not to expect the quantum-quantum term in the bath degrees of freedom $x_\alpha^q[G_\alpha^{-1}]^K x_\alpha^q$ to be obtained in the manner described, and anticipate only off diagonal terms. This term arises from careful consideration of the boundary conditions which are not explicit in equation (3.25)

(see e.g.refs [111, 143]). Furthermore such considerations require the Fourier space condition

$$G_\alpha^{\mathrm{K}}(\omega) = \coth\left(\frac{\omega}{2T}\right)\left[G_\alpha^{\mathrm{R}}(\omega) - G_\alpha^{\mathrm{A}}(\omega)\right] \tag{3.27}$$

where the Keldysh, advanced and retarded correlators are related to the objects in equation (3.26) by

$$\begin{pmatrix} 0 & [G_\alpha^{\mathrm{A}}]^{-1} \\ [G_\alpha^{\mathrm{R}}]^{-1} & [G_\alpha^{-1}]^{\mathrm{K}} \end{pmatrix} = \begin{pmatrix} G_\alpha^{\mathrm{K}} & G_\alpha^{\mathrm{R}} \\ G_\alpha^{\mathrm{A}} & 0 \end{pmatrix}^{-1}. \tag{3.28}$$

The quadratic choice of bath has left us with a Gaussian integral over the $(x_\alpha, x_\alpha^{\mathrm{q}})$, thus we can integrate these out to obtain

$$\mathcal{S} = \int_{-\infty}^{\infty} \mathrm{d}t \left[ 2\sum_i \phi_i^q \left( \frac{\partial L_0}{\partial \phi} - \frac{\mathrm{d}}{\mathrm{d}t}\frac{\partial L_0}{\partial \dot{\phi}} \right) + \begin{pmatrix} F & \sum_i \frac{\partial F}{\partial \phi_i}\phi_i^q \end{pmatrix} \begin{pmatrix} 0 & G^A \\ G^R & G^K \end{pmatrix} \begin{pmatrix} F \\ \sum_i \frac{\partial F}{\partial \phi_i}\phi_i^q \end{pmatrix} \right]. \tag{3.29}$$

where we have introduced $G^A = \sum_\alpha g_{i,\alpha}^2 G_\alpha^A$, and similarly for $G^R$ and $G^K$. We can then decouple the quantum-quantum ($\phi_{\mathrm{q}}$, $\phi_{\mathrm{q}}$) term using a Hubbard-Stratonovich transformation. For brevity we do this with a Markovian approximation ($G^{A/R}(t-t') = \pm\gamma\delta(t-t')\partial_{t'}$). This yields

$$\mathcal{S} = \int_{-\infty}^{\infty} \mathrm{d}t \left[ 2\sum_i \phi_i^q \left( \frac{\partial L_0}{\partial \phi} - \frac{\mathrm{d}}{\mathrm{d}t}\frac{\partial L_0}{\partial \dot{\phi}} \right) - 2\gamma \sum_i \phi_i^q \frac{\partial F}{\partial \phi_i}\frac{\mathrm{d}F}{\mathrm{d}t} + 2\sum_i \phi_i^q \frac{\partial F}{\partial \phi_i}\eta + \eta\left[G^K\right]^{-1}\eta \right]. \tag{3.30}$$

Since the integrand is now linear in $\phi_i^q$ integrating out this variable results in delta function which asserts the dynamical equation

$$\underbrace{\frac{\mathrm{d}}{\mathrm{d}t}\frac{\partial L_0}{\partial \dot{\phi}_i} - \frac{\partial L_0}{\partial \phi_i}}_{\text{Free evolution}} + \underbrace{\gamma \frac{\partial F}{\partial \phi_i}\frac{\mathrm{d}F}{\mathrm{d}t}}_{\text{Dissipation}} = \underbrace{\frac{\partial F}{\partial \phi_i}\eta}_{\text{Fluctuations}}. \tag{3.31}$$

where $\eta$ describes a Gaussian stochastic process drawn from the ensemble $\langle\eta(t)\rangle = 0$, $\langle\eta(t)\eta(t')\rangle = \mathrm{i}G^{\mathrm{K}}(t-t')/2$. If the temperature of the bath is much greater its characteristic frequency we can further approximate $\langle\eta(t)\eta(t')\rangle \approx 2\gamma T\delta(t-t')$. We have labelled the three parts of equation (3.31) with their interpretations. The fact that both the dissipative term, and the bath correlator $\langle\eta(t)\eta(t')\rangle$ scale with $\gamma$ is due to the fluctuation dissipation theorem.[①]

### A simple check using equipartition of energy

As a sanity test we can test drive equation (3.31) on the simple case of a single particle described by the free Lagrangian

$$L_0 = \frac{m}{2}\dot{x}^2 - V(x) \tag{3.33}$$

if we have a coupling $F = x$ to the bath, we obtain a familiar dynamical equation

$$m\ddot{x} + \gamma\dot{x} + \partial_x V(x) = \eta \tag{3.34}$$

to show most quickly that this satisfies the fluctuation dissipation relation, we can follow the canonical example due to Einstein [136] in reducing this first order problem by considering the

[①] As a point of curiosity, we note that in equation (3.27) the dissipative term can be written in the form of a Rayleigh dissipation function, casting the dynamics in the form

$$\frac{\mathrm{d}}{\mathrm{d}t}\frac{\partial L_0}{\partial \dot{\phi}_i} - \frac{\partial L_0}{\partial \phi_i} + \frac{\partial D}{\partial \dot{\phi}_i} = \xi_i \quad \text{where} \quad D = \frac{\gamma}{4}\dot{F}^2. \tag{3.32}$$

where $\xi_i = \partial F/\partial\phi_i$. This allows easy identification of the rate of work done by the system on the environment from the relation $\dot{W} = 2D$, and providing a novel occurrence of Rayleigh's construction [144]. Casting the dynamics in this form possible whenever the bath is Markovian (or approximated as such) and the dynamics are hence time local.

further simplifications $v = \dot{x}$ and $\partial_x V = 0$ to obtain

$$m\dot{v} + \gamma v = \eta \tag{3.35}$$

which can be integrated to give

$$v(t) = \frac{1}{m}\int_{-\infty}^{t} \mathrm{d}t' \mathrm{e}^{-\frac{\gamma}{m}(t-t')}\eta(t') \tag{3.36}$$

from which we can calculate the mean kinetic energy

$$\langle E_{\mathrm{kin}}\rangle = \frac{1}{2}m\left\langle v^2\right\rangle = \frac{1}{2m}\int_{-\infty}^{t}\int_{-\infty}^{t} \mathrm{d}t'\mathrm{d}t'' \mathrm{e}^{-\frac{\gamma}{m}(2t-t'-t'')}\left\langle \eta(t')\eta(t'')\right\rangle = \frac{1}{2m}\frac{m\left(2\gamma T\right)}{2\gamma} = \frac{T}{2}. \tag{3.37}$$

where we have used the Markovian limit $\langle \eta(t)\eta(t')\rangle = 2\gamma T\delta(t-t')$. Rather than go further and prove the steady state distribution is the Gibbs state we can make the simpler check that this agrees with equipartition theorem. Equipartition theorem requires that, as here, at equilibrium the mean energy of any degree of freedom in which the energy is quadratic must be $T/2$. The correct equilibrium state, and hence the correct equilibrium mean energy of $\langle E_{\mathrm{kin}}\rangle$ is only possible if energy leaving the system (via dissipation) and entering the system (via fluctuations) are balanced in the correct way.

### A generic coupling to an oscillator bath

In more general case, in which we consider multiple $F_n$ operators coupling to the bath, and avoid making Markovian approximations, it is easy to convince ourselves that the same derivation *mutatis mutandis* takes the Hamiltonian

$$H = H_0 + \sum_{n\alpha} g_{n\alpha}x_{n\alpha}F_n + \frac{1}{2}\sum_{n\alpha}\left(p_{n\alpha}^2 + \omega_{n\alpha}^2 x_{n\alpha}^2\right) \tag{3.38}$$

and gives the dynamical equation

$$\frac{\mathrm{d}}{\mathrm{d}t}\frac{\partial L_0}{\partial \dot{\phi}_i} - \frac{\partial L_0}{\partial \phi_i} - \sum_n \frac{\partial F_n}{\partial \phi_i}\left(\eta_n(t) - \int_{-\infty}^{t}\mathrm{d}t'\Gamma_n(t-t')\frac{\mathrm{d}F_n(\phi(t'))}{\mathrm{d}t'}\right) = 0 \tag{3.39}$$

where the only significant difference is that avoiding the Markovian approximation has allowed the drag term to incorporate memory effects from the Bath. In equation (3.39) we have used

$$\Gamma_n(t) = \int_{-\infty}^{t}\mathrm{d}t' G_n^{\mathrm{R}}(t') \tag{3.40}$$

$$G_n^{\mathrm{R/A}}(t) = \pm\frac{\theta(\pm t)}{2\pi}\int_0^{\infty}\mathrm{d}\omega J_n(\omega)\sin(\omega t) \tag{3.41}$$

$$\langle \eta_n(t)\eta_m(t')\rangle = \frac{\mathrm{i}\delta_{nm}}{2}G_n^{\mathrm{K}}(t) = \frac{\delta_{nm}}{4\pi}\int_0^{\infty}\mathrm{d}\omega J_n(\omega)\cos(\omega t)\coth\left(\frac{\omega}{2T}\right). \tag{3.42}$$

The fluctuation dissipation theorem is explicit here, since both $G^{\mathrm{K}}$ and $G^{\mathrm{R}}$ are set by the bath density of states $J(\omega)$ (with some manipulation they can also be shown to satisfy equation (3.27)) which in turn is related to the original parameters of the system by[①]

$$J_n(\omega) = \pi\sum_{\alpha}\frac{g_{n\alpha}^2}{\omega_\alpha}\delta(\omega-\omega_\alpha) \tag{3.43}$$

[①]It can furthermore be shown, that substituting equation (3.43) into equation (3.40) recovers equation (E.6), showing the consistency of these approaches.

where in most physical circumstances all the $J_n$ correspond either the same bath, or bath of the same spectra, and so usually the label $n$ is redundant.

### 3.2.4 A stochastic Schrödinger equation and the Landau-Lifshitz-Gilbert equation

Using the generic Lagrangian of equation (3.20) with the dynamical equation (3.39) a dissipative Schroödinger equation is obtained

$$\mathrm{i}|\dot{\psi}\rangle = H\,|\psi\rangle - \sum_n F_n\,|\psi\rangle\left(\eta_n - \int_{-\infty}^{t}\mathrm{d}t'\Gamma_n(t-t')\frac{\mathrm{d}\langle\psi|F_n|\psi\rangle}{\mathrm{d}t'}\right) \tag{3.44}$$

moving to the Ehrenfest picture by evaluating the evolution of an operator expectation value $\langle X\rangle$ we obtain

$$\langle\dot{X}\rangle = \langle\mathrm{i}\,[H,X]\rangle - \sum_n \langle\mathrm{i}\,[F_n,X]\rangle\left(\eta_n - \int_{-\infty}^{t}\mathrm{d}t'\Gamma_n(t-t')\frac{\mathrm{d}\,\langle F_n\rangle}{\mathrm{d}t'}\right) \tag{3.45}$$

evaluating this for a spins $\boldsymbol{s} = \langle\boldsymbol{\sigma}\rangle = \langle X\rangle$ with $H = -\boldsymbol{\sigma}\cdot\boldsymbol{B}/2$ and $F_n = \sigma_n$ yields

$$\dot{\boldsymbol{s}} = \boldsymbol{s}\times\boldsymbol{B} + \boldsymbol{s}\times\left(\boldsymbol{\eta} - \int_{-\infty}^{t}\mathrm{d}t'\Gamma(t-t')\dot{\boldsymbol{s}}(t')\right) \tag{3.46}$$

and making a Markovian approximation, we obtain the Landau-Lifshitz-Gilbert equation (3.9a). However, following our discussion of the physics of flux qubits in Section 3.1.1 we are interested in the case $F = \sigma_z$ where only the one operator is coupled to the bath. This yields the maximally anisotropic Landau-Lifshitz-Gilbert equation

$$\dot{\boldsymbol{s}} = \boldsymbol{s}\times\boldsymbol{B} + \boldsymbol{s}\times\hat{\boldsymbol{z}}\,\hat{\boldsymbol{z}}\cdot\left(\boldsymbol{\eta} - \int_{-\infty}^{t}\mathrm{d}t'\Gamma(t-t')\dot{\boldsymbol{s}}(t')\right) \tag{3.47}$$

where $\hat{\boldsymbol{z}}$ is the unit vector. Taking the Markovian limit, and studying a system of many spins, these can be put into forms analogous to the isotropic equation (3.9)

$$\dot{\boldsymbol{s}}_i = \boldsymbol{s}_i\times(\boldsymbol{B}_i + \boldsymbol{\eta}_i - \gamma\hat{\boldsymbol{z}}(\hat{\boldsymbol{z}}\cdot\dot{\boldsymbol{s}}_i))\,, \tag{3.48a}$$

$$\dot{\boldsymbol{s}}_i = \boldsymbol{s}_i\times(\boldsymbol{B}_i + \boldsymbol{\eta}_i) - \gamma\,\boldsymbol{s}_i\times\hat{\boldsymbol{z}}\,[\hat{\boldsymbol{z}}\cdot(\boldsymbol{s}_i\times\boldsymbol{B}_i)]\,. \tag{3.48b}$$

#### A discussion of approximation

We briefly discuss what degree of approximation we have made in writing down the stochastic Schrödinger-Langevin equation (3.44). From the derivation it seems the approximation might be severe: in the expansion of the action about the classical fields, in equation (3.26), we discarded all terms which were higher than quadratic order in the quantum variables. We might therefore imagine that we have discarded almost all the quantum dynamics! Indeed in the single particle dynamics we studied in Section (3.2.3), the equations of motion were entirely classical. However contrast this with the Schrödinger-Langevin equation (3.44) where setting $F_n = 0$ (i.e. decoupling the system from the environment) recovers the Schrödinger equation, suggesting we have not lost any of the quantum dynamics.

So how do we reconcile these pictures? In discarding the higher order terms we have lost information about fluctuations away from the saddle point dynamics. The severity of this approximation depends on how good our original saddle point approximation is (if the saddle point is exact, we do not need the higher order terms at all). Generally this depends on the restrictiveness of the manifold of states in our functional integration.[①]

[①]Extending path integral methods to include larger manifolds of states, in particular entangled states, is a current

For the single particle case in Section (3.2.3) we used the Feynman path integral Lagrangian, from equation (3.16), which resolves states over the $|x\rangle$ basis. So in taking the saddle point, we approximate the systems dynamics by using a description which has a well defined position. This restriction is severe, and so we obtain only the classical dynamics.

In obtaining the Schrödinger-Langevin equation (3.44) we used the fully quantum Lagrangian of equation (3.20), which, when $|\psi\rangle$ is allowed to vary over the full Hilbert space, the saddle points of this encode the exact closed system dynamics. Naively this might suggest there is no approximation. The restriction we have made though in our saddle point dynamics is to restrict to product states of the bath and the system. This understanding is consistent with an alternative derivation of the LLG dynamics in which we are explicitly required to make the same approximation in appendix E.1.

## 3.3 Dynamics of a dissipative two level system

We now explore the novel dynamics in the presence of anisotropic coupling to the bath in its different parameter regimes. This model, equations (3.48a) and (3.48b), describes the dissipative dynamics of a system of interacting, non-entangled flux qubits, with environmental coupling solely through the $\hat{s}_z$ operator. There are important differences between the effects of isotropic environmental couplings, equations (3.9a) and (3.9b), and anisotropic couplings, equations (3.48a) and (3.48b). The energy conserving dynamics of these two models are the same, consisting of precession about the external field, and they both relax to the same thermal equilibrium distribution. We shall concentrate on the case where thermal fluctuations are small in the sense that the equilibrium thermal distribution subtends a small solid angle on the Bloch sphere. This requires that $\langle\theta^2\rangle \approx T/B \ll \pi^2$, or alternatively $B \gg T$. In this limit, we may sensibly discuss a large deviation from thermal equilibrium and consider the dissipative relaxation to it. These dynamics are very different in the presence of an isotropic, equations (3.9a) and (3.9b), and anisotropic coupling, equations (3.48a) and (3.48b), to the bath.

The Landau-Lifshitz-Gilbert equation constitute a special case where the Hamiltonian and dissipative dynamics separate in the equations of motion. This separation is clear when written in polar coordinates. For brevity we neglect stochastic terms and let $\boldsymbol{B} \parallel \boldsymbol{z}$, we find

$$\dot{\theta} = -\frac{\gamma s B}{1+\gamma^2 s^2}\sin\theta, \qquad \dot{\phi} = \frac{B}{1+\gamma^2 s^2}. \tag{3.49}$$

These equations generate motion in perpendicular directions and, there is no interplay between their dynamics.

In contrast, in more general dissipative models there is no such separation of the effects of precession and dissipation, and their interplay remains important. In the Langevin equation for $\hat{s}_z$ coupling, equation (3.48b), the system relaxes indirectly, through the interplay of dynamics and the state dependent modulation of the rate of dissipation. The effect of this interplay is highlighted by the appearance of regions of novel behaviour, visible in Figure 3.4, such as dissipation free precession, retrograde motion, and effective dimensional reduction.

To discuss the dynamics of the $\hat{s}_z$-coupling model, it is useful to introduce the time-scales $\tau_{\mathrm{p}}^{-1} = B = |\boldsymbol{B}|$ and $\tau_{\mathrm{d}}^{-1} = \gamma s B \sin^2\theta^*$ where $\theta^*$ is the polar angle of the field $\boldsymbol{B}$ from $\boldsymbol{z}$. $\tau_{\mathrm{p}}$ and $\tau_{\mathrm{d}}$ which are characteristic of the precessional motion and dissipative motion, respectively. In the limits where these scales are widely separated, the system's behaviour is dominated by the faster dynamics on short time-scales, whilst some effective dynamics emerge on longer time-scales.

area of research [98].

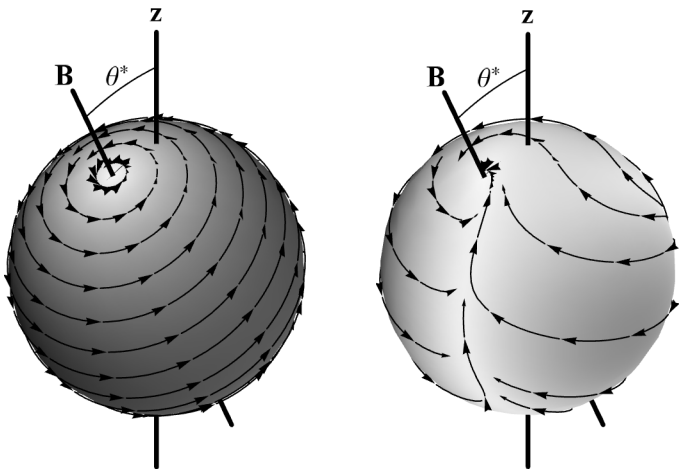


(a) $\theta^* = \frac{\pi}{8}, \gamma s = 0.6$ (b) $\theta^* = \frac{\pi}{8}, \gamma s = 6$

Figure 3.4: *Dynamics of spins in the presence of anisotropic dissipation.* The direction and rate of evolution over the sphere surface are indicated by the streamlines and grayscale density, darker regions indicate faster evolution. (a) For *weak anisotropic coupling* the state precesses similarly to isotropic coupling. (b) For *strong anisotropic coupling* dynamics is markedly different. The system rapidly relaxes to a reduced O(2) manifold where it undergoes constrained dynamics.

### 3.3.1 Weak coupling limit, $\tau_\mathrm{p} \ll \tau_\mathrm{d}$

For weak coupling, the system's behaviour remains dominated by the precession found in the fully closed system dynamics. As shown in fig. 3.4a, the spin will general perform many rotations about the magnetic field, $\boldsymbol{B}$, before reaching the neighbourhood of the ground state. This allows the dissipation and noise to be averaged over these rotations. In this regime the Langevin equation may be approximated by a Landau-Lifshitz-Gilbert equation

$$\dot{\boldsymbol{s}} = \boldsymbol{s} \times [(\boldsymbol{B} + \boldsymbol{\eta}_\mathrm{eff}) - \gamma_\mathrm{eff}\, \boldsymbol{s} \times (\boldsymbol{B} + \boldsymbol{\eta}_\mathrm{eff})] \tag{3.50}$$

where $\gamma_\mathrm{eff} = \frac{1}{2}\gamma \sin\theta^*$ is the effective dissipation, This results in dynamics characteristically similar to the isotropic case (equations (3.9a) and (3.9b)), thus the limit $\tau_\mathrm{p} \ll \tau_\mathrm{d}$ offers no novel dynamics.

### 3.3.2 Strong coupling limit, $\tau_\mathrm{p} \gg \tau_\mathrm{d}$

In the limit $\tau_\mathrm{p} \gg \tau_\mathrm{d}$, when the effects of anisotropy show up most profoundly, the system's dynamics are dominated by the dissipative term. This term is state dependent and drives rotation about the $\boldsymbol{z}$ axis, however the dissipation goes to zero when $\boldsymbol{B}$, $\boldsymbol{s}$ and $\boldsymbol{z}$ are coplanar.

Exactly how this reveals itself in the dynamics depends on the bath memory and temperature, though the net effect is similar in all cases: we see a separation of time-scales and a reduction of the full O(3) qubit dynamics to effective O(2) dynamics characterised by fast decay towards, or oscillation around, a reduced manifold.

#### The Markovian approximation

In the first instance, it is easiest to analyse our model within an Markovian approximation. Separating equation (3.48b) into the slow $\theta$ and fast $\phi$ dynamics we obtain

$$\begin{aligned} \dot{\theta} &= -B \sin\theta^* \sin\phi, \\ \dot{\phi} &= B\left(\cos\theta^* - \sin\theta^* \left(\cos\phi \cot\theta + s\gamma \sin\theta \sin\phi\right)\right) + \eta. \end{aligned} \tag{3.51}$$

where $\phi$ typically relaxes with a characteristic time-scale

$$\tau_\phi = \frac{1}{\gamma s B \sin\theta \sin\theta^*} \tag{3.52}$$

during which time $\theta$ makes a very small change. Thus we can treat the appearance of $\phi$ in the $\theta$ dynamics as a stochastic variable sampling the quasi-static distribution of the $\phi$ dynamics. This distribution is given approximately by

$$p(\phi) \propto \mathrm{e}^{-A(\theta)\cos(\phi-\phi^*)} \tag{3.53}$$

where

$$\begin{aligned} A(\theta) &= (\gamma T \tau_\phi \cos\phi^*)^{-1} \\ \tan\phi^* &= \frac{\sin(\theta-\theta^*)}{s\gamma \sin^2\theta \sin\theta^*}. \end{aligned} \tag{3.54}$$

and describes the effects of quasi thermal-equilibrium fluctuations in $\phi$. General effective dynamics in the slow $\theta$ variable are obtained in appendix E.2, the high and low $T$ cases are discussed here:

For $T \ll B$ the system quickly relaxes to a state in which the $\phi$ distribution is sharply peaked around the dynamical fixed point close to $\phi^* \approx 0$. This confining behaviour, as shown in fig. 3.4b occurs when the dissipative dynamics drive the system towards a one dimensional manifold on the fast time-scale $\tau_\mathrm{d}$, after which a much slower interplay between the Hamiltonian and dissipative dynamics sees the system relax to its ground state. These latter dynamics are described by

$$\dot\theta = \frac{B\sin(\theta^*-\theta)}{s\gamma\sin^2\theta} + \eta' \tag{3.55}$$

where the noise $\langle\eta(t)\rangle = 0$ has correlations $\langle\eta'(t)\eta'(t')\rangle = 2\gamma T(\tau_\phi B\sin\theta^*)^2\delta(t-t')$. In this limit the stochastic effect of the bath is weak (in the sense that thermal fluctuations subtend only a small angle on the Bloch sphere), whereas it strongly biases the trajectories to dissipate energy. In this manner the effect is akin to the trajectory ensemble approach [145] with a transition to dynamics confined to $\phi \approx \phi^*$. Due to the known relationship between these dyanmics [146–148] this Langevin equation can also be related to a Monte Carlo O(2) model on appropriate time-scales.

For $T \gg B$ the noise is sufficiently strong that $\phi$ makes large excursions away from the dynamical fixed point. However, due to the separation of time-scales, in both cases the long time dynamics are captured by an effective theory in the slow variable $\theta$. This constitutes a dissipative reduction of the phase space from O(3) to effective O(2) dynamics. In the $T \gg B$ limit, this reduced dynamics is described by

$$\dot\theta = \frac{B^2\sin(\theta^*-\theta)\sin\theta^*}{2T\gamma\sin\theta} + \eta' \tag{3.56}$$

where the noise has correlations $\langle\eta'(t)\eta'(t')\rangle = \tau_\phi(B\sin\theta^*)^2\delta(t-t')$.

The limit in which the dynamics become Markovian is subtle. Often Markovian dynamics can be obtained by assuming an Ohmic bath $J(\omega) = 4\gamma\omega$. When the temperature is much greater than the characteristic frequency of the system (the frequency at which the bath dynamics are sampled) the bath falls in its classical limit, $\coth(\omega/2T) \to 2T/\omega$, so that the noise in equation (3.42) becomes $\delta$-correlated. In this regime, however, thermal motion generally dominates—in the sense that thermal fluctuations cover the entire Bloch sphere; $\langle\theta^2\rangle \sim \pi^2$. There are alternative—more physical—circumstances for which for which the Markovian limit arises naturally, which in which the thermal noise does not dominate.

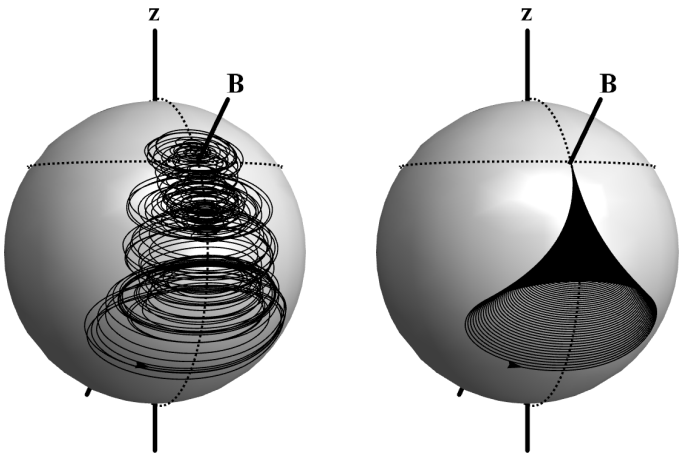


(a) (b)

Figure 3.5: *Typical oscillatory stochastic dynamics of spins in the presence of anisotropic dissipation with a Drude bath.* (a) A trajectory (solid) with parameters $\gamma = 400$, $B = 50/3T = 50\,\omega_{\rm d}$, plotted on the Bloch sphere. (b) The same trajectory plotted with the unphysical choice of $T = 0$ to illustrate the deterministic part of the dynamics: The system oscillates around the O(2) manifold with decaying amplitude. The lines $\phi = 0$ and $\theta = \theta^*$ (dashed) are shown, and an arrowhead indicates the initial state.

### Drude dynamics

We consider a bath which is peaked at a characteristic frequency $\omega_{\rm d}$. For ease of calculation we use the Drude bath which has density of states given by

$$J(\omega) = 4\gamma\omega \frac{\omega_{\rm d}^2}{\omega^2 + \omega_{\rm d}^2} \tag{3.57}$$

where the Drude frequency, $\omega_{\rm d}$, defines the bath cutoff. The new energy scale allows the bath to be in its classical limit, $T \gg \omega_{\rm d}$, even when the equilibrium thermal fluctuations of the system are small, $T \ll B$. It is then sensible to discuss the dissipation-dominated realaxation to this equilibrium distribution.

The Drude bath has a memory on time-scales determined by the cut-off, $\omega_d^{-1}$. The dynamical dependence on the history of the bath is captured by introducing a time-dependent field term

$$\dot{\boldsymbol{s}}_i = \boldsymbol{s}_i \times (\boldsymbol{B}_i + \boldsymbol{B}_{\rm diss})\,, \tag{3.58a}$$

$$\dot{\boldsymbol{B}}_{\rm diss} = -\omega_{\rm d}\left(\boldsymbol{B}_{\rm diss} + \gamma\hat{\boldsymbol{z}}\left[\hat{\boldsymbol{z}} \cdot (\boldsymbol{s}_i \times \boldsymbol{B}_i)\right] - \boldsymbol{\eta}\right), \tag{3.58b}$$

where $\langle \eta_z(t)\eta_z(t')) \rangle = 2\gamma T\delta(t - t')$ and as before and we take $\omega_d \ll T$. This is shown in detail in Appendix E.3. The previously discussed limit is clear as $\omega_{\rm d} \to \infty$.

As $\boldsymbol{B}_{\rm diss} \parallel \boldsymbol{z}$, the main effect of the bath is to induce oscillations in $\phi$ about the Markovian trajectory. In this strongly dissipative limit the oscillations have a frequency $\sqrt{\omega_{\rm d}/\tau_\phi}$ and describe fluctuations that are small in the $\theta$ direction and decay away on the bath memory time-scale $1/\omega_{\rm d}$. When the oscillation decay is much faster than the decay of $\theta$—i.e $\omega_{\rm d} \gg B/s\gamma$—we recover the Markovian O(2) dynamics described by eqs (3.55). A derivation of this is shown in appendix E.3. The characteristic qualities of a typical trajectory are depicted in Figure 3.5, whilst a simulation of the dynamics of equation (3.58) showing the separation of characteristic time-scales is shown in Figures 3.6 and 3.7.

To conclude this discussion we summarise the physical limits we have studied:

- We have assumed we are working in the strong coupling limit where the dynamical $B\gamma s \gg B$. In this limit the dissipative dynamics in $\phi$ are much faster than the precessional dynamics

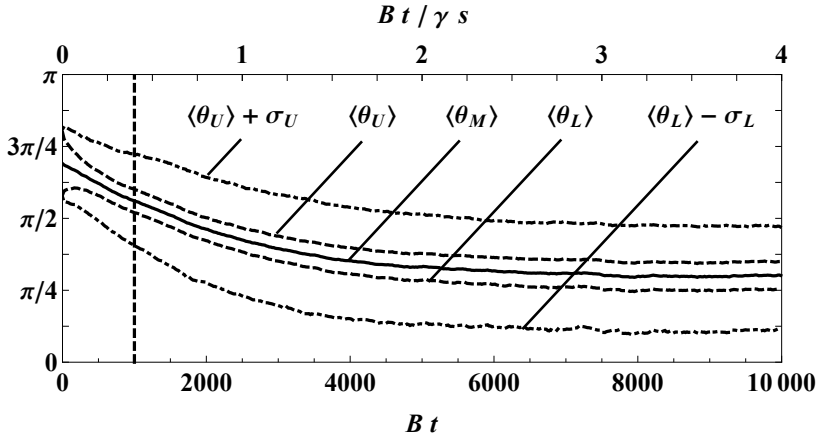


(a) relaxation of $\theta$ up to $t = 10^4/B$ shown by the mean upper bound $\theta_U$, mid-point $\theta_M$, and lower bound $\theta_L$ of the trajectory envelopes. The vertical line indicates the range of plot (b).

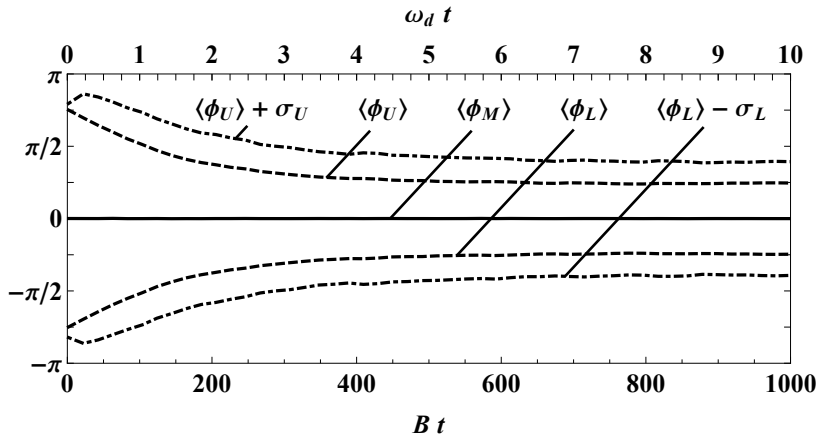


(b) relaxation of $\phi$ up to $t = 10^3/B$ shown by the mean upper bound $\phi_U$, mid-point $\phi_M$, and lower bound $\phi_L$ of the trajectory. (10× rescaling)

Figure 3.6: *Different time-scales of relaxation in the stochastic dynamics of (a) $\theta$ and (b) $\phi$ when coupled to a Drude bath (Note the different plot ranges).* An ensemble of 1000 spins ($s = 1/2$) initially at $\theta = 3\pi/4$, $\phi = 3\pi/4$ when $t = 0$ evolve with a magnetic field in the $\theta^* = \pi/4$, $\phi^* = 0$ direction. The coupling is $\gamma = 5 \times 10^3$, with energy scales $B = 10T = 100\omega_{\rm d}$, satisfying $B \gg T \gg \omega_{\rm d} \gg B/\gamma s$.On the time-scales of $\theta$ dynamics the fast oscillations in the trajectories (see Figure 3.7c) means that the trajectories are best characterised by an envelope with upper bound $\theta_U$, lower bound $\theta_L$ and mid-point $\theta_M$, these are simply read off the oscillating trajectory as shown in Figure 3.7c. Since the initial conditions is an extrema of the fast oscillations the initial point lies on $\theta_U$ and $\phi_U$. The ensemble averages $\langle\theta_M\rangle$ (solid) and $\langle\theta_U\rangle, \langle\theta_L\rangle$ (dashed) are shown with $\langle\theta_U\rangle + \sigma_U = \langle\theta_U\rangle + \sqrt{\langle\theta_U^2\rangle - \langle\theta_U\rangle^2}$, and $\langle\theta_L\rangle - \sigma_L = \langle\theta_L\rangle - \sqrt{\langle\theta_L^2\rangle - \langle\theta_L\rangle^2}$ (both dot–dashed) illustrating the ensemble width. (a) The slow theta coordinate relaxes towards the equilibrium value $\theta^* = \pi/4$ on a time-scale $\gamma s/B$, approaching it at $t \approx 10^4/B$. The vertical line indicates the range of plot (b). (b) The same statistics are presented for the $\phi$ dynamics: The $\phi$ dynamics relaxes to its equilibrium distribution much faster on a characteristic time-scale $\tau \sim 1/\omega_{\rm d}$ and is fully relaxed by $t \approx 500/B$.

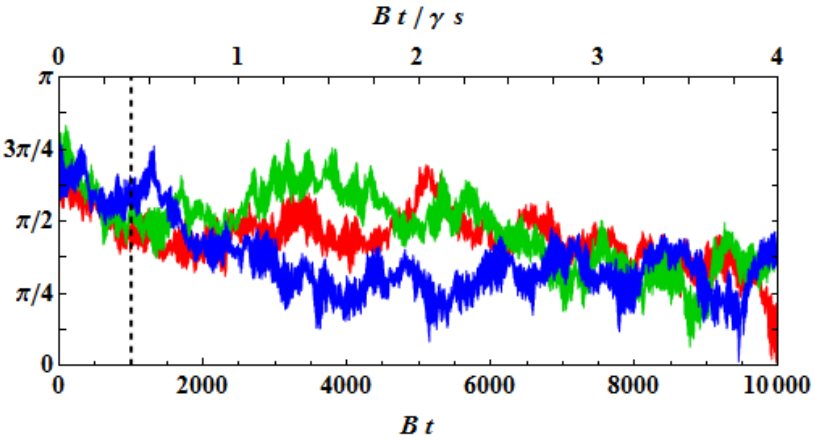


(a) $\theta$ relaxation on a long time-scale, up to $t = 10^4/B$.

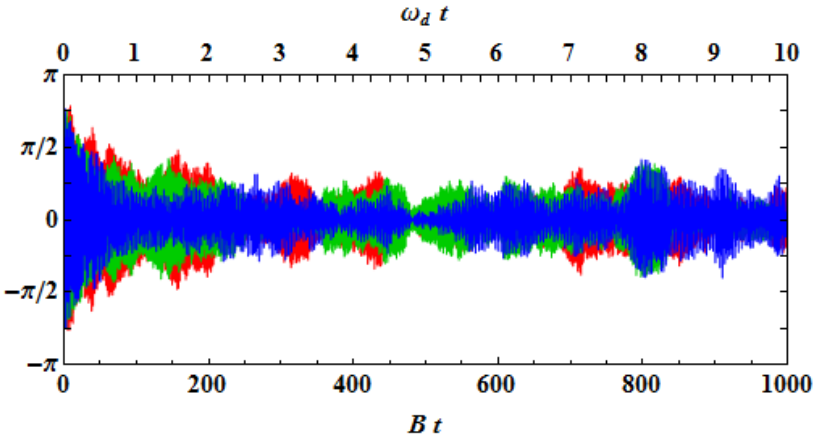


(b) $\phi$ relaxation on a shorter time-scale, plotted up to $t = 10^3/B$ (10× rescaling).

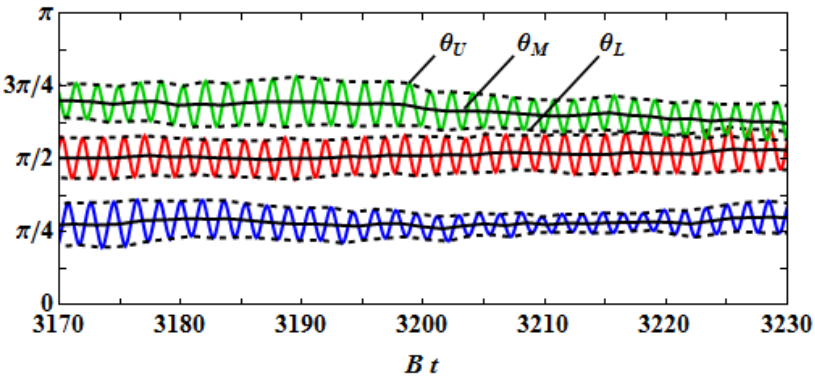


(c) very short time-scale oscillatory behaviour in $\theta$ induced by bath memory (see equation E.22).

Figure 3.7: *Different dynamical time-scales of typical trajectories in $\theta$ and $\phi$ when coupled to a Drude bath.* A plot of three sample trajectories from the ensemble studied in Figure 3.6. Being drawn from the ensemble these spins ($s = 1/2$) evolved in the same conditions: initially prepared at $\theta = 3\pi/4$, $\phi = 3\pi/4$ at $t = 0$ and evolve with a magnetic field in the $\theta = \pi/4$, $\phi = 0$ direction. The coupling is $\gamma = 5 \times 10^3$, with energy scales $B = 10T = 100\omega_\mathrm{d}$, satisfying $B \gg T \gg \omega_\mathrm{d} \gg B/\gamma s$. (a) Trajectories in $\theta$ relax on a long time scale. The vertical dashed line indicates the range of plot (b). (b) $\phi$ relaxes on a shorter time-scale, the confinement of $\phi$ is evidenced by the typically small excursions from $\phi = 0$. (c) Oscillatory behaviour induced by the bath occurring on shorter time-scales $\tau \sim \sqrt{\tau_\phi/\omega_\mathrm{d}}$ is plotted for $\theta$, similar behaviour occurs for $\phi$. This behaviour is expanded on in appendix E.3, where the oscillations appear in equation E.22. Each oscillatory trajectory can be characterised by the upper and lower edges $\theta_U$ and $\theta_L$ of its envelope, and its midpoint $\theta_M$. The ensemble statistics of these quantities are studied in Figure 3.6.

about the field $\boldsymbol{B}$.

- We have assumed that the equilibrium thermal fluctuations are small $B \gg T$ and that the environmental coupling is strong.
- We have further assumed that temperature prevents quantum correlations persisting in the bath, $T \gg \omega_{\mathrm{d}}$–though this condition may be relaxed at the cost of losing the Markovian quality of the dynamics.

Our analysis shows an effective reduction in phase space from, O(3) to O(2), resulting from the confinement of the $\phi$ coordinate to a typically small region around $\phi = 0$. This occurs when $B \gg T \gg \omega_{\mathrm{d}} \gg B/\gamma s$. In this parameter regime we have also shown that when coupled to the more general Drude bath (3.57), the system is described by the Markovian O(2) dynamics of equation (3.55) on time-scales greater than the bath memory, $1/\omega_{\mathrm{d}}$.

## 3.4 Consequences of anisotropic dissipation

The Langevin equation derived in the previous section exhibits markedly distinct behaviours in different regimes. This has implications both for attempts to fit experimental data to such models and, ultimately, for the usefulness of a system described by them for computation.

### 3.4.1 Different behaviours for the same system

For a qubit to be useful for quantum computation it must be sufficiently manipulable [149]. For even this most simple system of a single qubit, this in effect requires the implementation of at least two non-parallel magnetic fields. The field, $\boldsymbol{B}$, is necessarily assumed to be a tunable parameter of the system, whereas the environmental coupling, $\gamma$, is assumed non-tunable and fixed at some finite value.[①]

For the anisotropic $\sigma^z$ coupling to the environment studied here, the strength of dissipation depends not only on the fixed parameter $\gamma$, but also on the orientation of the magnetic field, $\boldsymbol{B}$. This is important when characterising such a device. In particular a system that is analysed under conditions when $\boldsymbol{B}$ and $\boldsymbol{z}$ are nearly aligned will appear weakly coupled, whereas for other orientations of $\boldsymbol{B}$ the dynamics may be entirely dominated by environment-induced dissipative dynamics.

It is a general feature of qubit systems that inhomogeneous environmental couplings will result in dynamics that are correspondingly inhomogeneous [112, 125, 150, 151]. We see here that certain states evolve with minimal dissipation, whilst others are dominated by dissipative or noisy dynamics. In extreme cases this may amount to a reduction in the effective state space.

### 3.4.2 A model for lossy qubit arrays

A natural application of our analysis is to understand some puzzling features of the D-Wave machine [152]. This machine consists of a tuneable array of coupled Josephson junctions whose dynamics may be controlled to perform a quantum annealing or adiabatic computation. Various models have been posited for this system which are reviewed in ref [128]. These include Bloch-Redfield simulations, Landau-Lifshitz-Gilbert models and two different O(2) models. Our analysis sheds light on the relationship between these different models and why apparently quite different models yield surprisingly similar results. In particular, the salient features of the two O(2) models proposed in the under-damped [51] and over-damped [52, 53] regimes can be found in different limits of the Landau-Lifshitz-Gilbert model when proper attention is paid to the effects of the

[①] If $\gamma$ were tunable we assume it would be fixed at its minimum value.

bath. These models are appropriate in a limit where decoherence renders entanglement effects negligible. Bloch-Redfield simulations—the only one of the above to include entanglement—are expected to yield similar results in this limit.

In the *underdamped limit*, the qubit precesses about the adiabatic minimum. Projecting this motion onto the polar angle $\theta$ results in harmonic oscillations of the polar angle about its adiabatic minimum. This is essentially the O(2) model of Ref [51], though strictly the effective kinetic term depends on the local effective field felt by the quantum bit and so varys through the computation.[①] This model is expected to accurately reflect the dynamics up to the point where it deviates markedly from adiabatic, accounting for its success in predicting the probability of correctly performing adiabatic computation in some circumstances [153].

In this chapter we have focussed on the *overdamped limit*. A model of over-damped classical rotors undergoing a thermal exploration of the O(2) state space was introduced in Ref [52]. This model reproduced additional, apparently quantum, effects [126], though it is interesting that the underdamped non-thermal O(2) model was also able to reproduce these results. Further statistics presented in evidence of quantum effects [128] were reproduced only by the over-damped classical model [53]—and not the underdamped model. The overdamped model of Refs [52] and [53] can be obtained by artificially confining the motion of overdamped classical O(3) spins to the O(2) phase space [154]. Our analysis in Section 3.3.2 shows that, remarkably, anisotropic dissipation can bias the dynamics towards just such a confinement: the O(3) dynamics of dissipative spin dynamics (equations (3.48) and (3.58)) are reduced to the effective O(2) dynamics of equation (3.55) as illustrated in Figures 3.6 and 3.7. An unanticipated feature of this relaxation to an $O(2)$ manifold is the restriction of the system dynamics to half of the $O(2)$ submanifold. The whole of this submanifold is a fixed point of the initial rapid decay, but half forms a stable and half an unstable fixed point.

The representation of over-damped classical rotors in Refs [52] and [53] is at first glance rather different from the Langevin equation (3.55). However, Metropolis-Hastings dynamics describes a dissipative relaxation to thermal equilibrium and have been used previously to model dynamics described by a Langevin equation [146–148],[②] The *ad hoc.* model of Refs [52] and [53] do not include the biasing of trajectories to half of the $O(2)$ manifold that naturally arises from microscopic considerations. However, the dynamics of the component of qubit projected onto the direction of the local field is rather similar (see Appendix E.4), perhaps accounting for the success of Refs [52] and [53] despite their models not being strictly derivable from microscopic considerations.

These analyses raise an immediate question of whether the D-Wave system is in an *overdamped or underdamped limit*. This is subtle. As discussed in 3.4.1, the strength of damping depends on the microscopic details of coupling to the bath, the orientation of the effective field relative to the $z$-axis, and the instantaneous position of the qubit on the Bloch sphere. Because of the latter effects, the dissipation is largest at the start of D-Wave computation, when the effective field and Bloch spins are in the $xy$-plane, and decreases to zero as the computation proceeds. Even when the coupling to the bath is strong, and the initial dynamics overdamped, there is a transition to underdamped dynamics at some point in the computation. Whether or not the over- or under-damped dynamics determines the success or failure of a computation depends on precisely when this cross-over occurs.

So is the D-Wave system initially over-or under-damped? This question does not appear to be resolved by published experimental data. To our knowledge no direct measurements of $T_1$ or $T_2$ times on the D-Wave are available. Measurements of high frequency flux noise *via* macroscopic

[①] It can be derived in a spinwave-like expansion, integrating out the components that do not lie in the great circle traversed by the adiabatic minimum.

[②] The relation of the Metropolis algorithm to Fokker-Planck diffusion has been noted previously in general terms in Ref [146] whilst other Monte–Carlo methods have been specifically connected with Langevin type dynamics in Refs [147] and [148]

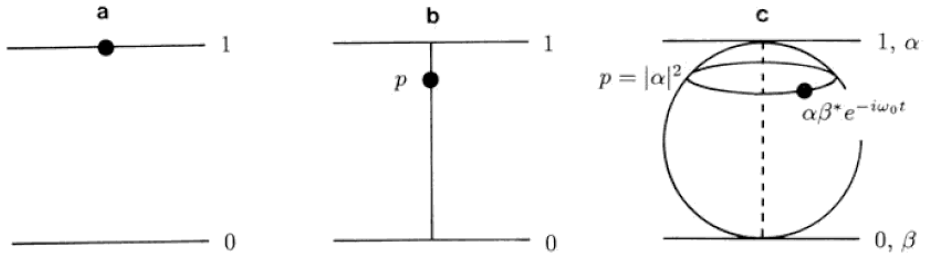


Figure 3.8: The two level system (a) in one of two well defined classical state (b) in statistically uncertain classical state given by the line of values of $p$ and (c) a quantum state, defined by the position on the ball of quantum state—the Bloch sphere. Dissipative equations of motion for the behaviour of these three models can be obtained from very similar arguments. Figure from [158]

resonant tunnelling [155] indicate that above a cutoff $\omega_{\rm HF} = 0.5\,{\rm GHz}$ noise is Ohmic with $\gamma_{\rm HF} = \Phi_0^2 S_\phi(0)/2\hbar k_{\rm B} T L^2 \approx 2$, where the values for inductance $L = 265.4{\rm pH}$ and shunt resistance $R = 2kTL^2/S_\Phi(0) = 20k\Omega$ measured in Ref [155], and $\Phi_0$ is the magnetic flux quantum.[①] However, our analysis shows that the qubit is also sensitive to noise with frequency lower than the system frequency. At the lowest frequencies, the noise is of $1/f$ form [131]. There is a large window between the high frequency [155] and the low frequency measurements [131] in which the noise has not been directly measured. The measured current noise characteristics do not, therefore, preclude the possibility of larger $\gamma$ and initial over-damped dynamics.

## 3.5 The ensemble dynamics

We close this chapter with a comparison between the more commonly seen Lindblad description of open systems dynamics, and the a description of the the ensemble dynamics found in this study. We comment briefly on the discrepancy between the two sets of dynamics.

### 3.5.1 The stochastic Schrödinger equation and the Lindblad Master equation

Here we present an interesting physical picture due to Carmichael [156, 157] which allows us to obtain the Lindblad description of a weakly coupled open quantum system. This is found via a stochastic Schrödinger equation and which puts the potentially slightly exotic dynamics of equation (3.44) in the context of an established literature on stochastic Schroödinger descriptions of open systems.

#### Classical system

First we consider a classical two-level system coupled to an environment and extend this to a quantum picture in order to understand the open system dynamics. We consider the simplest case of a environment at $T = 0$. The two states of the system are labelled $|0\rangle$ and $|1\rangle$, and have energies $E_0 < E_1$. There being only two states, there are thus only two transitions which our system can undertake: (i) Excitation $|0\rangle \to |1\rangle$, which does not occur since the bath as at zero temperature, and so cannot provide energy to the system, and (ii) Emission $|0\rangle \to |1\rangle$. Thus the evolution of

[①] This form can be seen as follows: from equation (3.2) we see that the fluctuations $\eta$ are related to the fluctuations in $\phi_{\rm ext}$ by a factor $\Phi_0/L$. Hence

$$S_\phi(t-t') = \langle \phi(t)\phi(t')\rangle - \langle\phi\rangle^2 = \Phi_0^2 \langle \eta(t')\eta(t)\rangle / L^2 = 2\gamma(t-t')T\Phi_0^2/L^2. \tag{3.59}$$

The result in the main text is obtained by Fourier transforming and taking $S_\phi(\omega = 0)$.

this system over an interval $\delta t$ is captured by the update rules

$$\text{decision rule: } p_{\text{decay}} = \begin{cases} \gamma\delta t, & \text{if } |1\rangle \\ 0, & \text{if } |0\rangle \end{cases} \tag{3.60a}$$

$$\text{dynamical rule: } \begin{cases} \text{if decay} & |1\rangle \to |0\rangle \\ \text{if no decay} & |1\rangle \to |1\rangle \\ & |0\rangle \to |0\rangle\,. \end{cases} \tag{3.60b}$$

**Classical system with statistical uncertainty**

For the probabilistic cases, in which the system is in state $|1\rangle$ with some probability $p$, and $|0\rangle$ with $1-p$, we have to additionally consider the information obtained by observing (or not observing) the emission of a quantum of energy from the system. This is captured by applying Bayes' rule. This tells us that if we observe no decay for an interval $\delta t$ that the updated probability is

$$p_{1|\text{no decay}} = \frac{p_{\text{no decay}|1}p_1}{p_{\text{no decay}}} = \frac{p_{\text{no decay}|1}p_1}{p_{\text{no decay}|1}p_1 + p_{\text{no decay}|0}p_0} = \frac{(1-\gamma\delta t)p}{(1-\gamma\delta t)p + (1-p)}. \tag{3.61}$$

Thus, expanding to linear order in $\delta t$ the decision rule for the dissipative classical two level system is given by

$$\text{decision rule: } p_{\text{decay}} = p\gamma\delta t \tag{3.62a}$$

$$\text{dynamical rule: } \begin{cases} \text{if decay} & p \to 0 \\ \text{if no decay} & p \to p - p(1-p)\gamma\delta t + \mathrm{O}(\delta t^2). \end{cases} \tag{3.62b}$$

**Quantum system**

To translate this into the behaviour of a dissipative quantum system we substitute the probabilities for amplitudes related by $p_1 = |\alpha|^2$ and $p_0 = |\beta|^2$ of a state vector $|\psi\rangle = \alpha\,|1\rangle + \beta\,|0\rangle$ and that the update of the quantum system is given by

$$\text{decision rule: } p_{\text{decay}} = |\alpha|^2\gamma\delta t \tag{3.63a}$$

$$\text{dynamical rule: } \begin{cases} \text{if decay} & \begin{pmatrix}\alpha\\ \beta\end{pmatrix} \to \begin{pmatrix}0\\ 1\end{pmatrix} \\ \text{if no decay} & \begin{pmatrix}\alpha\\ \beta\end{pmatrix} \to \begin{pmatrix}\alpha - \frac{\gamma}{2}\alpha|\beta|^2\delta t\\ \beta + \frac{\gamma}{2}\beta|\alpha|^2\delta t\end{pmatrix} + \begin{pmatrix}-\frac{\mathrm{i}\omega}{2}\alpha\\ \frac{\mathrm{i}\omega}{2}\beta\end{pmatrix}. \end{cases} \tag{3.63b}$$

where $\omega = E_1 - E_0$. Written in the usual bra-ket notation this becomes

$$\text{decision rule: } p_{\text{decay}} = \langle\psi|\sigma^+\sigma^-|\psi\rangle\delta t \tag{3.64a}$$

$$\text{dynamical rule: } \begin{cases} \text{if decay} & |\psi\rangle \to \frac{\sigma^-|\psi\rangle}{\sqrt{\langle\psi|\sigma^+\sigma^-|\psi\rangle}} \\ \text{if no decay} & |\dot{\psi}\rangle = \underbrace{-iH\,|\psi\rangle}_{\substack{\text{coherent}\\ \text{evolution}}} - \underbrace{\frac{\gamma}{2}\sigma^+\sigma^-\,|\psi\rangle}_{\substack{\text{dissipative}\\ \text{evolution}}} + \underbrace{\frac{\gamma}{2}\,|\psi\rangle\,\langle\psi|\sigma^+\sigma^-|\psi\rangle}_{\substack{\text{preserves}\\ \text{normalisation}}}. \end{cases} \tag{3.64b}$$

where the three terms which appear in the dynamics are easily interpreted as shown in the labels. If we are happy to deal with the increased number of variables we can swap the stochastic evolution

of this state vector for the deterministic evolution of a density matrix $\rho = |\psi\rangle\langle\psi|$

$$\begin{aligned}\dot{\rho} &= p_{\text{decay}}\dot{\rho}_{\text{decay}} + (1-p_{\text{decay}})\dot{\rho}_{\text{no decay}} \\ &= \mathrm{i}\,[\rho, H] - \frac{\gamma}{2}\left(\sigma^+\sigma^-\rho + \rho\sigma^+\sigma^- - 2\sigma^-\rho\sigma^+\right)\end{aligned} \tag{3.65}$$

which is indeed a Lindblad master equation of a dissipative two level system. More generally if we consider a quantum system which undergoes a transition $|\psi\rangle \to L_i|\psi\rangle$ with probability $p = \langle\psi|L_i^\dagger L_i|\psi\rangle\delta t$ in each interval $[t, t+\delta t]$ and we obtain the general Lindblad master equation

$$\dot{\rho} = \mathrm{i}\,[\rho, H] - \frac{1}{2}\sum_i\left(L_i^\dagger L_i\rho + \rho L_i^\dagger L_i\right) - \sum_i L_i\rho L_i^\dagger \tag{3.66}$$

This relationship between stochastic jump quantum processes and the Lindblad equation [159].

One can ask: is there any physical meaning to these stochastic jump processes? In general it would appear not as the Lindblad equation is invariant under the transformation

$$L_n \to L_n + i\lambda_n, \qquad H \to H - \frac{1}{2}\sum_n\left(\lambda_n^* L_n + \lambda_n L_n^\dagger\right) \tag{3.67}$$

as can be seen in equation 3.64b is not a symmetry of the jump trajectory formalism. This entails a plethora ensembles of very characteristically different trajectories which leads to the same statistical behaviour of the density operator $\rho$. There is however a unique jump trajectory in which the evolution is local in the Hilbert space (i.e. the jumps are always infinitesimal). This is given by the stochastic process

$$|\dot{\psi}\rangle = -iH|\psi\rangle - \frac{1}{2}\sum_i\left(X_i\left\langle L_i^\dagger\right\rangle - X_i^\dagger\langle L_i\rangle - X_i^\dagger X_i\right)|\psi\rangle + \sum_i X_i|\psi\rangle\,\mathrm{d}W_i \tag{3.68}$$

where $X_i = L_i - \langle L_i\rangle$ and $\eta_i$ is a complex Itô process satisfying $\left\langle \mathrm{d}W_i \mathrm{d}W_j^*\right\rangle = \delta_{ij}\mathrm{d}t$ [159–161]. This equation is shown to be equivalent (in the limiting case of infinitely many infinitesimal jumps) to the jump diffusion approach and hence to the Lindblad equation in ref [159]. The three terms of equation 3.68 can be immediately identified with the three terms of equation (3.66) which we can similarly identify as (deterministic) coherent evolution, (deterministic) dissipation and (stochastic) fluctuations.

This relationship shows when stochastic wavefunction processes are equivalent to the Lindblad description of open systems.

### 3.5.2 Comparison of ensemble Dynamics

#### Lindblad description of a two level system

To put an open systems Master equation into Lindblad form (equation (3.66)) the secular approximation is made, this requires that the $L_i$ satisfy $\mathrm{i}[H, L_i] = \omega_i L_i$. For a two level system with $H = -B\sigma^{\mathrm{z}}/2$ the full range of possible couplings is $L_i = \sqrt{\gamma_+}\sigma^+, \sqrt{\gamma_-}\sigma^-, \sqrt{\gamma_{\mathrm{z}}}\sigma^{\mathrm{z}}$.[①] Furthermore $\gamma_+ = \gamma_-\mathrm{e}^{-\beta B}$ is required by fluctuation dissipation theorem.

The resulting dynamics are exactly solvable. Writing the ensemble polarisation in terms of its components parallel are perpendicular to $\boldsymbol{B}$ we have $\boldsymbol{m} = \langle\boldsymbol{\sigma}\rangle/2 = \mathrm{tr}\,[\boldsymbol{\sigma}\rho]/2 = \boldsymbol{m}_\parallel + \boldsymbol{m}_\perp$ whose dynamics are

$$\begin{aligned}\boldsymbol{m}_\parallel &= \boldsymbol{m}_{\text{eq}} + \mathrm{e}^{-t/t_1}(\boldsymbol{m} - \boldsymbol{m}_{\text{eq}}) \\ \boldsymbol{m}_\perp &= \mathrm{e}^{-t/t_2}(\boldsymbol{m}_\perp \times \boldsymbol{B})\end{aligned} \tag{3.69}$$

[①] This is of course a spanning set of operators for a two-level-system, however the $L_i$ do note combine linearly, and so this does not permit a general operator on the system. For example we have ruled out possibilities such as $L_i = \sigma^{\mathrm{y}}$ as $\mathrm{i}\,[H, \sigma^{\mathrm{y}}] = B\sigma^x \neq \omega_{\mathrm{y}}\sigma^{\mathrm{y}}$

where $1/t_1 = \gamma_+ + \gamma_-$ and $1/t_2 = (\gamma_+ + \gamma_- + 4\gamma_z)/2$ are the usual characteristic times of relaxation and dephasing, where the equilibrium magnetisation $\boldsymbol{m}_{\text{eq}}$ is defined by $|\boldsymbol{m}_{\text{eq}}| = \tanh(\beta B/2)/2$ and $\boldsymbol{m}_{\text{eq}} \parallel \boldsymbol{B}$. This solution does not feature the anisotropic dynamics studied in Section 3.3, this is maybe permissible as the Lindblad derivation assumes weak coupling, and so should be compared with the weak coupling dynamics Section 3.3.1 where the effects of the anisotropy are weak.

However, the Lindblad description contains only a minimal reference to the nature of the microscopic coupling to the environment encapsulated by the ratio $t_1/t_2$. Furthermore equation (3.69) shows that it does not have the capacity to capture the anisotropic dynamics. The solution has axial symmetry without any such assumption having been made about the microscopic Hamiltonian. Thus the Lindblad approach appears to result in a solution with higher symmetry than the microscopic problem.

#### Ensemble dynamics of the anisotropic LLG

The dynamics of the ensemble polarisation, found by summing the anisotropic LLG equation (3.48) over different realisations of the bath, is calculated in appendix E.4 within a first-moment approximation. The dynamics are given by

$$\dot{\boldsymbol{m}} = \boldsymbol{m} \times \boldsymbol{B} - \tilde{\gamma}(m)\boldsymbol{m} \times \hat{\boldsymbol{z}}\left[\hat{\boldsymbol{z}} \cdot (\boldsymbol{m} \times \boldsymbol{B})\right] - \gamma T\left(\mathbf{1} - \hat{\boldsymbol{z}}\hat{\boldsymbol{z}}^T\right)\left(\boldsymbol{m} - \frac{m}{\xi T}\boldsymbol{B}\right). \tag{3.70}$$

where $|\boldsymbol{m}| = m$, $\tilde{\gamma}(m) = \gamma[1/(4m^2) - 3/(\xi m)]$ and $\xi$ is defined implicitly by $m = \coth(\xi/2)/2 - 1/\xi$. In the limit of strong polarisation ($m \to 1/2$) we recover $\tilde{\gamma} = \gamma$. These dynamics show that this framework is able to capture effects of the anisotropy persist at ensemble level.

## 3.6 Conclusion

Our main result has been to show how anisotropic dissipation can bias quantum trajectories towards particular sub-manifolds of the system's Hilbert space. We have found a Langevin description of the dynamics of qubits that allows for anisotropic coupling to the environment. This is a natural generalisation of the Landau-Lifshitz-Gilbert equations which describe the dissipative dynamics of spins with isotropic coupling to the environment. The fluctuation-dissipation relation has the important consequence that the anisotropic noise generated by this coupling inevitably leads to anisotropic dissipation.

This model applies explicitly to qubits experiencing dissipation due to fluctuations in the level separation (environmental coupling to the $\hat{s}_z$ operator). When the coupling to the bath is strong the anisotropic dissipation drives rapid relaxation to a reduced O(2) manifold of constrained dynamics. This emergence of this effective dynamics from the underlying microscopics reproduces some salient features of the dynamics of the models of Refs [52, 53]. These models were capable of reproducing several observed behaviours of the D-Wave machine which had previously been argued to evidence quantum dynamics. This highlights the necessity of understanding the dynamics in dissipative and strong coupling cases when interpreting the dynamics of an experimental system.

Entanglement, which we neglect here, is crucial for full quantum dynamics, and necessary to get the exponential scaling between the quantum state space and number of qubits. It has been argued recently in Refs [129, 130] to act as a resource for adiabatic computation. These works modelled quantum adiabatic computation with artificial constraints on the entanglement analogous to the artificial constraint of a local subsystem to an O(2) manifold. However one may anticipate that the effects of dissipation could naturally bias the trajectories to these restricted manifolds. Understanding this will be key to determining how best to use limited or dissipating entanglement resources in computation.

Understanding of the effects of state-dependent noise and anisotropic coupling to the environment is crucial for the proper control of quantum devices. As we have shown in the case of the D-Wave machine, these effects can bias the system dynamics in unexpected ways. Used constructively, this may be harnessed to useful ends. If ignored, the dynamics may completely different from that intended.

# 4 | Thermalization and Entanglement in a simple model of Adiabatic Quantum Computation

This chapter presents some preliminary results from ongoing work which has been carried out in collaboration with V Oganesyan and A Green. The work investigates the role of the environment in influencing the dynamics of entanglement in a simple spin system. Specific attention is paid to the context of Adiabatic computation where we investigate in what circumstances adiabatic computation fails due to environmental coupling.

Entanglement is fundamental to many-body quantum systems. It is this property of quantum systems, that the statistics of particles cannot be described individually, but that the system must be described as a whole. This makes possible the linearity of quantum mechanics, the unitarity of time evolution, and absence of chaotic dynamics. Restricting entanglement suppresses tunnelling, introduces non-linearities into the dynamics and ultimately allows the possibility of chaos.

We study this in the simplest possible case, that of a pair of coupled spin-1/2 systems. We study the suppression entanglement both due to artificial restrictions introduced by hand, analogous to the approaches of truncating Schmidt rank, and by slowing down the effective dynamics of entanglement and microscopically by coupling the two spins to independent harmonic baths. We also show in the latter case how the effect of the environment in restricting entanglement is reflected in effective equations of motion, reducing the full Schrödinger to coupled Landau-Lifshitz-Gilbert equation.

Our main tool is a quantum Langevin equation for motion over the two-spin Hilbert space. Such an approach offers some insight into questions of entanglement structure not possible with the usual density matrix approach as it separates issues of admixture and entanglement that are difficult to separate in the density matrix.

## 4.1 The Hamiltonian dynamics of coupled spins

In this section we provide a parametrisation of a two-spin dimer that is very natural for considering separately the dynamics of classical (i.e. local) degrees of freedom, and quantum (i.e. entanglement) degrees of freedom. We then obtain the dynamics in these coordinates.

We are familiar with the notion of the Hopf-fibration as providing a map from the SU(2) state space of the two level system to the 3-sphere $S^2$. In the language of the TDVP, Section 2.1, this constitutes a parameterisation of the relevant Hilbert space with the polar and azimuthal angles $\theta$ and $\phi$ as

$$|\boldsymbol{s}\rangle = \mathrm{e}^{-\mathrm{i}\phi/2}\cos\frac{\theta}{2}\,|\uparrow\rangle + \mathrm{e}^{\mathrm{i}\phi/2}\sin\frac{\theta}{2}\,|\downarrow\rangle\,, \tag{4.1}$$

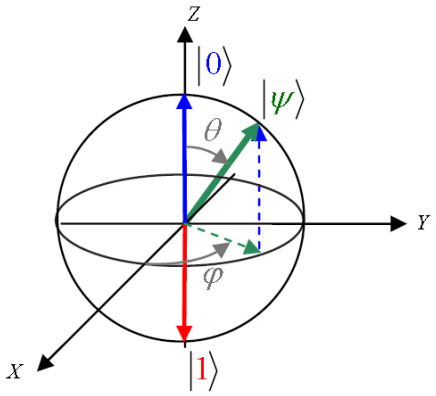


Figure 4.1: *The Bloch Sphere:* The state $|\psi\rangle = \alpha\,|0\rangle + \beta\,|1\rangle$ ostensibly has four degrees of freedom (two complex numbers) however the global phase and norm are unphysical. The physical states, those of the projective Hilbert space, can be parametrised by the $|\psi\rangle = \mathrm{e}^{-\mathrm{i}\phi/2}\cos(\theta/2)\,|0\rangle + \mathrm{e}^{\mathrm{i}\phi/2}\sin(\theta/2)\,|1\rangle$ using only two degrees of freedom, the angles $\theta$ and $\phi$. Each state can then be identified with the corresponding point $(\theta, \phi)$ on the 'Bloch sphere'.

where the vector $\boldsymbol{s}$ is given in the usual way

$$\langle \boldsymbol{s}|\,\hat{\boldsymbol{S}}\,|\boldsymbol{s}\rangle = s\,\langle \boldsymbol{s}|\,\sigma\,|\boldsymbol{s}\rangle = s\begin{pmatrix}\sin\theta\cos\phi\\ \sin\theta\sin\phi\\ \cos\theta\end{pmatrix} = \boldsymbol{s}. \tag{4.2}$$

where $s = 1/2$. These spherical coordinates then define a position on the Bloch sphere, shown in Figure 4.1. In direct analogy we may parametrise the state space of two coupled spin-1/2 subsystems by three spheres

$$|\psi\rangle = \cos\frac{\alpha}{2}\mathrm{e}^{-i\beta/2}\,|\boldsymbol{s}_1\rangle\,|\boldsymbol{s}_2\rangle + \sin\frac{\alpha}{2}\mathrm{e}^{i\beta/2}\,|-\boldsymbol{s}_1\rangle\,|-\boldsymbol{s}_1\rangle\,. \tag{4.3}$$

Two of these spheres are the usual Bloch spheres, with vectors $\boldsymbol{s}_1$ and $\boldsymbol{s}_2$ which describe the polarisation at each physical site. The third one, with vector

$$\boldsymbol{n} = \begin{pmatrix}\sin\alpha\cos\beta\\ \sin\alpha\sin\beta\\ \cos\alpha\end{pmatrix} \tag{4.4}$$

describes the entanglement between the two sites. When $\alpha = 0, \pi$ the system is not entangled, where as when $\alpha = \pi/2$ it is maximally entangled. The parametrisation in equation (4.3) can be understood as the matrix product state in canonical form on the simple system of a two-site chain.

Following the prescription of Section 2.1 we then obtain the equations of motion of this parametrisation. These are most easily acquired from the functional derivative of the action

$$\begin{aligned} S &= \int \mathrm{d}t L = \int \mathrm{d}t\,\langle\psi|\,i\partial_t - H\,|\psi\rangle \\ &= \int \mathrm{d}t\left(s\cos\alpha\left(\dot{\beta} + \dot{\phi_1}\cos\theta_1 + \dot{\phi_2}\cos\theta_2\right) - H(\alpha,\beta,\ldots)\right). \end{aligned} \tag{4.5}$$

This yields

$$\frac{\mathrm{d}}{\mathrm{d}t}\frac{\partial L}{\partial \dot{\alpha}} - \frac{\partial L}{\partial \alpha} = s\sin\alpha(\dot{\beta} + \dot{\phi}_1\cos\theta_1 + \dot{\phi}_2\cos\theta_2) + \frac{\partial H}{\partial \alpha} = 0, \tag{4.6a}$$

$$\frac{\mathrm{d}}{\mathrm{d}t}\frac{\partial L}{\partial \dot{\beta}} - \frac{\partial L}{\partial \beta} = -s\dot{\alpha}\sin\alpha + \frac{\partial H}{\partial \beta} = 0, \tag{4.6b}$$

$$\frac{\mathrm{d}}{\mathrm{d}t}\frac{\partial L}{\partial \dot{\theta_n}} - \frac{\partial L}{\partial \theta_n} = s\dot{\phi_n}\sin\theta_n\cos\alpha + \frac{\partial H}{\partial \theta_n} = 0, \tag{4.6c}$$

$$\frac{\mathrm{d}}{\mathrm{d}t}\frac{\partial L}{\partial \dot{\phi_n}} - \frac{\partial L}{\partial \phi_n} = -s\dot{\alpha}\sin\alpha\cos\theta_n - s\dot{\theta}_n\sin\theta_n\cos\alpha + \frac{\partial H}{\partial \phi_n} = 0. \tag{4.6d}$$

The function $H(\alpha, \beta, \ldots)$ is the expectation value of the Hamiltonian, calculated easily using that, for $n = 1, 2$

$$\langle\psi|\,\hat{\boldsymbol{s}}_n\,|\psi\rangle = \cos\alpha\,\boldsymbol{s}_n \tag{4.7}$$

$$\begin{aligned}\langle\psi|\,\boldsymbol{s}_1^i\boldsymbol{s}_2^j\,|\psi\rangle &= s_1^i s_2^j + s^2\sin\alpha\cos\beta\left(\theta_1^i\theta_2^j - \phi_1^i\phi_2^j\right) + s^2\sin\alpha\sin\beta\left(\theta_1^i\phi_2^j + \phi_1^i\theta_2^j\right) \\ &= \boldsymbol{s}_1^i\boldsymbol{s}_2^j + \mathrm{Re}\left[(n^x + \mathrm{i}n^y)(\theta_1^i - \mathrm{i}\phi_1^i)(\theta_2^j - \mathrm{i}\phi_2^j)\right]\end{aligned} \tag{4.8}$$

where the recovery of the classical values for unentangled states is clear by setting $\alpha = 0$. The vectors $s_n^i$, $\theta_n^i$, $\phi_n^i$, with $n = 1, 2$ and $i = x, y, z$ are the usual O(3) basis vectors

$$\boldsymbol{s}_n = s\begin{pmatrix}\sin\theta_n\cos\phi_n\\ \sin\theta_n\sin\phi_n\\ \cos\theta_n\end{pmatrix}, \qquad \boldsymbol{\theta}_n = \begin{pmatrix}\cos\theta_n\cos\phi_n\\ \cos\theta_n\sin\phi_n\\ \sin\theta_n\end{pmatrix} \qquad \boldsymbol{\phi}_n = \begin{pmatrix}-\sin\phi_n\\ \cos\phi_n\\ 0\end{pmatrix}, \tag{4.9}$$

which live on the usual two Bloch spheres, and the entanglement vector $\boldsymbol{n}$ exists on the 3rd Bloch sphere, corresponding to the non-classical degrees of freedom.

## 4.2 The influence of the environment on entanglement

Coupling to local baths can be achieved in the manner presented in Section 3.2. We consider a coupling to a bath that acts isotropically on each spin, that is we consider oscillator baths coupled to all six Pauli operators $\sigma_n^i$. From equation (3.31) we then obtain

$$0 = \dot{\beta} + s_1^z\dot{\phi}_1 + s_2^z\dot{\phi}_2 + \frac{\partial H}{\partial n^z} + \gamma\left(2\dot{n}^z + \boldsymbol{s}_1\cdot\boldsymbol{\eta}_1 + \boldsymbol{s}_2\cdot\boldsymbol{\eta}_2\right), \tag{4.10a}$$

$$0 = \dot{n}^z + \frac{\partial H}{\partial \beta}, \tag{4.10b}$$

$$0 = \boldsymbol{s}_i\times\dot{\boldsymbol{s}}_i + \partial_{\boldsymbol{s}_i}H - \boldsymbol{\phi}_i\frac{s_i^z}{s_i^\perp}\partial_\beta H - \gamma n^z\boldsymbol{s}_i\times(\boldsymbol{s}_i\times\dot{\boldsymbol{s}}_i) + n^z\boldsymbol{\eta}_i \tag{4.10c}$$

where $\boldsymbol{n}$ and $\boldsymbol{s}$ are given by equations (4.9), and it can easily be verified that equations (4.6) are recovered in the limit of $\gamma = 0$.

To illustrate the effect of the local baths on the entanglement dynamics, we can consider the simple case of the anti-ferromagnetic coupling

$$H = J\boldsymbol{\sigma}_1\cdot\boldsymbol{\sigma}_2. \tag{4.11}$$

The ground state of this Hamiltonian is the singlet $|\psi\rangle = (|\uparrow\downarrow\rangle - |\downarrow\uparrow\rangle)/\sqrt{2}$. If we initialise in the state $|\uparrow\downarrow\rangle$ (a superposition of the singlet and a triplet state) the exact solution is

$$|\psi\rangle = \frac{1}{\sqrt{2}}\left[\cos(2Jt)\,|\uparrow\downarrow\rangle - \mathrm{i}\sin(2Jt)\,|\downarrow\uparrow\rangle\right]. \tag{4.12}$$

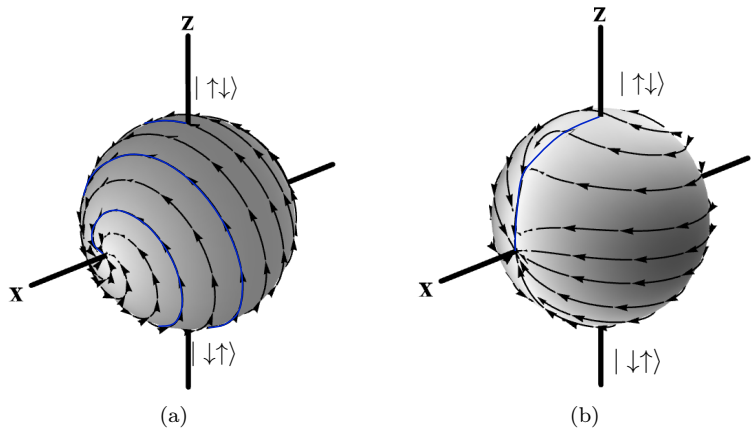


Figure 4.2: *The dissipative dynamics of the entanglement coordinate* $\boldsymbol{n}$*:*

For this state $\langle\psi|H|\psi\rangle = J(2n^x - 1)$, and hence in the language of equations (4.9) this describes entanglement dynamics

$$\boldsymbol{n} \times \dot{\boldsymbol{n}} = 2J\boldsymbol{x} \tag{4.13}$$

whereas the $\boldsymbol{s}_i$ have no dynamics. The dynamics of this trajectory are thus purely entanglement dynamics, and as expected the corresponding classical trajectory has no dynamics. For this reasons it makes an interesting case study.

When we introduce the local baths on each spin, this makes the dynamics both noisy and dissipative. The $\boldsymbol{s}_i$ still have no deterministic dynamics though they will now begin to drift under the action of the stochastic noise term. On dynamical time scales lower than this diffusive time scale it is possible to take a leading order approximation in which the $\boldsymbol{s}_i$ remain static, and the $\boldsymbol{n}$ evolves according to

$$\boldsymbol{n} \times \dot{\boldsymbol{n}} = 2J\boldsymbol{x} - 2\gamma\boldsymbol{z}(\boldsymbol{z}\cdot\boldsymbol{n}) + \boldsymbol{z}(\eta_1 + \eta_2) \tag{4.14}$$

where $\eta_i = \boldsymbol{s}_i \cdot \boldsymbol{\eta}_i$. This is precisely the dynamical equation (3.48). As a result we find that the conclusions of chapter 3 precisely describe the character and dynamics described by this equation and the regime in which the dissipative dynamics dominate over the stochastic noise. These dynamics are depicted for strong and weak coupling in Figure 4.2. In the limit of $\gamma = 0$, the dynamics of equation (4.13) are recovered and the entanglement vector simply precesses in a great circle about the $x$-axis.

Here we see that we recover the anisotropic LLG equation in a new circumstance as a description of the entanglement degrees of freedom of a two spin-1/2 quantum dimer. In the limit of dissipation dominating over noise (corresponding to a low temperature bath) the dynamics relaxes to a region close to the ground state, which is the antiferromagnetic singlet state.

### 4.2.1 The failure of the adiabatic protocol

Here we consider the dynamics of the system under the adiabatic protocol defined by

$$H = J\boldsymbol{\sigma}_1 \cdot \boldsymbol{\sigma}_2 + vt(\sigma_1^z - \sigma_2^z). \tag{4.15}$$

For $v > 0$ the ground state rotates from $|\uparrow\downarrow\rangle$ at $t = -\infty$ to $|\downarrow\uparrow\rangle$ at $t = \infty$. This change is concentrated around the avoided crossing at $|vt| < J$. In the case of full entanglement the result is an adiabatic rotation from $|\uparrow\downarrow\rangle$ to $|\downarrow\uparrow\rangle$. In the classical dynamics, in which there is no entanglement, there are no dynamics. Hence this model offers a controlled opportunity to study how suppressing entanglement affects adiabatic computation.

As before there are no dynamics (either adiabatic or diabatic) that cause the $\boldsymbol{s}_i$ to move away

from alignment with the $z$-axis in the isolated system. Thus we find again that the only dynamics is on the entanglement coordinate

$$\langle\psi|H|\psi\rangle = J(2n^x - 1) + 2vtn^z \tag{4.16}$$

$$\boldsymbol{n} \times \dot{\boldsymbol{n}} = 2J\boldsymbol{x} + 2vt\boldsymbol{z} \tag{4.17}$$

As before we consider the open system dynamics in the limit in which the diffusive time-scale does not dominate, and the $\boldsymbol{s}_i$ remain closely aligned to the $z$-axis. In this case, the dissipative influence of the environment is only felt by the entanglement coordinate.

$$\boldsymbol{n} \times \dot{\boldsymbol{n}} = 2J\boldsymbol{x} + 2vt\boldsymbol{z} - 2\gamma\boldsymbol{z}(\boldsymbol{z} \cdot \dot{\boldsymbol{n}}) + \boldsymbol{z}(\eta_1 + \eta_2). \tag{4.18}$$

This equation is identical to that of an individual spin in response to a field that rotates (adiabatically) from the $-z$-direction to the $+z$-direction and which is coupled to a z-component harmonic bath. To gain some insight, we will consider the two limits of (i) dissipation dominant and (ii) noise dominant

#### Dissipation dominant limit

The anisotropy of the coupling to the environment is such that dissipation is stronger when $\boldsymbol{n}$ approaches the $x$-$y$-plane. The dynamics is most constrained by this effect near $h = 0$ and when $\gamma > 1$. In this case, sweep time is determined by viscous time scales. These time scales can be obtained as in chapter 3. By taking account of a relatively rapid equilibration of the azimuthal angle $\beta$ followed by a slower relaxation of $n^z$. The resulting time-scale of motion (which can be read off equation (3.55)) is $t_{\text{viscous}} \sim \gamma/2J$ for $\gamma \gg 1$ in the low-temperature limit. For the success of the adiabatic protocol it is necessary that this is much shorter that the time-scale $t_{\text{GS}} \sim J/v$ which describes the rate of change of the ground-state, and hence the effective field $J\boldsymbol{x} + 2vt\boldsymbol{z}$ which the entanglement coordinate $\boldsymbol{n}$ experiences.

Asserting this condition $t_{\text{viscous}} \ll t_{\text{GS}}$ yields a condition for the success of the adiabatic protocol $\gamma v \ll J^2$, which indicates how a strong $\gamma \gg 1$ environmental coupling affects the usual adiabaticity condition, which in this case is $v \ll J^2$ (we will show this later in Section 5.1.3). This shows the adiabatic protocol must be performed even more slowly in order for the bath to remain in equilibrium with the slowly changing Hamiltonian. If the this protocol is not performed slowly enough then the back reaction of the bath will exert a force on the system which will consistently act drive the system from the adiabatic path.

#### Noise dominant limit

In the limit of weak dissipation we can treat the noise alone as the only addition to the dynamics. In this case the dynamics are given by

$$\boldsymbol{n} \times \dot{\boldsymbol{n}} = 2J\boldsymbol{x} + 2vt\boldsymbol{z} + \boldsymbol{z}\eta. \tag{4.19}$$

Where $\eta = \eta_1 + \eta_2$. These can be mapped onto the complex plane using the stereographic projection

$$w = \frac{n^x + \mathrm{i}n^y}{1 - n^z}. \tag{4.20}$$

where the three coordinates have been reduced to two by using $|\boldsymbol{n}| = 1$, and for which it is useful to note that $n^x + \mathrm{i}n^y = 2w/(1 + |w|^2)$ and $n^z = (|w|^2 - 1)/(|w|^2 + 1)$. The equations of motion

then take a reasonably simple form

$$\dot{w} = \mathrm{i}J(1-w^2) + \mathrm{i}w(2vt+\eta). \tag{4.21}$$

These can be integrated and averaged over $\tilde{\eta}$ in much the same way as before to obtain

$$w(t) = -\mathrm{i}J\int_{-\infty}^{t} d\tau \exp\left(\mathrm{i}\int_{\tau}^{t}\left[2vt+\tilde{\eta}(t')+Jw(t')\right]dt'\right) \tag{4.22}$$

disorder averaging this equation we obtain

$$w(t) = \mathrm{i}J\int_{-\infty}^{t} d\tau \exp\left(\mathrm{i}\int_{\tau}^{t}\left[2h(t')+2\mathrm{i}\gamma T+Jw(t')\right]dt'\right) \tag{4.23}$$

In doing this we have neglected the correlations between $w(t')$ and $\tilde{\eta}(t)$. This result implies an effective dynamical equation for $\langle w\rangle$

$$\dot{w} = -\mathrm{i}J(1-w^2) + \mathrm{i}w(2h+2\mathrm{i}\gamma T\ \mathrm{sign}[1-|w|^2]) \tag{4.24}$$

where the factor of $\mathrm{sign}[1-|w|^2])$ comes from considering the transformation $n^z \to -n^z$ or $w \to 1/w$.

Similar modifications can be made by adding additional terms to the other forms of the equation of motion: $\dot{\theta} = ... - \gamma T \sin\theta\ \mathrm{sign}[\cos\theta]$ , or in terms of $\mathbf{n}$, $\dot{\mathbf{n}} = ... + \gamma T(1-{n^z}^2)\mathrm{sign}[n^z]\mathbf{z}$. These terms act in a similar way to the *ad hoc* suppression of entanglement dynamics: they suppress the growth of in-plane components of the entanglement field.

Focussing on the equations in polar form, we find that $n^z$ never passes through zero for $\gamma T \geq 2J$, suggesting this as a limit for adiabatic computation. Figure 4.3 shows the flow fields for this averaged dynamics for different strengths of the environmental noise.

## 4.3 Artificial restriction of entanglement

In this section we take a Sojourn into the unphysical and consider different deformations of quantum dynamics.

It is well-known that classical dynamics is obtained as a limiting case of quantum dynamics. This is the correspondence principle due to Bohr [162]. This states that the behaviour of quantum systems reproduces classical physics in the limit of large quantum numbers. In spin systems this is the limit of large spin $S$. In this limit quantum effects dephase very rapidly compared to the dynamical time-scales of local expectation values.

However, this involves the awkward process of taking a limit in which we dramatically increase the volume of the state space in order to recover a theory with a reduced number of degrees of freedom. From the perspective of identifying the relevant degrees of freedom for understanding and simulating many body systems, it would be preferable to obtain an interpolation between quantum and classical dynamics in which quantum degrees of freedom were removed.[①] If a relevant interpolation scheme could be identified it could be employed to exploit similarities between the real-time dynamics of classical and quantum disordered systems in numerical experiments.

### 4.3.1 Truncated Schmidt spectrum

The crudest, and most easily implemented, restriction of entanglement is via truncation of the Schmidt spectrum, introduced in Section 1.3.1. It is this approximation that underpins matrix

[①] Apart from this motivation, the exploration of counterfactual theories serve to remind us which of the features we consider to be intrinsically quantum can be reproduced by models based on different assumptions.

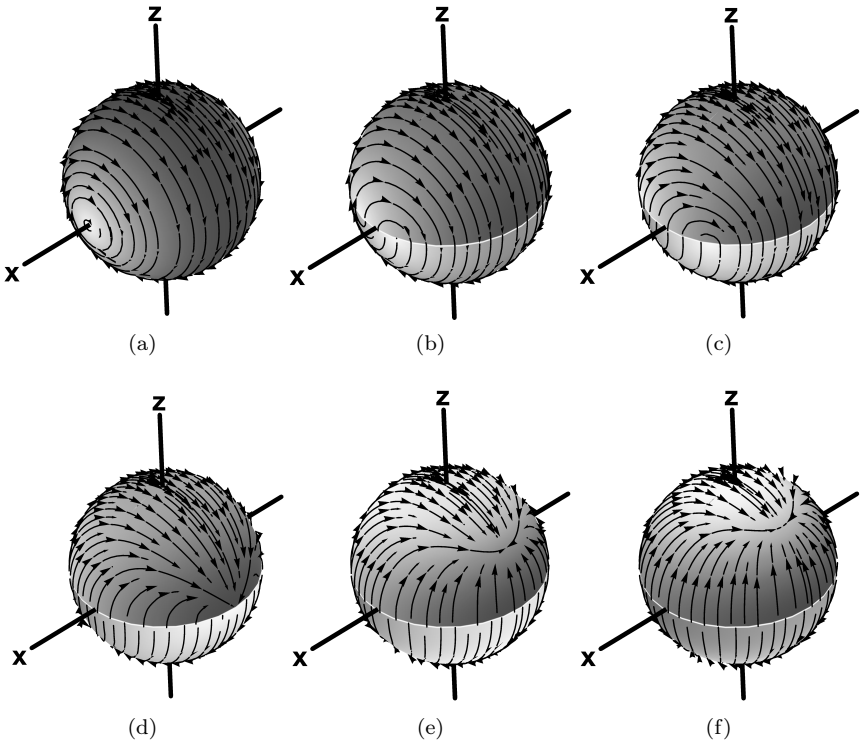


Figure 4.3: *Ensemble averaged dynamics with strong noise:* Here we plot flow fields for various trajectories, in the limit where noise dominates over dissipation and averaged over realisations of the noise $\langle \mathbf{n}(t) \rangle$. We show different strengths of the noise relative to the field in the $x$-direction. a) $\gamma T/J = 0$, b) $\gamma T/J = 0.5$ c) $\gamma T/J = 1$, d) $\gamma T/J = 2$, e) $\gamma T/J = 4$, and f) $\gamma T/J = 8$. Notice that the trajectory starting from $\mathbf{n} = \mathbf{z}$ becomes disconnected from $-\mathbf{z}$ at $\gamma T/J = 2$. This is the threshold for complete suppression of tunnelling by decoherence and failure of the adiabatic protocol.

product states and density matrix renormalization group. However, in our simple system of a pair of interacting spin-1/2 subsystems the maximum possible Schmidt rank is $\chi = 2$, and so the only possible truncation is to the minimum possible value of $\chi = 1$. In terms of the dynamical equations 4.6, the Schmdit spectrum is given by the spinor

$$\binom{n_1}{n_2} = \begin{pmatrix} \mathrm{e}^{-\mathrm{i}\beta/2} \cos(\alpha/2) \\ \mathrm{e}^{\mathrm{i}\beta/2} \sin(\alpha/2) \end{pmatrix} \tag{4.25}$$

and so the truncating of this spectrum is achieved by fixing of $\alpha = 0$.

As expected this yields that classical dynamics given by the dissipation free Landau-Lifshitz-Gilbert equation.

$$\boldsymbol{s}_n \times \dot{\boldsymbol{s}}_n = \partial_{\boldsymbol{s}_n} H \tag{4.26}$$

The discrete nature of this truncation leads one to investigate whether there is a meaningful way of continuously interpolating between the classical and quantum dynamics

### 4.3.2 Slowed quantum dynamics

Here we consider an interpolation scheme in which the purely quantum dynamics part of the dynamics are slowed. A system of two spin-1/2 degrees of freedom admits well defined, unique, time reversible, energy conserving dynamics in which the quantum correlations develop slower than in full quantum dynamics. A heuristic picture for understanding these dynamics is that single site

expectations evolve in the usual way, whereas for the two site expectation values the rank-1 part evolves as usual whereas the remaining rank-2 part, corresponding to quantum correlations, is slowed.

These dynamics correspond to integrating the usual Schrödinger equation with the state dependent effective Hamiltonian

$$\tilde{H} = (1-\epsilon)H + \frac{\epsilon}{2}\left(\frac{\boldsymbol{\sigma}_1 \cdot \langle \boldsymbol{\sigma}_1 \rangle \times \langle \mathrm{i}\,[H, \boldsymbol{\sigma}_1]\rangle}{\langle \boldsymbol{\sigma}_1\rangle \cdot \langle \boldsymbol{\sigma}_1\rangle} + \frac{\boldsymbol{\sigma}_2 \cdot \langle \boldsymbol{\sigma}_2 \rangle \times \langle \mathrm{i}\,[H, \boldsymbol{\sigma}_2]\rangle}{\langle \boldsymbol{\sigma}_2\rangle \cdot \langle \boldsymbol{\sigma}_2\rangle}\right) \tag{4.27}$$

where $\epsilon = 0$ recovers full quantum dynamics and $\epsilon = 1$ recovers classical dynamics. A derivation of these dynamics is given in Appendix F.1. For example, the dynamics of single site expectation values with these dynamics is given by

$$\langle \dot{\boldsymbol{\sigma}}_1 \rangle = \langle \boldsymbol{\sigma}_1 \rangle \times \boldsymbol{B}_1 + J\langle \boldsymbol{\sigma}_1 \times \boldsymbol{\sigma}_2 \rangle - J\epsilon \langle \boldsymbol{\sigma}_1 \rangle \left(\frac{\langle \boldsymbol{\sigma}_1\rangle \cdot \langle \boldsymbol{\sigma}_1 \times \boldsymbol{\sigma}_2\rangle}{\langle \boldsymbol{\sigma}_1\rangle \cdot \langle \boldsymbol{\sigma}_1\rangle}\right). \tag{4.28}$$

preliminary analysis of the simulations with these dynamics indicate that the dynamics remain integrable for small values of $\epsilon$, and have many of the features of quantum dynamics including pure point Fourier spectra of observables. In the classical limit of $\epsilon \to 1$ this chaoticity causes this spectrum to become broadband. The possibility of relating this to integrability breaking and the results of KAM theorem [54–56] remains an active line of investigation.

However these dynamics are complicated to work with, and another, similarly *ad hoc*, interpolation scheme which allows for simple calculations is studied in the next section.

### 4.3.3 Dynamics generated by a quantum-classical Hamiltonian

Previously in Section 2.1 we have shown how, regardless of the co-ordinates chosen to parametrise the system, the Hamiltonian expectation value remains the generator of time dynamics. This is true for both quantum and classical dynamics. Here we develop an alternative scheme for interpolating between these two limits: By continuing to work in the Ehrenfest picture in which we record the dynamical evolution of observable correlations, we then make the replacement

$$\langle \boldsymbol{\sigma} \cdot \boldsymbol{\sigma} \rangle \to q\left[\langle \boldsymbol{\sigma} \cdot \boldsymbol{\sigma}\rangle - \langle \boldsymbol{\sigma}\rangle \cdot \langle \boldsymbol{\sigma}\rangle\right] + \langle \boldsymbol{\sigma}\rangle \cdot \langle \boldsymbol{\sigma}\rangle \tag{4.29}$$

in the Hamiltonian expectation value $\langle H \rangle$ used to generate dynamics. In this replacement $q \in [0,1]$ with $q = 0$ corresponding to the classical limit and $q = 1$ corresponding to quantum dynamics. As in Section 4.3.2 this again overcomes the disadvantages of the usual Schmidt spectrum (bond order) truncation which allows for discrete restriction of the entanglement structure. This progressive restriction will allow a more detailed investigation.

#### Anti-ferromagnetic dynamics

If we consider again the anti-ferromagnetic Hamiltonian (4.11), the expectation of $H$ is then given in terms of the parameters of Section 4.1 by

$$\begin{aligned}\langle H \rangle &= J\langle \boldsymbol{s}_1 \cdot \boldsymbol{s}_2 \rangle \\ &= qJ\left[\boldsymbol{s}_1 \cdot \boldsymbol{s}_2 + \mathrm{Re}(n^x - in^y)(\boldsymbol{\theta}_1 + i\boldsymbol{\phi}_1)\cdot(\boldsymbol{\theta}_2 + i\boldsymbol{\phi}_2)\right] + (1-q)J\left(n^z\right)^2 \boldsymbol{s}_1 \cdot \boldsymbol{s}_2.\end{aligned} \tag{4.30}$$

In the limit $q \to 0$, the entanglement dynamics are completely frozen. Provided we start in a product state, $n^z = 1$, we remain in a product state. The advantage is that we can also investigate intermediate cases.

To study the entanglement dynamics, as before, we start with an initial configuration with $\boldsymbol{s}_1 = -\boldsymbol{s}_2 = \boldsymbol{z}$. Due to the symmetry of the problem, these parameters remain in these initial

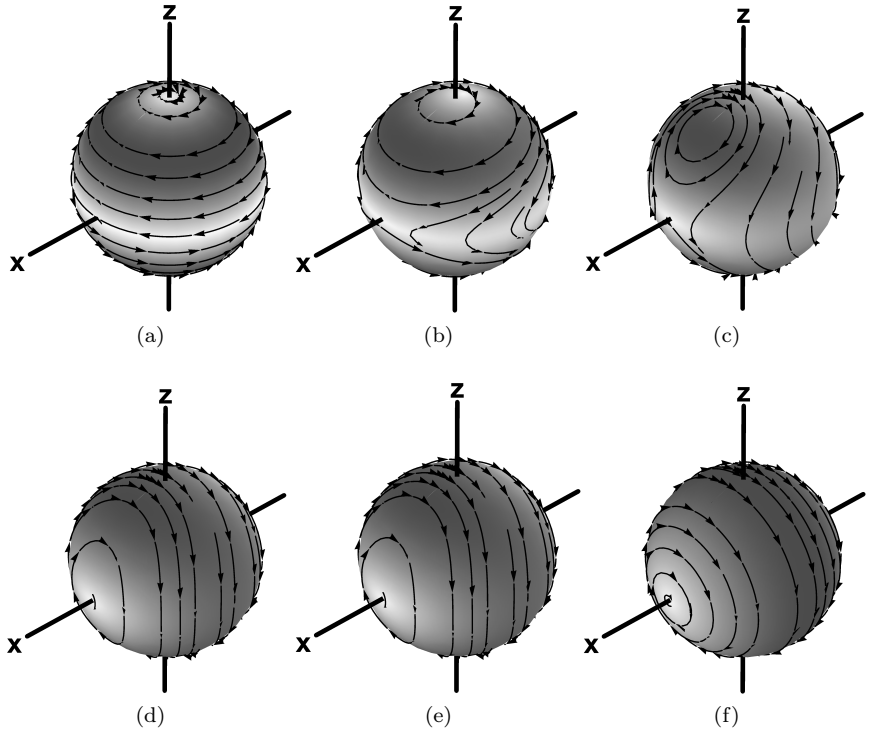


Figure 4.4: *Suppression of Tunneling with Restricted Entanglement:* Dynamics of the entaglement field $\mathbf{n}$ with $\mathbf{l}_1 = -\mathbf{l}_2$, an antiferromagnetic interaction, and different values of $q$; a) $q = 0$, b) $q = 0.1$, c) $q = 0.\dot{3}$, d) $q = 0.4$ e) $q = 0.6$ and f) $q = 1$. A bifurcation occurs when $q = 0.5$ and at $q = 0.\dot{3}$ the $|\uparrow\downarrow\rangle$ state no longer evolves to $|\downarrow\uparrow\rangle$

values for all times. The residual $q$-deformed Hamiltonian for $\boldsymbol{n}$ is then

$$\langle H\rangle = qJ\,[2n^x - 1] - (1-q)J\,n^{z\,2}. \tag{4.31}$$

The resulting equations of motion for $\boldsymbol{n}$ reduce to

$$\boldsymbol{n}\times\dot{\boldsymbol{n}} = \partial_{\boldsymbol{n}}\langle H\rangle = 2Jq\boldsymbol{x} - 2(1-q)J\boldsymbol{z}n^z, \tag{4.32}$$

which reduce to the previous equations (4.13) when $q \to 1$ and freeze $\boldsymbol{n} = \boldsymbol{z}$ when $q \to 0$.

The flow fields that result from integrating these equations of motion are shown in Fig.4.4 for a range of values of the suppression parameter $q$. Notable features include:

- The equations show a bifurcation at $q = 0.5$. At this value of $q$, two new fixed points ($\dot{\boldsymbol{n}} = 0$) appear at $\boldsymbol{n} = \cos\alpha\boldsymbol{x} + \sin\alpha\boldsymbol{z}$ where $\cos\alpha = \frac{q}{1-q}$

- Tunnelling is completely suppressed at $q = 1/3$. At $q = 1/3$ the dynamics is such that an initial state $|\uparrow\downarrow\rangle$ does not reach the state $|\downarrow\uparrow\rangle$ and tunnelling is suppressed. This can be seen analytically by finding the point where $\langle H\rangle|_{\boldsymbol{n}=-\boldsymbol{x}} = \langle H\rangle|_{\boldsymbol{n}=\boldsymbol{z}} \to -3qJ = -J$.

### Dynamics in the adiabatic protocol

We consider the same $q$-deformed dynamics under the adiabatic protocol of equation (4.15). Following Eq.(4.30) with an initial configuration of $\boldsymbol{s}_1 = -\boldsymbol{s}_2$ (which is again preserved by the dynamics),

the Hamiltonian and equation of motion are given by

$$\langle H \rangle = qJ(2n^x - 1) - (1-q)Jn^{z\,2} + 2h(t)n^z, \tag{4.33}$$

$$\boldsymbol{n} \times \dot{\boldsymbol{n}} = 2qJ\boldsymbol{x} + 2h(t)\boldsymbol{z} - 2(1-q)Jn^z\boldsymbol{z}, \tag{4.34}$$

which corresponds to the dynamics of a spin evolving in the presence of both an effective field $\boldsymbol{B}_{\text{eff}} = 2qJ\boldsymbol{x} + 2h(t)\boldsymbol{z}$ together with an easy-axis anisotropy $-(1-q)Jn^{z\,2}$.

A key feature of these dynamics is the failure of the adiabatic protocol when $q < 2/3$ — even if $h$ is varied adiabatically slowly. This can be seen by analysing the solution at $h = 0$. When $q < 2/3$ this is no longer in the $\boldsymbol{x}$ direction as would be the case for adiabatic transport. A second solution with lower energy is appears at $\sin\theta^* = q/(2(1-q))$.

The adiabatic trajectory becomes disconnected at $q = 2/3$. There is a bifurcation of trajectories— which gives a first hint of chaos emerging in the dynamics, and which we will investigate further in this ongoing project.

## 4.4 Discussion

In this section we have extended the analysis of chapter 3 to a problem of entangled degrees of freedom. We have studied this in the context of adiabatic quantum computation, analysing the conditions under which computation proceeds in a simple toy model. Following this we then explored some schemes that allow for a meaningful interpolation between classical and quantum dynamics. The classical dimer supports chaotic dynamics [163–165], whereas the quantum dimer does not. Studying the emergence of chaotic dynamics as one tunes either the coupling $\gamma$ to a bath of oscillators, or the dynamics of entanglement as introduced by the parameter $q$, will allow for consideration of the transition from quantum ergodicity to classical chaos.

# 5 | Benchmarking Analogue Quantum Computation

Adiabatic transport provides a powerful way to manipulate quantum states. By preparing a system in a readily initialized state and then slowly changing its Hamiltonian, one may achieve quantum states that would otherwise be inaccessible. Moreover, a judicious choice of final Hamiltonian whose ground state encodes the solution to a problem allows adiabatic transport to be used for universal quantum computation. However, the effects of the environment limit the quantum correlations that an open system can support and degrade the power of such adiabatic computation. We quantify this effect by allowing the system to evolve over a restricted set of quantum states, providing a link between physically inspired classical optimization algorithms and quantum adiabatic optimization. This perspective allows us to develop benchmarks to bound the quantum correlations harnessed by an adiabatic computation. We apply these to the D-Wave Vesuvius machine with revealing—though not conclusive—results.

The original work in this chapter, covered in Section 5.2 and onwards, was done in collaboration with T Đurić, W Vinci, PA Warburton, AG Green, and published as ref [129].

Nature does remarkably well at performing complex optimisations. These occur on all scales in the natural sciences; from evolutionary processes optimising a species for a particular ecological niche, to atoms combining to find low energy crystalline structures. Separately, many of the most challenging problems of computation involve performing complex optimisation. Many algorithms inspired by natural processes have proven very successful in solving them [166–170]. Here we focus on *adiabatic computation* [171–177]. This paradigm of computation involves slowly changing a potential that the system experiences, from a starting potential, of which the system is prepared in the minimum energy state, to a target whose optimum configuration we require. Classical examples of adiabatic computation are of limited usefulness. As an example, one might imagine a toy in which a ball bearing must be guided through a maze by gentle tilting, or a waiter carrying glasses of wine across a room without the drink sloshing out of the glasses. Both of these are examples of supervised adiabatic computations. An unsupervised version would amount to using a predetermined sequence of tilts of the maze, or motions of the waiters tray. One would not expect these to be very successful without prior knowledge of the maze's solution and a clear path across the waiters restaurant.

However, it is a remarkable that in quantum mechanics, the quantum adiabatic theorem implies that, for an isolated system, such a protocol will always work, provided this transition is performed sufficiently slowly [173]. Here, we investigate the power of this adiabatic optimisation given access to limited quantum resources. We do this by including a controlled amount of entanglement classical dynamics, or equivalently by restricting the quantum correlations in the quantum dynamics. Much analogous to the manner in which only limited quantum correlations survive in an open quantum system. The resulting picture of open-system quantum dynamics enables an appealing geometrical interpretation of the limitations of adiabatic computation; the existence or otherwise of a connected adiabatic computational path. We use this to develop benchmarks that can quantify

the degree of quantum mechanics employed by a putative adiabatic quantum computation.

In the final section, we apply this framework to computation using the D-Wave Vesuvius machine. Although spectroscopic probes have shown evidence of entanglement [178], our tests proved inconclusive, largely due to the relatively high temperature of operation of the machine.

## 5.1 Background

### 5.1.1 Optimisation as Langevin dynamics

We consider here the problem of optimisation. This consists of configuring some system in a way as to minimise some cost function $V(x)$ over some pre-defined domain $x \in X$. Such optimisations appear frequently in nature, whether it be a great number of atoms aligning themselves into a crystalline pattern to minimise their energy; evolution maximising an organisms survivability; a swarm of ants searching for the shortest path from a food source to the colony; or the pruning of neurons as to solidify a child's learning language.

There are many computational algorithms inspired by these natural processes [166, 167]. Of these physically inspired algorithms many can be summarised in the Langevin equation, derived in Section 3.2.3, for the Brownian motion of a particle:

$$m\ddot{\boldsymbol{x}} + \gamma\dot{\boldsymbol{x}} + \partial_{\boldsymbol{x}} V(\boldsymbol{x}) = \boldsymbol{\eta}, \qquad \langle \eta_i(t)\eta_j(t')\rangle = 2\gamma T\delta_{ij}\delta(t-t'). \tag{5.1}$$

This equation describes the motion of a particle at position $\boldsymbol{x}$ in some potential $V(\boldsymbol{x})$ with dissipation, characterised by $\gamma$ and fluctuations, characterised by the temperature of the random force $\boldsymbol{\eta}(t)$.

In this picture of the Langevin equation as an optimization metaheuristic we consider $\boldsymbol{x}$ to be, not the position of a particle, but the state of a system in its (potentially very high dimensional) state space. This heuristic then allows us to tackle complex optimisations of many degrees of freedom. There are many optimisation algorithms described by this metaheuristic

- *Gradient descent:* Setting the inertial mass $m$ and fluctuating force $\boldsymbol{\eta}$ to zero reduces the Langevin dynamics to gradient descent.

- *Memoized searches:* Keeping the inertial mass $m = 0$, and extending the data $\boldsymbol{x}$ to include memory of the path history $\boldsymbol{x} \to \boldsymbol{x}' = (\boldsymbol{x}_t, \boldsymbol{x}_{t-1}, \boldsymbol{x}_{t-2}, \cdots)$ a wider class of memory enhanced problems gradient descent problems, such as the *TABU algorithm* are captured.

- *Swarm algorithms:* Extending the system to encode the state space positions of many particles $\boldsymbol{x}_i$ and potentially some shared global data $\boldsymbol{p}$ via $\boldsymbol{x} \to \boldsymbol{x}' = (\boldsymbol{p}, \boldsymbol{x}_1, \boldsymbol{x}_2, \boldsymbol{x}_3, \cdots)$ which do not experience a force from the potential, but only from other swarm members, and their shared global knowledge $V(\boldsymbol{x}) \to V'(\boldsymbol{x}') = \sum_i U(\boldsymbol{x}_i, \boldsymbol{p}) + \sum_{ij} T(\boldsymbol{x}_i, \boldsymbol{x}_j)$ we recover *particle swarm optimisation.* In which the natural intelligence of swarms is harnessed for optimisation.

- One of the foremost physics-inspired algorithms is *simulated annealing* [179]. The simulated annealing algorithm essentially involves integrating equation (5.1) forwards in time whilst slowly reducing the amplitude of the random forcing $\boldsymbol{\eta}$ with time. Named for the metallurgical process by which a piece of material is repeatedly heated and cooled through its recrystallization temperature, this algorithm mimics the remarkable fidelity with which a collection of atoms may form complex crystals by simply heating them up and then cooling down slowly. It is this topic which we shall discuss further.

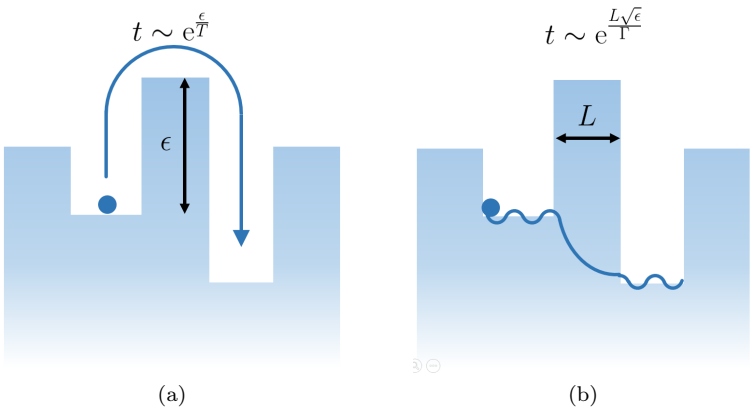


Figure 5.1: *Simulated annealing and quantum annealing.* (a) The bottle necks in simulated annealing consist of large barriers. The typical number of attempts required to jump a barrier is exponentially large. The anneal is controlled by the temperature that is taken $T \to 0$ at the end of the algorithm (b) In a quantum system the particle wavefunction is wave-like in the wells, whereas it exponentially decays when penetrating the classically forbidden barrier region. A quantum process is thus able to tunnel through the barrier, the penetration depth is given by the particles momentum which goes as $\sim \sqrt{\epsilon}$ giving a quantum enhancement providing the barrier is not wide. The quantum annealing algorithm is controlled by the tunnelling energy which is taken $\Gamma \to 0$ at the end of the algorithm.

### 5.1.2 Simulated annealing, and quantum annealing

Simulated annealing provides a means to search for the minimum of a cost function $V(x)$ which in this language we consider to be an energy functional. In each step of the algorithm we update the state of the system in some local way with a probability which satisfies detailed balance (i.e. fluctuation dissipation) hence this mimics the behaviour of a thermal process. The temperature of this process is adjusted according to a schedule which concludes with it being tuned $T \to 0$, whereby the dynamics becomes frozen, and the optimisation is complete. For a sufficiently well chose protocol, global optimisation can be guaranteed [180].

The bottlenecks in this process are correspond to large potential barriers in the energy landscape. At a given attempt the optimisation will pass one of these one of these barriers with a probability $p \sim \exp[-\beta\epsilon]$. Quantum dynamics offers the appealing possibility of simply tunnelling through one of these barriers. As we see in Figure 5.1 the, quantum tunnelling allows us to escape the exponentially slow process of jumping over a barrier, for an exponentially slow process in tunnelling through a barrier. We note though that The quantum process is slow in the product $\textit{width} \times \sqrt{\textit{height}}$ of the barrier, whereas the classical process is slow in the *height* of the barrier. For a problem in which the barrier height is the bottleneck, this gives a quantum enhancement [181]. In typical many body problems, the energy of the barriers is extensive $\mathrm{O}(N)$ whereas we expect the barrier widths to saturate. This $\mathrm{O}(\sqrt{N})$ advantage of the quantum algorithm is typical for search problems [181, 182]. This was first demonstrated by Grover [183, 184], and later shown to be the optimal quantum scaling [185, 186]

As mentioned, in simulated annealing the state space is sampled by a thermal process, whose associated temperature is tuned to zero at the end of the optimisation. In quantum annealing we imagine that the classical state space is instead being sampled by quantum dynamics, which generates fluctuations that are tuned to zero at the conclusion of the optimisation.

We have been discussing the dynamics of a system as partitioned into a classical energetics and quantum tunnelling. In order to understand dynamics in this way we must privilege a certain basis of the system as the classical basis. Thus we write down a diagonal (i.e. classical) Hamiltonian $H_{\text{target}}$ which describes the energetic landscape over which we wish to optimise. It is the energy $\langle\psi|H_{\text{target}}|\psi\rangle$ of a state that we wish to minimise. This energy is minimised by the ground state,

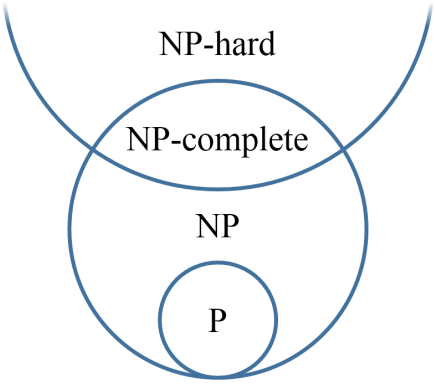


Figure 5.2: *The relationship of P and NP complexity classes:* The vertical direction represents increasing complexity. P is the class of problems solvable in polynomial time by a deterministic Turing machine (a classical computer). NP is the class of problems solvable in polynomial time by a non-deterministic Turing machine (a classical computer that always makes lucky guesses). NP-hard is the set of problems (which may or may not be in NP) which are at-least as hard as the hardest problems in NP. NP-complete is the intersection of NP and NP-hard, i.e. it is the hardest problems in NP.

which we know must also be a classical state in this restricted formulation of the problem.

We now introduce the archetypal set up in quantum annealing problems. This consists of a transverse field Ising model in which the time dependent Hamiltonian $H(t)$ is tuned from initial pure transverse field

$$H_{\text{start}} = -\sum_i \sigma_i^{\text{x}} \tag{5.2}$$

to its final form as a disordered classical Ising model[①]

$$H_{\text{target}} = \sum_{ij} J_{ij}\sigma_i^{\text{z}}\sigma_j^{\text{z}} + \sum_i h_i\sigma_i^{\text{z}}. \tag{5.3}$$

To relate quantum annealing and simulated annealing we see that they can be considered as commutations of the different limits of taking quantum tunnelling (i.e. off diagonal elements of the Hamiltonian) $\to 0$ and taking temperature $\to 0$. *Not without caveats*, quantum and simulated annealing then will evaluate the ground states successfully providing these limits are taken sufficiently slowly.

### 5.1.3 Adiabatic quantum computation

It is a useful feature of quantum mechanics that we can make rigorous the seemingly heuristic approach of searching for the ground state by annealing $H_{\text{start}} \to H_{\text{target}}$. This is achieved using the quantum adiabatic theorem, which states that if a quantum state is prepared in the ground state of a time-evolving Hamiltonian, it remains in the instantaneous ground state of this Hamiltonian, in the limit that the evolution is infinitely slow. It is a useful feature that it also works approximately

[①]This form $H_{\text{target}}$ may seem an overly restrictive choice, and its choice is something of an accident of technological progress. As an aside we discuss the usefulness of solving this problem: Finding the ground state of $H_{\text{target}}$ constitutes the Quadratic Unconstrained Binary Optimization (QUBO) problem. QUBO has a range of useful applications including the 2-SAT problem, machine scheduling [187], the traffic message management problem [188], computer-aided design [189], budgeting problems [190], molecular conformation problems [191] and maps onto many other canonical problems in complexity theory [192]. In one dimension the ground state can be computed exactly for nearest neighbour interactions by bond decimation in order O($N$) time, and furthermore for $k$-local interactions using transfer matrices in O($kN$) time. However when we extend to two dimensions the problem is in the complexity class NP-complete [49]. NP-complete is class of polynomially equivalent problems includes some relevant and computationally challenging problems. The relationship of this to other problem classes is shown in Figure 5.2. It is considered unlikely that there exist any polynomial algorithms to solve any NP-complete problems, as it is strongly believed, though not proven, that P $\neq$ NP.

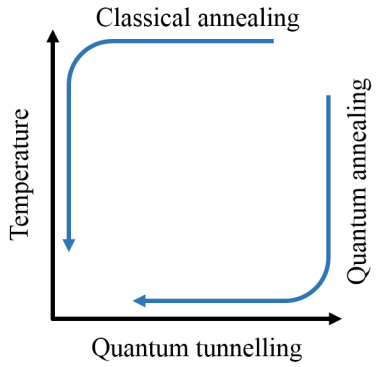


Figure 5.3: *The relation of quantum annealing and simulated annealing:* Both algorithms can be understood as extremal paths through the same parameter space. In classical annealing the quantum tunnelling is taken to zero before the temperature, and *vice versa* for quantum annealing. In performing these algorithms the first leg of each of these paths is omitted, as the states at the turning points is unimportant for classical annealing and can be written down *a priori* for quantum annealing.

provided the evolution of the Hamiltonian is sufficiently slow.

But what is sufficiently slow? To define what sufficiently slow means we imagine a Hamiltonian which is evolved by the monotonically increasing control parameter $s$ which evolves from $0 \to 1$, our anneal/adiabatic protocol is then defined by $H(s)$ where $H(0) = H_{\text{start}}$ and $H(1) = H_{\text{start}}$, the requirement of adiabaticity is then, that the time-scale evolution time-scale $T \sim 1/\dot{s}$ goes as

$$T \gg \frac{|H'|}{\Delta^2} \tag{5.4}$$

where $H' = \frac{\partial H}{\partial s}$.

Detailed and rigorous proofs of this can be found in refs [193–196] as well as ref [197] which provides a slightly different perspective. Instead of recapitulating these we give a simple argument for the form of equation (5.4): When we perform an instantaneous quench, the systems Hamiltonian is changed instantaneously. The state which cannot respond instantaneously, is left unchanged. The state amplitudes in the new eigenbasis are found by simply projecting the same state into the new eigenbasis. Considering adiabatic transport as the limit of infinitely many infinitesimal quenches it is clear rate the amplitude transfer from eigenstate $|n\rangle$ to eigenstate $|m\rangle$ of the Hamiltonian $H$ is given by $\langle m|\dot{n}\rangle\langle n|\psi\rangle$. From simple non-degenerate perturbation theory we know that this rate is given by

$$R_{\text{Transfer}} \sim |\langle m|\dot{n}\rangle| = \left|\frac{\langle m|\,\dot{H}\,|n\rangle}{E_n - E_m}\right|. \tag{5.5}$$

There is another time-scale of relevance: the relative rate of rotation of the two amplitudes in question, given by $R_{\text{Rotation}} = E_n - E_m$.

In the spirit of the rotating wave approximation we observe that if $R_{\text{Rotation}}$, is much greater than the rate of amplitude transfer, $\langle m|\dot{n}\rangle$ will be rapidly oscillating, and hence the transfer will be zero on average even though $|\langle m|\dot{n}\rangle|$ is not. This condition is

$$1 \gg \frac{R_{\text{Transfer}}}{R_{\text{Rotation}}} \sim \frac{\left|\langle m|\,\dot{H}\,|n\rangle\right|}{|E_n - E_m|^2} \sim \frac{|\dot{H}|}{\Delta^2} = \frac{|H'|}{T\Delta^2} \tag{5.6}$$

where in the final steps we have assumed that excitation is dominated by transfer into the first excited state, yielding (5.4). We emphasise that this derivation is not rigorous, but merely an

illustration, as there do exist cases when conditions such as $\left|\langle m|\,\dot{H}\,|n\rangle\right| \ll |E_n - E_m|^2$ do not guarantee adiabaticity [198, 199].

**Relation of adiabatic quantum computation and quantum annealing**

We have introduced quantum annealing as a heuristic solver for optimization problems, and adiabatic quantum computation as a slightly more general, approach which comes with the benefit of a proof of its efficacy, and its equivalence to universal quantum computation (shown in Section G.1). These topics are closely related but are distinct, *quantum annealing is an optimization meta heuristic, where as adiabatic quantum computation is a computational paradigm.* In this sense the cases of D-Wave dynamics that we study in the following investigation constitute an example of quantum annealing implemented using a non-universal adiabatic quantum computer, whereas conversely the numerical simulations we do constitute and implementation of quantum annealing on a classical computer.

Given a problem that can be mapped onto an instance of equation (5.3), this mapping, together with the anneal protocol, and any necessary repeated runs or post-processing can be though of constituting an algorithm. The anneal itself is implemented using computational paradigm of adiabatic quantum computation.

Some also consider quantum annealing as having relaxed the requirements of zero-temperature and adiabaticity, though throws the baby out with the bathwater to some extent.

## 5.2 Langevin description of quantum annealing

In addition to the examples of Section 5.1.1, quantum annealing, and indeed adiabatic quantum computation, may be cast in the language of the Langevin equation 5.1.

Our aim is to develop a Langevin description of the dynamics, in which we incorporate the effects of the environment by systematically tuning the degree of quantum resources which survive in the presence of this interaction. This provides a framework for tuning between the classical and quantum limits, and the dynamics may then be systematically compared with the behaviour of a putative quantum annealer to asses it capability.

This is achieved by considering the dissipative restriction of the dynamics to a variational manifold. The strength of the dissipation leads to correspondingly different severities of restriction on the quantum correlations. This goes beyond previous works, in which a quantum annealer has been compared with fully classical and fully quantum models [51, 126, 128, 153]. Furthermore, by studying the amount of quantum correlations required to reproduce a certain degree of computational efficacy, and hence the classical data required to describe these correlations, we are able to make a connection with complexity theory and comment on the computational resource represented by any observed quantum enhancement.

### 5.2.1 Langevin dynamics of qubits

The Langevin dynamics of a single qubit, coupled isotropically to its environment is given by

$$\boldsymbol{s}_i \times \dot{\boldsymbol{s}}_i - \gamma \dot{\boldsymbol{s}}_i = \partial_{\boldsymbol{s}_i} \langle H \rangle - \boldsymbol{\eta} \tag{5.7}$$

This is the well-known Landau-Lifshitz-Gilbert equation [132, 133] which, in Section 3.2.3, was recovered from the saddle points of a Keldysh path integral [111]. This equation governs the dynamics of qubits coupled to their environment. The effects of the environment are explicit here in multiple ways:

- *Dissipation:* the dissipative term, whose strength is set by $\gamma$, drives the system deterministically towards a lower energy state.
- *Fluctuations:* the stochastic term $\eta$ introduces energy from the environment into the system in a non-deterministic manner. In the Markovian limit dissipation and fluctuations are related by $\langle \eta_i(t)\eta_j(t')\rangle = 2\gamma T\delta(t-t')$ and are not correlated between sites. The appearance here of $\gamma$ is due to the fluctuation dissipation theorem. The approach of chapter 3 shows how we can consistently recover a limit of low $T$ in which environmental effects are dominated by dissipation. We note that the stochastic form of this equation can be converted to the usual density matrix formalism by integrating over realisations of the noise together with some further approximations.
- *Absence of entanglement* we have assumed in using equation 5.7 to describe a system of many interacting qubits that the dissipative effects of the environment have degraded the entanglement to such a degree that the only residual quantum mechanics is local superposition.

### 5.2.2 Introducing entanglement

In order to faithfully and systematically describe the dynamics of an open system which retains a finite degree of entanglement we require a suitable class of variational states which generalise equation (5.7) and allow us to control the degree of quantum resources, such as an entanglement. This allows us to connect with ideas of classical complexity.

Matrix product states (MPS) provide such a manifold of states. These one-dimensional states, which constitute a parametrisation of weakly entangled states, were introduced in Section 1.3.1. Each manifold of MPS is characterised by an integer $\chi$, the bond order. The entropy of entanglement $\mathcal{E}$ across any bipartition of an MPS state into two contiguous parts is bounded by $\mathcal{E} \leq \log \chi$. Due to the ease with which it can be controlled we will use the bond order as a convenient quantification of the quantumness in a putative adiabatic quantum computer. Whilst there are other ways to quantify quantumness, and potentially other variational wave functions that embody them, we choose matrix product states as they are well studied, and there are well-known efficient algorithms for evolving and calculating with them [27, 33, 36].

MPS generalise product states, which correspond to the special case of $\chi = 1$, as follows: A familiar product state is given by

$$|\psi\rangle = |x_1\rangle\,|x_2\rangle\,|x_3\rangle\cdots|x_N\rangle =$$


, (5.8)

the matrix product state extends this in the simple manner by summing over a range of product states

$$|\psi\rangle = \sum_{ijk\cdots m} \left|x_1^i\right\rangle \left|x_2^{ij}\right\rangle \left|x_2^{jk}\right\rangle \cdots |x_N^m\rangle =$$

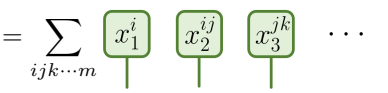


$$=$$

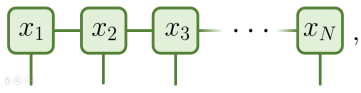


, (5.9)

where each state $|x_n\rangle$ has been replaced by the matrix of states $\left|x_n^{ij}\right\rangle$ in which the indices $ijk\cdots m$ run from 1 to $\chi$. The classical data required to represent an MPS state of bond order $\chi$ scales as $Nd\chi^2$ where $d$ is the local Hilbert space dimension, for qubits $d = 2$, this is compared with data scaling $d^N$ for a generic quantum state.

Here we have presented a constructive picture of this manifold of states staring with the well-known classical product state. The states can also be seen as an approximation scheme: a generic

quantum state can approximated with an MPS of bond order $\chi$ by a series of Schmidt decompositions at each bipartition (i.e. at each bond), as in equations (1.21) and (1.22). A sweep across the system is made and at each consecutive bipartition the state is replaced with the closed approximation of bond order $\chi$ found via the Schmidt decomposition. In this sense the manifold of MPS states provides the best approximation to the full Hilbert space given when we are restricted to a fixed classical data storage of $Nd\chi^2$ complex floats.[①]

Following the prescription of Section 2.1 the tensor valued coordinates $x_i$ have closed system dynamics given by equation (2.7) as

$$\Omega_{ij}\dot{x}^j = h_i \tag{5.10}$$

where the force $-h_i$ is given by $h_i = \partial_i \left(\langle\psi|H|\psi\rangle/\langle\psi|\psi\rangle\right)$, and antisymmetric curvature tensor $\Omega_{ij}$, given by (2.12), as before. The implementation of integration of these equations of motion with MPS states is reviewed in appendix B. Following Section 3.2.3 the corresponding unravelled open system dynamics are given by equation (3.44). In the Markovian case this is written using the prescription of Section 2.1 as a Langevin equation[②]

$$\left(\Omega_{ij} - \Gamma_{ij}\right)\dot{x}^j = h_i - \eta_i \tag{5.14}$$

where, assuming the indices $i, j$ label the MPS coordinates, and the index $n$ labels the couplings to the bath (as in Section 3.44), and consistent with previous notation we have defined the hermitian dissipation tensor $\Gamma_{ij} = \sum_n \gamma_n f_{n,i} f_{n,j}$ and corresponding fluctuations $\eta_i = \sum_n f_{n,i}\eta_n$ which are written in terms of the couplings to the bath projected on to the variational manifold $f_{n,i} = \partial_i \left(\frac{\langle\psi|F_n|\psi\rangle}{\langle\psi|\psi\rangle}\right)$, and the operators $F_n$ which couple the system to the bath are introduced in equation (3.38), the dissipation factors $\gamma_n$ are from equation (3.31).

Using equation (5.14) we can describe the dynamics of a one-dimensional open system that retains a limited degree of entanglement. The rationale for doing this is that coupling to an external bath leads to decoherence that reduces the quantum correlations in the system, and hence the bond order required to model it. This effect counterbalances the natural tendency of evolution under a Hamiltonian to cause the entanglement to grow after a quench.

As in the case of the Landau-Lifshitz-Gilbert equation (5.14), should be interpreted as an evolution over a mixed state, found by summing over realisations of the bath, whose micro-states posses residual quantum correlations that can be faithfully represented by a matrix product state.

The explicit effects of the environment here are the fluctuations and dissipation characterised by $\gamma$. These are recovered from the derivation of this *via* the Keldysh path integral given in sections 2.1 and 3.2.

Perhaps the most severe effect of the environment is implicit in equation (5.14), and is the restriction in the degree of entanglement that the system can support in the presence of the environment. This was not shown as a direct result of coupling to the bath, but has been assumed

[①] This assumes a generic state. If we know further information known about the structure of correlations of the quantum state we seek to approximate then other ansätze may provide a closer approximation.

[②] To show this we start with the unravelled Markovian stochastic Schrödinger equation

$$\mathrm{i}\left|\dot{\psi}\right\rangle = H\left|\psi\right\rangle - \sum_n F_n\left|\psi\right\rangle\left(\eta_n - \gamma\frac{\mathrm{d}\langle\psi|F_n|\psi\rangle}{\mathrm{d}t}\right) \tag{5.11}$$

projecting this onto a variational manifold using $\left|\dot{\psi}\right\rangle \to |\mathrm{D}_i\psi\rangle\,\dot{x}^i$, and closing with $\langle\mathrm{D}_j\psi|$ we obtain

$$\mathrm{i}\langle\mathrm{D}_i\psi|\mathrm{D}_j\psi\rangle\dot{x}^j = \langle\mathrm{D}_i\psi|\,H\,|\psi\rangle - \sum_n \langle\mathrm{D}_i\psi|\,F_n\,|\psi\rangle\left(\eta_n - \gamma\frac{\mathrm{d}\langle\psi|F_n|\psi\rangle}{\mathrm{d}t}\right) \tag{5.12}$$

taking the real part of this equation, and using $\Omega_{ij} = \mathrm{i}\langle\mathrm{D}_j\psi|\mathrm{D}_i\psi\rangle/\langle\psi|\psi\rangle - \mathrm{h.c.}$ as before we obtain

$$\Omega_{ij}\dot{x}^j = h_i - f_{n,i}\left(\eta_n - \gamma\dot{f}_n\right) \tag{5.13}$$

the deisred form is then obtained by noting that $\dot{f}_n = f_{n,i}\dot{x}^i$, and defining $\eta_i = \sum_n f_{n,i}\eta_n$.

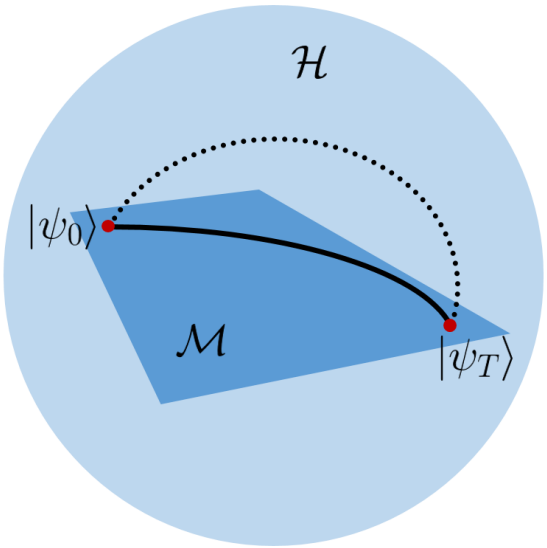


Figure 5.4: *Dissipative reduction to a variational manifold of states:* In equations (5.7) and (5.14) we consider dynamics which are continuously projected onto a variational manifold $\mathcal{M}$ of states (dark planar region), which have restricted quantum correlations. $\mathcal{M}$ is a sub-manifold of the full Hilbert space $\mathcal{H}$ (light round region). The microscopic detail of this process is shown in Figure 2.1. The results of this process is that the dynamics can be described by a semi-classical theory in terms of the co-ordinates of the variational manifold. Here the variational dynamics (solid black) are used to approximate an adiabatic protocol whose exact solution (dotted black) makes a large excursion from $\mathcal{M}$. In this case the variational dynamics is shown to succeed in adiabatically approaching the correct final state $|\psi_T\rangle$. If the manifold is too restrictive, and the degree of quantum correlations is insufficient, this will not be the case, and the projected theory will have a distinct end-point to the exact solution.

from an intuition regarding the impact of environmental coupling. This intuition is that certain quantum correlations will decay very quickly, and those that decay sufficiently fast do not exist on the dynamical time-scales of those that persist for much longer. One might ask, does there exist such a bath whose dynamics on intermediate time-scales approximates matrix product states? We would regard the existence of a bath which drives states towards a matrix product state manifold as unlikely.[①] For many body quantum systems however, we argue that using this manifold of states to represent the dissipatively reduced state space of a quantum annealer, constitutes giving the annealer the benefit of the doubt, and modelling its dynamics as minimally affected by the environmental coupling beyond the key characteristic features, i.e. the reduced entanglement. This is in the sense that we have degraded the quantum dynamics in such a way as to preserve fidelity of the exact dynamics where possible, but has concretely decreased the classical complexity class of simulating the dynamics, as a generic state requires $\mathrm{O}(\exp(N))$ data, whereas a matrix product state requires $\mathrm{O}(\chi^2 N)$ data. Considering the environment is this way results in dynamics that are projected onto a variational manifold, shown in Figure 5.4.

In the following sub-sections, we will develop these ideas to address the question of how quantum mechanical is a given adiabatic computation. Or rather, since we wish to develop a set of benchmark problems, "What degree of quantum computational resources does a given problem require in order to compute it adiabatically?" As we shall see, an unambiguous answer to this question can only be found in the zero-temperature limit, when the effects of noise are suppressed, leaving only the effects of dissipation.

[①] Such a thing would imply the bath was somehow coupled to the entanglement of the state, and generally the entanglement cannot be interrogated with local measurements.

## 5.3 The geometry of adiabatic computation at zero temperature

With certain caveats, the quantum adiabatic theorem guarantees the existence of an adiabatic path between two points in Hilbert space. In principle we can then find the ground state of a trivial initial Hamiltonian, and adiabatically change this into the target Hamiltonian which encodes the problem of interest, this transports the state into the ground state of the target Hamiltonian providing this change is sufficiently slow accoridng to (5.4). The scaling of the gap thus determines whether a particular computation can be performed efficiently [174, 193–197]. This leads to important constraints on adiabatic computation. However, there are other ways in which a computation might fail in an open system:

### 5.3.1 Adiabatic connectivity of dissipatively restricted manifold

As previously argued, in an open system dissipation renders only a subset of states in the Hilbert space accessible. This means only for a restricted set of anneal protocols, each defined by a time dependent Hamiltonian $H(s)$, will the variational manifold be able to represent the correct ground state at every point along the adiabatic path. Both adiabaticity and accessibility of all points on the adiabatic path must be satisfied in order for us to have reason to expect an adiabatic computation to succeed. Thus we expect that by interrogating the latter, that we be able to address how quantum mechanical is a given adiabatic computation.

### 5.3.2 The critical resources required for computation

For a closed system all points in the Hilbert space can be reached adiabatically (some caveats to this are discussed below). Sweeping at a finite rate introduces diabatic errors, and certain paths cannot be followed. These most severe errors are induced by closely avoided crossings which cause the ground state to rapidly move across the Hilbert space as its character switches from one of states in the avoided crossing to the other. The smaller the minimum gap $\Delta$ of the avoided crossing, the more rapid this transition of the corresponding state.[①] In general we expect there is a minimum sweep time $T^*$ for each path $H(s)$ for which there is a tolerable error. In general these events also require more entanglement to capture, and often more so the closer the crossing.

When the system is open, dissipation limits entanglement and prohibit the system from reaching points in the Hilbert space and it may be unable to follow the adiabatic path through the avoided crossing. Thus the computation must proceed by a different and suboptimal path, causing the state to be driven away from the exact path. However we can associate with the exact ground state, an energetic basin on the variational manifold, and if the state remains sufficiently low in this basin of attraction the computation may proceed with acceptable fidelity. When a critically large fraction $f^*$ of the Hilbert space has been made inaccessible this can no longer occur, and the exact ground state is always lost by variational dynamics. Here, we use bond order $\chi$ of the MPS as a measure of the accessible region of Hilbert space.

It is found that these somewhat orthogonal sources of diabatic error and restricted entanglement can be traded off against each other, and that what accuracy is lost in terms of fraction $f$ of Hilbert space, can up to a threshold, be made up to some degree by with a longer anneal time $T$. This picture is summarised in Figure 5.5.

[①] A simple example of this is the Landau-Zener problem $H = (\nu t\sigma^z + \Delta\sigma^x)/2$ in which the ground state goes from $|\uparrow\rangle$ for $t \ll 0$ to $|\downarrow\rangle$ for $t \gg 0$ on a time-scale $\tau \sim \Delta/\nu$, highlighting the relevance of the minimum in setting the time-scale of the problem. Per equation (5.4) it is necessary to go even slower to have small total diabatic error

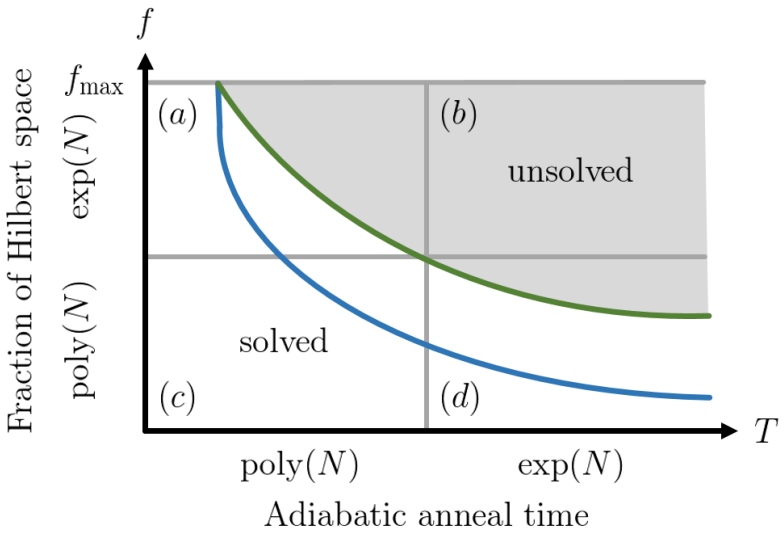


Figure 5.5: *The adiabatic success critical line for two problems:* The adiabatic computation only succeeds if there are sufficient quantum resources, given by fraction $f$ of accessible Hilbert space, and classical resources, given by the anneal time $T$. The critical line between successful and unsuccessful computation is a monotonically decreasing function in this space. The minimum computation time $T^*$ occurs when the entire Hilbert space is accessible (i.e. at $f = f_{\max} = 1$). The minimum fraction of Hilbert space for which the computation is successful occurs at $f^*$ which corresponds to the horizontal asymptote. In this work we use the Schmidt rank $\chi$ as a proxy for $f$. This notion is connected to classical complexity by dividing each axis into poly($N$) and exp($N$) regions. The critical line of two problems are shown: a classically easy calculation (solid blue) passes through the region ($c$) in which the adiabatic evolution, simulated with polynomial classical data, for a polynomial time reaches the correct answer. A classically hard but quantum mechanically easy calculation (solid green) passes through only regions ($a$) and ($d$).

### 5.3.3 Caveats: when adiabatic quantum computation fails

As caveats to our earlier initial statement that that any state in the Hilbert space can be reached by Adiabatic transition, we note that

- *Locality of Hamiltonians presents a further constraint:* Physically we can realise only local Hamiltonians, this limits the points in Hilbert space that can be reached from a given starting point [200].[①] In principle one could add an additional axis in Figure 5.5 measuring the locality of the Hamiltonian. With increasing range of terms in the Hamiltonian, an increasing fraction of the Hilbert space can become accessible is accessible and more problems can be solved. This issue may be important for understanding what problems are soluble by a given adiabatic computer, but a detailed analysis goes beyond the scope of this work.

- *Reasonable run time presents a further constraint:* Practically quantum annealing is only useful for solving problems which do not take an exponential time. Thus we are not interested in the fraction of the many body Hilbert space $\mathcal{H}$ that can only be reached in exponential time. This unreachable fraction constitutes a majority of $\mathcal{H}$, and the reachable part an exponentially small minority [26].

### 5.3.4 Quantum and classical in adiabatic computation

The picture of adiabatic computation in open systems presented in equation (5.14) reduces it to a classical algorithm. However adiabatic quantum computation is universal [201, 202] (this relation

[①]This proof is shown for the very loose definition of local as restricted to $k$-body interactions for finite $k$. If interactions are further restricted to be local with respect to some lattice geometry, presumably this restriction becomes even more severe.

is outlined in simple terms in appendix G.1). How do we reconcile these two positions? Since the classical simulation and adiabatic quantum computation have the same sweep time, and since we do not believe classical and quantum computation be equivalent, then any increased computational power must be made up by the requirement for access to increasingly entangled parts of the Hilbert space, which are classically hard to simulate.

Thus it makes sense to distinguish between resource requirements that are exponential (hard) and polynomial (easy) in the system size on both of our two resources of adiabatic anneal time $T$, and fraction of the Hilbert space $f$. This results in the four quadrants of the graph in Figure 5.5. This division corresponds to easy and hard in sweep time, and to classical and quantum in Hilbert space fraction.

Each problem can be associated with a line of critical resource requirements. Problems can then be classified according to the quadrants of this graph through which the corresponding critical line passes. For example, a calculation that is both quantum and classically easy can be performed in polynomial time with only a small fraction of the Hilbert space. In Figure 5.5 its critical line would pass through the quadrants $(a)$, $(c)$ and $(d)$. A quantum mechanically easy, classically hard computation will pass through quadrants $(a)$ and $(d)$. Finally, an adiabatic computation that requires a large degree of quantum correlations might have a critical line that passes through quadrants $(a)$ and $(b)$.

Thus, though an adiabatic computer may harness significant quantum correlations, unless the accessible region of Hilbert space grows sufficiently rapidly with the size of the system, the class of soluble problems will be classical. Alternatively stated, this suggests that finite range quantum correlations[①] can only provide a constant pre-factor speed-up, and no improvement in scaling. Problematically, in the absence of error correction, a saturation in the length scale of entanglement, and hence the reversion to classical asymptotic scaling, seems inevitable, highlighting the need for further development of error correction for adiabatic computation [204, 205].

This appears to be the source of much of the polarisation of the debate regarding the 'quantumness' of a putative adiabatic computer. Such a computer may harness a significant degree of quantum mechanics in its operation [178], but nevertheless provide no computational resource in excess of a classical computer [50]. Nevertheless, even if they are polynomially equivalent, if this polynomially rescaling is significantly large, then, from a pragmatic point of view, the not-quite-quantum computer may nonetheless be very useful.

### 5.3.5 Quantifying quantumness and the breakdown of adiabatic computability

At the threshold of adiabatic computability any further reduction in the resources $f$, the accessible fraction of Hilbert space, or $T$, the adiabatic anneal time, will cause the computation to fail. This may be for a variety of reasons:

- *Approximation error of the variational manifold:* The dissipative confinement to a reduced variational manifold $\mathcal{M}$ prevents an accurate representation of all quantum states in the Hilbert space $\mathcal{H}$. The further from $\mathcal{M}$ the exact ground state is, the more excited the approximation becomes. This situation is shown in Figure 5.6. This can result in failure of the computation, or alternatively the situation may be recovered, as shown in Figure 5.4. Physically this corresponds to a case when the quantum correlations required to represent the exact ground state are too fragile too persist on dynamical time-scales.

- *Local minima in the variational manifold:* It is a special feature of the full Hilbert space $\mathcal{H}$ that there are no local energetic minima. However this is not true for the projected

[①] cf "What is the Computational Value of Finite Range Tunnelling?" of ref [203]

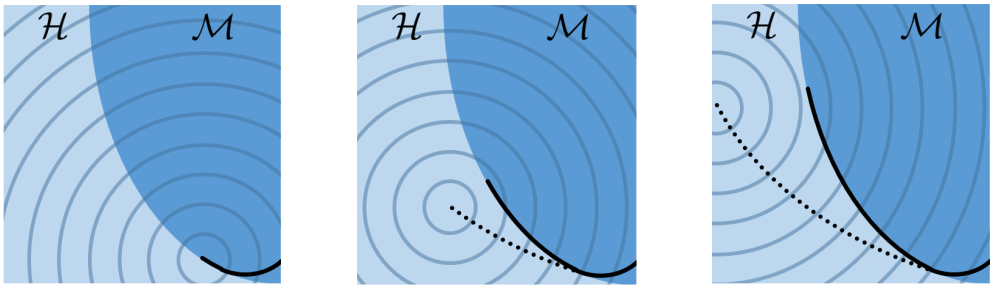


(a) (b) (c)

Figure 5.6: *Computational failure due to approximation error of the variational manifold:* The variational adiabatic trajectory (solid black) is confined to $\mathcal{M}$ whereas the exact trajectory (dotted black) is general. The contours correspond to energetic isolines. As the exact trajectory goes further from the manifold $\mathcal{M}$ the approximated evolution is forced higher in the energetic well.

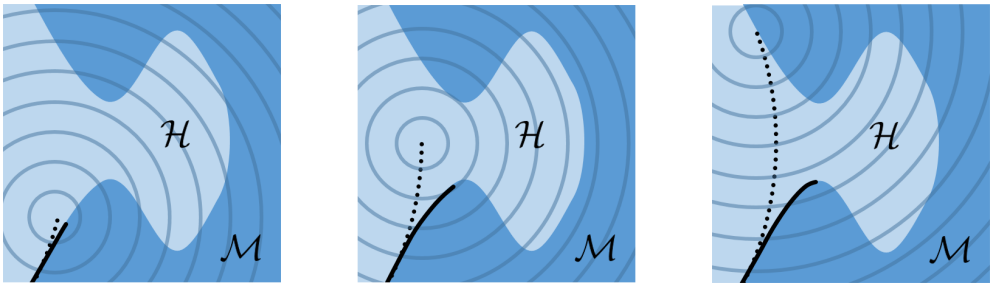


(a) (b) (c)

Figure 5.7: *Computational failure due to local minima in the variational manifold:* The variational adiabatic trajectory (solid black) is confined to $\mathcal{M}$ whereas the exact trajectory (dotted black) is general. The contours correspond to energetic isolines. In this example the exact trajectory crosses a region of Hilbert space which lies outside of $\mathcal{M}$ before rejoining. This causes the minimum in $\mathcal{M}$ in which the projected trajectory sits to change from a global to a local minimum. If $\mathcal{M}$ corresponded to classical states the trajectory of the exact solution would correspond to a tunnelling process which cannot be captured by the classical dynamics. When $\mathcal{M}$ has its own quantum correlations it is a simple generalisation of this concept.

dynamics, and a point that was the global minimum can be relegated to local minimum by the comparative deepening of other minima in the system. This situation is depicted in Figure 5.7. The dissipative confinement to a local minimum in this way corresponds to a point when the exact trajectory undergoes a tunnelling event requiring longer range coherence than is able to persist on dynamical time-scales due to dissipation.

- *Increased susceptibility to diabatic error:* When the exact ground state goes thorough an avoided crossing this causes a fast change in the character of the ground-state. If the computation is not sufficiently adiabatic and the state cannot respond sufficiently fast, the computational state will begin to oscillating around the ground state. This can be understood as analogous to the sloshing in a glass of wine induced by abruptly moving the glass, and this situation is shown for the exact dynamics Figure 5.8. This problem can be more severe in the variational dynamics for two reasons: (*a*) When the global ground state is not in the variational manifold, the state is forced to sit higher in the energetic minimum, as discussed in Figure 5.7, alternatively we could say the energetic minimum in the variation manifold $\mathcal{M}$ is much shallower than the global minimum in $\mathcal{H}$, either way the projected evolution requires a less severe diabatic error to be displaced. (*b*) The existence of local minima in the variational manifold means that the 'sloshing' induced by diabatic error can result in the system exciting into a region where it will become trapped.

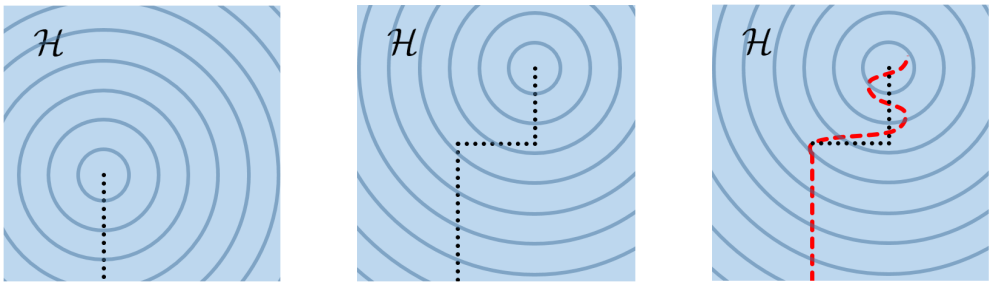


(a) (b) (c)

Figure 5.8: *Computational failure due to diabatic error:* The exact ground state trajectory (dotted black), and the finite time trajectory (dashed red) in the Hilbert space $\mathcal{H}$. The contours correspond to energetic isolines. Here the exact ground state goes through an avoided crossing and its character is rapidly altered. When this adiabatic anneal is performed at a finite rate the computational state will be unable to respond sufficiently quickly to and will begin oscillating around the exact ground state minimum.

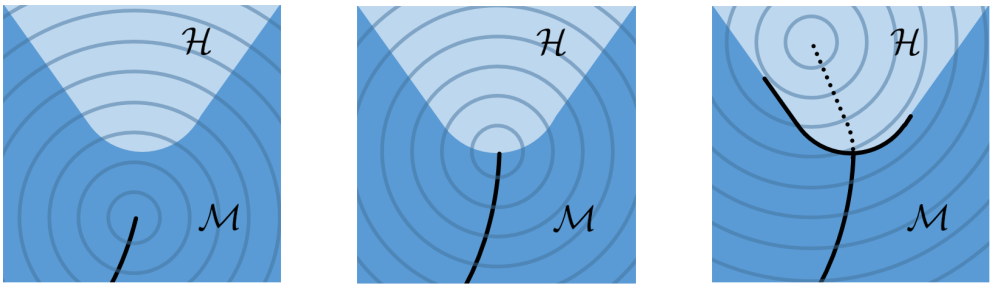


(a) (b) (c)

Figure 5.9: *Computational failure due to loss of dynamical stability in the variational dynamics*: The variational adiabatic trajectory (solid black) is confined to $\mathcal{M}$ whereas the exact trajectory (dotted black) is general. The contours correspond to energetic isolines. There are many examples of dynamics instability that one could envisage. Here we consider a case where global minimum tunnels out of the variational manifold in such a way that there is a stagnation point in the variational dynamics about which there are multiple diverging trajectories in $\mathcal{M}$ which approximate the dynamics well. As a result a small error which biases the trajectory towards one or the other outcome may be amplified to a large change in the later trajectory.

- *Loss of dynamical stability of the variational dynamics:* The exact quantum dynamics are linear, thus dynamical instability, characterised by positive Lyapunov exponents is not possible. In the projected dynamics, this is not the case, and even very small errors, either from the initial state, from thermal noise, or from setting errors in the Hamiltonian, may be amplified sufficiently to drive the dynamics away from the minimum. This situation is shown in Figure 5.9.

This simple, geometrical picture suggests how we might quantify the degree of entanglement in a potential adiabatic computer.

We classify sets of one-dimensional target Hamiltonians by the minimum Schmidt rank or bond order $\chi$ of matrix product states[①] whose zero-temperature, projected adiabatic evolution gives the correct solution giving the bond order of this problem. Testing an adiabatic computer with problems of different bond order we expect to find a transition in computability from low rank problems which the machine finds easy (i.e. solves frequently), to high rank problems which it finds hard (i.e. fails frequently). The associated value of $\chi$ at which this occurs is indicative of the entanglement supported by this machine and hence its computational capability.

[①]Bond order gives a fairly crude, discrete measure of the fraction of the accessible fraction of Hilbert space. A more complete, continuous measure might perhaps be constructed from the Schmidt spectrum. However constructing dynamics with such a constraint is hard, and without an efficient way of representing such states, the connection with classical complexity is lost.

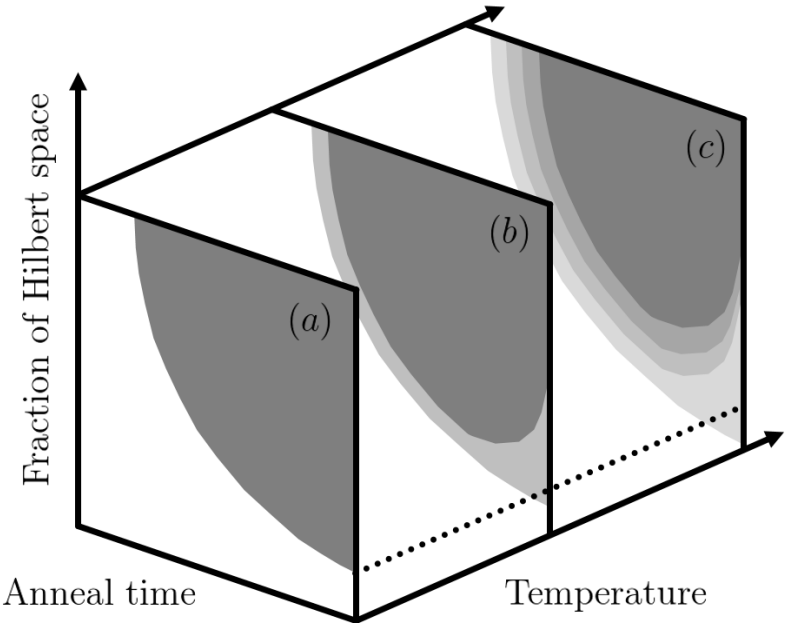


Figure 5.10: *The adiabatic success critical boundary becomes diffuse at finite temperature:* The boundary is no longer hard as in Figure 5.5 but now blurred, with a probability of success (represented by the density) across a region of the plot. This effect is more severe at higher temperature. At infinite temperature the success probability is independent of all parameters of the system and anneal protocol, and depends only on the final Hamiltonian. Furthermore the dependence on anneal time has become non-monotonic, with the probability at large anneal time set by the thermal equilibrium state of the final Hamiltonian.

In the following sections, characterise a particular set of one-dimensional test problems in this way, and use this to benchmark the D-Wave Vesuvius computer. First, however, we discuss how the effects of noise—as distinct from dissipation—might impede this analysis at finite temperature.

## 5.4 Adiabatic computation at finite temperature

A real adiabatic computer necessarily operates at finite temperature. We have discussed how a determination of the degree of quantum mechanics employed by such a computer can be made at zero temperature. We now elaborate on why this determination cannot be made unambiguously at finite temperature where dynamics is non-deterministic.

The effects of noise are different from those of dissipation and sweep time. This renders the dynamics stochastic which is monotonically detrimental to adiabatic computation. This is easy to see even in the full and unrestricted Hilbert space: consider a computational protocol which succeeds only with a given probability $p_0$ at zero temperature due to diabatic error at an avoided crossing. If we consider the same process at finite temperature, and add an arbitrarily long waiting time to the end of the protocol, the systems final state will be thermal equilibrium. This will generally have a non-negligible probability $p_T$ of being in the ground state. Since $p_0$ depends on the properties at avoided crossings, whereas $p_T$ depends on the final Hamiltonian, it is possible to choose $p_T < p_0$, in which case the finite temperature has improved the success probability of the computation. In the framework which we have studied, finite temperature effects allow all sorts of probabilistic phenomena permitting the escape of local minima, the avoidance of chaotic regions, and the potential to re-find the global minimum after diabatic errors. Furthermore as noted, noise renders the dependence on sweep time potentially non-monotonic, since increasing anneal time $T$ increases the time of exposure to noise, at $T$ [206]. This is illustrated in Figure 5.10 in which and additional axis has been added to Figure 5.5.

The non-monotonic effect of noise that makes it hard to distinguish classical and quantum effects at finite temperature. It may be possible to separate the contributions of noise and dissipation through their different temperature dependence. However, a device which harnesses the power of the adiabatic theorem to compute must be well approximated by the low-temperature limit. Thus we classify benchmark problems classified by the resources required to solve them at zero-temperature.

### 5.4.1 Developing a set of benchmark problems

We now use these ideas to develop a set of test problems. These will consist of a set of one-dimensional Ising Hamiltonians of the form given in equations (5.2) and (5.3). These will be sorted according to the minimum bond order, $\chi^*$, required to solve them.

For each problem we i) determine its minimum energy state[①] ii) follow its projected evolution in a variational manifold parametrized by matrix product states of fixed Schmidt rank using equation (5.14). iii) Since our aim is to characterise the zero-temperature quantum resources required to achieve the correct target state via a projected adiabatic evolution we repeat this evolution for many values of the bond order $\chi$. The minimum bond order, $\chi^*$, at which the projected evolution takes the system to the exact minimum. We emphasise that time-evolving in this way is not an attempt to simulate any particular system. Rather, it provides a bound on the quantum resources required to minimise a given target Hamiltonian adiabatically.

Our choice of target Hamiltonian is restricted in several ways: we must be able to find its ground state exactly in reasonable time by exhaustive search; it must also be embeddable given the connectivity of the D-Wave hardware (the so-called Chimera graph shown in Figure 5.12); it must be of geometry that makes is efficiently simulable by classical algorithms. For these reasons we have considered 500 randomly chosen on one-dimensional 100-site spin chains. The nearest neighbour couplings of these one-dimensional Ising models were randomly drawn from $J_{ij} \in \pm\{0.2, 0.4, 0.6, 0.8, 1\}$ while the local fields were drawn from $h_i \in \pm\{0, 0.2, 0.4, 0.6, 0.8, 1\}$. Though the ground states of these target Hamiltonians are easily found, they proved surprisingly challenging for quantum annealing. We also considered other geometries, including the two-leg ladder which we found less able to discriminate.

The intermediate times are thus given by a transverse field Ising model

$$\begin{aligned} H(t) &= A(t)H_{\text{start}} + B(t)H_{\text{target}} \\ &= A(t)\left[-\sum_i \sigma_i^{\text{x}}\right] + B(t)\left[\sum_{ij} J_{ij}\sigma_i^{\text{z}}\sigma_j^{\text{z}} + \sum_i h_i\sigma_i^{\text{z}}\right]. \end{aligned} \tag{5.15}$$

Surprisingly, although ground states of the transverse field Ising model generally require high bond order to be faithfully represented with matrix product states, we find that all generated instances were solved for bond order $\chi^* \leq 2$.[②] In order to populate a diagram analogous to Figure 5.5, we ran our simulations at Schmidt ranks $\chi = 1, 2, 3, 4$ and for anneal times $T = T_0, 2T_0, 4T_0, 8T_0$ (where $T_0$ was an arbitrary large multiple of the fundamental intrinsic time-scale of the Josephson junction).

### 5.4.2 Entanglement in the D-wave Vesuvius machine

D-Wave is a commercial enterprise which has produced several putative quantum annealers. In this work we consider the D-Wave Vesuvius device. The D-Wave Vesuvius is a 503 qubit array

[①] to do this efficiently we use that for one dimensional Ising problems the partition function can be easily written down in terms of transfer matrices

[②] Except for a very small number of problems which we believe were due to numerical error

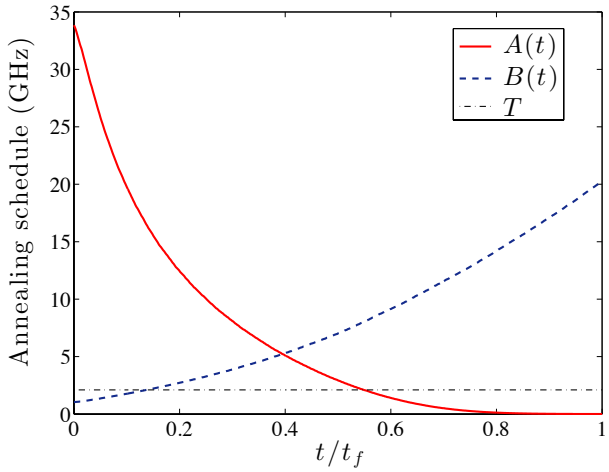


Figure 5.11: *The D-Wave anneal schedule* The horizontal dashed line corresponds to the operating temperature (18mK) of the device. The large $A(0)/T$ value ensures that the initial state is the ground state of the transverse field Hamiltonian. The large $B(t_f)/T$ value ensures that thermal excitations are suppressed and that the final state reached is stable. At intermediate times it is likely that thermal fluctuations become relevant. Unfortunately the schedule is fixed by the hardware and cannot be altered by a user.

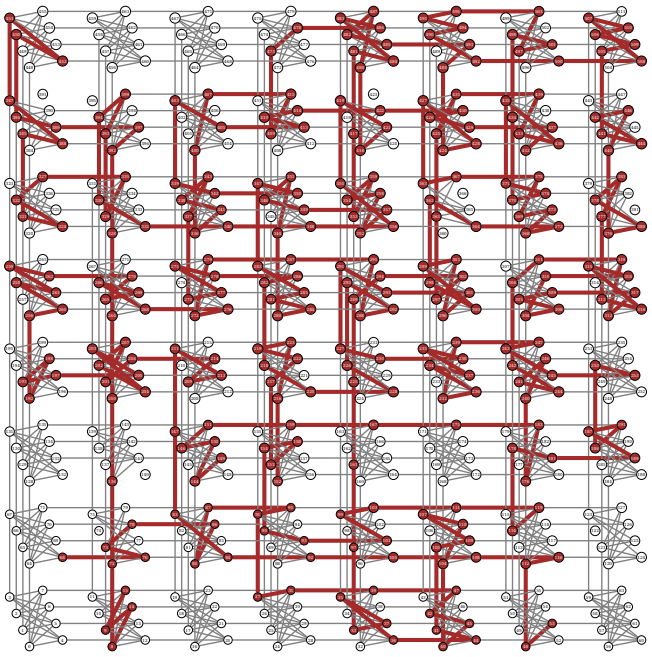

Figure 5.12: *Flux qubit connectivity on the D-Wave:* 503 flux qubits are usable. 9 qubits (which are disconnected) cannot be reliably calibrated and are not usable. The qubits and the couplers highlighted in red represent 3 different randomly chosen implementations of a 100 spin chain. Averaging over different implementations in this manner allows us to average over hardware defects and setting errors.

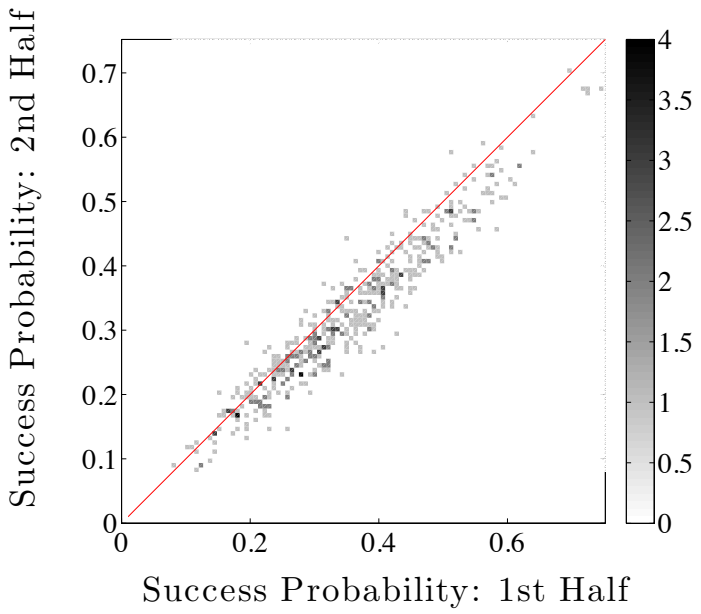


Figure 5.13: *Autocorrelation of gauge averaged success probabilities from the D-Wave machine*: Each problem was embedded in the D-Wave in 1000 distinct ways to average over hardware error, for each embedding of each problem the anneal was run 20 times to average over statistical errors. Here we study the combined source of these errors across the 1000 distinct Hamiltonians studied. For each problem that 20,000 runs are partitioned randomly, into two equal parts. The success probability for the two partitions is plotted.

of Josephson junctions with tunable $J_{ij}$ and $h_i$. The device implements the anneal described by equation 5.15, where the driving functions $A(t)$ and $B(t)$ are changed in time according to the annealing procedure shown in Figure 5.11 [152].

The connectivity of the Ising Hamiltonian $H_{\text{target}}$ is limited by the hardware—an implementation of the so-called Chimera graph—which is depicted in Figure 5.12. Each coupling and longitudinal field can be set to a value within $J_{ij} \in [-1, 1]$ and each field within $h_i \in [-2, 2]$, giving $\approx 1400$ independently tunable parameters in $H_{\text{target}}$.

The company was at the centre of controversy in 2013 after the D-Wave founder Geordie Rose was widely and uncritically reported to have accomplished his goal of building a "quantum computer" that is “better at something than any other option available” [207]. These claims of quantum speed-up were subsequently disputed [50, 208]. Other attempts to attribute statistical effects to quantum dynamics [126, 127, 153, 154] were similarly disputed [51–53]. This lead to more robust evidence [178, 209, 210] of quantum dynamics and which credibly evidenced the existence of non-trivial quantum effects (as well as apparently significant thermal effects).

The result is that there is evidence of entanglement within the 8-bit clusters that form the fundamental motif of the D-Wave machine [178, 209, 210]. However evidence that these quantum correlations extend to a large scale, or crucially, provide a quantum speed-up, has proven elusive [50–53, 126, 127, 152, 153, 210]. Efforts to study this problem have focussed on comparing the fully classical or fully quantum dynamics to see which provides a better fit to the observed behaviour of the D-Wave machine, and the resulting debate has been polarised.

### 5.4.3 Benchmarking methodology

Our approach aims to add nuance to this picture by taking a gradation of dynamics instead of comparing fully classical or fully quantum model. The aim is that this will provide framework for black-box benchmarking that is sensitive to cases that lie between these quantum and classical

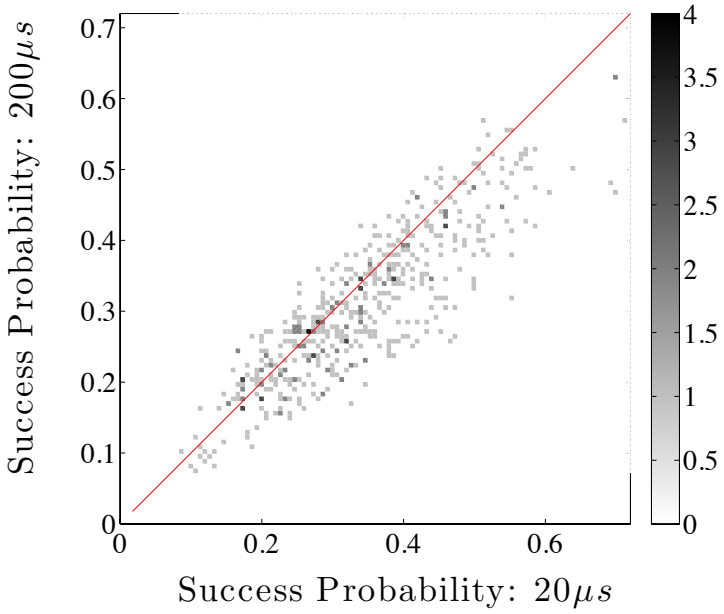


Figure 5.14: *Increased anneal time decreases the probability of finding the ground state in the D-Wave machince*: Here data is plotted for the same problems as in Figure 5.13 with anneal times of $20\mu s$ (as in Figure 5.13) and anneal times of $10\times$ this value. In addition to the intrinsic spread visible in Figure 5.13, there is a distinct decrease in the success probability of with increased anneal time. This is consistent with the expectation developed in Section 5.4 and further indicates that the D-Wave is operating with an above-optimal anneal time [211]

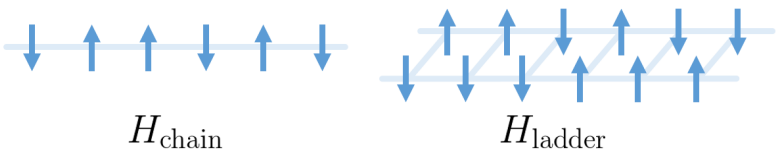


Figure 5.15: *Problem Hamiltonians*: one-dimensional spin chains and quasi-one-dimensional 2-leg ladders were both studied, these were then classified on the basis of the resources required to solve them. Due to the hardware restrictions of the Chimera graph (Figure 5.12) it is not possible to embed a general two-leg ladder: for every along the legs of the ladder, only the $J$ coupling on the left leg can be non-zero.

extremes.

We first studied instances of the one-dimensional chain. After classifying the problems by bond order $\chi^*$ using the previously introduced process, we ran these problems on the D-Wave vesuvius. Each problem was run many times, with different embeddings of the one-dimensional problem in the Chimera graph, as shown in Figure 5.12, in order to average over any hardware defects.

Gauge averaging furthermore allows us to average out the effect of setting errors, caused by inaccurate tuning of the fields and couplings of the final Hamiltonian [126]. This effect is quantified in Figure 5.13 by studying the auto-correlations between results obtained for different runs of the same problem on the D-Wave. In a similar vein thermal effects can also be quantified by studying the effect of increasing the anneal time, thus increasing the exposure time to the noise, shown in Figure 5.14. For this reason each anneal was done with the minimum anneal time allowed by the D-Wave software of $T = 20\mu$s.

This process was repeated for the quasi-one-dimensional two-leg ladder, shown in Figure 5.15, for the purposes of studying these with MPS code each 'rung' of the ladder was treated as a two-spin 'super site'.

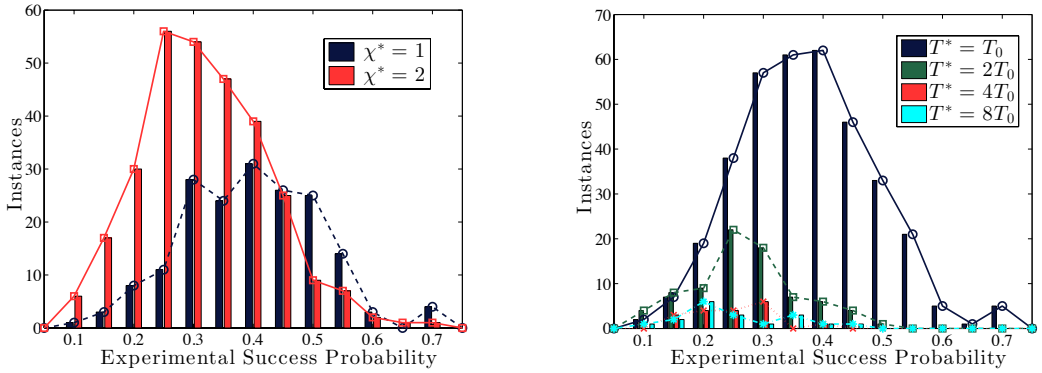


Figure 5.16: *Success probabilities for the one-dimensional chain*: (a) Success probability correlated with critical bond order $\chi^*$ required for successful adiabatic computation. These histograms record the number of instances of each classification of problem that in each interval of experimental success frequency. We show data for the 500 instances of the one dimensional chain at $L = 100$. The correlation shows that problem instances which require more quantum resources (i.e. higher $\chi^*$) are more difficult for the D-Wave machine. (b) Success probability correlated with critical anneal time required for adiabatic computation. All the 500 instances had critical bond order $\chi^* = 2$, and are further divided according to the critical anneal time $T^*$ which was required to solve them. A correlation with the performance of the D-Wave machine is again evident, with the D-Wave machine performing worse on problems that were more resource intensive.

### 5.4.4 Results

The results of the benchmarking process with the one-dimensional chain is summarised in Figures 5.16 and 5.17.

The probability of successful computation on Vesuvius is weakly correlated with $\chi^*$ the entanglement required for adiabatic computability. Similarly there is a weak correlation with the difficulty of the problem determined by the minimum theoretical sweep rate. A major cause of this appears to be thermal fluctuations. Unfortunately it is difficult to disentangle thermal and quantum effects and making our results inconclusive.

At the lowest temperature we would anticipate a much sharper division between success and failure to occur on increasing $\chi^*$ which characterises that quantum resources required to solve the problem, however at high temperature we expect this to be much more diffuse.

In Figure 5.14 we see that the D-Wave performs less favourably on problems which required a slower anneal. This might hint suggest that the D-Wave anneal was too short, and with a slower adiabatic transition it may perform better. However this is not the case, and as shown in Figure 5.14 we see that the success probability is decreased by increasing the anneal time, consistent with previous observations that the D-Wave anneal time is longer than optimal [211]. Incidentally this does provide circumstantial evidence is inhibited by longer exposure to thermal fluctuations, and hence is proceeding by another mechanism, namely quantum dynamics

## 5.5 Discussion

In this chapter we have explored a new perspective on adiabatic quantum computation, and we have used this perspective to discuss the reasons why adiabatic quantum computation might fail, distinguishing between the effects of fluctuations, dissipation, and diabatic error. Coupling to the environment leads to two of these effects—noisy fluctuations and dissipation. The latter constrains the quantum correlations that the system can support. This determines the fraction of Hilbert space that the computation can utilise, and hence the extent to which quantum dynamics may be

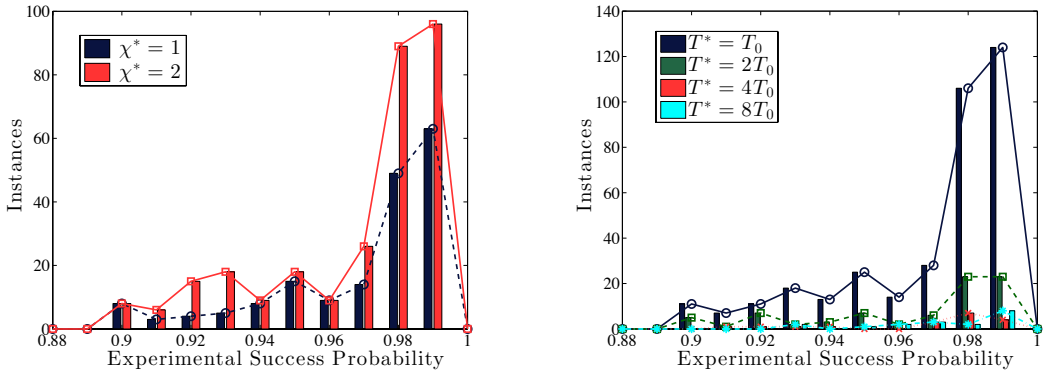


Figure 5.17: *Success probabilities for the quasi-one-dimensional two-leg*: (a) Success probability correlated with critical bond order $\chi^*$ required for successful adiabatic computation. These histograms record the number of instances of each classification of problem that in each interval of experimental success frequency. We show data for the 500 instances of the one dimensional chain at $L = 100$. The absence of correlation here, compared with Figure 5.16, shows that these problems were significantly less good probe problems than the one dimensional chain. (b) Success probability correlated with critical anneal time required for adiabatic computation. All the 500 instances had critical bond order $\chi^* = 2$, and are further divided according to the critical anneal time $T^*$ which was required to solve them. These results were also much poorer than the one dimensional chain.

harnessed for computational means. Noise complicates this picture, and it is no longer possible to unambiguously determine whether quantum dynamics played a key role in making a calculation possible.

The insights gained into this picture of adiabatic computation are most usefully summarised by the adiabatic success critical line, shown in Figure 5.5. This line demarcates the region where the accessible quantum correlations and adiabatic anneal time are sufficient to make a problem soluble. We have discussed how this can be related to notions of computational complexity.

Motivated by this picture we have classified a class of problems by the quantum resources that are required to solve them. This classification of problems was then used for the benchmarking of the D-Wave Vesuvius device. This device consists of an array of tunable compound Josephson junction flux qubits [131] and constitutes the first large scale implementation of a quantum annealing device. The device was at the centre of controversy following bold claims that it was harnessing quantum mechanics or a large scale [126, 127, 153], and unsubstantiated claims that it outperformed classical computers [207, 212] all of which were disputed [50–53, 208]. Following this quantum effects and entanglement have been evidenced [178, 209], and though the D-Wave has proven superior to certain off-the-shelf optimisation routines, such as thermal annealing [203], it has been established that classical algorithms optimised for the D-Wave native problem (QUBO on the Chimera graph), such as the Hamze-de Freitas-Selby algorithm [213, 214] and others [215], are able to comfortably outperform the D-Wave.

In this work we have gone beyond the previous studies of quantum dynamics on the D-Wave machine, and applied the aforementioned insights to develop a framework for determining not just the presence (or otherwise) of quantum dynamics, but the *degree* to which they are harnessed to solve problems on the D-Wave machine. This was approached by developing a set of benchmark problems which were established to require different degrees of resources (critical entanglement (bond order) $\chi^*$, and critical anneal time $T^*$) to solve. Unfortunately this analysis was hindered by several issues: (i) The one-dimensional chain problems were all solved at $\chi^* = 1, 2$ reducing the already crude discrete integer measure of entanglement to a binary one, whilst other quasi-one-dimensional problems we developed to tackle this proved to be even poorer probes (ii) The presence of significant thermal effects makes extremely challenging the task of identifying whether a problem

was solved by thermal exploration of the phase space, or quantum tunnelling. Nevertheless, though the correlation is weak, our results indicate that the problems identified by our approach proved more challenging for the D-Wave machine.

In both cases the D-Wave machines performance was found to be worsened by studying successively harder problem classes. The machine solved problems which required no quantum mechanics, $\chi^* = 1$, relatively easily. It was less successful with problems that required the smallest amount of non-zero entanglement that can be discriminated by bond order, $\chi^* = 2$, which these constituted the hardest problems we could construct. This suggests two things: (i) that the machine is not able to easily provide this small level of entanglement; (ii) that this small level of entanglement was surprisingly effective at solving the (relatively easy) one-dimensional Ising problems given that the exact ground state will typically be of very large bond order. This analysis was not conclusively able to evidence the existence of entanglement (or lack of it) in the D-Wave machine, largely due to the presence of probabilistic thermal process, but does provide evidence that, when used for one-dimensional problems the machine is able to, albeit inconsistently, provide a computational resource equivalent to a low bond-order matrix product state.

Future development of this methodology evidently requires an ability to capture the dominance of thermal processes if it is likely to be of use for benchmarking the current generation of quantum annealers. In the future we hope that the development of error-correction protocols [173, 205] will make quantum annealing with significantly thermal noise possible, whereby we expect this methodology would prove significantly more useful.

# 6 | Absence of thermalization due to weak disorder and Kinetic Constraints

In this chapter we investigate the circumstances in which a system may be prevented from thermalizing with its surroundings. We study a kinetically constrained spin model that has previously been shown to exhibit certain characteristics of many body localization in translationally invariant systems. We find that in certain regimes arbitrarily weak disorder is able to localize sufficiently low-lying states of the system. In this region, a mobility edge separates low lying localized states from ergodic mid-spectrum states. We find an approximate form for this mobility edge that is found to agree well with numerics. This novel effect affects a vanishingly small fraction of states in the thermodynamic limit constituting a different type of phenomenon than that which has been observed in strongly disordered systems.

The original work in this chapter is covered in Section 6.2 and onwards.

It has been common in the study of the properties of many-body condensed matter systems to focus on perfect or near-perfect crystalline materials. In these systems the lattice-translational and point-group symmetries dramatically simplify the mathematical analysis. Such pictures correctly capture the physics of many systems of interest, but are often not representative of the underlying physical reality. Given the ubiquitous presence of disorder it is thus necessary to test the robustness of our predictions to the presence of disorder in the course of our analysis. In his seminal paper [66] Anderson showed that even the properties of the canonical tight-binding model, the simplest model of particle hopping, which captures many key phenomena and which underpins conventional band theory, are altered dramatically by the introduction of even weak disorder in dimensions $D = 1, 2$ and critically strong disorder for $D = 3$ [66, 216–218].

The conventional thermalizing behaviour of a system is that dynamical processes mix up information. An initial state is evolved under the dynamics of the system through several stages:

1. **Transient persistence of the initial state**: Initially the microscopic detail of the initial state is required to predict the dynamics of local observables.

2. ***Local* thermodynamic equilibrium**: at this intermediate stage the local values of the density of energy, charge or other conserved quantities become well defined. Statistically these become the only necessary quantities to capture the behaviour of local observables. The dynamics is defined by the hydrodynamics of these locally defined conserved quantities. The memory of the initial state persists in the local values of hydrodynamic quantities.

3. ***Global* thermodynamic equilibrium**: In the long time limit the transient dynamics hydrodynamic quantities decays away as they become uniform distributed. Local observables relax to the values predicted by statistical mechanics.

This progression is of course contingent on the ability of the system to move energy, charge, etc from regions of high density to regions of low density, i.e. that the system conducts.

The appearance of a disorder driven 'localized' phase in Anderson's paper, in which the conductivity goes to zero, rules out this progression. Instead in such systems there is an absence of thermalization. In the absence of strong evidence many had suspected this to be a uniquely single-body effect, and that in the presence of non-negligible interactions between particles the localized phase would not survive. However recent progress has evidenced the existence of a many body localized (MBL) phase through analytical calculations [219–221], numerical studies [222–226] and experimental observations [227]. The MBL phase is now widely accepted to be a robust phase of matter in sufficiently disordered systems in one dimension.

In this chapter we explore the properties of this phase, and study a specific model of interest to explore the possibility of MBL in the absence of strong disorder, we find a regime in which the lowest lying fraction states localise at arbitrarily weak disorder. This fraction falls off $1/L$ with systems size but increase with uniform field strength $h$. So exists at all systems sizes, albeit at increasingly extreme field strengths.

## 6.1 Background

We begin by reviewing the features of the localized and many-body localized phases.

### 6.1.1 Anderson localization

Here we briefly introduce Anderson's original perspective on single particle localization, more complete reviews [228, 229] and more rigorous proofs [216–218, 230, 231] are available.

Anderson considered the behaviour of a system of non-interacting particles hopping on a disordered lattice [66]. Due to the lack of interactions we can work in the single particle picture, in which the Hamiltonian is given by

$$H = -J \sum_{\langle n,m \rangle} \Big( |n\rangle \langle m| + |m\rangle \langle n| \Big) + \sum_n W_n |n\rangle \langle n| , \tag{6.1}$$

where $\langle n, m\rangle$ denotes nearest neighbours on the lattice, and the on-site energies $W_n$ are iid random variables. The parameter $W$ sets the characteristic width of the disorder distribution.[①] In the limit of zero disorder $W \to 0$ we recover the familiar tight binding model whose eigenstates a labelled by momenta $k \in [-\pi, \pi]$ and have energies $E_k = -2J \cos k$. For this disorderless case, finite conductivity is self evident. However a useful indicator of this is the return amplitude, given by

$$\langle n|\mathrm{e}^{-\mathrm{i}Ht}|n\rangle = \sum_k \mathrm{e}^{2\mathrm{i}Jt\cos k} \langle n|k\rangle\langle k|n\rangle = \frac{1}{L}\sum_k \mathrm{e}^{2\mathrm{i}Jt\cos k} = J_0(2Jt), \tag{6.2}$$

where $J_0(\cdot)$ is the zeroth Bessel function of the first kind, and we have assumed we are in one dimension where $\sum_k \to \frac{L}{2\pi}\int \mathrm{d}k$ as $L \to \infty$. The signature of conducting behaviour is already evident in the fact that this quantity decays to 0. The Greens function, obtained by Fourier transforming this object is then

$$G_{nn}(\omega) = -\mathrm{i}\lim_{\eta\to 0}\int_0^\infty \mathrm{d}t\, \mathrm{e}^{\mathrm{i}\omega t - \eta t}\langle n|\mathrm{e}^{-\mathrm{i}Ht}|n\rangle = \frac{1}{\omega\sqrt{1-\frac{4J^2}{\omega^2}}} \tag{6.3}$$

[①] It is common to consider the uniform box distribution $W_i \in [-W/2, W/2]$, likely because is one dimension this rules out the possibility that the long distance physics is being dominated by extremely rare large deviations in the $W_n$ which would effectively decouple different parts of the system. However this distribution has other pathological properties [232]. Since it established that the course grained properties are not particularly sensitive to the details of the distribution chosen, we will abandon it later.

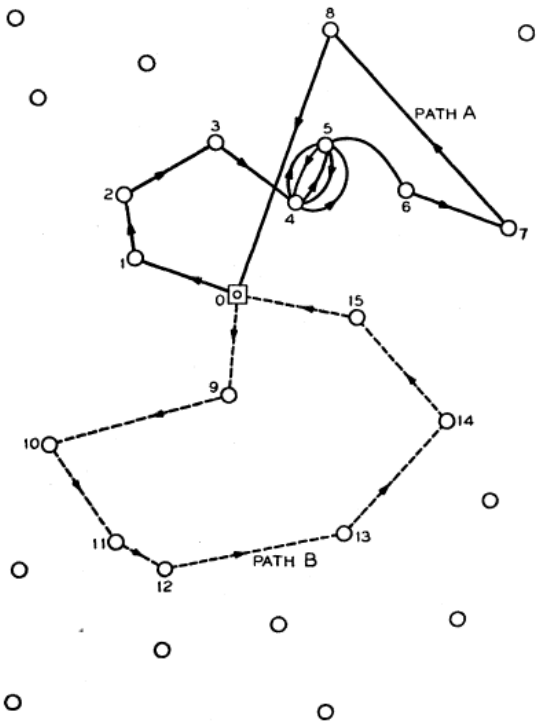


Figure 6.1: *Two paths A and B which appear as terms in the locator expansion*: The locator expansion expands perturbatively about stationary particles by summing the contributions from excursions away from a fixed initial and final site, labelled 0. Paths may visit the same site many times. Indeed where there are resonances, such contributions may be large. This case is shown on path $A$. In the localized phase the locator expansion converges. Figure from ref [66]

similarly the non-interacting Greens function $G_0$ is found by taking $J \to 0$. The decaying nature of the return amplitude is signalled by the appearance of an imaginary part of $G$ for $J > 0$. Using $G$ we can calculate the self energy $\Sigma_n$ defined via $G = G_0 + G_0 \Sigma G$.

We now interpret the meaning of the quantity $\Sigma_n$. Loosely speaking the real and imaginary components of $\Sigma_n$ inherit their meanings from $G$: the real part of $\Sigma_n$ originate in the oscillatory part of $G_{nn}(t)$, whilst the finite imaginary part of $\Sigma_n$ is synonymous with a decaying Greens function $G_{nn}(t)$, and hence a decaying probability of finding the particle on the site $n$. For the tight binding model we see that this imaginary component $\Gamma(\omega) = -\mathrm{Im}\,\Sigma_n(\omega) > 0$ for $|\omega| < 2J$. This follows from equation (6.3).

Anderson studied the object $\Sigma_n$ perturbatively in the limit of strong disorder, expanding in $J/W$, known historically as the locator[①] expansion. For sufficiently strong disorder, this perturbation series converges

$$\Sigma_n(\omega) = W_n + J^2 \sum_m \frac{1}{\omega - W_m} + J^3 \sum_{m,l} \frac{1}{\omega - W_m} \frac{1}{\omega - W_l} + \ldots, \tag{6.4}$$

where the sums $m, l \cdots$ correspond to paths of nearest neighbours starting and ending on a neighbour of $n$, as shown pictorially in Figure 6.1. Anderson showed that this series converges. This convergence has the consequence that $\Sigma_n$ is necessarily real as every term in is real. Imaginary parts can only be obtained through effects not captured by the locator expansion. Physically this indicates that an excitation initialised at $n$ remains near $n$ for all time, and hence the absence of conduction in the system. This is the localised phase.

In contrast to the conducting phase, which exists only for $W = 0$ in dimensions $D \leq 2$, the quasiparticle decay rate $\Gamma(\omega) = -\mathrm{Im}\Sigma_n(\omega)$ is then found to have characteristically different

[①]By analogy with the propagator which is obtained by constructing an analogous object in the momentum basis.

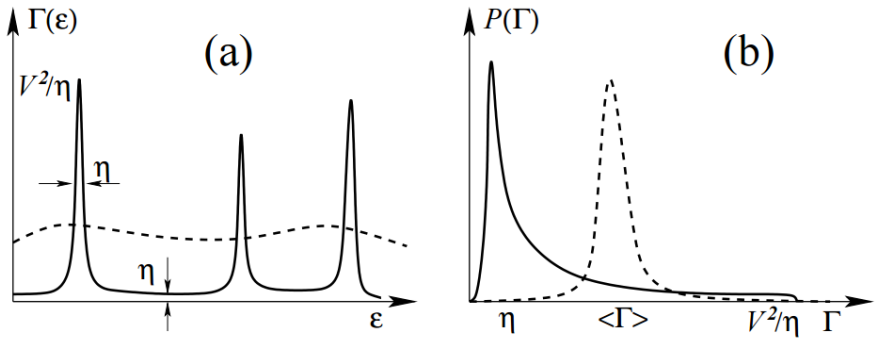


Figure 6.2: *The quasi-particle decay rate* $\Gamma(\omega) = -\mathrm{Im}\Sigma_n(\omega)$: (a) The behaviour of $\Gamma(\omega)$ for localized (solid) and delocalized (dashed) systems. $\eta$ is the infinitesimal in equation (6.3). For de-localised systems the pure point spectra of oscillations is smeared out by the dissipative parameter $\eta$ and gains an imaginary component. This disappears almost everywhere as $\eta \to 0$. For the delocalized system a finite $\Gamma(\omega)$ persists as $\eta \to 0$. (b) The distribution of values of $\Gamma$ for localized (solid) and delocalized (dashed) systems. In the localised phase $\Gamma \sim \eta$ almost everywhere whereas in the delocalized phase it is distributed around a finite value. Figure from ref [220].

behaviours in the two phases. If we leave the limit $\eta \to 0$ untaken until the last step of the calculation (to see a distinction between these two phases it is important the the mean level spacing $\delta\bar{E} < \eta$), we find that

$$\lim_{\eta\to 0}\lim_{L\to\infty} P(\Gamma > 0) = \begin{cases} 0 & \text{for localised phase} \\ \text{finite} & \text{for delocalised phase} \end{cases} \tag{6.5}$$

This behaviour is shown in Figure 6.2.

### 6.1.2 Phenomenology of Anderson localization

- **Zero DC conductivity at** $T = 0$: As discussed the convergence of the locator expansion is itself evidence of the onset of zero conductivity.

  Owing to the difficulty of observing this we note that a signature of this behaviour persists at finite coupling to an ergodic system. When thermal fluctuations are permitted by an external source (such as lattice modes) we find the re-emergence of finite conductivity at finite temperature. This conductivity has a characteristic $\sigma \sim \exp\left(-E_0/T\right)^{\nu}$ with $\nu = 4$ [233, 234]. The process by which this occurs is known as Mott variable range hopping. This form is found by trading off the exponentially small tunnelling of the localized phase with the increasing numbers of states to tunnel to at longer range. This form is distinct from a band-gap-insulator for which $\nu = 1$ recovers the Boltzmann factor. The inclusion of weak coulomb repulsion in this changes the scaling to $\nu = 2$ [235].

- **Non thermalizing**: Without the ability to conduct, the system is unable to thermalize under its own dynamics. The only mode by which relaxation of any kind may proceed is via coupling to an external environment as discussed previously.

- **Localization length**: How do we reconcile the picture that the system does not conduct particles with the existence of a hopping term in the Hamiltonian that acts to translate the particles? This is resolved once we understand the structure of the eigenstates. We first consider the trivial limits: in the weak disorder limit of $W/J \to 0$ the eigenstates are $|k\rangle$ states, which are equally delocalized over all sites, whereas in the strong disorder limit of $W/J \to \infty$ the eigenstates are the site-localised basis states $|i\rangle$ (with probability 1). At intermediate values within the localized phase the eigenstates interpolate between these

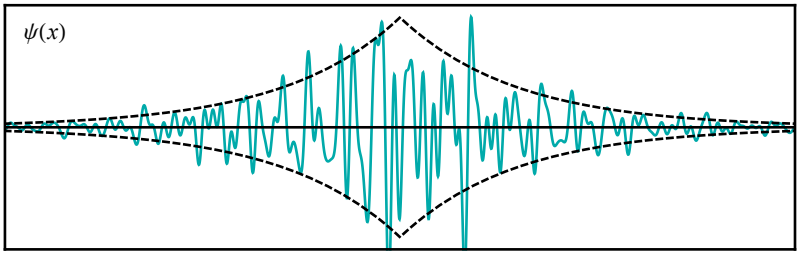


(a)

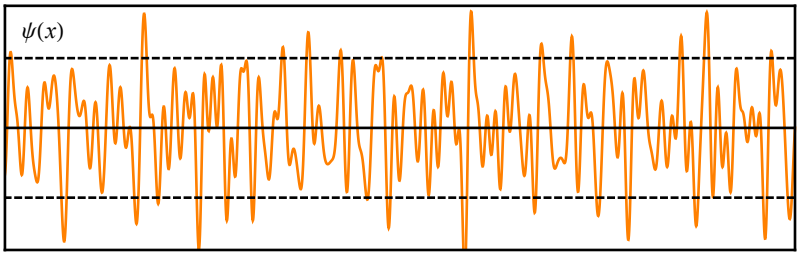


(b)

Figure 6.3: *(a) localized and (b) extended single particle eigenstates in A one-dimensional disordered medium*: The localized states have an envelope which is exponentially decaying away from the localization centre.

limits: each eigenstate $|\psi_n\rangle$ is found to be exponentially localized around the site $n$, thus $|\langle m|\psi_n\rangle| \sim \mathrm{e}^{-|n-m|/\xi_n}$. This situation is depicted in Figure 6.3. From comparison with the locator expansion of equation 6.4 we can identify that typically $1/\xi_n \sim 1/\xi \sim |\log(W/J)|$.[①] We find that quantum fluctuations generate by the hopping term allow the particles to move, but they will only travel a finite distance $\sim \xi$ even over an infinite amount of time.

This memory of its initial position is an interference effect, the disorder causes interference to always become destructive at large distances (hence the convergence of the locator expansion in equation (6.4)).

- **Eigenstates are close to the lattice basis**: The exponentially decaying spatial structure of the eigenstates allows for a meaningful one-to-one identification between eigenstates and the lattice basis states that correspond to their localization centres. It is in this sense that the bases of lattice sites and eigenstates are close to each other. This notion can by formalised be considering the inverse participation ratio

$$I = \left\langle \frac{1}{\sum_n p_{n|\psi}^2} \right\rangle = \left\langle \frac{1}{\sum_n |\langle\psi|n\rangle|^4} \right\rangle \tag{6.6}$$

where the average $\langle\cdot\rangle$ is over eigenstates $|\psi\rangle$ and disorder realisations $W_i$. For a system of $N$ lattice sites in $d$-dimensions in the extremal case of perfect localization $\sum_n |\langle\psi|n\rangle|^4 = 1^4 + 0^4 + 0^4 + \ldots$ yielding $I = 1$, whereas for a disorder free conductor $\sum_n |\langle\psi|n\rangle|^4 = N^{-2} + N^{-2} + \ldots$ and we find $I \sim N = L^d$. Generally we find that $I \sim L^d$ for ergodic states, $I \sim L^0$ for localized states, whilst $I$ exhibits anomalous scaling with an intermediate exponent at the critical point [237].

- **Local integrals of motion**: A point that is trivial to make for single particle localized systems, but which will prove much more insightful when we consider many body systems is the existence of an extensive set of local integrals of motion $\tau_i$. These are given by the eigenstate projectors $\tau_i = |\psi_i\rangle\langle\psi_i|$ where $|\psi_i\rangle$ is the eigenstate localized around the $i$th

[①] Though we note there are large fluctuations in the individual $\xi_n$ [236].

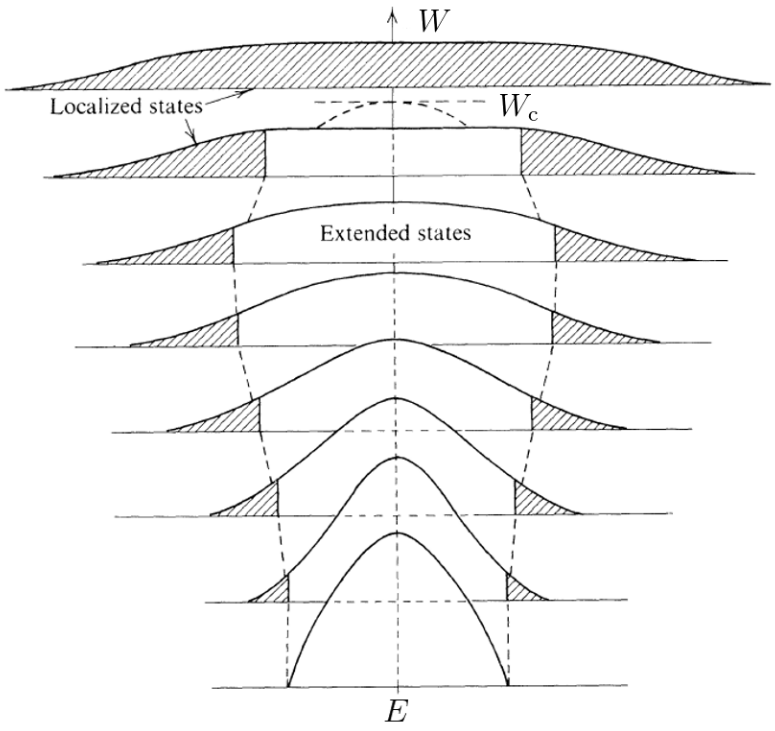


Figure 6.4: *Mobility edge in single particle localization*: Vertically displaced plots of the density of states $\rho(E)$ versus energy $E$ for different strengths of disorder $W$. These are overlaid on a sketch of the conducting region of the $E, W$ plane (dashed line). The solid white and hatched regions of $\rho$ correspond to extended and localized states. Above a critical disorder $W_c$ there are no longer any extended states. The distinct character of states in these regions is shown in Figure 6.3. Figure from ref [238]

lattice site. These operators are local in that measurement of their values up to arbitrary finite accuracy can be made by interrogating only a finite region of the system.

- **Mobility edge**: In dimensions $d \leq 2$ the single particle system localizes for arbitrarily weak disorder (as is argued by the famous scaling argument [217]) however for $d > 2$ a critical disorder is required, and in the vicinity of the transition it is possible for a system to support both localized and delocalized (i.e. extended) eigenstates at different energies. This is depicted in Figure 6.4. The energy that demarcates the boundary of a localized and a delocalized region of the spectrum is known as the mobility edge. The non-coexistence of localized and extended states at the same energy follows from the instability of this situation to perturbation: two states of the same energy will hybridise under an arbitrarily small perturbation, if *either* of them is extended so will be *both* of the states resulting from hybridisation.

- **Spectral signatures**: In the $W/J \to 0$ limit the spectrum of $H$ becomes dense, and the density of states becomes a continuous function. In the limit of $W/J \to \infty$ it corresponds to the pure point distribution of the $W_i$, and the density of states is not continuous unless smoothed. This distinction between pure point and continuous spectra is a feature of the localization-delocalization transition.

  A signature of this change in the spectral properties of the system at the localization transition is found in the level statistics which transition from Wigner-Dyson to Poissonian. This is captured by random matrix statistics, such the level spacing ratio, which we will now discuss in more detail.

### 6.1.3 Random matrix theory

Here we discuss Random Matrix theory in the context of localization. Though studied in mathematics by Hsu, Wishart, and others, the understanding of the physical significance of random matrix theory began with an experimental observation: Porter and Thomas [239] noted that nuclear resonance widths $\gamma$ were distributed according to

$$p(\gamma) \sim \gamma^{-1/2} \mathrm{e}^{-\gamma/2\bar{\gamma}}. \tag{6.7}$$

This quantity has a simple interpretation: the scattering channels $|j\rangle$ define a basis, as do the eigenstates $|E_i\rangle$ of the nuclear Hamiltonian $H$. Let $U_{ij}$ be the unitary that maps between these bases, diagonalising $H$. The strength of the resonance then goes as $\gamma \sim |U_{ij}|^2$. The distribution $p(\gamma)$ can then be calculated from the distribution of $|U_{ij}|^2$. For a suitable class of random matrices one finds equation (6.7).

#### Wigner's surmise

Approaching the blackboard at Oak Ridge, Wigner bemoaned the failure of the theoreticians to have predicted the form of $p(\gamma)$: "All of us theoreticians should feel a little embarrassed. We know the theoretical interpretation of the reduced width $\gamma$: it is the value of a wave function at the boundary, and we should have been able to guess what the distribution of such a quantity is. However, none of us were courageous enough to do that... Perhaps I am now too courageous when I try to guess the distribution of the distances between successive levels."[①] Far from too courageous, Wigner, joined by Dyson, went on to develop much of the theory for applying random matrix theory to the statistical properties of heavy nuclei [240–245], a comprehensive resource on the topic can be found in ref [246].

In the prediction that immediately followed his lament Wigner used the statistical properties of random matrices in the same way as the result of Porter and Thomas. He predicted that the spacings of consecutive levels $s = E_{i+1} - E_i$ would be distributed according to

$$p(x) \approx \frac{\pi x}{2} \mathrm{e}^{-\pi x^2/4}. \tag{6.8}$$

where $x = s/\langle s \rangle$.

#### Delocalised level spacing distribution

Wigner's prediction can be reached exactly for $2 \times 2$ Hamiltonians. We begin by assuming first assume that $H$ is drawn from the Gaussian Orthogonal ensemble (GOE), for $2 \times 2$ matrices this corresponds to the distribution

$$p(H) \sim \exp\left( -\tfrac{1}{2} \mathrm{tr}\left[ H^2 \right] \right) \tag{6.9}$$

in which each element is an iid Gaussian variable. A comparison between the distribution $p(x)$ and data collected on the level spacings of atomic nuclei, as Wigner was considering when he made his prediction, is shown in Figure 6.5. To find the distribution of level spacing we then make the change of coordinates using

$$\begin{pmatrix} H_{11} & H_{12} \\ H_{21} & H_{22} \end{pmatrix} = \frac{1}{2} \begin{pmatrix} \cos\theta & \sin\theta \\ -\sin\theta & \cos\theta \end{pmatrix} \begin{pmatrix} \tau + s & 0 \\ 0 & \tau - s \end{pmatrix} \begin{pmatrix} \cos\theta & -\sin\theta \\ \sin\theta & \cos\theta \end{pmatrix} \tag{6.10}$$

[①] This is recorded by Carlo Beenakker in his lectures on Random Matrices. Beenakker adds that Wigner's lament was at the conference "Neutron Physics by Time-of-Flight", held at the Oak Ridge National Laboratory in 1957 and immediately preceded his surmise.

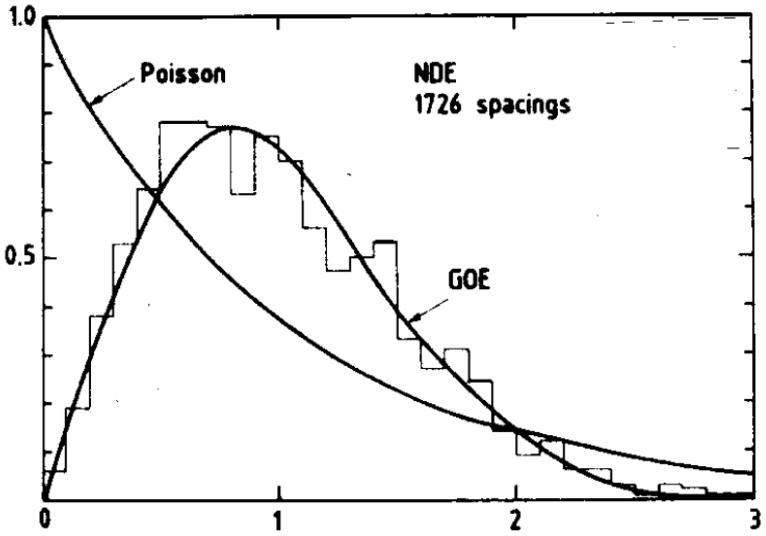


Figure 6.5: *Wigner's surmise and nuclear level spacings:* Level spacing distribution for a 'nuclear data ensemble' of 1726 spacings compared to the GOE prediction and the uncorrelated Poisson distribution. Figure from ref [247]

where $\tau$ is the trace, $s$ the level spacing, and $\mathrm{tr}\left[H^2\right] = (\tau^2 + s^2)/2$ and the Jacobian of the transformation is given by

$$\frac{\partial(H_{11}, H_{12}, H_{22})}{\partial(\tau, s, \theta)} = \frac{s}{2}. \tag{6.11}$$

From this we find

$$p(\tau, s, \theta) = p(H)\frac{\partial(H_{11}, H_{12}, H_{22})}{\partial(\tau, s, \theta)} \sim s\mathrm{e}^{-(\tau^2+s^2)/4}. \tag{6.12}$$

from which integrating over $\tau$ and $\theta$, normalising, and changing coordinates to $x = s/\langle s \rangle$ one quickly obtains equation 6.8.

Wingers surmise constituted the prediction that the statistics of atomic level spacings would be captured by a model in which the Hamiltonian matrix elements can be treated as Gaussian iid random variables. Since the $2 \times 2$ result remains an accurate distribution for much larger matrices, this can be used in this broader scope.

**Localised level spacing distribution**

The GOE prediction captures the spectral statistics of the delocalized phase. We now consider the equivalent property of the localized phase. In the delocalized phase eigenstates are extended, and so a local perturbation will couple strongly to all of them. The off diagonal elements generated will be typically large, and the level repulsion is induced. In the localized phase however, a local perturbation will couple strongly only to those eigenstates with physically close localization centres. However, nearby energy levels do not typically correspond to states with physically close localization centres, but are localized at arbitrary points in the lattice. The off diagonal elements generated will thus typically be exponentially small in the distance between these localization centres. Hence level repulsion is exponentially small in the typical distance between lattice sites. Hence introducing local perturbations in the localised phase does not result in level repulsion.

At zero-hopping the levels spacings are captured by a Poisson process which considers the energy of each level to be independent of the energies of all other levels. If we consider introducing hopping to the system, through a series of local perturbations, in the localised phase this induces only weak level repulsion and we find that the Poisson statistics survive the introduction of hopping.

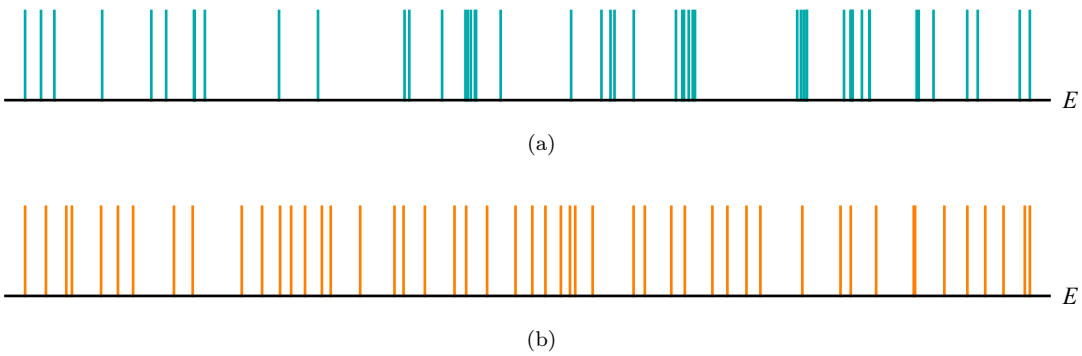


Figure 6.6: *Sample of 50 levels from (a) Poissonian and (b) GOE spectra* corresponding to localized and de-localized systems respectively. The energy levels repel for the de-localized system and hence are more evenly distributed.

Thus in the localized phase we find the level statistics are captured by a Poissonian spacing distribution

$$p(x) = \mathrm{e}^{-x}. \tag{6.13}$$

This allows the statistics of the eigen-energy spacings to be used to determine what phase the Hamiltonian equation (6.1) is in: on the delocalized side it will be GOE, and on the localized side Poissonian. The transition from localized to delocalized levels statistics can be seen in Figure 1.6.

### Further developments in random matrix theory

In numerical experiments one finds that the parameter $x = s/\langle s\rangle = (E_{i+1} - E_i)/\langle E_{i+1} - E_i\rangle$, where each spacing is normalised to the ensemble mean spacing, turns out to provide relatively poor statistics. This is due to the difficulty of accurately estimating $\langle s\rangle$ (the problem of 'unfolding') and the significant variation in typical values of $s$ with position in the spectrum.

A slightly better solution has been to use an estimate for $\langle s\rangle$ local to the position in the spectrum. The limit of a maximally local estimate is attained by considering only the adjacent spacing [222]. This gives the levels spacing ratio $r = (E_{i+1} - E_i)/(E_i - E_{i-1})$. $r$ however is unbounded from above, the problem of these arbitrarily large values is handled by always putting the smaller of the two intervals in the numerator, thus we consider the statistic.

$$\bar{r} = \min\left(r, \frac{1}{r}\right) = \frac{\min(|E_{i+1} - E_i|, |E_i - E_{i-1}|)}{\max(|E_{i+1} - E_i|, |E_i - E_{i-1}|)}. \tag{6.14}$$

This has becomes a frequently used statistic in the study of disordered systems. Useful properties of this statistic for different ensembles are summarised in Table 6.1.

### Universality and random matrix theory

It might seem surprising that the level statistics of the Anderson model (equation (6.1)) in the delocalized phase are captured by GOE statistics. The $N$-site Anderson model Hamiltonian is definitely not a GOE matrix. Only a vanishingly small fraction $\sim 1/N$ of the elements of $H$ are random, or indeed non-zero at all. This becomes even more severe when we consider many-body systems, where an $N$-site model with single site disorder has a Hamiltonian matrix of size $2^N \times 2^N$, but only $N$ random variables, and a similarly *exponentially* small fraction of non-zero elements.

Similarly, Wigner's original motivation for looking at this, the properties of nuclear resonances, are not systems described by random matrices. The fact that a statistical approach is able to capture the properties of these systems is an example of universality. This is the idea that the statistical properties of complex physical systems fall into a small number of universal classes with

| Ensemble | $p(H)$ | $p(x)$ | $p(\bar{r})$ | $\langle\bar{r}\rangle$ (calculated) | $\langle\bar{r}\rangle$ (numerical) |
|---|---|---|---|---|---|
| GOE ($H \in \mathbb{R}^{n\times n}$) | $\frac{1}{Z_{\mathrm{GOE}}}\mathrm{e}^{-\frac{n}{4}\mathrm{tr}[H^2]}$ | $\frac{\pi}{2}x\mathrm{e}^{-\pi x^2/4}$ | $\frac{3^3}{2^2}\frac{(\bar{r}^2+\bar{r})}{(1+\bar{r}+\bar{r}^2)^{5/2}}$ | $4-2\sqrt{3}=0.5359\ldots$ | 0.5307(1) |
| GUE ($H \in \mathbb{C}^{n\times n}$) | $\frac{1}{Z_{\mathrm{GUE}}}\mathrm{e}^{-\frac{n}{2}\mathrm{tr}[H^2]}$ | $\frac{2^5}{\pi^2}x^2\mathrm{e}^{-4x^2/\pi}$ | $\frac{3^4\sqrt{3}}{2\pi}\frac{(\bar{r}^2+\bar{r})^2}{(1+\bar{r}+\bar{r}^2)^4}$ | $\frac{2\sqrt{3}}{\pi}-\frac{1}{2}=0.6027\ldots$ | 0.5996(1) |
| GSE ($H \in \mathbb{H}^{n\times n}$) | $\frac{1}{Z_{\mathrm{GSE}}}\mathrm{e}^{-n\mathrm{tr}[H^2]}$ | $\frac{2^{18}}{3^6\pi^3}x^4\mathrm{e}^{-2^6x^2/3^2\pi}$ | $\frac{3^6\sqrt{3}}{2\pi}\frac{(\bar{r}^2+\bar{r})^4}{(1+\bar{r}+\bar{r}^2)^7}$ | $\frac{2^5}{5\pi\sqrt{3}}-\frac{1}{2}=0.6762\ldots$ | 0.6744(1) |
| Poisson ($H \in \mathbb{R}^n$) | iid diagonal elements | $\mathrm{e}^{-x}$ | $\frac{2}{(1+\bar{r})^2}$ | $2\log 2-1=0.3863\ldots$ | – |

Table 6.1: The statistical properties of the Gaussian Matrix Ensembles GOE, GUE, GSE contrasted with the iid statistics of a Poissonian level spacing. The distribution of level spacing ratios $p(\bar{r})$ is calculated assuming that two neighbouring level spacings constitute iid variables drawn from a distribution given by the relevant Wigner surmise $p(x)$. This is compared with numerical estimates from ref [248] indicating a high degree of accuracy of the Wigner surmise. Note in particular that for the ergodic phases GOE, GUE, GSE that, for $\bar{r}\approx 0$, $p(\bar{r})\sim\bar{r}^\beta$ with $\beta=1,2,4$, indicating the repulsion of levels, whereas for Poisson statistics $\bar{r}=0$ maximises $p(\bar{r})$. The distributions $p(\bar{r})$ all have the necessary symmetry $p(\bar{r})\mathrm{d}r = p(\frac{1}{\bar{r}})\mathrm{d}\left(\frac{1}{\bar{r}}\right)$.

similar behaviour.

To make this easier to swallow we consider a more familiar example: in statistics we are very familiar with the idea that the distribution of a sample mean will tend towards a Gaussian for a wide range of starting distributions. This is the central limit theorem, and in the same spirit we find that for very large matrices, certain statistics of their spectra fall into universal categories.

We do not believe that the reason Wigner's surmise captures the level statistics of the delocalized Anderson model, or atomic nuclear spectra is because these matrices are random GOE matrices, or even because they are well approximated by GOE matrices (they are not). We believe it is rather because they fall into the same universality class of spectral behaviour.

### 6.1.4 Thermalization in closed many body quantum systems

In this section we will more completely develop notions of thermalization in closed quantum systems. By looking for the possibility of breakdown in this phenomenon, we will also be able to substantiate our notion of localization in many body quantum systems. We will focus on parts of this topic relevant for our investigation, more complete discussion can be found in refs [65, 249].

In the case of the single particle problem, our notion of relaxation was a simple one—we wanted the density profile of our initial state to become smeared out over the system after time evolution for a sufficiently long interval. We found that disorder can cause violations of this behaviour, and induce the localization of non-interacting particles. This caused all particles to be restricted to a region of extent $\sim \xi$ around their initial position. This characteristic length scale is the localization length. We argued that this precludes the possibility of thermalization, since any initial particle density profile will be unable to relax to that predicted by equilibrium statistical mechanics, Instead there is infinite time memory of the initial state.

However in considering a closed quantum system, we are not obviously within the purview of much of the canon of statistical mechanics, and so it might be wise to check that this expectation of relaxation was a valid one. Indeed one might have good reason to be suspicious: we know that the dynamics of a closed quantum system are described by the Schrödinger equation $\mathrm{i}\partial_t |\psi\rangle = H |\psi\rangle$ which is not capable of evolving from a non-thermal state to the thermal state

$$\rho_{\mathrm{th}} = \frac{1}{Z} \mathrm{e}^{-\beta(H - \mu N \cdots)}, \tag{6.15}$$

predicted by statistical mechanics. In $\rho_{\mathrm{th}}$ there is one Lagrange multiplier $\beta, \mu, \ldots$ for each global conservation law. Indeed the von-Neumann entropy is a conserved quantity of the Schrödinger equation. It might seem that the unitary dynamics of the closed system preserve too much information for us to have any notion of thermalization at all in closed quantum systems.

However, as discussed in Section 1.5 this can be resolved by considering only physically accessible measurements. In general it is not possible to implement highly non local measurements. An experimenter is restricted to measuring physical observables that consist of correlation functions over small finite numbers of sites. If we instead investigate the long time behaviour of only these such observables $O$ we can ask if

$$\langle O(t) \rangle = \langle \psi(t) | O | \psi(t) \rangle \xrightarrow{t \to \infty} \mathrm{tr}\left[\rho_{\mathrm{th}} O\right]. \tag{6.16}$$

This, it turns out, is possible, and is believed to be satisfied for many of the many-body systems typically studied in quantum mechanics. This notion of thermalization is contingent only on the much more manageable requirement that we see the thermalization of the reduced density matrix

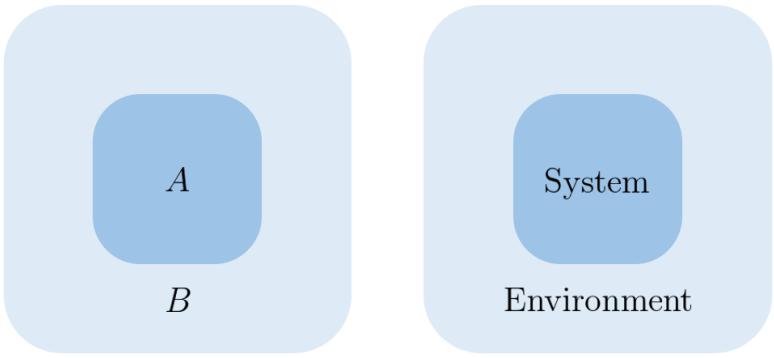


Figure 6.7: *Quantum statistical mechanics of closed systems*: to understand the notion of thermalization in closed quantum systems we consider a finite subsystem $A$ whose complement $B$ is thermodynamically large. This is closely related to the very similar set up used in the study of open quantum systems, the only difference is that our choice of $A$ is not fixed.

of any finite subsystem $A$, found by tracing out its much larger complement $B$[①]

$$\mathrm{tr}_B \left[ |\psi(t)\rangle \langle \psi(t)| \right] \xrightarrow{t\to\infty} \mathrm{tr}_B \left[ \rho_{\mathrm{th}} \right]. \tag{6.17}$$

As shown in Figure 6.7 this is essentially the normal picture of open quantum systems, in which instead of $A$ and $B$ we simply have 'system' and 'environment'. The difference here is that $A$ need not be defined at the outset, and we require that *any* choice of finite subsystem $A$ thermalizes. For equation (6.17) to hold for any initial state it must hold for eigenstates. Since these have no dynamics, their form at $t \to \infty$ is trivial. The requirement becomes

$$\mathrm{tr}_B \left[ |E\rangle \langle E| \right] = \mathrm{tr}_B \left[ \rho_{\mathrm{th}} \right]. \tag{6.18}$$

Equation (6.18) is a statement of eigenstate thermalization hypothesis (ETH) [61–64], and with some weak assumptions the equation (6.16) follow if this is satisfied. When first encountered many find this a surprising statement: it requires that for a system to thermalize, there must exist a strict relationship between on one hand, the thermal state $\rho_{\mathrm{th}}$, something we acquire from the postulates of statistical mechanics with limited reference to linear algebra and quantum mechanics, and on the other hand the eigenstates of the arbitrary local hermitian hamiltonian $H$, which are a mathematical construct, which know nothing of physics whatsoever, and do not correspond to anything that can be prepared or observed in a laboratory. This might leave one somewhat surprised at the relation (6.18). From a different perspective, it also seems an entirely reasonable, even tautological, requirement that in a stable static solution to the quantum dynamical equations, each region must be in equilibrium with its surroundings. After all, a stable static solution of the equations of motion is the definition of equilibrium.

### Consequences of ETH

Since the statement of ETH in equation (6.18) constitutes are relation between mathematical object, it has concrete consequences which can be verified in numerical experiments:

- **Volume law entanglement in the mid-spectrum**: A concrete consequence of ETH is that, due to equation (6.18), the single eigenstate entanglement entropy $\mathcal{E}_{AB}$ between any finite subsystem $A$ and the remainder of the system $B$ must be equal to the equilibrium

[①]Note that this is not quite the same as the usual result of open systems using the Master equation: in this case $\rho_A$ is found to relax to a thermal state of $H_A = \mathrm{tr}_B [H]$. The equivalence of this to equation 6.17 is only well approximated if the coupling between $A$ and $B$ is very weak.

thermal entropy $S_A$ of $A$. Since the thermal entropy obeys volume law scaling $S_A \sim L^d$, this implies that the eigenstates of a thermalizing system have volume law entanglement.

This is true in the mid-spectrum, but close to the ground state the eigenstates have special properties, as discussed in Section 1.2.2.

- **Diagonal elements of local operators are continuous functions of energy**: A further consequence regards the matrix elements of operators in the eigenbasis of the system. Taking equation (6.18) and looking at a local expectation value on $A$ we find

$$\langle E_\alpha | O | E_\alpha \rangle = \mathrm{tr}\left[O\rho_{\mathrm{th}}\right]. \tag{6.19}$$

The left-hand side is a function of $|E_\alpha\rangle$ whereas the right-hand side is a function only of thermodynamic quantities such as the energy density in the system $E_\alpha$. For this to be generally true we see that the diagonal matrix elements in the eigenbasis $O_{\alpha\alpha} = \langle E_\alpha | O | E_\alpha \rangle$ must be a continuous function of the energy $O_{\alpha\alpha} \sim O(E_\alpha)$.[①]

ETH however is a hypothesis, and may not be found to hold for all eigenstates of certain systems. There is strong evidence that in thermalizing systems ETH holds for *almost all* eigenstates, and that this is sufficient to recover thermalizing behaviour [65, 250–253], and some evidence for the stronger statement that *all* eigenstates thermalise [254]. Intriguingly ETH has been found to be *violated* for macroscopically many, or indeed *all* eigenstates, in a novel class of many body localized (MBL) systems.

### 6.1.5 Violations of ETH and many-body localization

Mott's result of finite conductivity in the presence of a heat bath (in electronic systems this role is due to interactions with phonons, i.e. lattice excitations) leads us to consider whether particle-particle interactions generally play this role: are interacting particles always able to act as their own heat bath? If yes, we would expect the localized phase to be unstable to a perturbation which introduces interactions, in favour of a conducting phase consistent with ETH. If not this heralds the existence of a many-body localized phase.

Early investigations into this problem of whether an Anderson-localized system would remain localized with the introduction of interactions between particles indicated the stability of the phase to leading order in perturbation theory [255, 256]. However these insights offered little indication of whether higher order or non-perturbative effects left this picture intact. The seminal work of Basko, Aleiner and Altshuler (BAA) [219, 220] established the persistence of the many-body localized phase to all orders in perturbation theory, at sufficiently low temperatures.

Since this progress, and with the realisation that there is a natural language for the problem which makes it much more amenable to numerical investigation [257, 258], a significant amount of understanding has been gained via numerical studies [222–226, 259–264], (see also ref [65] and references therein) and there is now a rigorous proof[②] of the existence of the MBL phase [221].

### 6.1.6 The phenomenology of MBL and a zoo of numerical statistics

In MBL we are considering many body dynamics, for concreteness we assume we are dealing with a lattice of spin-1/2 degrees of freedom in the presence of on-site disorder. Unlike in Anderson localization, where our Hilbert space was a direct sum of states corresponding to lattice sites, in

[①] Here we have used the canonical ensemble, sometimes the micro-canonical ensemble is used, the statement is equivalent provided $A$ is a finite subsystem of an infinite system.

[②] Modulo the assumption of 'limited level attraction' between eigenstate energies, violations of which are not expected, particularly given that they generically repel.

| **Thermal phase** | **Anderson localized** | **Many-body localized** |
|---|---|---|
| Memory of initial conditions 'hidden' in global operators at long times | Some memory of local initial conditions preserved in local observables at long times | Some memory of local initial conditions preserved in local observables at long times. |
| ETH true | ETH false | ETH false |
| May have non-zero DC conductivity | Zero DC conductivity | Zero DC conductivity |
| Continuous local spectrum | Discrete local spectrum | Discrete local spectrum |
| Eigenstates with volume-law entanglement | Eigenstates with area-law entanglement | Eigenstates with area-law entanglement |
| Power-law spreading of entanglement from non-entangled initial condition | No spreading of entanglement from non-entangled initial condition | Logarithmic spreading of entanglement |
| Dephasing and dissipation | No dephasing, no dissipation | Dephasing but no dissipation |

Table 6.2: *A comparison of the MBL and single particle localized phases*: A list of some of the more strongly established characteristic properties of the many-body-localized phase, contrasted with equivalent properties of the thermal and the single-particle-localized phases. Table from ref [65].

the many body case our Hilbert space is a direct product of single site sub-spaces. As previously discussed in Section 1.2, this entails an exponential growth of the Hilbert space with the system size giving a far greater possibility for resonances. This enhanced possibility for resonances leads to a less robust phase of matter, and some characteristic differences to the single particle localised phase. A comparison of the difference of MBL and Anderson localization are given in table 6.2. Here we consider some of the properties of MBL in more detail.

- **Spectral statistics:** The MBL phase falls in the same universal class of spectral behaviour as the Anderson localized phase. As a result we see Poissonian spectral statistics. This is captured by the ensemble averaged level spacing ratio. $\bar{r}$ [222, 226, 265], as per Section 6.1.3.
- **Zero DC conductivity**: As in the single particle case, the MBL phase is characterised by zero DC conductivity. Thus estimation of such transport coefficients [266] can be used as a diagnostic tool. The corresponding AC conductivity is estimated to be power law $\sigma(\omega) \sim \omega^{\alpha}$ [267].
- **Perturbation theory converges**: Similar to Anderson's result in the single particle case, the treatment by BAA bounded the spread of a local perturbation [219, 220]. In this spirit, the logarithm of the first order correction due to a local perturbation $O$ has been proposed as an indicator of localization $\mathcal{G} = \left\langle \log \frac{\langle E_\alpha | O | E_{\alpha+1} \rangle}{E_\alpha - E_{\alpha+1}} \right\rangle_\alpha$ [268]. For localizing behaviour this quantity falls with increasing system size, and for ergodic behaviour it grows with system size.
- **Violation of ETH**: As discussed previously ETH requires that, for a system in a global eigenstate, the reduced density matrix on a local subsystem will be a thermal state. This has the corollary that, up to some uncertainty, the eigenstate expectation value $O_\alpha = \langle E_\alpha | O | E_\alpha \rangle$ of a local operator $O$ will be a continuous function of the eigen-energy $E_\alpha$. ETH requires that the difference $\delta O_\alpha = O_\alpha - O_{\alpha-1}$ is exponentially small in the system size, whereas in the MBL phase we expect $O_\alpha$ and $O_{\alpha-1}$ to be uncorrelated, and drawn from a distribution of width set by the spectral width of $O$. In the MBL phase $\delta O_\alpha$ is anticipated to be independent of system size. This distinction allows $\langle \delta O_\alpha \rangle_\alpha$ to be used as an indicator of violations of ETH [226].

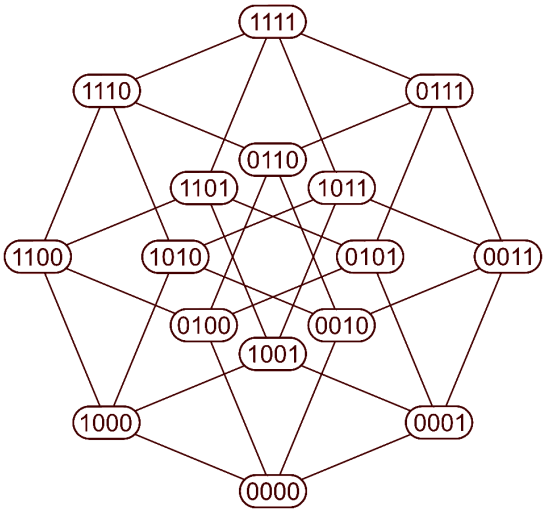


Figure 6.8: *Configuration space of a many body system:* For a system of $N$ sites there is a basis of $2^N$ classical configurations which can be labelled with bit strings or spins using a convention $1 = \uparrow$, $0 = \downarrow$. The edges correspond to configurations connected by a single spin flip. Many body localization in one dimension can be viewed as Anderson localization on the Hypercube (with correlated disorder).

- **Eigenstates are close to basis states:** The state of a many body system may be represented by a point in configuration space. In this sense Many body localization can be viewed as single particle localization on the lattice of classical configurations. For a one-dimensional system this is a hypercube as shown in Figure 6.8.[①] This allows us to identify a classical configuration, or bit-string, with the each eigenstate of the many body system. This behaviour allows the inverse participation ratio, equation (6.6), to be used as a signature of MBL [265, 269–272].

- **Extensive set of local integrals of motion (LIOM)**: As with Anderson localization the projectors onto the eigenstates are local in the configuration space Figure 6.8, however they are no longer local in real space. Refs [257, 258] noted that since the eigenstates are close to classical configuration states, and can therefore be meaningfully *labelled* with classical configurations, we can similarly define a Pauli algebra $\tau_n^i$ ('localised bit' or 'l-bit') algebra, where $n$ labels sites, and $i = 1, 2, 3$) that operates on these bit-string-labelled-eigenstates in the same way as the physical ('physical bit' or 'p-bit') Pauli algebra $\sigma_n^i$ acts on the classical basis states. The $\tau_n^i$ obey

$$[H, \tau_n^z] = 0, \tag{6.20}$$
$$\left[\tau_n^i, \tau_m^j\right] = \delta_{nm}\epsilon_{ijk}\tau_n^k \tag{6.21}$$

  The $\tau_n^z$ and their products then define a basis of all possible hermitian operators which commute with $H$. Thus writing $H$ in this basis we obtain

$$H = \sum_n J_n^{(1)}\tau_n^z + \sum_{nm} J_{nm}^{(2)}\tau_n^z\tau_m^z + \sum_{nmp} J_{nmp}^{(3)}\tau_n^z\tau_m^z\tau_p^z + \dots. \tag{6.22}$$

  Furthermore the action of $\tau_n^{\pm} = (\tau_n^x \pm \mathrm{i}\tau_n^y)/2$ on an eigenstate produces another eigenstate with the creation/destruction of local excitation. This algebra can also be resolved in the

[①] This analogy should be treated with some caution, as incorrect identification of the 'classical' configurations will lead to wildly different answers, e.g.$|\uparrow\uparrow\uparrow\cdots\rangle$ it maximally localized in the $z$-basis and maximally delocalized in the $x$-basis

physical basis by writing

$$\tau_n^i = \sum_{m,j} [T^{(1)}]^{i|j}_{n|m} \sigma^j_m + \sum_{mp,jk} [T^{(2)}]^{i|jk}_{n|mp} \sigma^j_m \sigma^k_p + \sum_{mpq,jkl} [T^{(3)}]^{i|jkl}_{n|mpq} \sigma^j_m \sigma^k_p \sigma^l_q. \tag{6.23}$$

In general a similar of Pauli operators is always possible, whether or not the system is localized, and this statement is little more that noting that an extensive set of operators that commute with the Hamiltonian provide a useful algebra for working in the diagonal basis. The key additional feature in the localized phase is that these operators are local. This in the sense that the $T^{(N)}_{n|mpq\ldots}$ and $J^{(N)}_{nmp\ldots}$ are exponentially in the length scale associated with their support (e.g.the for $J^{(3)}_{nmp}$ length $\ell = \max(|n-m|, |m-p|, |p-n|)$). The characteristic length scale of this exponential decay is $\xi$, the localization length.

Each of the $\tau^z_n$ can be identified with a lattice site which is the localization centre of the operator. This is analogous to how we identified eigenstates in the Anderson localized phase with lattice sites. As a result, the good quantum numbers represented by the bit-strings are addressable and manipulable to high precision using finite range operators. There have been analytical [273, 274] and numerical [275, 276] attempts to approximate or construct the $\tau^z_n$.

- **Area Law Entanglement of Eigenstates**: All of the eigenstates are related through the action of the local operators $\tau^{\pm}_n$. Each eigenstate consists of some number of exponentially localized excitations. From this it follows that the Area Law Entanglement, usually restricted to ground states, persists through the entire spectrum [277].

  This has various consequences

  - The transition into the MBL is heralded by a marked drop in entanglement in the mid-spectrum states from volume-law scaling (predicted by ETH) to the area-law scaling of the localized phase. The entanglement entropy across an even bipartition of the system can be used as a diagnostic tool [269, 278].
  - All eigenstates of an MBL system can be captured accurately by an tensor network ansatz. E.g., in one-dimensional systems one can use matrix product states [261, 263, 279].
  - The unitary matrix $U$ that maps between classical configurations states and eigenstates associated with the same bit-string (i.e. $U$ that diagonalises the Hamiltonian) is a finite range operator, and hence can be represented as a finite rank matrix product operator [260].
  - Correlations between distance points in an eigenstate decay exponentially with their separation [18, 19]. Which has been used as an indicator of MBL [226].

- **Logarithmic Light Cone**: Entanglement in MBL systems can be understood as generated by the dephasing of the l-bits. Since all of the l-bits are integrals of motion, their quantum numbers are preserved by evolution, and they entangle only through dephasing. By studying equation (6.22) we can see that the effective interaction between two l-bits

$$J^{\text{eff}}_{nm} = J^{(2)}_{nm} + \sum_{nmp} J^{(3)}_{nmp} \tau^z_p + \sum_{nmpq} J^{(4)}_{nmpq} \tau^z_p \tau^z_q + \ldots \tag{6.24}$$

in the MBL phase $J^{\text{eff}}_{nm} \sim \mathrm{e}^{-L/\xi}$ where $L$ is the distance from $n$ to $m$. As a result their time to entangle $t \sim 1/J^{\text{eff}}_{nm} \sim \mathrm{e}^{L/\xi}$. This is known as the logarithmic light cone $L \sim \xi \log t$ which can be more rigorously proven [280, 281] and has been observed in simulations [282]. This causes the Universally slow [259] (but unbounded [283]) growth of entanglement. The slow

growth of entanglement or slow spread of perturbations has also been used to identify MBL behaviour [272, 284]

- **Infinite memory of initial conditions**: The LIOM $\tau_i^z$ define a set of local good quantum numbers. The persistence of correlations at finite [269,271,285–288] and infinite [272,275,285] time correlations have been studied to evidence this behaviour.

- **Possible absence of mobility edges**: Contrary to the case in single particle systems, it is argued that MBL systems will not have mobility edges. The toy argument is that fluctuations in local energy density in an eigenstate will result in regions that are hotter than the average energy density, hence the local behaviour can be that of a much hotter region. This would allow any states below a mobility edge to behave locally like states above the edge by 'borrowing' energy from their surroundings. These local ergodic bubbles would then not be restricted by localized behaviour and would thermalize the system [270].

## 6.2 Numerical construction of the local integrals of Motion

In this section we develop a tool for numerically constructing the LIOM of the MBL phase. We use this in part of the analysis of an interesting model presented in the next section. During the course of developing this method, other authors arrived at this independently [276].

The local integrals of motion are at the heart of the MBL phase, and given access to these object one can in principle determine a great deal about the system. The construction of the LIOM is not a trivial task. The most obvious approaches fail

- **Exact Diagonalisation**: Given the exact eigenstates $|E\rangle$ of the many body Hamiltonian any equal partition of these into two sets $a$ and $b$ defines a Pauli-matrix

$$\tau_n^z = \sum_{E\in a} |E\rangle\langle E| - \sum_{E\in b} |E\rangle\langle E| . \tag{6.25}$$

  A system of spin-1/2 on a lattice of size $N$ has with has $2^N$ eigenstates. There are thus $\binom{2^N}{2^{N-1}}/2$ choices $\tau_i^z$ in equation (6.25). To define a second $\tau_j^z$ satisfying the necessary condition there are $\binom{2^{N-1}}{2^{N-2}}^2/2$ remaining choices. To define all $N$ such local integrals of motion, there are in total

$$M = \frac{1}{N!2^N}\binom{2^N}{2^{N-1}}\binom{2^{N-1}}{2^{N-2}}^2\binom{2^{N-2}}{2^{N-3}}^4\binom{2^{N-3}}{2^{N-4}}^8\cdots\binom{4}{2}^{2^{N-2}}\binom{2}{1}^{2^{N-1}} = \frac{2^N!}{N!2^N} \tag{6.26}$$

  possible independent choices. This is an extremely large number. Even for a modest system of 5 sites this number is $M > 10^{33}$, by 10 sites it is $M > 10^{2633}$. Only one of these configurations is expected to be maximally local, all others will in general be highly non-local, thus they all $M$ combinations must be exhaustively searched making this method infeasible.

- **Adiabatic continuation/perturbation theory**: Is it possible to construct the LIOM perturbatively around the strong disorder limit by analogy to the Anderson locator expansion? In this picture we imagine a hamiltonian of the form $H = H_0 + JH_1$ where $H_0 = \sum_i W_i\sigma_i^z$ consists of only on-site disorder, and $H_1$ consists of an (often translationally invariant) interaction term. If we expand $\tau_n^z$ perturbatively we find

$$\tau_i^z = +\sum_{n=}^{\infty}\left(\frac{J}{W}\right)^n \tau_i^{(n),z}. \tag{6.27}$$

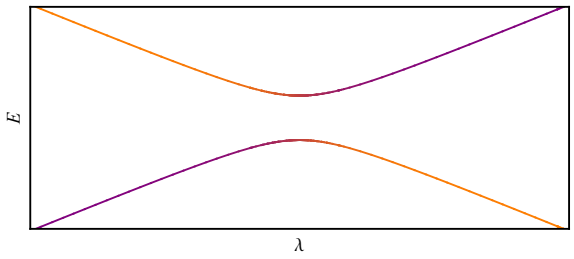


Figure 6.9: *Avoided crossings invert the character of eigenstates*: The physical character of the two eigenstates is indicated by their colour. Orange equals full overlap with the state $|1\rangle$ and purple full overlap with the state $|2\rangle$. A construction that continues eigenstates to increased values of interaction strength must no resolve avoided crossings if it is intended to match states of similar physical character.

With $\sigma_i^z = \tau_i^{(0),z}$. The LIOM satisfy $[H, \tau_n^z] = 0$, by comparing coefficients of $(J/W)^n$ we find

$$[H_0, \tau_i^{(n+1),z}] + [H_1, \tau_i^{(n),z}] = 0. \tag{6.28}$$

Solving[①] this equation for $\tau_i^{(n+1),z}$ (most easily done in the eigenbasis of $H_0$) we can recursively define $\tau_i^{(n),z}$. Akin to the Locator expansion of Anderson, in the MBL phase this is found to converge. The $\tau_i^{(n+1),z}$ are not however uniquely defined, and it can be seen from equation (6.28), that the diagonal part of $\tau_i^{(n+1),z}$ can be freely chosen (otherwise stated, $\tau_i^{(n+1),z} \to \tau_i^{(n+1),z} + F_i$ is also a solution if $[H_0, F_i] = 0$). This yields

$$\langle E_\alpha | \tau_n^{(n+1),z} | E_\beta \rangle = \begin{cases} \frac{\langle E_\alpha | [H_1, \tau_i^{(n),z}] | E_\beta \rangle}{E_\alpha - E_\beta} & \text{if } \alpha \neq \beta \\ \langle E_\alpha | F_i | E_\alpha \rangle & \text{if } \alpha = \beta \end{cases} \tag{6.29}$$

The $F$ degrees of freedom are fixed by requiring that $\tau_i^z$ has the correct Pauli spectrum $(1, 1, 1, \cdots, -1, -1, -1)$, i.e. that $\tau_i^z$ and $\sigma_i^z$ are unitarily related. With this degree of freedom fixed it becomes apparent that this unitary is the adiabatic transition S-matrix $S$. This can be seen by solving equation (6.28) as

$$\tau_n^{(n+1),z} = \mathrm{i} \lim_{\eta \to 0} \int_0^\infty \mathrm{d}t \mathrm{e}^{-\eta t} \mathrm{e}^{\mathrm{i}H_0 t} [H_1, \tau_i^{(n),z}] \mathrm{e}^{\mathrm{i}H_0 t}. \tag{6.30}$$

Using this relation recursively to write $\tau_n^{(n),z}$ in terms of $\tau_n^{0,z}$, it is clear these are the terms of the Dyson series corresponding to the adiabatic protocol.

Once this is understood it is clear why this method fails: the adiabatic protocol resolves avoided crossings. Each such avoided crossing effectively inverts the physical character of two eigenstates, as shown in Figures 6.9 and 6.10. This process has the action of mapping the LIOM being tracked by the adiabatic transition onto arbitrary non-local products of the LIOM of the target Hamiltonian.

This produces integrals of motion, but process destroys the locality of the operators. Since operators the existence of operators that commute with the Hamiltonian are a generic property of an arbitrary system these operators are not interesting. To make these operators local we must consider products of them, and solve a search problem as hard as that in the case of exact-diagonalisation.

This failure occurs even in the finite systems. In thermodynamic systems there is the additional problem that there is no adiabatic limit in the localized phase [290].

[①] This perturbative expansion of the LIOM has been applied previously in the unpublished work of ref [289], although in this case the equations are solved in a very complicated manner, and seemingly without due regard for degeneracies of $H_0$.

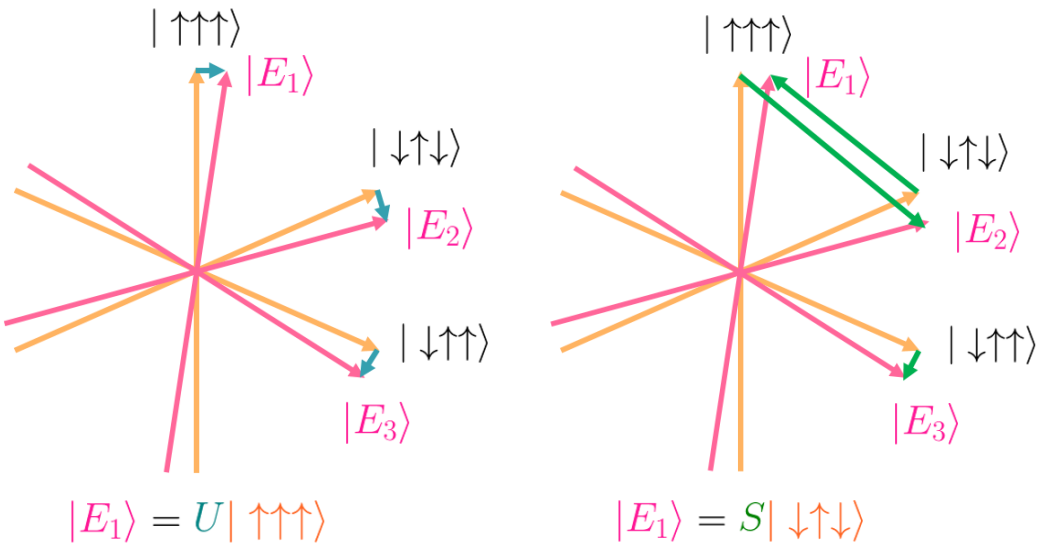


Figure 6.10: *Eigenstates and configuration states in the Hilbert space.* We consider the two orthonormal basis sets of the Eigenstates (pink) and the configuration states (orange) in the Hilbert space. In the MBL phase we understand that each eigenstate is close to a classical configuration state. (a) The unitary $U$ (blue) which maps each classical configuration to its corresponding eigenstate will similarly map each p-bit to an l-bit. (b) The problem of resonances (avoided crossings) in perturbation theory (adiabatic continuation) means that the $S$ matrix (green) constructed by this method maps configuration states to potentially distant eigenstates. As a result $S$ maps the p-bits onto generally non-local operators, which are not useful for characterising the MBL phase.

### 6.2.1 Construction of eigenstates

The problem is solved if we identify the one-to-one mapping of the many-body eigenstates $|E_i\rangle$ onto their nearest classical configuration states $|C_i\rangle$. The unitary that maps the $\sigma_i^z$ onto the $\tau_i^z$ is then given by $U = \sum_i |E_i\rangle \langle C_i|$.

So how do we identify the closest eigenstate to a given configuration state? If we can develop a notion of 'distance from being an eigenstate of $H$' then we can simply perform a steepest descent using this distance as a cost function. This will minimise $\Delta$ arriving at an eigenstate. The variance of the energy serves serves this purpose

$$\Delta(\psi) = \langle\psi|H^2|\psi\rangle - \langle\psi|H|\psi\rangle^2 = \left\langle H^2\right\rangle - \langle H\rangle^2 \tag{6.31}$$

where $\psi$ is a minimum of $\Delta$ if and only if $\Delta(\psi) = 0$ and hence $\psi$ is an eigenstate of $H$.

By performing gradient descent over the space of unitary rotations it is then possible to flow towards the eigenbasis. This flow, derived in appendix H.1, is given by

$$\frac{\mathrm{d}\,|\psi\rangle}{\mathrm{d}s} = \left(\left\langle (H - \langle H\rangle)^2\right\rangle - (H - \langle H\rangle)^2\right)|\psi\rangle \tag{6.32}$$

is monotonically towards the eigenbasis in the sense that

$$\frac{\mathrm{d}\Delta(\psi)}{\mathrm{d}s} < 0. \tag{6.33}$$

When this non-linear flow is integrated, it flows from any arbitrary initial state to the nearest many body eigenstate.

This process avoids the problems of usual perturbation theory (adiabatic continuation) whereby a state will converge on one particular eigenstate before at a high order in perturbation theory (an avoided crossing in the adiabatic protocol) the state will switch and begin to converge on an

eigenstate of quite different physical character.

### 6.2.2 Construction of LIOM

Previous methods to extract the LIOM have relied on numerically time averaging [275] or analytical [273] or numerical perturbative [289] construction. These methods, discussed in ref [274] produce conserved operators, but have some undesirable properties in that they do not preserve the spectrum of the operators, and hence the Pauli form is lost. Here we present a method for exact construction of a set of Pauli $\tau^z$ operators which commute with the Hamiltonian as well as their corresponding $\tau^x$, and $\tau^y$ operators.

By noticing that equation (6.31) can be recast as $\Delta = |[H, |\psi\rangle\langle\psi|]|^2$ where the norm is the Frobenius norm, it becomes clear how this can be easily generalised. By writing

$$\Delta(Z) = |[H, Z]|^2 \tag{6.34}$$

we again perform a steepest descent restricted over the space of possible unitary rotations. Via a process exactly analogous to that used to obtain the flow equation for eigenstates, detailed in appendix H.1, this yields the flow equations

$$\frac{\mathrm{d}Z}{\mathrm{d}s} = [Z, A], \quad \text{where} \quad A = [Z, [H, [H, Z]]]. \tag{6.35}$$

The unitarity of the flow, necessary to preserve the spectrum of $Z$, is explicit in the antisymmetric form of $A$. Since we are flowing a Pauli matrix, we use that $Z^2 = \mathbf{1}$ to simplify the equations

$$\frac{\mathrm{d}Z}{\mathrm{d}s} = ZHZ - HZHZH. \tag{6.36}$$

This flows from an arbitrary initial Pauli matrix to one that commutes with $H$. As before, under this flow, $\Delta$ is strictly decreasing, i.e.

$$\frac{\mathrm{d}}{\mathrm{d}s}|[H, Z]| < 0. \tag{6.37}$$

If the flow is initialised from a p-bit, i.e. $Z(s=0) = \sigma_i^z$ then this flows from the p-bit basis to the l-bit basis.

### 6.2.3 Wegner flow

One might attempt to recover the complete set of LIOM by repeated implementation of equation 6.36 starting from each p-bit in turn. There is however a problem: not only is this laborious, but the flow equation does not explicitly guarantee that of the l-bits found will be consistent. What may appear to optimal fixed point for one individual flowing operator, may not be a member of the globally optimal set of l-bits. Mathematically speaking, if we obtain two l-bits $\tau_i^z$, $\tau_j^z$ from equation 6.36 by initialising the flow at different p-bits $\sigma_i^z$, $\sigma_j^z$, there is no guarantee they will satisfy the necessary consistency condition $\mathrm{tr}\left[\tau_i^z \tau_j^z\right] = 0$ for $i \neq j$.

This can be fixed by flowing them together. Then the necessary algebra of the $\tau_j$ is guaranteed by the unitarity of the flow. This can be achieved by minimising the cost function

$$\Delta(\{Z_1, Z_2, \cdots Z_N\}) = \sum_X |[H, X]|^2 \tag{6.38}$$

where the sum $X$ runs over all the $2^N - 1$ Pauli operators given by the $Z_n$ and all their possible products. Following the same procedure as before we perform a steepest descent restricted over

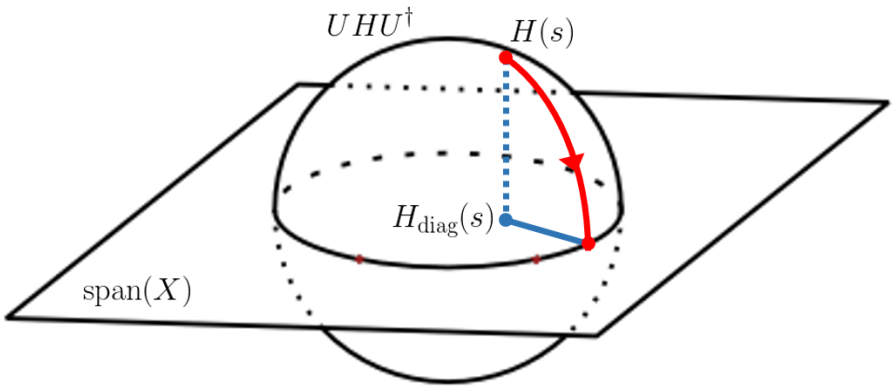


Figure 6.11: *Depiction of Wegner Flow:* The sphere represents the set of matrices $UHU^\dagger$ that are related to $H$ by a unitary rotation. The plane represents the set of matrices $\sum_X \alpha_X X$ spanned by the matrices $X$, the set of Pauli matrices $\sigma_i^z$ and their products. $H(s)$ is confined to the sphere, and $H_{\text{diag}}(s)$ is its projection onto the plane. Under the Wegner flow $H(s)$ follows the red trajectory, and $H_{\text{diag}}(s)$ follows the blue trajectory slave to $H(s)$. The red trajectory is a projection of the shortest path to the plane (blue dashed line) onto the sphere. The red and blue trajectories flow towards each other until they coalesce at the intersection of the plane and the sphere. In this image $H(s)$ starts far from the plane. In the MBL phase we understand that $H(s=0)$ is initially close to the plane.

the space of possible unitary rotations. This yields the flow equations

$$\frac{\mathrm{d}Z_n}{\mathrm{d}s} = [Z_n, A], \quad \text{where} \quad A = [H_{\text{diag}}, H] \tag{6.39}$$

where $H_{\text{diag}}$ is the diagonal part of the Hamiltonian *with respect to the instantaneous* $Z_n$ (and not the diagonalised Hamiltonian, of which we do not assume prior knowledge), evaluating this

$$\begin{aligned} H_{\text{diag}} &= \frac{1}{2^N}\sum_X X \mathrm{tr}\left[HX\right] \\ &= \frac{1}{2^N}\left[\sum_n Z_n \mathrm{tr}\left[HZ_n\right] + \sum_{n\neq m} Z_n Z_m \mathrm{tr}\left[HZ_nZ_m\right] + \sum_{n\neq m\neq p\neq n} Z_nZ_mZ_p \mathrm{tr}\left[HZ_nZ_mZ_p\right] + \ldots\right]. \end{aligned} \tag{6.40}$$

In a typical basis calculating $H_{\text{diag}}$ involves exponentially many operations on exponentially large matrices, as shown above. To avoid this it is convenient to transform to the flowing basis, in which the $Z_n = \sigma_n^z$ remain static, and $H$ flows from a generic to diagonal form

$$\frac{\mathrm{d}H}{\mathrm{d}s} = [A, H] = [[H_{\text{diag}}, H], H]. \tag{6.41}$$

In this basis, where the $Z_i$ remain in their diagonal physical basis forms, equation (6.40) is easily evaluated

$$[H_{\text{diag}}]_{ij} = \begin{cases} H_{ii} & \text{if } i = j \\ 0 & \text{otherwise} \end{cases} \tag{6.42}$$

thus $H_{\text{diag}}$ flows slave to $H$, and is its diagonal part in the flowing basis. This is the Wegner flow [291–295], in which the Hamiltonian flows towards its diagonal form, which has been applied to problems in MBL concurrently in ref [276]. Since we are interested in the LIOM, rather than the diagonalised Hamiltonian, during the flow we construct the unitary that relates these two bases

$$\frac{\mathrm{d}U}{\mathrm{d}s} = AU. \tag{6.43}$$

At the conclusion of the flow, the l-bits, the $\tau^z$, as well as the other corresponding Pauli operators $\tau_n^i$, can be easily evaluated $\tau_n^i = U\sigma_n^i U^\dagger$.

Here we have presented a derivation of the Wegner flow which permits an intuitive geometric operational interpretation, Figure 6.11. By comparison with Section 6.2.1 this shows the close relation of research into extracting the LIOM [276] and the mid-spectrum eigenstates [260,261,279]. This picture of Wegner flow suggests how the approach may be readily generalised to other cases where different choices of $\Delta$, equation 6.38, may result in preferable convergence criteria, or different fixed points which are useful for different kinds of analysis.

### 6.2.4 Convergence properties

The convergence properties of these flows are calculable by expanding around the fixed points. First we study the wavefunction flow given by equation 6.32. The attractive fixed points of this flow are the eigenstates $|E_i\rangle$. We expand about this solution by writing $|\psi\rangle = |E_i\rangle + \sum_{j\neq i} \delta\psi_j |E_j\rangle$. To leading order in $\delta\psi_i$ the evolution is

$$\frac{\mathrm{d}\delta\psi_j}{\mathrm{d}s} = -(E_i - E_j)^2 \delta\psi_j \tag{6.44}$$

which is easily solved

$$\delta\psi_j(s) = \delta\psi_j(0)\mathrm{e}^{-s(E_i-E_j)^2}. \tag{6.45}$$

This convergence appears rapid, exponentially good. However the range of velocities of the different $\delta\psi_{i>0}$ is given by the range of values of $(E_i - E_0)^2$, the smallest of which is the level spacing, and the largest of which is the bandwidth. These scales are separated by an exponential factor $2^N$. To avoid errors during integration, the step scale $\delta s$ must be set by the fastest of the $\delta_i$ yielding $\delta s \sim 1/\max(E_i - E_j)^2$, where as the time to convergence $s_\mathrm{f}$ is set by the slowest, i.e. $s_\mathrm{f} \sim 1/\min(E_i - E_j)^2$. The number of steps in the integration thus scales as

$$\text{integration time} \sim \frac{s_\mathrm{f}}{\delta s} \sim \left(\frac{\max(E_i - E_j)}{\min(E_i - E_j)}\right)^2 \sim 2^{2N}. \tag{6.46}$$

Performing the same analysis for equation (6.41) with the Wegner flow, equation (6.41) we find that the off diagonal elements evolve as according to

$$\frac{\mathrm{d}H_{ij}}{\mathrm{d}s} = -\sum_k (H_{ii} + H_{jj} - 2H_{kk}) H_{ik} H_{kj}. \tag{6.47}$$

The attractive fixed points of this flow are given by $H_{ij} = \delta_{ij} E_i$ where the $E_i$ are the eigen-energies. Thus near to convergence $H_{ij} \approx \delta_{ij} E_i + \delta H_{ij}$. Expanding to leading order in $\delta H_{ij}$ yields

$$\frac{\mathrm{d}H_{ij}}{\mathrm{d}s} \approx -(E_i - E_j)^2 \delta H_{ij} \tag{6.48}$$

which is identical to equation (6.44) and hence we find same requirement for exponentially long integration times.

## 6.3 Can there be localization without disorder

Single particle localisation can be induced by disorder [66], static electric fields [296], or time dependent Hamiltonians (i.e. floquet systems) [296–298].

One can similarly investigate the wider spectrum of dynamical possibilities Many body systems interact with localisation. Even in the classical case many body interactions introduce new dynam-

ical possibilities which might predispose a system towards localization. These include glassiness, in which the time-scale for the system to relax to a thermal ensemble becomes extremely long, and jamming,[①] in which the system fails to relax at all. In these cases the translational symmetry breaking occurs, not due to externally imposed quenched disorder, but due to 'configurational disorder' present in the initial conditions of the system.

### 6.3.1 Configurational disorder

This has led some to consider the possibility of MBL in the absence of disorder. The simplest approach is to frame the problem in a direct analogy to the case of Anderson localization. In this picture one might look for an MBL phase in which each particle is localized on a disordered potential provided by the random arrangement of other localized particles which make up the many body system.

This simple picture is spoiled by the dynamics of this potential-of-other-particles and thermalizes. One might hope with some additional ingredients it can be made to work. Previous investigations have tried including effective local selection rules for particle hops [299] which are almost always violated by typical excited states, or including multiple species of particles with vastly different dynamical time-scales [300, 301] such that one may more legitimately be considered to be a near-static potential on the dynamical time-scales of the other.[②]

These studies showed evidence that perturbation theory in the hopping converges before the onset of widespread hybridisation. This indicates the failure of the hopping to significantly alter the character of the static system. This may lead one to expect such behaviour in any system where typical Hamiltonian matrix elements, which couple configurations, are much smaller than the corresponding energy gap. However, it is possible that these putative localized phases are eroded by effects not captured by perturbation theory:[③] one strong argument is the presence of rare mobile 'ergodic bubbles' which reconfigure regions of the system through which they travel [304].[④] This indicates that this simple picture for localization in translationally invariant systems is not sufficient.

### 6.3.2 Kinetic constraints

Instead of attempting to construct disorder-free many body localization by looking for many body effects analogous to single particle localization, once can consider the somewhat orthogonal approach of looking for quantum analogues to disorder free classical many body glasses. In this picture we note that both glassy and localized behaviour result from a breakdown of the usual processes of thermal relaxation and attempt to understand the MBL phase as a quantum analogue to a classical glass. This is the approach taken in studies of the properties of kinetically constrained quantum systems. In these systems the Hamiltonian allows (local) dynamics only if the local configuration satisfies a selection rule. A simple example is the term kinetically constrained spin flip term in

$$H = -J \sum_{\langle ij \rangle} \left( n_i \sigma_j^x + n_j \sigma_i^x \right) + \frac{U}{2} \sum_{\langle ij \rangle} \sigma_i^z \sigma_j^z + \frac{h}{2} \sum_i \sigma_i^z \tag{6.49}$$

[①] Jamming requires time-reversal symmetry breaking, lest the system be capable of unjamming itself, in which case it is not jammed at all

[②] Though this intuition of a Born-Oppenheimer like separation of dynamical time-scales, introduced in ref [302], runs into serious problems given that there is no adiabatic limit in localized systems [290]

[③] We note that ref [300] presents numerical evidence in addition to perturbation theory, however this does not appear to be discernible from finite size effects [303].

[④] It remains unresolved the extent to which similar effects play a role in disordered systems. It has been argued that they rule out the possibility of mobility edges in many body systems, as energy density fluctuations in such systems introduce such ergodic bubbles. [270]

where $n_i$ is the projector $n_i = (1+\sigma_i^z)/2$. This allows a spin to flip (via action of the $\sigma^x$ operator) only if one of its neighbours is conFigured $\uparrow$. The structure of the kinetic term as a sum of (Projector) $\times$ (Dynamics) is typical of kinetically constrained models. Precisely this model is studied in the hope of finding signatures of many body localization in ref [305].

Such models are attractive when looking for dynamical terms that might predispose a system towards non-thermal behaviour. In any typical configuration such models will have long 'frozen' regions of the system that violate the kinetic constraint. For the example of equation 6.49 these would constitute long regions of $\downarrow$ spins. Such frozen regions have no dynamics, and so cannot thermalize under their own dynamics, instead they can be thermalized only by dynamical processes from their boundaries. Thus we would expected the model of equation 6.49 to be have significantly reduced dynamics versus the same model without kinetically constrained dynamics, given by the transverse field Ising model

$$H = -Jz\sum_i \sigma_i^x + \frac{U}{2}\sum_{\langle ij\rangle}\sigma_i^z\sigma_j^z + \frac{h}{2}\sum_i \sigma_i^z \tag{6.50}$$

where $z$ is the lattice coordination number. However the notion that constraints such as these will alone fundamentally alter the dynamics is misguided. For example the dynamics 6.49 include the translation of excitations at second order in perturbation theory via the process

$$|\cdots\downarrow\uparrow\downarrow\downarrow\cdots\rangle \overset{J}{\longleftrightarrow} |\cdots\downarrow\uparrow\uparrow\downarrow\cdots\rangle \overset{J}{\longleftrightarrow} |\cdots\downarrow\downarrow\uparrow\downarrow\cdots\rangle\,. \tag{6.51}$$

This second order process with energy $J^2/h$ couples exactly resonant configurations and so allows an excitation to propagate ballistically through a 'frozen' region on the system.

If we then consider the setting in which the dynamics might be expected to be maximally inhibited by frozen regions, i.e. when they are at their largest and most abundant. This the limit of low energy for $h > 0$. We find not localisation, but rapidly thermalising dynamics, of rare but ballistically propagating excitations. In ref [305] numerical evidence is given to suggest that (6.49) is many-body localized for $J > h$, however it is likely that this is a finite size effect due to the large value of $J/h$ and small system size inducing well separated spectral bands that disappear rapidly with growing system size [303].

Again one might hope with some additional ingredients that this process can be made to work: if we break the left-right symmetry then an excitation becomes unable to translate itself in the manner of equation 6.51: the first step of this process may proceed as before, but the second step is now forbidden. This is model we consider in the rest of this chapter.

### 6.3.3 Is it really MBL?

Before proceeding to study a kinetically constrained model in detail we discuss briefly some subtleties of looking for MBL in the absence of disorder.

MBL is a phenomena without strict definition. As discussed in Section 6.1.6 it is often equated with various inequivalent phenomena: the existence of an extensive set of local integrals of motion (LIOM) [257, 258, 274], violation of ETH, area law eigenstate entanglement through the full spectrum, vanishing transport coefficients, Poissonian spectral statistics etc. A translationally invariant system is intrinsically incapable of reproducing all of these. Its eigenstates and integrals of motion will respect this translational symmetry, leading to volume law entanglement and other results consistent with ETH. It can though support vanishing transport coefficients and non-ergodic spectral statistics. This would be the case if the system was being thermalized by a collective process that is vanishingly weak with increasing system size. If realised, such systems would be able to thermalize themselves only over unphysically long times—at which point the question of a strict

distinction between ergodic and localized becomes academic.

How might the established spectral tools distinguish such cases? In the case that the ergodic phase is thermalized by processes on unphysically long times, the eigenstate properties will be thermal, and so in the strict sense the system is ergodic. However, this ergodic phase would be very fragile, and unstable to the presence of weak disorder. This understanding provides some connection between the possibility of localization in clean systems and the canonical understanding developed in disordered systems.

In the next sections we consider this possibility in a left-right-asymmetric kinetically constrained spin model.

## 6.4 A model with kinetic constraints

We study the Quantum East Model (QEM), a kinetically constrained spin model with the Hamiltonian

$$H = -\frac{J}{2}\sum_i (1+\sigma_i^z)\sigma_{i+1}^x + \sum_i \frac{h_i}{2}\sigma_i^z \tag{6.52}$$

with periodic boundary conditions. We note that despite the unusual breaking of left-right symmetry, $H$ is hermitian, and time-reversal symmetric. $H$ consists of two terms: a kinetically constrained spin-flip interaction; and a non-interacting part consisting of random single site $z$-fields. The disorder fields $h_i$ are normally distributed with mean $h$ and standard deviation $W$.[①] For $W = 0$ the $h > J$ the 'all-down' $|\downarrow\downarrow\downarrow\cdots\rangle$ is the ground state. This ground state phase transition occurs at the Rokhsar-Kivelson (RK) point $J = h$.

The dynamics of the QEM are constrained by a selection rule: the $i+1$th spin can flip if and only if the $i$th spin is in the $\uparrow$ state,

$$\begin{aligned} |\cdots\uparrow\uparrow\cdots\rangle \quad &\overset{J}{\longleftrightarrow} \quad |\cdots\uparrow\downarrow\cdots\rangle\,, \\ |\cdots\downarrow\uparrow\cdots\rangle \quad &\not\longleftrightarrow \quad |\cdots\downarrow\downarrow\cdots\rangle\,. \end{aligned} \tag{6.53}$$

This is enforced by the projector in the kinetic term in (6.52). To highlight the key role of the kinetic constraint we will also compare with a model with the 'softened' constraint found by adding a perturbation. The perturbation we use is given by

$$\Delta H = -\gamma J \sum_i \sigma_i^z \sigma_{i+1}^x. \tag{6.54}$$

The addition of $\Delta H$ causes the $i+1$th spin to flip with an energy $J(1+\gamma)$ when the $i$th spin is $\uparrow$ or and a rate $J\gamma$ when it is $\downarrow$, giving very different rates for $0 < \gamma \ll 1$:

$$\begin{aligned} |\cdots\uparrow\uparrow\cdots\rangle \quad &\overset{J(1+\gamma)}{\longleftrightarrow} \quad |\cdots\uparrow\downarrow\cdots\rangle\,, \\ |\cdots\downarrow\uparrow\cdots\rangle \quad &\overset{J\gamma}{\longleftrightarrow} \quad |\cdots\downarrow\downarrow\cdots\rangle\,. \end{aligned} \tag{6.55}$$

This perturbation $\Delta H$ preserves the position of the Rokhsar Kivelson point and the ground state phase transition at $J = h$.

Previous authors have studied the disorder-free ($W = 0$) case in ref [272], and another related disorder-free model in ref [305], for evidence of an MBLD transition. These provided evidence of both statics and dynamics characteristic of the MBL transition, though it is not likely that finite size effects can be ruled out as an alternative explanation for these phenomena [303]. The $W = 0$ case has also been studied in the context of classical glasses where the equivalent classical

[①] We follow the suggestion of ref [232] in choosing a Normal distribution in place of the oft-used box distribution, as the finite size scaling bounds suggest the latter may have a poorer convergence with increasing system size

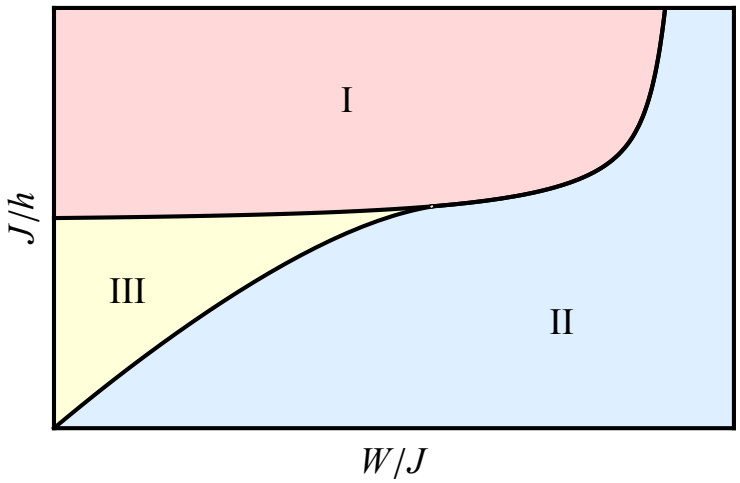


Figure 6.12: *Phase diagram:* At $h = 0$ (i.e. $J/h \to \infty$) the transition between the ergodic (I) and localized (II) phases occurs at a critical value of $W/J > 0$. When the competing energy scale $h$, corresponding to a uniform order which acts to detune many resonances, takes a sufficiently large value we see the appearance of a region (III) in which there is the low lying energy levels are localized. At low energies the system localizes, whereas at high energies it is ergodic. In region (III) a $\sim 1/L$ fraction of the states are localized meaning that the effect is not visible in the oft studied infinite temperature but only at sufficiently low temperature $T\ h/\log L$

model is known as the 'East Model'. The classical behaviour of the translationally invariant East model is characterised by a glassy super-Arrhenius growth in relaxation time-scales $\tau \sim \mathrm{e}^{A^2/T^2}$ with decreasing temperature [306–309]. In classical spin models, this slowdown is usually driven by the presence of disorder. Thus suggests this model may be an interesting candidate in searching for MBL, the 'quantum glass', in similarly clean systems. The classical East Model has a severe spectral asymmetry in the sense that the glassy behaviour is lost when one changes the sign of the energetics (by inverting the uniform field $h \to -h$, mapping the ground state to the maximally excited state and *vice versa*). We find this spectral asymmetry is also apparent in the quantum model and plays a central role in its interesting dynamics.

### 6.4.1 The dynamics of the model

The kinetic constraint introduces the possibility of configurational regions which have no dynamics. The behaviour of these 'frozen' regions of down spins is epitomized by that of the fully frozen 'all down' state. However the kinetic constraint alone does not generate interesting dynamics. There is an additional ingredient present: a key feature of the East model is the directional nature of the interactions, the result of this is that no configurational structure, no matter how large or internally ergodic, is able to translate itself under its own dynamics. Instead, structures only develop translational motion when facilitated by other $\uparrow$ spins. If the typical distance to other $\uparrow$ spins is large, this process will be a very high order in $J/h$. Hence any smallness of $J/h$ will be dramatically enhanced.

As discussed in Section 6.3, although arguments from symmetry indicate that in a fully interacting system, in the absence of disorder $W = 0$ ETH will not be violated , it is still conceivable that there is a disorder driven phase transition at very weak or zero disorder (as in the 1D or 2D Anderson systems).

### 6.4.2 Main results and outline of analysis

We find evidence that for a given value of $J/h$ the lowest magnetisation sectors are qualitatively different in character to higher sectors.

In Section 6.5 we consider the clean model, $W = 0$. In Section 6.5.1 we show via perturbative arguments that even in the absence of disorder that quantum dynamics fail to induce any significant hybridisation between these lowest sectors and other higher sectors of the model. The dynamics within these sectors is characterised by a timescale that is exponentially slow in the typical spacing between excitations, i.e. in the inverse energy density $1/\epsilon$.

In Section 6.5.2 we numerically evidence the conclusions of these peturbative arguments in the clean model. We show that these low-lying magnetisation sectors can be constructed perturbatively in the large system limit, we verify this with numerics and show that this behaviour is unique to systems with the kinetic constraint. In Section 6.5.3 we show the level statistics of these sectors are Poissonian, even though at higher energies the system is ergodic. In Section 6.6 We find similarly that exceptionally weak disorder is required to localise these sectors. Using several statistics we provide numerical evidence that, with the introduction of very weak disorder, that the lowing lying levels are many-body localized.

The overall picture is of a model which at large $J/h$ behaves in the usual way: it has an ergodic region separated from a localised region at a critical value of $W/J$. This is depicted by the boundary between regions I and II in Figure 6.12 which tends towards vertical at large $J/h$. At low values of $J/h$ however the model behaves characteristically differently. The bulk of the spectrum is localised at $W/J \sim J/h$. This is depicted by the boundary between regions II and III $W/J \sim J/h$. However levels with low energy density localise at $W/J \sim (\sqrt{2}J/h)^{4h/\epsilon}$, leading to extremely small critical disorder at low energy density $\epsilon \to 0$.

Thus the resulting picture is of a system described by Figure 6.12. This has three regions, and ergodic phase (I), the disorder driven fully many-body localised phase (II), and a region in which there exists mobility edge at low energies (III).

## 6.5 A crossover in the clean system $W = 0$

In this section we analyse the dynamics of the clean model and find evidence that at sufficiently low energy densities the uni-directional and kinetically constrained interaction is unable to induce significant interactions between resonant states, and so the hybridisation is broken by uncharacteristically weak disorder. We introduce this from a perturbative picture in the interactions, and find a crossover in the level statistics at low energies of the clean model.

The clean system has been previously studied as a candidate system for localizing behaviour in the absence of disorder in ref [272], where it was suggested there was an MBL transition at the RK point $J = h$. Contrary to this, we find a crossover in the character of the clean system which perturbative analysis indicates to occur across a range of values of $J/h$. This range of values is lower than and well separated from the RK point, beginning at $J/h \sim 1/\sqrt{2}$ and continuing for lower values. This crossover sees a significant reduction in the critical disorder, and has a signature in the level statistics of the clean system. However, due to the translational invariance eigenstate thermalization hypothesis is not violated.

An extreme example which highlights features of the QEM is the configuration of all down spins. This fully 'frozen' ferromagnetic $M = 0$ state $|\downarrow\downarrow\downarrow\cdots\rangle$ is an eigenstate for all $J, h, W$. For $W = 0$, $h > J$ this is the ground state.

Due to the kinetic constraint such frozen regions play an important role in the structure of states higher in the spectrum. For example single excitations above the fully frozen state (i.e. $\uparrow$ spins) are unable to generate their own dynamics, and instead can only 'facilitate' the dynamics of spins to their right. Crucially, without a neighbouring $\uparrow$ spin to its left, a spin is unable to compensate for the energy penalty introduced by flipping its right hand neighbour by itself flipping. An excitation is only able to induce dynamics in other excitations via entirely off shell processes which rearrange

parts of the system whose size is given by the typical spacing between ↑-spins. Anticipating this (and following ref [306]) we define *domains*, the basic structures which determine the dynamics, and denote them by the colons in

$$:\downarrow\uparrow:\downarrow\downarrow\downarrow\uparrow:\uparrow:\underbrace{\downarrow\downarrow\downarrow\downarrow\downarrow\downarrow\uparrow}_{\text{domain}}:\downarrow\downarrow\uparrow:\uparrow:\uparrow:\downarrow\downarrow\uparrow,$$

each domain consists of a single up spin and the string of down spins to its left.

### 6.5.1 Perturbative expansion

We first consider perturbation theory in $J/h$ about the classical configurations. We find the conditions under which this converges and discuss the meaning of this convergence.

In the $J \ll h$ limit transitions between magnetisation sectors are strongly suppressed and the short time dynamics are within sectors. To describe this consider the effective hopping of domain walls within a magnetisation sector by integrating out fluctuations into other sectors. This yields an effective Hamiltonian defined on one sector. Calculating the elements of this perturbatively we find the leading order dynamics for the hopping of domain wall by a single site is given by

$$\begin{aligned} J_{\text{eff}}^{d\to d-1} &= \langle \cdots \uparrow \underbrace{\downarrow \cdots \downarrow\downarrow\uparrow}_{\substack{d \text{ spin} \\ \text{domain}}} \cdots |H_{\text{eff}}| \cdots \uparrow \underbrace{\downarrow \cdots \downarrow\uparrow}_{\substack{d-1 \text{ spin} \\ \text{domain}}} \downarrow \cdots \rangle \\ &= J\frac{(J/h)^{2d-3}}{(d-2)!^2} + \cdots . \end{aligned} \tag{6.56}$$

where $d$ is initial domain length, and $d-1$ the final domain length. A derivation of this form of $J_{\text{eff}}$ is given in appendix I.1.1. Expanding to sub-leading order and including processes which induce arbitrary movements of domain walls, changing the domain from length $d$ to $d'$, we find a series

$$J_{\text{eff}}^{d\to d'} = \binom{d-1}{d'-1} \sum_{n=0} \frac{2^n J (J/h)^{2(d+n)-3}}{(d-n-1)!(d-n-2)!} \tag{6.57}$$

where we have assumed (without loss of generality) that $d > d'$. This is derived in appendix I.2.1. At each order $n$ in equation (6.57) is correct to leading order in $d$ (the sub-leading terms in $d$ are a factor $\sim (\log d)/d$ smaller). This series is approximately valid for $n \ll d$ beyond which the kinetic constraints cause a significant reduction in the number of permitted processes at each order, and equation (6.57) becomes an overestimate.

We can evaluate some the properties of this effective hopping in order to get a better feel for equation (6.57). As shown in appendix I.2.2 this summand is sharply peaked at a dominating value of $n = \max(d - \frac{h}{\sqrt{2}J}, 0)$. Substituting this value into equation (6.57) we see that the sum is that the sum is exponentially small in $d$. Furthermore, we see that this sum converges for which converges for $J/h < 1/\sqrt{2}$.

The exponential smallness of $J_{\text{eff}}$ with $d$ follows as the leading order process proceeds via a flip of the entire domain

$$|\uparrow\downarrow\cdots\downarrow\downarrow\uparrow\rangle \overset{J^{d-1}}{\to} |\uparrow\uparrow\cdots\uparrow\uparrow\uparrow\rangle \overset{J^{d-1}}{\to} |\uparrow\downarrow\cdots\downarrow\uparrow\downarrow\rangle$$

where there are no possible intermediate on shell steps. This means that not only is the process suppressed to high order for small $J/h$, but requires a large excursion off shell. Otherwise stated, the energy barriers in configuration space, which separate low energy resonant configurations, which suppress hybridisation are both high and wide. Leading to very effective suppression of tunnelling processes.

This leads to a strong spectral asymmetry, this distinction is particularly stark if we consider

the near maximally polarized sectors. For the state with magnetisation $M = L-1$, which consists of single $\downarrow$ spin in an otherwise $\uparrow$ polarised state, this defect (which constitutes a domain of length $d = 2$) is mobilised by the process

$$|\cdots\uparrow\uparrow\downarrow\uparrow\uparrow\cdots\rangle \xrightarrow{J} |\cdots\uparrow\uparrow\uparrow\uparrow\uparrow\cdots\rangle \xrightarrow{J} |\cdots\uparrow\uparrow\uparrow\downarrow\uparrow\cdots\rangle$$

which has an effective interaction strength $J_{\text{eff}} = J^2/h$.

However for the $M = 1-L$ case of a single $\uparrow$ spin in an otherwise down polarised state (constituting a domain equal to the system size $d = L$) is mobilised the process

$$|\cdots\downarrow\downarrow\uparrow\downarrow\downarrow\cdots\rangle \xrightarrow{J^{L-1}} |\cdots\uparrow\uparrow\uparrow\uparrow\uparrow\cdots\rangle \xrightarrow{J^{L-1}} |\cdots\downarrow\downarrow\downarrow\uparrow\downarrow\cdots\rangle$$

with the significantly smaller leading order term $J_{\text{eff}}^{(L)} \sim J(J/h)^{2L-3}/(L-2)!^2$.

As we show in appendix I.2.3 the equation (6.57) can be evaluated using the method of steepest descent. This yields

$$J_{\text{eff}}^{d\to d'} \approx \binom{d-1}{d'-1}\sqrt{\frac{8\pi h}{\sqrt{2}J}}\frac{J}{2^d\Gamma\left(h/(\sqrt{2}J)\right)^2}\left(\frac{\sqrt{2}J}{h}\right)^{4d-\sqrt{2}h/J-3} \tag{6.58}$$

where $\Gamma(z)$ is the Gamma function, and a typical value of $d$ is given by $\bar{d} = L/M = 1/m = h/\epsilon$ for $h \gg J$, where $m$ is the magnetisation density above the ground state (i.e. the density of up-spins), and $\epsilon$ is the energy density. The form of equation (6.58) is found by approximating the sum in equation (6.57) as is shown in appendix I.2.3. This form is valid for $h^2 < 2d^2J^2$, whereas for $d > 2d^2J^2$ one can simply use the leading terms of (6.57). In what follows we use $J_{\text{eff}}$ to refer to this evaluated form.

### 6.5.2 A numerical check on the convergence of perturbation theory

It is possible that the leading order analysis does not capture the physics, and that higher order terms dominate, and possibly cause the series to diverge, this would indicate significant hybridisation between sectors. For the leading order analysis to be accurate we require that this is not the case, and that the sub-leading terms in (6.56) are increasingly small.

Here we verify numerically when this approximation is valid, and show that vestiges of the non-interacting problem persist in the spectrum to finite $J/h$. The $J_{\text{eff}}$ are the matrix elements of the effective Hamiltonian defined on the reduced Hilbert space of a single magnetisation sector

$$\begin{aligned} H_{\text{eff}} &= H_{aa} + H_{ab}\frac{1}{Mh - H_{bb}}H_{ba} \\ &= P_aH_0P_a + \sum_{n=0}^{\infty} P_a\left[VP_b\frac{1}{Mh - H_0}P_b\right]^n VP_a \end{aligned} \tag{6.59}$$

where $M$ denotes the total magnetisation of the relevant sector $a$, and $b$ denotes *all other sectors*. $P_a$ and $P_b$ are the projectors onto these sectors, and satisfy $P_a + P_b = 1$. $H_0$ is the uniform field term, $V$ the Kinetically constrained interaction term. This is the usual method (of e.g.refs [310,311]) where $H_{\text{eff}}$ is found by projecting the resolvent. This yields an effective Hamiltonian with the correct spectrum to good approximation. Keeping the leading order terms of $H_{\text{eff}}$ yields the effective Hamiltonian

$$H_{\text{eff}} = \sum_i \sum_{0<j<k} J_{\text{eff}}^{k\to j}(1+\sigma_i^z)(\sigma_{i+j}^+\sigma_{i+k}^- + \text{h.c.}) + \sum_i h_i\sigma_i^z \tag{6.60}$$

with $J_{\text{eff}}^{k\to j}$ from equation (6.58). A simple condition for the validity of this perturbative analysis is that the expansion in equation 6.59 converges. A sufficient (but not necessary) condition for this is that the dominant eigenvalue $\lambda$ of the matrix $VP_b\left(hM - H_0\right)^{-1}P_b$ satisfies $|\lambda| < 1$. We evaluate this for the lowest magnetisation sector $M = 1 - L$ above the 'all-down' $M = -L$ state in finite systems of increasing size. We evaluate $|\lambda|$ for increasingly large values of $L$ to ascertain the condition for convergence. This is found to converge quickly to the condition $J/h < 0.7171$. This value is close to $1/\sqrt{2}$ as expected from the denominator of equation (6.57). The stability and rapidity of this convergence with increasing $L$ can be observed as the uppermost line plotted in Figure 6.13a.

Below this critical value of $J/h$ the exponentially small value of the effective hopping becomes apparent, the hybridisation between states in lowest magnetisation sector becomes very weak, and the momentum dispersion at the bottom of the spectrum goes to zero with increasing system size.

At successively smaller values of $J/h$ we see perturbation theory converging in progressively higher magnetisation sectors. This is shown in Figure 6.13. It is found that $(J/h)_{\text{crit}} \sim 1/\delta M$. This indicates that for fixed $J/h$ in the large system limit this effect is only felt by a fraction $1/L$ of the spectrum, and hence only at low temperatures $T \sim h/\log L$.

In Figure 6.14 we show that with the relaxation of the kinetic constraint, at $\gamma = 1/4$ this behaviour is no longer observed, and the critical $J/h$ any given which sector converges drifts downwards with increasing system size.

**The meaning of the convergence of perturbation theory**

This approach is vaguely reminiscent of the approach of Anderson, discussed in Section 6.1.1, in which he showed that perturbation theory around about a sector consisting of a single site converged. However despite this we have here shown the convergence of perturbation theory about a magnetisation sector. This alone does not rule out transport, and we require further consideration to relate this to localization.

This analysis tell us that, for the sectors which are convergent at a given value of $J/h$, when time evolved, a state remains close to its initial magnetisation. This is in the sense that, fluctuations in the magnetisation do not grow with the system size. A simple physical picture of this is that each $\uparrow$-spin, marking the boundary of a domain, induces a region of dynamical activity to its right. The extent of these active regions, and hence the fluctuations in $M$, do not grow with the addition of further new sites to the system providing the new sites are conFigured $\downarrow$ (i.e. that the additions do not change the value of $\delta M$, the magnetisation above that all down $M = -L$ state).

We consider what consequences these vestiges of the conservation of magnetisation have for the systems dynamics. The leading order process to move a domain wall requires flipping all the $\downarrow$ spins of an entire domain to $\uparrow$. This implies to move a domain wall of $d$ the system must overcome the energy barrier $hd$, and similarly undergo a quantum fluctuation in the magnetisation of $d$. By considering higher order process we are able to lower this energy barrier: the minimum possible barrier to move a domain wall of length $d$ is $h\lfloor \log_2 d \rfloor$ [306], requiring a corresponding fluctuation in magnetisation of $\lfloor \log_2 d \rfloor$. However, though this barrier is much lower, it is much wider, i.e. this process is suppressed to very high order in $J/h$. These effects must balanced, and the dominant process has a magnetisation fluctuation $\sim 2d - h/J\sqrt{2} - 2$.

Since: (i) for a given magnetisation sector $\delta M$ above the all-down $M = -L$ state, the processes by which excitations move require increasingly large fluctuations in magnetisation with increasing system size; (ii) fluctuation in the magnetisation do not grow with system size; this implies that effective coupling between resonant configurations becomes weaker with increasing system size.

In the convergent magnetisation sectors (which constitute a $\sim 1/L$ fraction of the bandwidth) this causes relaxation to proceed exponentially slowly in the typical domain length. For $W = 0$

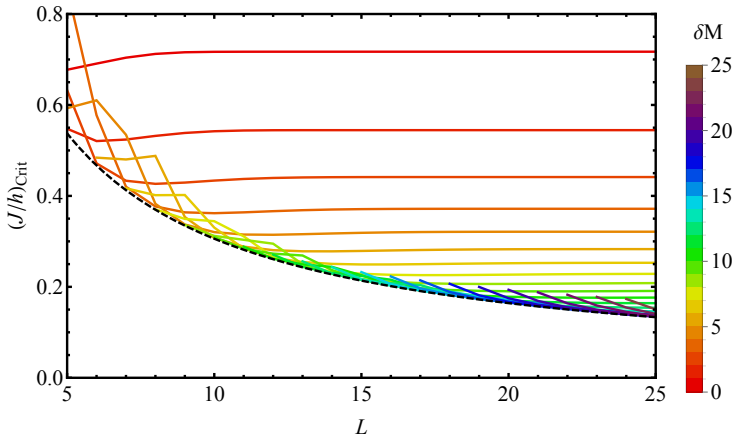


(a)

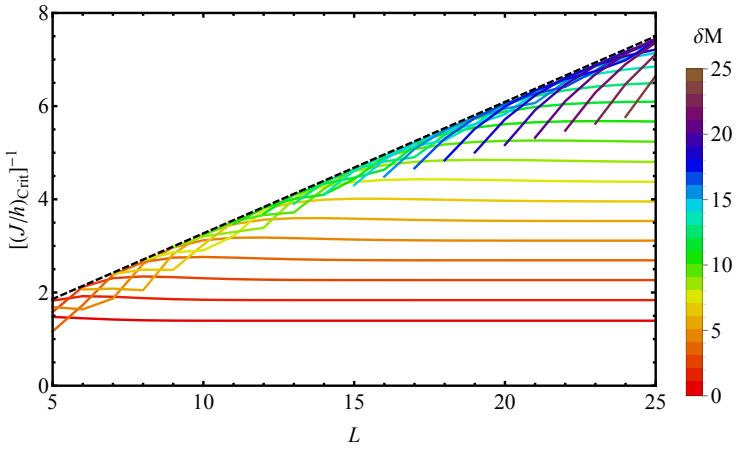


(b)

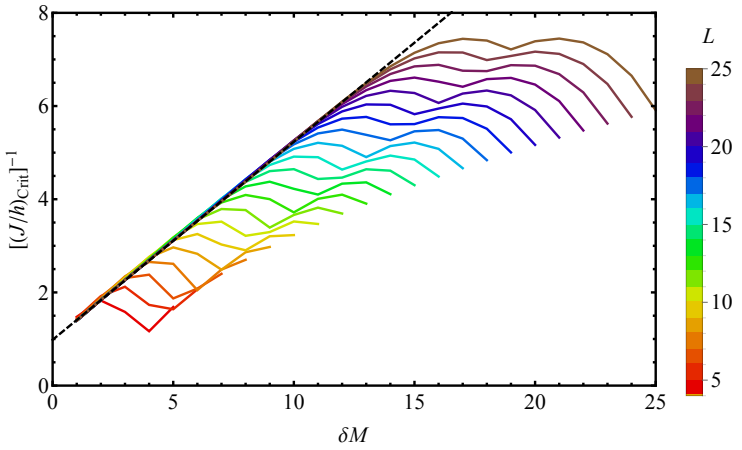


(c)

Figure 6.13: *Critical values of* $J/h$: (a) Values $(J/h)_{\text{crit}}$ for which perturbation theory around the different magnetisation sectors $\delta M = 1$ to $L$ converge for system sizes $L = 5$ to 25. For a system size $L$, $\delta M = 1, \cdots L$. Each slide coloured line corresponds to a different value of magnetisation $\delta M$ above the all down $M = -L$ state. The line $1/(0.282L + 0.450)$ is shown (black dot-dashed). Each sector is shown to rapidly converge to a fixed value $(J/h)_{\text{crit}}$. (b) The same data is plotted with the vertical axis inverted. The linear spacing of $1/(J/h)_{\text{crit}}$ with incrementally increasing $\delta M$ is evident. (c) The same data plotted vs $\delta M$, each line corresponds to a different value of $L$. The linear spacing evident in plot (b) manifests as the linear relationship $1/(J/h)_{\text{crit}} \sim \delta M$ visible for $\delta M < L/2$. The line $(0.425\delta M + 0.983)$ is plotted (solid dot dashed) to highlight this relationship.

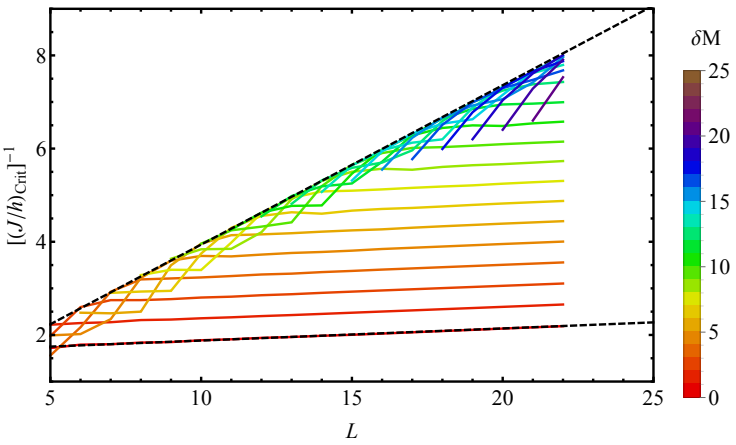


Figure 6.14: *Non-convergence of magnetisation sectors with $\gamma > 0$:* Plotted for direct comparison with Figure 6.13b, and counter to the behaviour seen in that plot, when the kinetic constraint is softened the magnetisation sectors no longer converge in the large system limit. This is visible as the critical value of $(J/h)^{-1}$ is seen to drift upwards for all sectors. The lines $0.342L + 0.52$ and $0.026L + 1.62$ are plotted as guides for the eye, to highlight the upward drift.

these exponentially small effective couplings couple exactly resonant configurations and so we expect strong hybridisation and ETH satisfying eigenstate statistics. However we expect that these sectors will localize for a correspondingly weak critical disorder, inducing a mobility edge in the spectrum. In the large $L$ limit we expect that this mobility edge enters the spectrum at infinitesimal disorder.

### 6.5.3 Level statistics at $W = 0$

Though we expect ETH-consistent eigenstate statistics, the weak effective coupling between levels in the same sector can lead to non-ergodic energy level statistics. In this section we provide numerical evidence for level statistics in the clean model which are consistent with localized behaviour in the QEM. This occurs in the lowest fraction of energy states.

The convergence of perturbation theory and the drop in effective coupling in the clean system is apparent in its level statistics shown in Figure 6.15. This is captured by the energy level spacing ratio $\bar{r} = \langle \min(r, 1/r) \rangle$, where $r = (E_{i+1} - E_i)/(E_i - E_{i-1})$. This is averaged over the mid-spectrum levels of each momentum sector, and over the momentum sectors of the Hamiltonian.[①] Lower level repulsion is indicated by a smaller value of $r$.

In Figure 6.15 the drop in $r$ at lower $J/h$ is not apparent in the corresponding data with $\gamma = 1/4$ indicating this feature is only present with the kinetic constraint. The feature is also observed to become less prominent at longer system sizes, as it only corresponds to a $1/L$ fraction of magnetisation sectors. The correlation between eigenstate energy $E_i$ and $r_i$ confirms that this feature is from states at low energies.

As discussed, despite this MBL-like spectral signature the eigenstates remain consistent with ETH and the eigenstate-entanglement remains volume law. This follows as the effective-hoppings, though weak, are competing with a difference in the energetics of classical configurations of exactly zero, and so hybridisation occurs. The system will thermalize eventually, albeit at very long times.

In this section we have established that there is change in character at low energies and low $J/h$ which leads to a change in the dynamics and spectral properties of the model. Perturbative arguments indicate that this is restricted to the lowest $\sim 1/(0.282L)$ states and hence is only visible at low temperatures $T \sim h/\log L$. In the next section we relate these observations to MBL

[①] Averaging over momentum sectors individually, rather than calculating the level spacing ratio for the full Hamiltonian, is the correct way to treat the translational symmetry of this Hamiltonian.

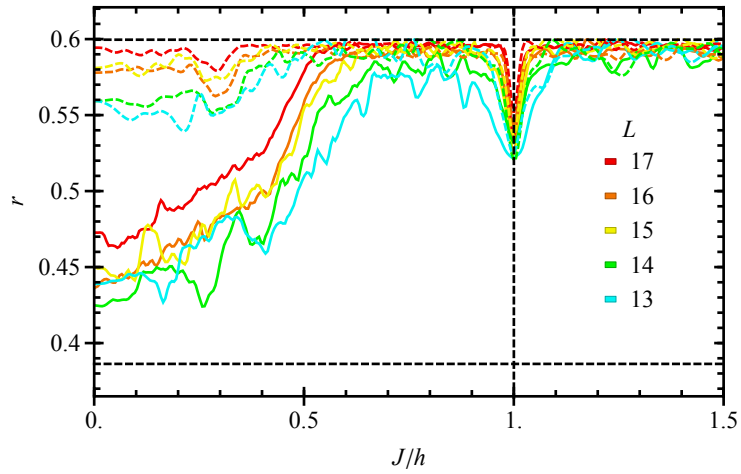


(a)

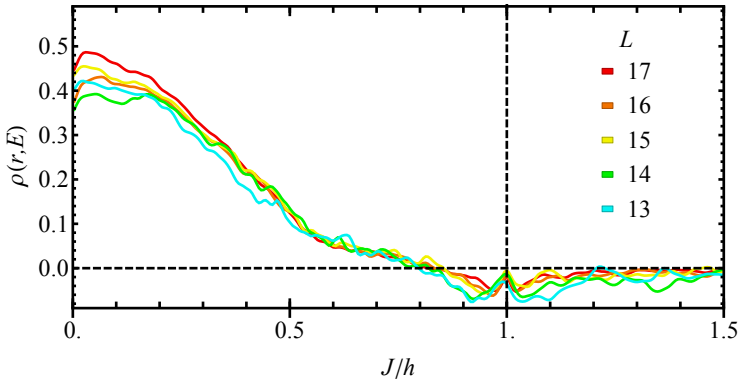


(b)

Figure 6.15: *Level statistics for $W = 0$:* (a) The level spacing ratio averaged over the middle third of all momentum sectors for $L = 13$ to 17. The dashed horizontal lines indicate the GUE and Poisson values $r_{\mathrm{GUE}} = 0.5996$ and $r_{\mathrm{Poi}} = 0.3863$ respectively [248]. The vertical line indicates $J/h = 1$, the RK point. At $J/h = 0.7171$ the lowest lying states become only weakly hybridised and the dispersion in the lowest lying momentum bands goes to zero in the thermodynamics limit. It is clear that this is a separate feature from the dip induced by the high-symmetry RK point, and that between these points the system appears GUE. The dotted lines consist of the same data taken from the softened ($\gamma > 0$) model with $W = 0$, $\gamma = 1/4$. In the softened model, in which the kinetic constraint is relaxed, there is no comparably large drop in $\bar{r}$. (b) The product-moment correlation $0 \leq \rho \leq 1$ between eigen-energy $E$ and level spacing ratio $r$. The positive value indicates that the drop in $r$ observed in (a) is principally due to changes in the spectrum at low energies.

behaviour.

## 6.6 localization for $W > 0$

MBL is often equated with various inequivalent phenomena: the existence of an extensive set of local integrals of motion (LIOM), violation of ETH, area law eigenstate entanglement through the full spectrum, zero DC conductivity, etc. A translationally invariant system is intrinsically incapable of reproducing all of these, but its response to disorder could be altered. we explore the possibility that the transition in the character of the clean ($W = 0$) system is related to a change in localizing behaviour of the disordered system.

We analyse this possibility through the localization length, and through the properties of eigenstates and energy levels.

These results indicate that for sufficiently small $J/h$ in which the effective-hopping picture is valid, the MBL phase onsets when the competition between the hybridising influence of effective hopping $J_{\text{eff}}$ and the localizing influence of the disorder $W$ is won out by the latter. This suggest a critical disorder $W_{\text{c}} \sim J_{\text{eff}}^{d\to d'}$ from (6.58). For low energy densities (and hence at low $T$) this $W_{\text{c}}$ becomes Exponentially small in $1/\epsilon$. In the other limit of $h \ll J$, there is no confounding influence of these qausi-conserved magnetisation sectors, $h$ becomes irrelevant, and as a result we have a simple competition between disorder and hybridization and a full spectral MBLD transition occurs as a simple function of $W/J$.

### 6.6.1 Spectral statistics

For a real Hamiltonian the MBL transition induces a change in level statistics from GOE (conducting) to Poissonian (localized). An order parameter for this transition is the aforementioned energy level spacing ratio $\bar{r}$. In the localized phase energy levels experience only weak repulsion, thus—assuming there are no additional correlations (due to e.g.symmetries)—their spacings remain Poissonian giving $\bar{r}_{\text{P}} = 2\log 2 - 1$. However in the conducting phase, strong level repulsion leads to a more even spacing, and a correspondingly larger value of $\bar{r}_{\text{G}} = 4 - 2\sqrt{3}$. [248].

Introducing disorder allows us to investigate whether the features visible in Figure 6.15 indicate the existence of an MBL phase at small $W/J$ at small values of $J/h$.

#### Spectral statistics at $J \gg h$, $W > 0$

However we first study large $J/h$ region of the phase diagram. In Figure 6.16a we see the familiar behaviour of $r$ in disordered systems: weak disorder does not perturb us from $r = r_{\text{GOE}}$ indicating a stable ergodic region. At finite critical $W$ we eventually see a transition to $r = r_{\text{Poi}}$ indicating MBL. In finite systems these regions are demarcated by a transition which becomes increasingly sharp at larger system sizes. As seen in previous studies [222, 262, 264] the crossing point drifts considerably and scaling analysis suggests a finite-size scaling exponent $\nu \approx 1$, in violation of the Harris bound [232]. Due to this violation we do not pursue this analysis in depth or to larger system sizes.[①]

#### Spectral statistics at $J \ll h$, $W > 0$

We now analyse the estimated critical disorder for a change in its behaviour at low $J/h$.

We see corresponding behaviour of the critical point. The critical point is estimated in finite systems as the point which does not drift with increasing system size [222], i.e. the crossing point

[①] particularly as more advanced numerical techniques which have been successful in extending to larger system sizes find that even at $L = 22$ we remain in the Harris-violating regime [262, 264].

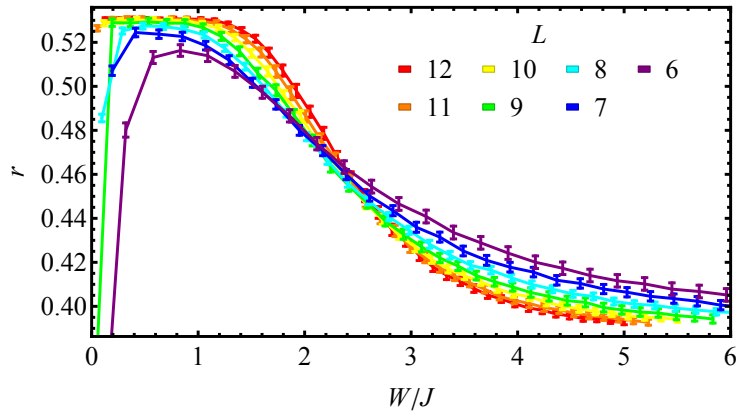


(a) $J/h = \infty$

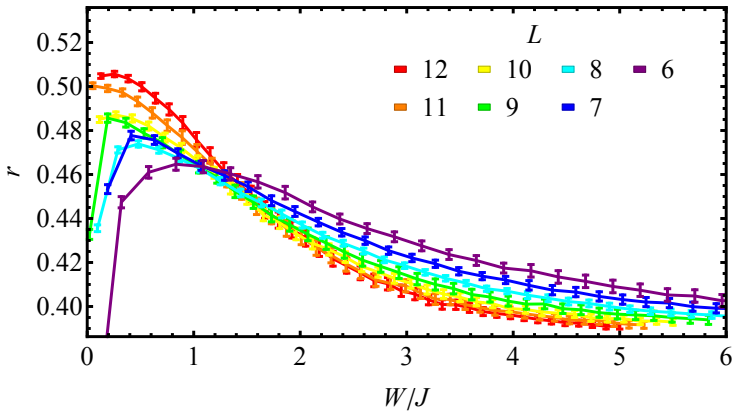


(b) $J/h = 1/2$

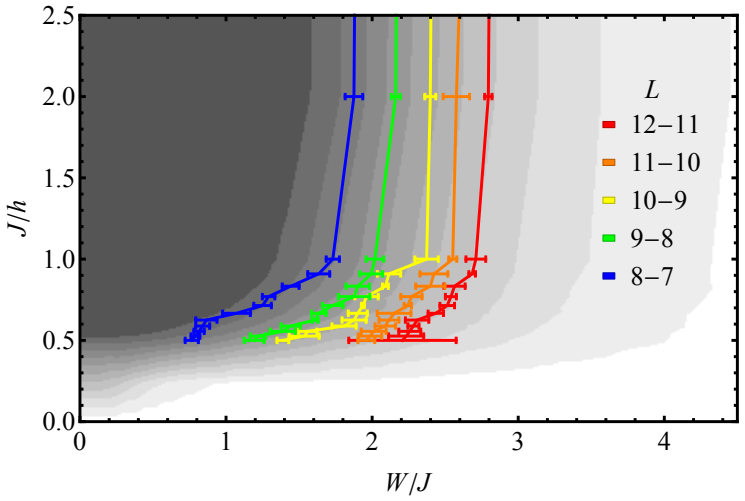


(c) Crossing points

Figure 6.16: *Level statistics* (a) $h = 0$ ($J/h = \infty$) the level statistics for successive system sizes behaves in the familiar way for large small $h$. At low $W$ the translational symmetry is felt and $\bar{r}$ leaves the expected range of $\bar{r}_{\text{Poi}} \approx 0.386$ to $\bar{r}_{\text{GOE}} \approx 0.536$. Error bars in (a) and (b) correspond to $5\sigma$ intervals (b) $J/h = 1/2$ As $h$ becomes larger the ergodic phase is suppressed, at accessible system sizes does not reach $r_{\text{GOE}}$ at all. (c) The crossing points $W_c$ of $r$-series from successive system sizes. Evaluating these at low $J/h$ was not possible as the lines become increasingly close to parallel at the crossing point. This data is shown over a density plot corresponding to the $\bar{r}$ values for $L = 12$. Error bars for (c) denote $1\sigma$ intervals.

of the two successive series of $r$ data. These crossing points also indicate that the critical disorder begins drifting to lower $W/J$ with decreasing $J/h$. Though these could not be reliably extracted at lower $J/h$ as successive series become increasingly close to parallel at their crossing points. This

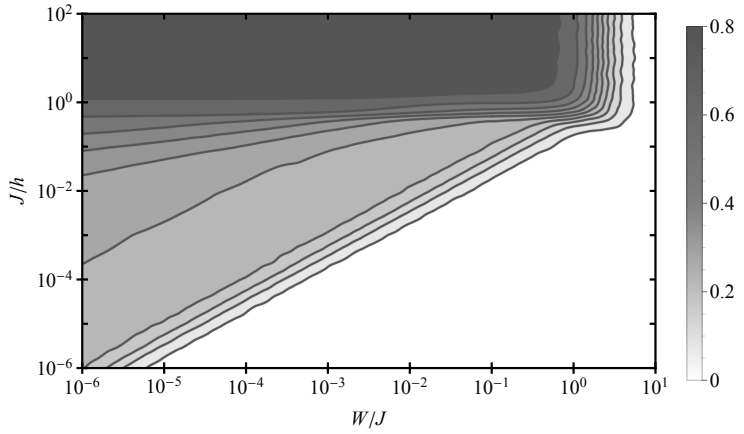


Figure 6.17: *Spectrally averaged entropy of entanglement shows the separation of the transition:* The eigenstate entropy of entanglement $S$ is plotted for $L = 12$. $S$ has been rescaled to the interval $[0, 1]$ by dividing by $(L \log 2)/2$. At large $J/h$ the transition scales as $W/J \sim$ cons. whereas at lower values a transition to $W/J \sim J/h$ becomes clear. However this transition does not induce the same degree of entanglement and one sees shallower contours corresponding to the successive subsidiary transitions at $W/J \sim (J/h)^n, n \in \mathbb{Z}$. This corresponds to the effective hopping in different parts of the spectrum.

is evident for the $L = 11, 12$ in Figure 6.16b.

The MBLD transition is not the only feature that affects the value of the level spacing ratio: the translational symmetry at $W = 0$ also causes $r$ to drop significantly. For finite-size systems this feature extends to finite $W/J$ but is a unrelated to localizing behaviour.[①] In Figure 6.16b, with smaller $J/h$, we find the transition point, and hence the ergodic region, are suppressed to lower $W/J$. At accessible system sizes the ergodic phase becomes sufficiently small $r$ does not reach $r_{\text{GOE}}$. In Figure 6.16c we explore this in the full parameter space of the model, the ergodic region, indicated by the density plot, is shown to disappear rapidly at the same point as the corresponding feature in Figure 6.15.

At large $J/h$ the dominant hybridising process is single spin flips, controlled by the parameter $J$. Hence in this regime we see, in Figure 6.16c, that the transition point scales as $W/J \sim$ cons. This process becomes unable to induce significant hybridisation at lower $J/h$ as it typically results in large violations of conservation of energy. However the second order of two successive spin flips does not, and typically this process, controlled by the energy scale $J^2/h$, takes over as the dominant channel for hybridisations. This indicates that the MBLD transition will switch from $W/J \sim$ cons to $W/J \sim J/h$, this change in behaviour is visible in both Figure 6.16c and Figure 6.17 where the spectrally average entanglement entropy is plotted on log-log scale. However due to the kinetic constraint, this second order process does not induce significant hybridisation if the density of excitations is too low for this process to reliably connect resonant configurations. As previously argued, at low magnetisation density $\delta M/L = M/L + 1$ above the ground state, it is typically necessary to rearrange domains of spins of length $d = L/\delta M$ to couple nearly resonant configurations, and we thus expect $W \sim J_{\text{eff}}^{d \to d'}$ for $d, d' \sim L/\delta M$. However to see this it is necessary to use a method which allows spectral resolution.

### 6.6.2 Eigenstate entropy of entanglement

In Figure 6.17 we plot the spectrally averaged eigenstate entropy of entanglement, in which it is apparent that the transition separates into different a crossover. Our previous arguments leads

[①] Figure 6.15 shows that when accounting for this symmetry the erroneous values of $r$ are not present, and the Gaussian statistics are recovered.

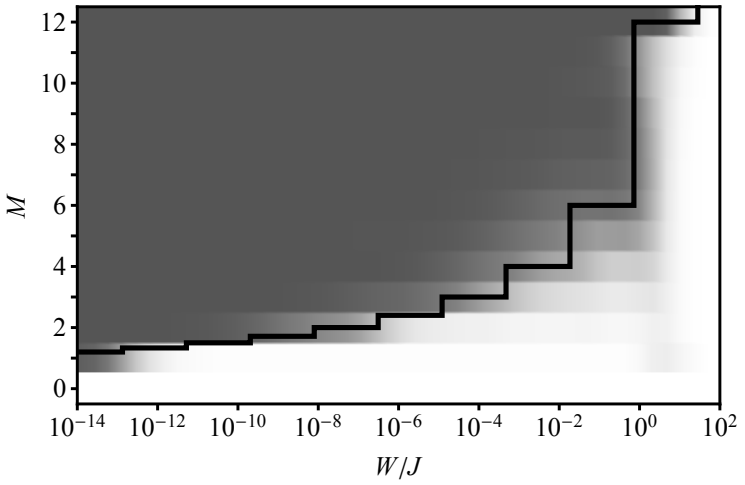


(a)

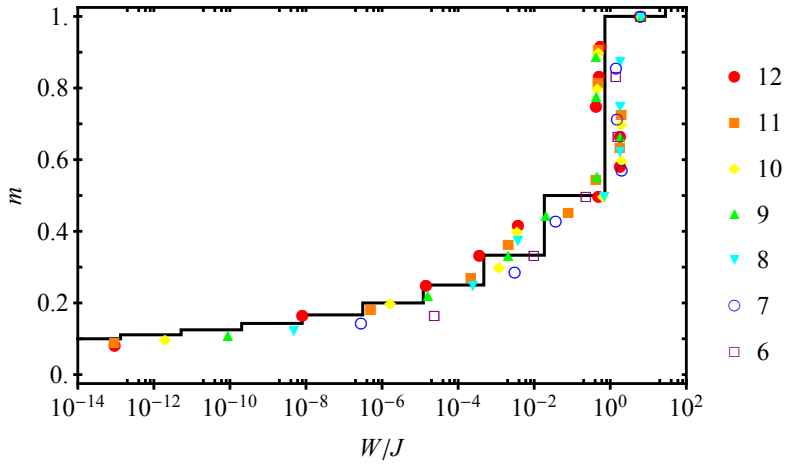


(b)

Figure 6.18: *Spectrally resolved entropy of entanglement shows the slow movement of the mobility edge through the spectrum with increasing disorder:* (a) Density plots of the average half-cut entropy of entanglement in eigenstates for different magnetisation sectors. The entanglement entropy for each sector has been normalised to $S \in [0, 1]$ by dividing by its $W = 0$ value. We see the mobility edge appear for extremely weak disorder, and move very slowly through the spectrum. Density data is shown from $L = 12$, $J/h = 0.4$. The perturbation theory estimate of this transition $J_{\text{eff}} = W$ is also shown (solid black) (b) Comparison of MBLD transition numerical data and perturbation theory. The transition point is estimated by taking $S(W^*) = S(0)/2$. Numerical data is plotted for system sizes 6 to 12. Approximate correspondence with the form of the leading order perturbation theory estimate $J_{\text{eff}} = W$ (solid black) is evident.

us to expect this separation corresponds to different parts of the spectrum. We will evidence this with a spectrally resolved study of eigenstate entanglement.

In the ergodic phase mid-spectrum eigenstates have volume law entanglement, whereas in the MBL phase the area law entanglement, usually characteristic of low-energy states, persists throughout the spectrum. The transition between these two is captured by the eigenstate entanglement entropy $S$ across a bipartition of the system into two equally sized contiguous pieces. For the ergodic phase $S$ scales with the volume $L$ whereas in the MBL region it will scale with the localization length $S \sim \xi$. Thus as $\xi$ becomes small we expect a drop in $S$. This quantity is studied for fixed $J/h = 0.4$ with increasing disorder in Figure 6.18. In this plot the entanglement entropy is calculated for each approximated quasi-magnetisation sector by averaging over $N = 50$ disorder realisations and over the eigenstates within the sector. We know *a priori* the frozen all-down $|\downarrow\downarrow\downarrow\downarrow\cdots\rangle$ state exactly corresponds to the $M = -L$ sector since this is always an eigenstate. To approximate other quasi-magnetisation sectors we sort the remaining eigenstates by energy, and take the lowest $\binom{L}{1}$ to be the $M = 1 - L$ sector, the next $\binom{L}{2}$ be the $M = 2 - L$ sector and so on (where $\binom{n}{m}$ is the binomial coefficient). In Figure 6.18a the drop in the entanglement at low magnetisation density $M/L$ can be seen to correspond to the form of the line $J_{\text{eff}} = W$ (using the form from equation (I.33) with $d = \lceil L/M \rceil$). In Figure 6.18b the critical disorder is compared with the form from perturbation theory of $J_{\text{eff}} = W$. Rigorous identification of the MBLD transition point by finite size scaling is not possible as systems of different lengths yield different possible values of $m \in \{1/L, 2/L, \cdots 1\}$ and cannot be easily compared. Instead we approximate the transition point as the value $W^*$ for which the entanglement entropy has half of its disorderless value, i.e. $S(W^*) = S(0)/2$.[①] The correspondence is both plots is evident across many orders of magnitude of $W/J$ despite the approximations made in estimating both the quasi-magnetisation sectors, the critical points, and perturbative analysis.

### 6.6.3 Eigenstate range of entanglement

Here we aim to evidence that the entanglement does indeed exhibit area law scaling below the putative mobility edge. To see the transition in the entanglement entropy from volume law to area law we study two quantities: the entanglement entropy directly, as well as the range of entanglement $\zeta$. To estimate $\zeta$ we calculate the probability $p_{\beta|\alpha} = |\langle E_\beta| X_i |E_\alpha\rangle|^2$ of measuring the system in the eigenstate $|E_\beta\rangle$ after having (i) prepared the system in the state $|E_\alpha\rangle$ and (ii) acted on $i$th site with an arbitrary local operator $X_i = \boldsymbol{x}\cdot\boldsymbol{\sigma}_i$ (where $|\boldsymbol{x}| = 1$ enforces normalisation of the resulting state). The distribution $p_{\beta|\alpha}$ will have the majority of its mass distributed over a number of eigenstates $\# \sim 2^\zeta$, where the length scale $\zeta$ can be understood as the number of 'bit' degrees of freedom reconFigured by the action of the local operator $X_i$. Thus the inverse participation ratio $I$ of the state $X_i |E_\alpha\rangle$ in the basis $|E_\beta\rangle$, given by

$$I = \left\langle \frac{1}{\sum_\beta p_{\beta|\alpha}^2} \right\rangle_{\alpha,\boldsymbol{x},i}, \tag{6.61}$$

will scale as $I \sim 2^\zeta$, where the average $\langle\cdot\rangle_{\alpha,x_i,i}$ is over $\alpha$ corresponding to initial states from chosen energy window, over local operators $X_i$, over sites $i$, and over disorder realisations. Defining $\zeta = \log_2 I$, we expect that in the ergodic phase $\zeta \sim L$ grows linearly with the system size, whereas in the MBL phase $\zeta \sim$ cons. with increasing system size. When the average over $\beta$ in equation (6.61) is made over the full spectrum we expect that $\zeta \sim \xi$ where $\xi$ is the localization length.

We can heuristically interpret this statistic as a spectrally resolved localization length. This quantity is plotted in Figure 6.19b for both the QEM (left panel) and with $\gamma = 1/4$ corresponding to

[①] This is likely to be an underestimate as the critical point is known to drift to lower $S$ with increasing system size.

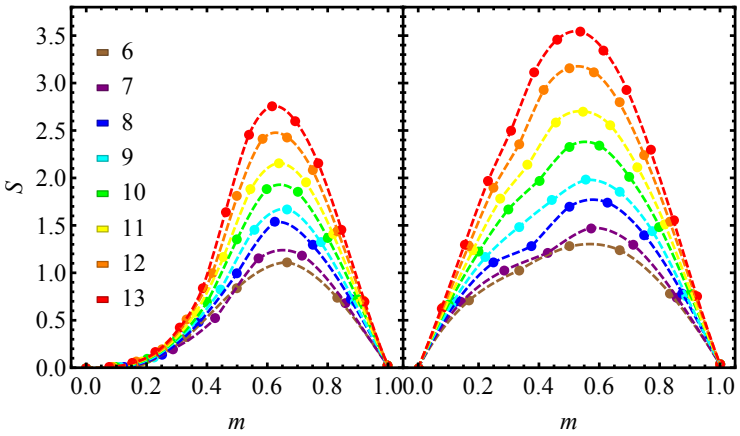


(a)

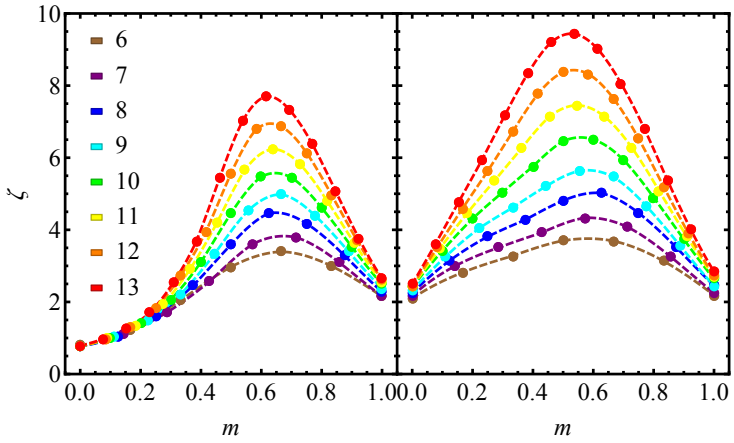


(b)

Figure 6.19: *Lack of growth of entanglement below the mobility edge:* Below the mobility edge both (a) the entanglement $S$ in eigenstates and (b) the range of entanglement $\zeta$ saturate with increasing system size for $\gamma = 0$ (left panels). There is no corresponding feature for $\gamma = 1/4$ (right panels) which does not have a mobility edge. This behaviour is observed only in the kinetically constrained model ($\gamma = 0$). The dashed curve interpolates between data (solid points) collected for $J/h = 0.4$, $W/J = 0.1$, $\gamma = 0, 0.25$

the softened kinetic constraint (right panel). For the softened constraint the $\zeta$ grows approximately linearly throughout the spectrum with increasing system size. This growth of $\zeta$ with the system size indicates that in longer systems the entanglement occurs over increasingly long length scales, which do not appear to saturate with the growth of the system, indicating the widespread hybridisation characteristic of the ergodic phase.

However for the kinetically constrained QEM we see that in the low energy region, below the putative mobility edge, corresponding to localized behaviour, the behaviour is markedly different, with the value of $\zeta$ becoming independent of the system size, as is characteristic of localized behaviour.

### 6.6.4 The localization length

In addition to the previously discussed length scale $\zeta$, we can access the localization length directly via the finding the LIOM using a Wegner-Flow [276, 291, 294] introduced in Section 6.2.3. This method uses a continuous flow to construct the local unitary which maps the physical $\sigma_i^z$ operators—the 'p-bits'—onto the LIOM—the 'l-bits'. Once one has obtained the LIOM one can estimate the localization length of the system. Properties of the flow and this procedure are detailed in Section 6.2.2. In the full-MBL phase the LIOM $\tau_i^z$ are a set of operators for which $[H, \tau_i^z] = 0$, and formally their locality requires that $\mathrm{tr}\left[\tau_i^z X\right] \sim |X| \mathrm{e}^{-d/\xi}$ where $d$ is the distance of the support of $X$ from the localization centre $i$, and $|X|$ an appropriate operator norm. To avoid conflating possible different effects from the choice of $X$ and the distance $d$ we choose to study only the single site operator overlaps[①] given by $\mathrm{tr}\left[\tau_i^z \sigma_j^\alpha\right] \sim \mathrm{e}^{-|i-j|/\xi}$.

This localization length $\xi$ is extracted by a linear regression of $|i-j|$ versus $\log\left(\mathrm{tr}\left[\tau_i^z \sigma_j^\alpha\right]\right)$ is and shown in Figure 6.20. In this Figure we see a sharper response to disorder at increased $J/h$.

Unfortunately this method suffers from several deficiencies: (i) the slowness of integration (discussed in Section 6.2.4) means that only modest system sizes are accessible (ii) The value of $\xi$ extracted via this appears to fail to go to zero in the ergodic phase. This is because in the presence of disorder, there will be significant random variation in $\mathrm{tr}\left[\tau_i^z \sigma_j^\alpha\right]$ in addition to the exponential decay which we are attempting to extract. This is very much analogous to the wavefunction in the single particle case, as shown in Figure 6.3. Unfortunately in such modest system sizes the peaks and troughs of these local random variations are not easily distinguishable from the global effects of the exponential decay induced by localization.

## 6.7 Conclusions and discussion

In this chapter we have studied a disordered kinetically constrained model, which in previous studies had been argued to show localizing behaviour in the absence of disorder [272, 305]. Introducing disorder allows us to explore how the behaviour of the clean model connects to established notions of MBL behaviour which focus of the disordered limit.

The model was obtained by quantising a classical toy model for spin-glass behaviour in the absence of disorder [306, 307]. It consists of a directional and kinetically constrained process in which a spin may flip only if its left neighbour is in the $\uparrow$ configuration. It is generally expected that the presence of many-body mobility edges are destabilised by the existence of mobile ergodic bubbles. However we find that in this model, the restrictive dynamics mean that there are no processes by which an ergodic patch may translate itself. If we consider such an patch of high energy density, in a configuration of otherwise typically low energy density, we find that such a

[①] In ref [276] the statistics of these operator overlaps were found to be independent of the support of $X$, where they depended only on the distance of the of the support of $X$ from the localization centre. We see some deviation from this behaviour: with support becoming irrelevant only when it was greater than one site, whereas overlaps between the $\tau^z$ and single site operators have larger than otherwise expected coefficients.

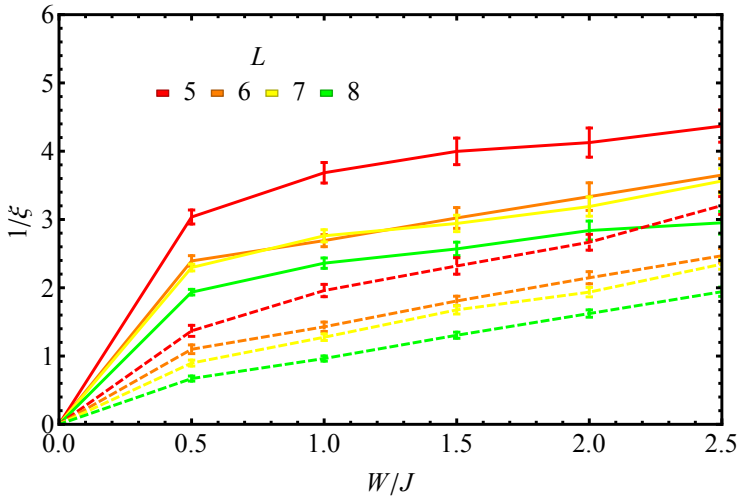


Figure 6.20: *localization lengths:* The values of the localization length extracted from the integrals of motion found using the Wegner flow (see Section 6.2.3) for $J/h = 1/3$ (solid) and $J/h = 3$ (dashed). Unfortunately the limitations of this method mean that only small system sizes are accessible. In these small system sizes the exponential decay cannot easily be separated from random variations in the ergodic phase. This leads to a non-zero localization length appearing in the ergodic phase. It seems these methods are not particularly useful for accessing the localization length.

patch may easily extend rightwards, but the time-scale for reforming in translated position is set by the dynamical time-scales of region of lower energy density to the left of the patch, and not by the internal dynamics of the patch. This appears to prevent rare ergodic patchs from moving rapidly through the system and melting the uncharacteristically slow dynamics, a process which has been suggested to prevent localizing behaviour in disorder free systems and a mobility edges in many body systems [270, 304] both of which we observe here.

Due to these constrained dynamics we find that vestiges of the magnetisation sectors of the non-interacting problem persist to finite interaction at low energies ($\sim 1/L$). Specifically we find from the numerical analysis of the convergence of perturbation theory, summarised by Figure 6.13, that lowest $N \approx 2.35h/J$ magnetisation sectors of the model have this uncharacteristically weak hybridisation, constituting a fraction $\approx 2.35h/(LJ)$ of the bandwidth. In Section 6.5.1 we found that a perturbative analysis of the model supported this picture. This was confirmed in finite size systems by numerics in Section 6.5.2 in which we that the perturbative expansion corrections of conserved magnetisation sectors of the non-interacting model converged. This behaviour as not observed when the kinetic constraint was relaxed. This emergent banding of the spectrum is usually only found as a result of wide separation of energy scales, but is found here for $J$, $h$ of similar value. This effect is known to induce localization like behaviour [303, 312]. In this system it results in slowed thermalizing dynamics, and induces a transition to Poissonian statistics to the spectrum at low energies. This behaviour is MBL-like but, consistent with what might be expected for a translation invariant system [313], does not lead to violations of ETH, and the eigenstate statistics remain ergodic. However, these statistic are altered by the presence of only weak disorder, in this case the low energy region becomes localized, and there is a many-body mobility edge. This situation is depicted in Figure 6.12 which should be compared directly with Figure 6.17 and Figure 6.16c.

The mobility edge sits at an energy $\sim h/L$ above the ground state. This disappears to infinitely small energies in the limit of infinite system size, consistent with ref [270], but is felt in any finite system below temperatures $T \sim h/\log L$, allowing this effect to be felt at larger system sizes. This spectral asymmetry was inherited directly from the classical model which has markedly different

dynamics at low energy density [306]. This was supported by numerics of the entanglement entropy in Section 6.6.2 and entanglement length scales in Section 6.6.3

When we consider the usual limit of infinite system size analysis indicates that in the clean system, in the limit of large $L$ and fixed $\delta M = M - L$ the time-scale for the relaxation of states below the mobility edge diverges as $\sim \left(\sqrt{2}J/h\right)^{4L/M}$, and the corresponding bands become asymptotically flat. However in this limit the localized states constitute a vanishing fraction of the spectrum and so this is arguably a multi-particle rather than true many-body effect. In this limit the localized states undergo an eigenstate phase transition from ETH-consistent to ETH-violating at arbitrarily weak disorder.

We determine that the key ingredients for the interesting behaviour of this model are as follows: (i) the existence of frozen regions in which excitations offer the only dynamics (ii) that no single excitation can translate itself (except for with a process of order that grows with the system size), but instead can only 'facilitate' translations of other excitations that require rearrangements of the entire frozen region separating the two excitations. This results in effective matrix elements that are exponentially small in the typical distance between excitations.

We have investigated via both perturbation theory and numerics in accessible system sizes to explore whether they are consistent with this understanding of the dynamics. We have studied the spectral properties, the extracted LIOM, and entanglement structure in both spectrally averaged and spectrally resolved statistics and found them to be consistent with this understanding.

We note lastly that the contrived structure of the dynamics may mean that it is unlikely that such systems naturally occur. A more fruitful line of investigation to observe these dynamics may be to manufacture such systems of qubits [314].

# 7 | Closing Remarks

In this thesis we have discussed results in the simulation and representation of many body quantum dynamics, and have applied this to the analysis of criticality in one dimensional systems, to the analysis of adiabatic quantum computation in open systems, and to a study on localizing behaviour in a kinetically constrained spin model. The central theme that connected this different studies is an interest in the structure of many-body quantum correlations, with particular interest in the notion of thermalization in these systems.

In Chapter 2 we developed tools for time-evolving an interesting variational ansatz, the correlator product state. We then focussed on a specific sub-class of these states, the uCPS, which allow for analysis of the thermodynamic limit. With these states we explored the fidelity with which they were able to capture various kinds of critical and non-critical phenomena. In particular we developed heuristics for ensuring the parameters of the ansatz are chosen to best capture the physics of a given system. We additionally found that CPS states provide a stable means by which to extract the central charge in a critical system.

In Chapter 3 we developed tools for dynamically evolving wavefunction ansätze in the presence of the thermalizing influence of the environment. We applied this to the study of qubit arrays and found that we were able to recover dynamics which are closely related to a heuristic model of the D-Wave computer. We extended this to the analysis of two-spin system in Chapter 4 and to many body systems in Chapter 5. In Chapter 5 we used this to develop a methodology for benchmarking adiabatic adiabatic quantum computers and used this to analyse the D-Wave machine. Our analysis indicated that the D-Wave is a machine whose function is strongly inhibited by thermalisation.

In Chapter 6 we analysed when thermalisation breaks down, and hence when local quantum information is protected from the thermalizing influence of its environment. We studied a kinetically constrained system for evidence of the many-body localised phase. We found evidence of a qualitatively different behaviour at low energies, which includes a violation of ETH for arbitrarily weak disorder at the bottom of the spectrum.

More detailed discussion of the results and findings has been given in each chapter. We use the remainder of the thesis as an opportunity to discuss the potential for further work

## 7.1 Further study on correlator product states

Our study or correlator product states followed the established ansatz in which the basis in which the states are defined is fixed. It was shown that there is a non-trivial sensitivity to this choice of basis, and that a poor choice of basis can negatively impact both the fidelity of the approximation, and the efficiency if any time integration. The natural resolution of this is naturally to include local basis rotations among the variational parameters of the system.

The correlator product state scheme is particularly interesting for the fact that certain heuristic optimisation routines exists which remain efficient non-stochastic in dimensions $D > 1$ [80], and that they similarly remain efficiently representable and samplable in arbitrary dimensions, and are naturally amenable to the corner transfer matrix method [315]. This leaves hope that they

may provide an interesting possibility for developing useful tools for the dynamical simulation of quantum systems in dimensions $D > 1$.

## 7.2 Further study on entanglement dynamics

In chapters 3 and 4 we studied how the effect of a bath very rapidly destroys certain quantum correlations while others persist for much longer time-scales. In chapter 5 we used this to motivate the idea of a computational manifold—in which the state contained only correlations which persisted on time-scales longer than the time for computation. As a computational manifold we chose weakly entangled states which can be efficiently simulated, as this allowed for a meaningful comparison with classical computational resources.

Establishing for a given system what the long time persistent correlations are, and computing only with these degrees of freedom would protect a system from decoherence. These ideas have been previously investigated in the context of universal quantum computation [316–321]. However they have not been investigated in analogue schemes, such as quantum annealing and AQC, in which the lack of requirement for linear dynamics in the computational subspace could make such schemes easier to work with.

## 7.3 Further study on localizing behaviour

### 7.3.1 Wegner flow

The Wegner flow suffers from poor convergence, as was found in chapter 6 and other studies [276, 322] this limits its utility and to modest system sizes. It is possible that different choices of the underlying costs function $\Delta$ (6.38) will lead to generators of the flow, equation (6.41), with better convergence properties, that could increase the utility of this tool. Combining such an improved variant of equation (6.32) may provide a method for extracting the mid-spectrum eigenstates whilst avoiding some of the stability problems of previous methods [260, 261, 279].

### 7.3.2 Kinetic constraints in higher dimensions

One can easily construct generalisation of the QEM in higher dimensions. For example in an $N$-dimensonal cubic geometry the model

$$H = -J \sum_{\boldsymbol{x},\boldsymbol{a}} (\sigma^z_{\boldsymbol{x}} + 1)\sigma^x_{\boldsymbol{x}+\boldsymbol{a}} - \sum_{\boldsymbol{x}} h_{\boldsymbol{x}} \sigma^z_{\boldsymbol{x}} \tag{7.1}$$

where $\boldsymbol{x}$ labels lattice sites and $\boldsymbol{a}$ are a set of $N$ primitive lattice vectors. In choosing $\boldsymbol{a}$ we have privileged a set of lattice directions (i.e. a particular orthant) in the same spirit as the left-right asymmetry of the QEM. It remains an open question whether full-spectral many-body localization can exist in higher dimensions, but there is an expectation that it will not. This is due to the toy argument that the exponential fall of in coupling to resonances $\sim (J/W)^d$ at larger distances $d$ cannot compete with the super exponential growth $\sim 2^{d^N}$ in many body basis states, which describe a $d \times d \times \ldots$ patch of system, with which a resonance is possible. This is unless the dimensionality of the lattice $N = 1$.

On the converse it is trivially clear that, for the model 7.1, in any dimension, if we consider a state of all $\downarrow$ spins but for one $\uparrow$ spin, this excitation is only delocalized by a process which wraps around the entire system. Thus this excitation does not delocalize in finite time as $L \to \infty$. Since these particular structure of kinetic constraints bias the system towards localization in a different

manner to disorder, it will be interesting to see if anything survives at similarly low energy in higher dimensions.

### 7.3.3 Kinetic constraints in the mid spectrum

The model studied in chapter 6 inherently only biased the low energy states towards localization, whilst conversely mid-spectrum and low-lying states were relatively unaffected. It may be possible to design kinetic constraints which have a more uniform influence. Though in conceiving such things one must be careful not to inadvertently split the model into a proliferation of independent sectors by construction, in which case with regard to MBL one is somewhat begging the question. For example the kinetic constraint

$$H = -\frac{J}{2}\sum_i (1+\sigma^z_{i-1})\sigma^x_i(1-\sigma^z_{i+1}) + \sum_i \frac{h_i}{2}\sigma^z_i \tag{7.2}$$

which contains only one process

$$|\cdots\uparrow\uparrow\downarrow\cdots\rangle \xleftrightarrow{2J} |\cdots\uparrow\downarrow\downarrow\cdots\rangle \tag{7.3}$$

which is not sufficient to connect any state with one with which it can hybridise.

### 7.3.4 Localization with translational invariance

There has been some interest in understanding the potentially novel circumstances in which we might find many-body localizing behaviour [269,272,285,299–302,305,323]. In chapter 6 we followed up some suggestive numerical results [272, 305] and investigated whether kinetic constraints can induce a localized phase. We found some non-trivial effects, but did not uncover a localizing tendency as strong as the full-spectral transition seen in strongly disordered systems. A perspective that may be worthy of further investigation would be to explicitly construct models that are both translationally invariant and within the purview of random matrix theory. This would again pit two notions against each other: (i) that a sufficiently disordered matrix will have Poisson statistics (ii) that translationally systems are ergodic. We found the coexistence of these features in the low lying energy states of the QEM. However it would be interesting to see if this can exist away from the edges of the spectrum to which it was relegated in the QEM. An potentially interest model for investigating this might be 'random mass' Tonks-Girardeau gas of many distinguishable hard-core bosons hopping on a lattice, each with their mass drawn from a characteristic distribution

$$H = -\sum_i \frac{1}{2m_i}\frac{\partial^2}{\partial x_i^2} + 2c\sum_{ij}\delta(x_i - x_j) \tag{7.4}$$

with $c \to \infty$ and $m_i$ drawn from $p(m)$. In particular it may be possible to go beyond numerics using recent results in Leib-Liniger models [324].

## 7.4 Further study on the quantum-classical dimer

In chapter 4 we explored how in the case of the two-spin dimer the classical classical dynamics are extended to the full quantum dynamics only by the additional two site cumulant $\left\langle \sigma_1^i \sigma_2^j \right\rangle - \left\langle \sigma_1^i \right\rangle \left\langle \sigma_2^j \right\rangle$ which is always zero for the classical case.

The more general situation of $N$ spins is naturally more complicated. However, the ideas above can still be generalized to many spin systems following the dimer example.

The dynamics of the classical configurations can be systematically dressed with higher and higher order correlators, generated a series analogous to the BBGKY hierarchy of classical kinetic theory.

This is structurally similar in spirit to the approximations of DMRG [325, 326] and tensor network states [24, 33] however in these cases the unbounded growth of entanglement in many body systems eventually makes evolution untenable without large approximations. In these approximations low lying values of the Schmidt spectrum are simply thrown away. An alternative approach would be to throw away specifically the correlations corresponding to high order cumulants, which at high order are unphysical and do not correspond to something which can be experimentally observed.

This may be particularly efficient in aiding descriptions of quantum matter in which strong quantum correlations develop in only rare regions. The explicit restrictions on quantum correlations in the localized phase, as set by the l-bits, introduces the interesting possibility that for weak interactions, and short time scales it may be possible to approximate well the quantum many body dynamics with classical models.

That the state of a localized system does not explore the full exponential complexity possible of the many body wavefunction follows from the very restricted nature of localized dynamics [259]. As local disorder become stronger, the dynamics of local expectation values is increasingly defined by local fields, and converges on the classical dynamics in the limit of strong disorder. In the quantum system this correspondence is spoiled by rare resonant patches which entangle quickly. Berry's conjecture implies that these will behave chaotically in the classical dynamics.

On longer time-scales this causes the classical trajectories to typically become ergodic due to instabilities, while quantum dynamics favour localization [327, 328]. However it may be possible to systematically fix this breakdown at its source, introducing the minimal set of quantum degrees of freedom necessary to locally fix such chaotic regions, and stabilise the integrable nature of the quantum many body dynamics.

Systematically 'repairing' the dynamics by dressing the classical equations of motion in this way provides an interpolation scheme between the classical and quantum dynamics that introduces a minimal set of quantum degrees of freedom required to capture the dynamical properties of the system. This bare bones representation may allow for efficient extraction of meaningful transport properties of the quantum system.

# Appendices

# A | Glossary of Abbreviations

| | |
|---|---|
| **AQC** | Adiabatic quantum computation |
| **BAA** | Basko Aleiner Altshuler, in particular with reference to refs [219, 220] |
| **CPS** | Correlator product states |
| **DMRG** | Density matrix renormalization group |
| **ETH** | Eigenstate thermalization hypothesis |
| **FM** | Ferromagnet |
| **FDT** | Fluctuation dissipation theorem |
| **GOE** | Gaussian orthogonal ensemble |
| **GSE** | Gaussian symplectic ensemble |
| **GUE** | Gaussian unitary ensemble |
| **iff** | If and only if |
| **iid** | Independent and identically distributed |
| **IOM** | Integral of motion |
| **KAM** | Kolmogorov, Arnol'd and Moser, in reference to their theorem. |
| **KCM** | Kinetically constrained model |
| **LHS** | Left hand side |
| **LIOM** | Local integral of motion |
| **LLG** | Landau Lifshitz Gilbert |
| **NP** | Non-deterministic polynomial time |
| **MBL** | Many body localization |
| **MBLD** | Many body localization-delocalization transition |
| **MERA** | Multiscale entanglement renormalization ansatz |
| **MPS** | Matrix product states |
| **P** | Polynomial time |
| **PEPS** | Projected entangled pair states |
| **PM** | Paramagnet |
| **QEM** | Quantum east model |
| **RF SQUID** | Radio frequency superconducting quantum interference device |
| **RHS** | Right hand side |
| **TDSE** | Time dependent Schrödinger equation |
| **TDVP** | Time dependent variational principle |

| | |
|---|---|
| **TLS** | Two level system |
| **TN** | Tensor network |
| **TTN** | Tree tensor network |

# B | Efficient implementation of TDVP with Matrix product states

In this chapter we review the integration of the projected Schrödinger equation for MPS using the TDVP.

## B.1 Efficient time integration of the TDVP

A matrix product state (MPS) takes the form:

$$|\Psi[A]\rangle = \sum_{i_1,i_2,\cdots,i_N}^{d} v_L^\dagger A_1^{i_1} A_2^{i_2} \cdots A_N^{i_N} v_R \, |i_1, i_2, \cdots, i_N\rangle \tag{B.1}$$

where $d$ is the number of physical (spin) degrees of freedom, and $A^{i_a}$ is a $\chi_{A-1} \times \chi_A$ matrix, while $v_L$ and $v_R$ are vectors of dimensionality $\chi_0$ and $\chi_N$ respectively. The dimension of these internal/virtual indices is the bond dimension $\chi$. The open boundary condition Ansatz is presented here for the sake of concreteness - the periodic boundary condition MPS Ansatz corresponds to taking a trace in place of contraction by $v_L^\dagger$ and $v_R$. Graphically the state (B.1) can be represented as:

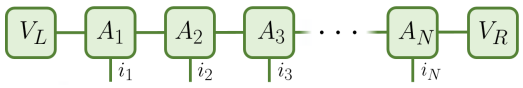

, (B.2)

where the horizontal lines represent the internal bond dimension indices, while the physical spins are denoted by the vertical lines with 'uncontracted' ends. Here and in what follows we will not graphically depict any variation in the dimensionality of physical or bond indices.

Transformations of the MPS matrices of the form:

$$A^{i_n} \to G_{n-1} A^{i_n} G_n^{-1} \, , \tag{B.3}$$

where $G_n, G_{n-1} \in GL(\chi, \mathbb{C})$, leave the state invariant, and are referred to as gauge transformations. The gauge transformations of the boundary (co)-vectors are given by $v_L^\dagger \to v_L^\dagger G_0^{-1}$, and $v_R \to G_N v_R$.

Applying the time-dependent variational principle (ie, TDVP, see introduction to Section 2.1) to the MPS variational class [94, 329] yields:

$$\dot{A}^*(t) = \underset{\dot{A}(t)}{\operatorname{argmin}} \left\| |\Phi(\dot{A}, A)\rangle + \mathrm{i} H(t) \, |\Psi(A(t))\rangle \right\| \, , \tag{B.4}$$

where the object $|\Phi(dA, A)\rangle$ is given by:

$$\begin{aligned}|\Phi(dA,A)\rangle = &\sum_{i_1,\cdots,i_N} v_L^\dagger dA_1^{i_1} A_2^{i_2}\cdots A_N^{i_N} v_R\,|i_1,i_2,\cdots,i_N\rangle \\ &+ \sum_{i_1,i_2,\cdots,i_N}^{d} v_L^\dagger A_1^{i_1} dA_2^{i_2}\cdots A_N^{i_N} v_R\,|i_1,i_2,\cdots,i_N\rangle \\ &+ \quad\cdots \\ &+ \sum_{i_1,i_2,\cdots,i_N}^{d} v_L^\dagger A_1^{i_1} A_2^{i_2}\cdots dA_N^{i_N} v_R\,|i_1,i_2,\cdots,i_N\rangle \\ &= \sum_\alpha dA^\alpha \frac{\partial}{\partial A^\alpha}|\Psi(A)\rangle \equiv \sum_\alpha dA^\alpha\,|\partial_\alpha\Psi(A)\rangle\ .\end{aligned} \tag{B.5}$$

The $\alpha$ index on the last line combines physical, virtual, and site indices. Unlike elements in the variational class of MPS, the objects $|\Phi(dA, A)\rangle$ form a vector space - and are in fact tangent vectors to the MPS manifold [94, 330]. The gauge invariance of MPS (B.3) can be shown to imply the invariance of tangent states under

$$dA^{i_n} \to dA^{i_n} + X_{n-1}A^{i_n} - A^{i_n}X_n\ , \tag{B.6}$$

where the matrices $X$ live in the Lie algebra of the gauge group.

In this appendix we will study MPS directly in the thermodynamic limit ($N \to \infty$), and will use a translation invariant Ansatz, taking the MPS tensors to be position independent (which clearly requires a constant bond dimension $\chi$). We refer to the class of such states as uniform MPS (uMPS). Graphically a uMPS is represented as:


(B.7)

The largest eigenvalue of the uMPS transfer matrix $E$,

$$E := \sum_i A^i \otimes \bar{A}^i\ , \tag{B.8}$$

needs to be fixed to unity in order to ensure finite normalisation. The state norm is given by $(l|r)$, where $(l|$ and $|r)$ are respectively the left and right eigenvectors of $E$ corresponding to eigenvalue 1, and since the eigenvectors can be rescaled freely the state can always be normalised to one.

The expectation value of a local operator acting on $n$ sites can now be written as:

$$\begin{aligned}&\langle\Psi[A]|\,O\,|\Psi[A]\rangle = \\ &\sum_{\substack{i_1,i_2,\cdots,i_n,\\ j_1,j_2,\cdots,j_n}}^{d} (l|O^{j_1\cdots j_n}_{i_1\cdots i_n}\left(A^{i_1}\cdots A^{i_n}\right)\otimes\left(\bar{A}_{j_1}\cdots\bar{A}_{j_n}\right)|r)\ .\end{aligned} \tag{B.9}$$

The cost of computing this object, using the optimal sequence of contractions, can be seen to scale as $O(nd\chi^3)$.

The uMPS parametrisation is invariant under gauge transformations:

$$A^i \to GA^iG^{-1}\ , \tag{B.10}$$

and these can be used to set either $\rho_l = \mathbf{1}$ or $\rho_r = \mathbf{1}$ (but in general not both), where $\rho_l$ is the $\chi^2$ dimensional co-vector $(l|$ reshaped to a $\chi\times\chi$ matrix, and similarly for $\rho_r$. The corresponding

gauge transformations in the tangent plane (see (B.6)) are given by $dA^i \to dA^i + XA^i - A^iX$, and this gauge freedom can be used to set either:

$$(l|\sum_i dA^i \otimes \bar{A}^i = 0 \quad \text{or} \quad \sum_i dA^i \otimes \bar{A}^i|r) = 0 \ , \tag{B.11}$$

but again in general not both. These are referred to as, respectively, the left and right tangent space gauge conditions.

The Gram matrix, given by:

$$\Omega_{\bar{\alpha}\beta} := \mathrm{i}\langle \partial_{\bar{\alpha}}\Psi(A)|\partial_\beta\Psi(A)\rangle \ , \tag{B.12}$$

defines a natural metric on the uMPS manifold [330]. The TDVP equations can be formally expressed as:

$$\sum_\beta \Omega_{\bar{\alpha}\beta}\dot{A^\beta} = \langle \partial_{\bar{\alpha}}\Psi(A)|\, \hat{H}(t)\, |\Psi(A(t))\rangle \ . \tag{B.13}$$

Imposing either the left or right tangent gauge condition (B.11) simplifies the equations significantly, and is in fact necessary to eliminate infinities in (B.13) stemming from transformations along the uMPS state itself. The expression for the overlap of two tangent vectors takes the simple form:

$$\sum_{\bar{\alpha},\beta} \bar{A}'^{\bar{\alpha}}\Omega_{\bar{\alpha}\beta}dA^\beta = -\mathrm{i}|\mathbb{Z}|(l|dA \otimes d\bar{A}'|r) \ , \tag{B.14}$$

since the left (or right) gauge condition implies that all terms for which the $dA$ and $d\bar{A}'$ tensors are not at the same site are zero. The Gram matrix then takes the simple form:

$$\Omega = -\mathrm{i}\rho_l \otimes \rho_r \ . \tag{B.15}$$

The nature of the right hand side of (B.13) is elucidated by contracting it with $d\bar{A}'^{\alpha}$:

$$\begin{aligned}\sum_{\bar{\alpha}} d\bar{A}'^{\bar{\alpha}}\, \langle \partial_{\bar{\alpha}}\Psi(A)|\, \hat{H}(t)\, |\Psi(A(t))\rangle = \\ |\mathbb{Z}|\, \big((l|H^{AA}_{dA'\bar{A}}|r) + (l|H^{AA}_{\bar{A}d\bar{A}'}|r) \\ +(l|H^{AA}_{\bar{A}\bar{A}}(\mathbf{1}-E)^{PI}(A\otimes d\bar{A}')\|r)\big) \ .\end{aligned} \tag{B.16}$$

Here $H^{AA}_{\bar{A}d\bar{A}'}$, for example, stands for the contraction of the two 'ket' indices of a local term in the Hamiltonian, which is assumed to be translation invariant, with two $A$ uMPS tensors, and the contraction of its 'bra' indices with $\bar{A}$ and $d\bar{A}'$ tensors. $PI$ indicates a pseudo-inverse on the subspace of $\chi^2 \times \chi^2$ matrices defined by the projector $\mathbf{1}_{\chi^2\times\chi^2} - |r)(l|$. This term stems form a summation over all contributions with the $d\bar{A}'$ tensor to the right of the local Hamiltonian terms (the terms when $d\bar{A}'$ is on the left are zero due to the left tangent gauge condition, which is assumed here).

# C | Efficient implementation of TDVP with uCPS

The integration of the equations of motion 2.62 and evaluation of local expectation values can be performed with computational costs $\mathrm{O}(\chi^3)$. Here we elaborate how this, naively unexpectedly high, efficiency is achieved at the two key bottlenecks

## C.1 Efficient time integration of the TDVP

As discussed at the end of Section 2.2.5, naively following an optimal uMPS contraction ordering in the uCPS setting will yield a computational cost that scales at best as $O(\log(\chi)\chi^3)$ for a local Hamiltonian, and we expect to be able to do better. Details of a contraction ordering such that the cost of calculating the right hand side of (2.62) scales as $O(\chi^3)$ are given in Appendix C.2.

In addition to this, it is necessary to find an $O(\chi^3)$ implementation for the action by the inverse of the $\chi^2 \times \chi^2$ matrix $\Omega$ on equation (2.62). Stemming from the fact that our parametrisation of variations $dC$ satisfying the tangent left gauge condition of equation (2.60) depends in a complicated way on the eigenvalue decomposition of the transfer matrix, the uCPS Gram-matrix turns out to be a much more complex object than its uMPS equivalent (given simply by $\rho_l \otimes \rho_r$ (B.15)).

We start by writing it in the basis of the left and right eigenvectors of the transfer matrix as

$$\Omega_{\tilde{\gamma}\delta|\tilde{\alpha}\beta} = \sum_{ij} \lambda^{ij} T^{ij}_{\tilde{\gamma}\delta|\tilde{\alpha}\beta} \ , \tag{C.1}$$

where

$$T^{ij}_{\tilde{\gamma}\delta|\tilde{\alpha}\beta} = \left(\bar{R}^i_{\tilde{\gamma}} \bar{L}^j_{\delta}\right)\left(R^i_{\tilde{\alpha}} L^j_{\beta}\right) \ , \tag{C.2}$$

and

$$\lambda^{ij} = \frac{L^i_1 R^j_1}{E_{ij}} \tag{C.3}$$

Naively, both the cost of calculating $\Omega^{-1}$, as well as its action on a vector, scales as $O(\chi^6)$; an obvious approach to reduce this cost would be to attempt to write $\Omega$ in a decomposition that would allow the action of its inverse on a vector to be calculated with cost $O(\chi^3)$, analogous to the manner in which a $O(d^2\chi^6) \to O(d\chi^3)$ reduction in cost is achieved for uMPS TDVP. As far as we have been able to ascertain, this is not possible for (C.1). While such an inverse *does* exist for the matrix obtained by replacing all tilde-indices in (C.1) by their non-tilde extensions, and is given by inverting all the constituent matrices and taking $\lambda^{ij} \to \left(\lambda^{ij}\right)^{-1}$, the truncation of the eigenvalue-one eigenvector seems to conclusively obstruct achieving any appropriate decomposition for $\Omega^{-1}$ itself. It is nevertheless possible to use an iterative method (such as the biconjugate gradient

algorithm) in order to calculate the action of $\Omega^{-1}$ and retain $O(\chi^3)$ efficiency, since this only requires that the action of $\Omega$ on an arbitrary vector be calculable with cost $O(\chi^3)$.

A further caveat to the above is that in order to achieve $O(\chi^3)$ scaling, the number of iterations in the iterative subroutine required to achieve some desired accuracy must scale as a constant for large enough $\chi$, and this is not guaranteed. For example, the number of iterations *does* scale worse than constant if the pre-conditioning step is not implemented appropriately (its implementation is described in Appendix C.3). However, beyond this observation, for all the examples studied in this chapter the iterative subroutine is observed to scale as $O(\chi^3)$.

Finally, it should be noted that while the general uMPS TDVP algorithm does not require an iterative subroutine for the Gram-matrix inverse step in order to achieve optimal efficiency, it does require such a subroutine in order to calculate the third term in (B.16) with cost $O(d\chi^3)$. The same term in uCPS TDVP, on the other hand, can be calculated explicitly with cost $O(\chi^3)$, as is described in Appendix C.2.

## C.2 Contracting uCPS with computational cost $O(\chi^3)$

As mentioned in Section 2.2.4 we show how to efficiently evaluate CPS contractions. Let us first consider the following term appearing on the right hand side of equation (2.62)

$$\langle \partial_{\tilde{\alpha}\beta}\psi | \, H \, |\psi\rangle =$$

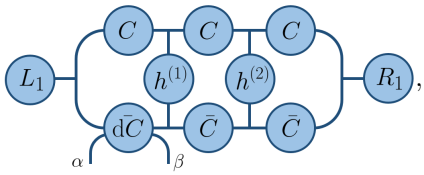


(C.4)

where a two-site Hamiltonian has been assumed. Symbolically this corresponds to:

$$h_{\tilde{\alpha}\beta} = \sum_{ijkmnpq} L_1^i \; C^{ij} \; h^{(1)}_{jp} \; C^{jk} \; h^{(1)}_{kq} \; C^{km} \; R_1^m$$
$$\qquad\qquad\qquad\qquad\quad \mathrm{d}\bar{C}^{ip}_{\alpha\beta} \qquad\qquad\quad \bar{C}^{pq} \qquad\qquad\quad \bar{C}^{qm} \tag{C.5}$$

where $h^{(1)}$ and $h^{(2)}$ constitute part of a two-site term of the Hamiltonian, and, per equation 2.60, $\mathrm{d}\bar{C}$ is given by

$$\mathrm{d}\bar{C}^{ik}_{\tilde{\alpha}\beta} = \frac{R^i_{\tilde{\alpha}} L^k_{\beta}}{\bar{C}^{ik}}. \tag{C.6}$$

The following contraction ordering (which starts from the right):

1. $a^{kq} = \sum_m C^{km}\bar{C}^{qm}R_1^m$ is obtained at cost $O(\chi^3)$,
2. $b^{kq} = {h^{(2)}}_{kq}a^{kq}$ is obtained at cost $O(\chi^2)$,
3. $c^{pk} = \sum_q \bar{C}^{pq}b^{kq}$ is obtained at cost $O(\chi^3)$,
4. $d^{jp} = \sum_k C^{jk}c^{pk}$ is obtained at cost $O(\chi^3)$,
5. $e^{jp} = h^{(1)}_{jp}d^{jp}$ is obtained at cost $O(\chi^2)$,
6. $f^{ip} = \sum_j L_1^i C^{ij}e^{jp}$ is obtained at cost $O(\chi^3)$,
7. $g^{ip} = f^{ip}\left(\bar{C}_{ip}\right)^{-1}$ is obtained at cost $O(\chi^2)$,
8. $h_{\tilde{\alpha}\beta} = g^{ip}R^i_{\tilde{\alpha}}L^p_{\beta}$ is obtained at cost $O(\chi^3)$,

can be seen to yield maximal cost $O(\chi^3)$ at any internal step. It is easy to find other contraction orderings that yield the same cost.

There are two more contributions to the right hand side of (2.62) that are similar to the above. One of these is obtained by substituting $d\bar{C}^{pq}_{\tilde{\alpha}\beta}$ in place of $\bar{C}^{pq}$ in (C.5), and the other by making the same substitution in place of $\bar{C}^{qm}$. A contraction ordering with $O(\chi^3)$ efficiency can be obtained for these in a very similar manner as what has been demonstrated above. Further efficiencies which do not alter the scaling but are nonetheless useful can be gained by re-using the tensors $a$, $b$, $c$, $d$, $e$, $f$ and $g$ where possible in these evaluations.

The remaining contribution to (2.62) corresponds to a sum over all terms with $d\bar{C}^{\tilde{\alpha}\beta}$ not coinciding with the Hamiltonian, and is given by:

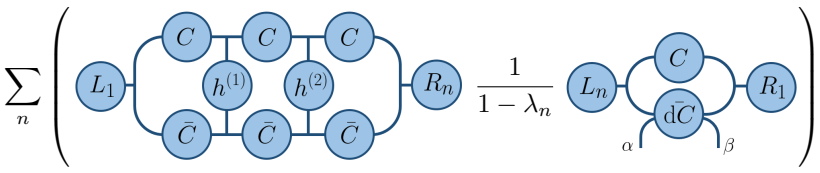


(C.7)

The uMPS expression corresponding to this is given by the term on the last line of (B.16); as with uMPS, the terms with $d\bar{C}$ to the left of the Hamiltonian are zero due to the left tangent gauge condition, which has been assumed here. It is worth noting that while the computation of the pseudo-inverse acting on a vector in the uMPS expression can only be achieved at cost $O(d\chi^3)$, by recourse to an iterative procedure such as the biconjugate gradient algorithm, the uCPS term above can be computed explicitly at cost $O(\chi^3)$ using a contraction ordering similar to that described for (C.5).

## C.3 uCPS Gram matrix inverse pre-conditioning

The uCPS Gram matrix is given by:

$$\Omega^{\tilde{\gamma}\delta|\tilde{\alpha}\beta} = \sum_{ij} \lambda_{ij} T_{ij}^{\tilde{\gamma}\delta|\tilde{\alpha}\beta} \ , \tag{C.8}$$

where

$$T_{ij}^{\tilde{\gamma}\delta|\tilde{\alpha}\beta} = \left(\bar{R}^i_{\tilde{\gamma}} \bar{L}^j_{\delta}\right)\left(R^i_{\tilde{\alpha}} L^j_{\beta}\right) \ . \tag{C.9}$$

The convention is that the non-tilde indices run over the whole range, 1 to $\chi$, while the tilde-indices correspond to a truncation and run from 2 to $\chi$, and $V^1_{(L)} \equiv V_{(L)}$ and $V^1_{(R)} \equiv V_{(R)}$ are the left and right eigenvectors corresponding to eigenvalue one.

Let us first consider the matrix:

$$\tilde{\Omega}_{\tilde{\gamma}\delta|\tilde{\alpha}\beta} = \sum_{ij} \frac{1}{\lambda_{ij}} \tilde{T}_{ij}^{\tilde{\gamma}\delta|\tilde{\alpha}\beta} \ , \tag{C.10}$$

where

$$\tilde{T}_{ij}^{\tilde{\gamma}\delta|\tilde{\alpha}\beta} = \left(\bar{L}^i_{\tilde{\gamma}} \bar{R}^j_{\delta}\right)\left(L^i_{\tilde{\alpha}} R^j_{\beta}\right) \tag{C.11}$$

(note the $L \leftrightarrow R$ swap versus equation (C.9)). The obstruction to $\tilde{G}$ being the inverse of $G$ can be understood as originating in the truncation of the eigenvalue one eigenvector in our implementation

of the left tangent gauge condition (2.60). Namely, the eigenvector matrices obey:

$$L^i_\delta R^i_\epsilon = \delta_{\delta\epsilon} \ , \tag{C.12a}$$
$$\bar{R}^j_\epsilon L^m_\epsilon = \delta^{jm} \ , \tag{C.12b}$$
$$R^i_{\tilde{\delta}} L^i_{\tilde{\epsilon}} = \delta_{\tilde{\delta}\tilde{\epsilon}} \ , \tag{C.12c}$$
$$\bar{L}^j_\epsilon R^m_\epsilon = \delta^{jm} \ , \tag{C.12d}$$
$$L^j_{\tilde{\gamma}} \bar{R}^m_{\tilde{\gamma}} = \delta^{jm} - L^j R^m \ , \tag{C.12e}$$
$$\bar{R}^j_{\tilde{\gamma}} L^m_{\tilde{\gamma}} = \delta^{jm} - R^j \bar{L}^m \ , \tag{C.12f}$$

where summation over repeated indices is understood. The presence of projectors in the last two lines expresses the deformation of the exact orthogonality relations due to the $\alpha \to \tilde{\alpha}$ truncation, which prevents (C.10) from being the Gram matrix inverse.

In order to explicitly compute the action of the inverse of $\Omega$ on a vector with computational cost scaling as $O(\chi^3)$, it is necessary to be able to express $\Omega^{-1}$ in the general form (C.10), or at least as a sum of a constant number of terms of this form. We have not managed to find any suitable solution that would bypass the obstruction described above (but have also not proved that doing so is impossible). However, in order to achieve $O(\chi^3)$ scaling, one can instead make use of an iterative algorithm, the bi-conjugate gradient (stabilised) method. This algorithm provides a solution for $\vec{x}$ in the equation $\mathbb{A}\vec{x} = \vec{b}$, where $\mathbb{A}$ is some invertible matrix; as input only the action of the matrix $\mathbb{A}$ on a vector needs to be supplied. For the present problem this can be achieved with cost $O(\chi^3)$, using a contraction scheme along the lines of Appendix C.2.

Achieving $O(\chi^3)$ scaling assumes that, in the limit of large bond dimension $\chi$, the number of iterations needed for the bi-conjugate gradient algorithm to converge to some desired accuracy scales as roughly a constant. In practice this may not always be the case. Using the bi-conjugate algorithm as described above, $O(\chi^3)$ scaling is indeed spoiled for a general uCPS TDVP computation. This is ultimately related to the fact that uCPS, viewed as a restriction of uMPS, fixes nearly all the gauge freedom, which in general causes $G$ to become badly conditioned in the course of a TDVP run - even when Schmidt values of the uCPS state itself are much larger than machine precision. One solution to this problem is to make a judicious choice of a pre-conditioner matrix. In general, this refers to a matrix $M^{-1}$, in $M^{-1}N\vec{a} = M^{-1}\vec{b}$, which can be employed in the iterative algorithm in order to make the problem better conditioned. For the present case, taking $M^{-1} = \tilde{\Omega}$ in fact seems to be the optimal choice (again, the iterative algorithm only needs to be supplied with the action of $\tilde{\Omega}$ on a vector, which can be achieved with cost $O(\chi^3)$). It should be noted that without the pre-conditioning step, for most of the examples in this chapter, it would only have been practically feasible to compute quenches and ground state approximations with very small overlap sizes, and many of the computations performed in this chapter would not have been accessible.

# D | Fluctuation Dissipation Relation

In this appendix we provide the well-known statement and justification of the formal fluctuation dissipation relation.

The fluctuation dissipation relation is introduced in physical terms in Section 3.1.5. Here we justify a more formal statement. Let $X$ be an observable, fluctuations in $X$ measured by an observer are represented via the time ordered correlator

$$\begin{aligned} G^{\mathrm{T}}(t_1 - t_2) &= -i \left\langle \mathcal{T} X_1(t_1) X_2(t_2) \right\rangle \\ &= \theta(t_1 - t_2) \left\langle X_1(t_1) X_2(t_2) \right\rangle + \theta(t_2 - t_1) \left\langle X_2(t_2) X_1(t_1) \right\rangle \end{aligned} \tag{D.1}$$

where $\mathcal{T}$ is the time ordering operator. Conversely the susceptibility of the system to a perturbing field is characterised by the retarded correlator

$$G^{\mathrm{R}}(t_1 - t_2) = -i\theta(t_1 - t_2) \left\langle [X_1(t_1), X_2(t_2)] \right\rangle . \tag{D.2}$$

For bosonic systems the fourier transforms of these function are related by

$$\mathrm{Re}G^{\mathrm{T}}(\omega) = \mathrm{Re}G^{\mathrm{R}}(\omega) = \mathrm{Re}G^{\mathrm{A}}(\omega) \tag{D.3}$$

$$\mathrm{Im}G^{\mathrm{T}}(\omega) = \mathrm{Im}G^{\mathrm{R}}(\omega) \coth\left(\frac{\beta\omega}{2}\right) = -\mathrm{Im}G^{\mathrm{A}}(\omega) \coth\left(\frac{\beta\omega}{2}\right) \tag{D.4}$$

where we have also defined the advanced correlator $G^{\mathrm{R}}(t_1 - t_2) = \left[G^{\mathrm{A}}(t_2 - t_1)\right]^{\dagger}$. In the Keldysh formalism the same relations are simply recast as

$$G^{\mathrm{K}}(\omega) = \coth\left(\frac{\beta\omega}{2}\right) \left(G^{\mathrm{R}}(\omega) - G^{\mathrm{A}}(\omega)\right). \tag{D.5}$$

These statements are justified below.

## D.1 The relation of the retarded correlator to susceptibility

We consider a system with the Hamiltonian $H_0$ and ask, how does the $\langle X \rangle$ change when we weakly perturb the system with the operator $X$. The perturbation is introduced via the adiabatic transition matrix $S = U_f^{\dagger} U_0$ where

$$U = \mathcal{T} \exp\left[-\mathrm{i} \int_{-\infty}^{t} \mathrm{d}t' \left(H_0 + f(t')X\right)\right] \tag{D.6}$$

which defines

$$X_f = S X S^{\dagger}. \tag{D.7}$$

For sufficiently weak perturbation weak can expand this to leading order in $f$ obtaining

$$S = \mathbf{1} + \mathrm{i}\int_{-\infty}^{t} \mathrm{d}t' f(t')X(t') + \cdots \tag{D.8}$$

where $X(t)$ implies the Heisenberg picture. This yields

$$\langle X_f(t)\rangle = -\mathrm{i}\int \mathrm{d}t'\theta(t-t')f(t')\left\langle [X(t),X(t')]\right\rangle = \int \mathrm{d}t' G^R(t-t')f(t'). \tag{D.9}$$

which establishes the retarded correlators role in determining susceptibility to perturbation.

## D.2 Fluctuation dissipation relation in the Lehmann representation

The statement of the fluctuation dissipation relation is easily shown in the Lehmann representation which is found by resolving the bath over the many body eigenbasis $|E_\alpha\rangle$. In this picture

$$\begin{aligned} G^{>}(t_1-t_2) &= -\mathrm{i}\left\langle X(t_1)X(t_2)\right\rangle \\ &= -\mathrm{i}Z^{-1}\sum_{\alpha\beta}\left(\mathrm{e}^{-\mathrm{i}E_\alpha t_1}X_{\alpha\beta}\mathrm{e}^{\mathrm{i}E_\alpha t_2}\right)\left(\mathrm{e}^{-\mathrm{i}E_\beta t_2}X_{\beta\alpha}\mathrm{e}^{\mathrm{i}E_\beta t_2}\right)\rho_\alpha \\ &= -\mathrm{i}Z^{-1}\sum_{\alpha\beta}\mathrm{e}^{-\mathrm{i}\omega_{\alpha\beta}(t_1-t_2)}|X_{\alpha\beta}|^2\rho_\beta. \end{aligned} \tag{D.10}$$

Where $\rho_\alpha$ defines the initial distribution. We also define a Fourier transform

$$G(\omega) = \int \mathrm{d}t\,\mathrm{e}^{\mathrm{i}\omega t - 0^+|t|}G(t) \tag{D.11}$$

where the convergence factor $0^+$ prevents infinities at the boundaries. Using these we readily obtain

$$G^{\mathrm{T}}(\omega) = Z^{-1}\sum_{\alpha\beta}|X_{\alpha\beta}|^2\rho_\beta\left[\frac{1}{\omega+\omega_{\alpha\beta}+\mathrm{i}0^+} - \frac{1}{\omega-\omega_{\alpha\beta}-\mathrm{i}0^+}\right] \tag{D.12}$$

$$G^{\mathrm{R}}(\omega) = Z^{-1}\sum_{\alpha\beta}|X_{\alpha\beta}|^2\rho_\beta\left[\frac{1}{\omega+\omega_{\alpha\beta}+\mathrm{i}0^+} - \frac{1}{\omega-\omega_{\alpha\beta}+\mathrm{i}0^+}\right] \tag{D.13}$$

$$G^{\mathrm{A}}(\omega) = Z^{-1}\sum_{\alpha\beta}|X_{\alpha\beta}|^2\rho_\beta\left[\frac{1}{\omega+\omega_{\alpha\beta}-\mathrm{i}0^+} - \frac{1}{\omega-\omega_{\alpha\beta}-\mathrm{i}0^+}\right] \tag{D.14}$$

where the only difference is on the sign structure of the imaginary perturbations, and from which equations (D.3) and (D.4) are readily verified for bosonic correlators using $|[a^\dagger]_{\alpha\beta}|^2 = \alpha\delta_{\alpha,\beta+1}$ and $\omega_{\alpha\beta} = \omega_0(\alpha-\beta)$.

For the Keldysh correlator we must be more careful, as this is defined via the classical fields which mix fields on the two branches of the Keldysh integral.

$$G^{\mathrm{K}}(t_1-t_2) = \frac{1}{2}\left(G^{++}(t_1-t_2) + G^{--}(t_1-t_2) + G^{-+}(t_1-t_2) + G^{+-}(t_1-t_2)\right) \tag{D.15}$$

where the labels denote the branches of the Keldysh contour (labelled in Figure 3.3). Where operators are contour-ordered. This ordering is such that when the branches are different, the evaluations are branch-ordered (+ before −) and the branches are the same they are time-ordered

for + and anti-time-ordered for −. Thus we obtain

$$G^{\mathrm{K}}(t_1 - t_2) = \frac{1}{2}\left(G^{\mathrm{T}}(t_1 - t_2) - \left[G^{\mathrm{T}}(t_1 - t_2)\right]^{\dagger} + G^{>}(t_1 - t_2) - \left[G^{>}(t_1 - t_2)\right]^{\dagger}\right) \tag{D.16}$$

which in the Lehmann representation reads

$$G^{\mathrm{K}}(t_1 - t_2) = -\mathrm{i}Z^{-1}\sum_{\alpha\beta} \mathrm{e}^{-\mathrm{i}\omega_{\alpha\beta}(t_1 - t_2)}|X_{\alpha\beta}|^2\left(\rho_\alpha + \rho_\beta\right) \tag{D.17}$$

and the Fourier transform

$$G^{\mathrm{K}}(\omega) = Z^{-1}\sum_{\alpha\beta}|X_{\alpha\beta}|^2(\rho_\alpha + \rho_\beta)\left[\frac{1}{\omega - \omega_{\alpha\beta} + \mathrm{i}0^+} - \frac{1}{\omega - \omega_{\alpha\beta} - \mathrm{i}0^+}\right]. \tag{D.18}$$

From this point it is a matter of manipulation to show that

$$G^K(\omega) = 2\mathrm{i}\,\mathrm{Im}G^T(\omega) \tag{D.19}$$

and from this and equation (D.12) follows the result of equation (D.5)

# E | Dissipative dynamics of a two level system

## E.1 The dissipative dynamics of individual quantum spins

A derivation of a dissipative equation of motion for quantum spins can be made in the Heisenberg picture using the approach of quantum Langevin equations. In this approach dissipative stochastic equations, are found to describe the dynamics of operators.[②] These equations are analogous to the stochastic Langevin equations of classical physics. Beginning with the Hamiltonian

$$\begin{aligned} H &= H_{\mathrm{S}} + H_{\mathrm{I}} + H_{\mathrm{E}} \\ H_{\mathrm{S}} &= -\frac{1}{2}\sum_i B_i \sigma_i \\ H_{\mathrm{I}} &= \frac{1}{2}\sum_{i,\omega} g_\omega \sigma_i x_{i,\omega} = \frac{1}{2}\sum_{i,\omega} \frac{g_\omega}{\sqrt{2\omega}} \sigma_i \left(b_{i,\omega} + b_{i,\omega}^\dagger\right) \\ H_{\mathrm{E}} &= \frac{1}{2}\sum_i \left(p_{i,\omega}^2 + \omega^2 x_{i,\omega}^2\right) = \sum_{i,\omega} \omega\, b_{i,\omega}^\dagger b_{i,\omega}, \end{aligned} \tag{E.1}$$

where the index $i$ runs over spatial dimensions, and the three terms of the Hamiltonian describe the system (a spin degree of freedom), interactions, and the environment (an oscillator bath) respectively. The dynamics of this system are then given by the Heisenberg equation of motion

$$\begin{aligned} \dot{\boldsymbol{\sigma}} &= i\left[H, \boldsymbol{\sigma}\right] = \boldsymbol{\sigma} \times \boldsymbol{B} - \boldsymbol{\sigma} \times \sum_\omega \frac{g_\omega}{\sqrt{2\omega}} \left(\boldsymbol{b}_\omega + \boldsymbol{b}_\omega^\dagger\right) \\ \dot{\boldsymbol{b}}_\omega &= i\left[H, \boldsymbol{b}_\omega\right] = -i\omega\, \boldsymbol{b}_\omega - \frac{i g_\omega}{2\sqrt{2\omega}} \boldsymbol{\sigma} \end{aligned} \tag{E.2}$$

where the bold-face indicates a vector of operators. The second of these equations can be formally integrated to yield

$$\begin{aligned} \boldsymbol{b}_\omega(t) &= \boldsymbol{b}_\omega(t_0) \mathrm{e}^{-i\omega(t-t_0)} - \frac{i g_\omega}{2\sqrt{2\omega}} \int_{t_0}^t \mathrm{d}t' \boldsymbol{\sigma}(t') \mathrm{e}^{-i\omega(t-t')} \\ &= \boldsymbol{b}_\omega(t_0) \mathrm{e}^{-i\omega(t-t_0)} - \frac{g_\omega}{2\omega\sqrt{2\omega}} \boldsymbol{\sigma}(t) + \frac{g_\omega}{2\omega\sqrt{2\omega}} \int_{t_0}^t \mathrm{d}t' \dot{\boldsymbol{\sigma}}(t') \mathrm{e}^{-i\omega(t-t')} \end{aligned} \tag{E.3}$$

where in the second line we have integrated by parts. Rearranging this we obtain a form for the interaction

$$\sum_\omega \frac{g_\omega}{\sqrt{2\omega}} \left(\boldsymbol{b}_\omega(t) + \boldsymbol{b}_\omega^\dagger(t)\right) = -\boldsymbol{\eta}(t) - \sum_\omega \frac{g_\omega^2}{4\omega^2} \boldsymbol{\sigma}(t) + \int_{t_0}^t \mathrm{d}t \gamma(t-t') \dot{\boldsymbol{\sigma}}(t') \tag{E.4}$$

[②] A detailed overview of this approach is available in ref [331].

where we have defined a force operator $\boldsymbol{\eta}$ and a memory function $\gamma$ given by

$$\boldsymbol{\eta}(t) = -\sum_{\omega} \frac{g_\omega}{\sqrt{2\omega}} \boldsymbol{b}_\omega(t_0) \mathrm{e}^{i\omega(t-t_0)} + \text{h.c.} \tag{E.5}$$

$$\gamma(t) = \sum_{\omega} \frac{g_\omega^2}{2\omega^2} \cos\omega t. \tag{E.6}$$

Substituting this back into the equation of motion for $\boldsymbol{\sigma}$ we obtain the LLG equation in operator form

$$\dot{\boldsymbol{\sigma}}(t) = \boldsymbol{\sigma}(t) \times \left( \boldsymbol{B} + \boldsymbol{\eta} - \int_{t_0}^{t} \mathrm{d}t' \gamma(t-t')\, \dot{\boldsymbol{\sigma}}(t') \right). \tag{E.7}$$

Taking expectation value of all operators, and making the simplifying assumption that there are no persistent quantum correlations between the system and the bath, i.e. that $\langle \sigma_i(t) \dot{\sigma_j}(t') \rangle \approx \langle \sigma_i(t) \rangle \langle \dot{\sigma_j}(t') \rangle = s_i(t) \dot{s_j}(t')$ we obtain

$$\dot{\boldsymbol{s}}(t) = \boldsymbol{s}(t) \times \left( \boldsymbol{B} + \boldsymbol{\eta} - \int_{t_0}^{t} \mathrm{d}t' \gamma(t-t')\, \dot{\boldsymbol{s}}(t') \right) \tag{E.8}$$

which is precisely equation (3.46). Careful evaluation shows that the Gaussian form of the bath that we chose results in $\boldsymbol{\eta}$ is a Gaussian noise term characterised by the correlator $\langle \eta(t)\eta(t') \rangle = T\gamma(t-t')$ for $t > t'$.

In the Markovian approximation $\gamma(t-t') = \gamma\delta(t-t')$ yielding the well-known Landau-Lifshitz-Gilbert (LLG) equation (3.9a) in its usual equivalent form is obtained. This describes the dynamics of a quantum spin-1/2 degree of freedom interacting with a bath of harmonic oscillators. We have neglected the possibility of entanglement between the system and environment. Together with the Markovian approximation this amounts to an entirely classical treatment of the environment.

Although we were able to obtain the dissipative dynamical equations in this simple case the approach used will quickly become unwieldy in larger systems. Hence in the main text we use a more general proscription for obtaining dissipative dynamical equations using Keldysh theory.

## E.2 Markovian dynamics

In this appendix we derive the effective O(2) dynamics given in equations (3.55) and (3.56), in which the Markovian model features a confinement of $\phi$. In the dissipative limit $\tau_p \gg \tau_d$ the spin dynamics are given by equation (3.51). To leading order in the long time-scale, the $\phi$ dynamics take the form

$$\dot{\phi} = -s\gamma B \sin\theta^* \sin\theta \sin\phi + \eta = -\tau_\phi^{-1} \sin\phi + \eta. \tag{E.9}$$

where as before $\tau_\phi^{-1} = \gamma s B \sin\theta \sin\theta^*$. This corresponds to a Fokker–Planck equation

$$\frac{\partial p}{\partial t} = -\frac{\partial}{\partial \phi} \left( \frac{\sin\phi}{\tau_\phi} - \gamma T \frac{\partial}{\partial \phi} \right) p. \tag{E.10}$$

for an ensemble distribution $p$. The equilibrium solution to equation (E.10) is given by

$$p = \frac{\exp\left(A\cos\phi\right)}{2\pi I_0(A)}, \tag{E.11}$$

where $A = \left(\gamma T \tau_\phi\right)^{-1}$ and $I_n(\cdot)$ are the modified Bessel functions of the first kind. Including the additional sub-leading terms (those in equation (3.51) that are missing from equation (E.9)) leads to a Fokker-Planck equation with no closed form solution. However, the salient features are captured by making an appropriate shift to $\phi$ and rescaling of $A$. This leads to an equilibrium

solution

$$\begin{aligned} p &= \frac{\exp\left(A\cos(\phi-\phi^*)\right)}{2\pi I_0(A)}, \\ \tan\phi^* &= \frac{\sin(\theta-\theta^*)}{s\gamma\sin^2\theta\sin\theta^*}, \end{aligned} \tag{E.12}$$

where $A = (\gamma T\tau_\phi\cos\phi^*)^{-1}$, which deviates from the exact solution only far from the distribution peak. In terms of $\theta$, $A$ takes the form $A = B\sqrt{s^2\gamma^2\sin^4\theta\sin^2\theta^* + \sin^2(\theta-\theta^*)}/(\gamma T\sin\theta)$.

Assuming a separation of time-scales, the remaining $\theta$ dynamics can be found by averaging equation (3.51) over the equilibrium distribution of $\phi$ given in equation (E.12). This leaves a single equation giving the $\theta$ dynamics,

$$\dot{\theta} = -B\sin\theta^*\ \langle\sin\phi\rangle + \eta', \tag{E.13}$$

where $\theta$ is subject to a drift term originating from the mean value of the fast $\phi$ dynamics and a stochastic term which originates from the fluctuations in the $\phi$ dynamics away from their mean value. This approximation becomes accurate on time-scales $t \gg \tau_\phi$. Evaluating this exactly we obtain

$$\langle\sin\phi\rangle = \int \mathrm{d}\phi\, p(\phi)\ \sin\phi = \sin\phi^*\frac{I_1(A)}{I_0(A)} \tag{E.14}$$

for the mean, whereas the noise term is defined by its mean $\langle\eta'(t)\rangle = 0$ and covariance

$$\begin{aligned} \langle\eta'(t)\eta'(t')\rangle &= (B\sin\theta^*)^2\left(\langle\sin\phi(t)\sin\phi(t')\rangle - \langle\sin\phi(t)\rangle\langle\sin\phi(t')\rangle\right) \\ &\approx (B\sin\theta^*)^2\exp(-|t-t'|/\tau_\phi)\left(\langle\sin^2\phi\rangle - \langle\sin\phi\rangle^2\right) \\ &\approx 2\tau_\phi(B\sin\theta^*)^2\delta(t-t')\left(\langle\sin^2\phi\rangle - \langle\sin\phi\rangle^2\right) \\ &= 2\tau_\phi(B\sin\theta^*)^2\delta(t-t')\left[\sin^2\phi^*\left(1-\frac{I_1(A)}{AI_0(A)}-\frac{I_1^2(A)}{I_0^2(A)}\right)+\cos^2\phi^*\frac{I_1(A)}{AI_0(A)}\right]. \end{aligned} \tag{E.15}$$

We consider the limiting cases in which the above form simplifies:

- For $T \ll B$, we have $A \gg 1$ and $I_1(A)/I_0(A) = 1 - 1/(2A), +O(A^{-2})$ which gives, to leading order

$$\begin{aligned} \langle\sin\phi\rangle &= \frac{\sin(\theta-\theta_0)}{s\gamma\sin^2\theta\sin\theta^*}, \\ \langle\eta'(t)\eta'(t')\rangle &= 2\gamma T(B\tau_\phi\sin\theta^*)^2\delta(t-t'). \end{aligned} \tag{E.16}$$

- For $T \gg B$, we have $A \ll 1$ and $I_1(A)/I_0(A) = A/2 + O(A^2)$, which gives, to leading order in $\tau_\mathrm{d}/\tau_\mathrm{p}$,

$$\begin{aligned} \langle\sin\phi\rangle &= \frac{B\sin(\theta-\theta_0)}{2T\gamma\sin\theta}, \\ \langle\eta'(t)\eta'(t')\rangle &= \tau_\phi(B\sin\theta^*)^2\delta(t-t') \end{aligned} \tag{E.17}$$

  Substituting the values of equation (E.16) and (E.17) into equation (E.13) gives the forms equation (3.55) and (3.56) respectively in chapter 3.

## E.3 Drude dynamics

In this appendix we derive the dynamical equation of a single spin coupled to a Drude bath and show that in an appropriate limit the long time-scale $\theta$ dynamics are given by the Markovian equation (3.55) with $\phi$ remaining typically close to $\phi \approx 0$. Using the Drude density of states and evaluating eqs (3.42) and (3.40), in the limit of $T \gg \omega_\mathrm{d}$, one obtains $\langle\eta(t)\eta(t')\rangle = T\gamma(t-t') = T\gamma\omega_\mathrm{d}\exp(-\omega_\mathrm{d}|t-t'|)$. This particular noise $\eta(t)$ can be written in terms of a $\delta$-correlated

stochastic dummy variable $\eta'$ as

$$\eta(t) = -\omega_{\mathrm{d}} \int_{-\infty}^{t} \mathrm{d}t' \mathrm{e}^{-\omega_{\mathrm{d}}(t-t')} \eta'(t') \tag{E.18}$$

which satisfies $\langle \eta'(t)\eta'(t')\rangle = 2\gamma T\delta(t-t')$. Rewriting equation (3.47) the dynamics are obtained as

$$\begin{aligned} \dot{\boldsymbol{s}}_i &= -\boldsymbol{s}_i \times (\boldsymbol{B}_i + \boldsymbol{B}_{\mathrm{diss}}(t)) \\ \boldsymbol{B}_{\mathrm{diss}}(t) &= -\omega_{\mathrm{d}} \int_{-\infty}^{t} \mathrm{d}t' \mathrm{e}^{-\omega_{\mathrm{d}}(t-t')} \left(\gamma \dot{s}_{i,z}(t') - \eta'\right) \hat{\boldsymbol{z}}. \end{aligned} \tag{E.19}$$

Writing the second equation in its differential form we find

$$\begin{aligned} \dot{\boldsymbol{B}}_{\mathrm{diss}} &= -\omega_{\mathrm{d}} \left(\boldsymbol{B}_{\mathrm{diss}} + \gamma \dot{s}_{i,z} \hat{\boldsymbol{z}} - \eta' \hat{\boldsymbol{z}}\right) \\ &= -\omega_{\mathrm{d}} \left(\boldsymbol{B}_{\mathrm{diss}} - \gamma \hat{\boldsymbol{z}} \left[\hat{\boldsymbol{z}} \cdot (\boldsymbol{s}_i \times \boldsymbol{B}_i)\right] - \eta' \hat{\boldsymbol{z}}\right) \end{aligned} \tag{E.20}$$

where the second part follows by substituting $\dot{s}_{i,z}$ and noting that $\hat{\boldsymbol{z}} \cdot (\boldsymbol{s}_i \times \boldsymbol{B}_{\mathrm{diss}}) = 0$. These dynamics equate to equation (3.58) after trivial relabelling.

Separating equation (E.20) into the fast $(\phi, B_{\mathrm{diss}}^{(z)})$ and slow $(\theta)$ degrees of freedom and solving the linearised equations of motion for $\phi$ and $B_{\mathrm{diss}}^{(z)}$ we find that

$$\begin{aligned} \dot{\theta} =& - B \sin\theta^* \ \langle \sin\phi\rangle + \eta', \\ \langle \sin\phi\rangle =& \frac{\sin(\theta-\theta_0)}{s\gamma \sin^2\theta \sin\theta^*} \\ \langle \eta'(t)\eta'(t')\rangle =& (B\sin\theta^*)^2 \mathrm{Cov}(t,t') \end{aligned} \tag{E.21}$$

as before in equation (E.16). However now there are long lasting oscillations in the noise, characterised by $\mathrm{Cov}(t,t') = \langle \sin\phi(t)\sin\phi(t')\rangle - \langle \sin\phi(t)\rangle \langle \sin\phi(t')\rangle$. Evaluating this one finds that

$$\begin{aligned} \langle \eta'(t)\eta'(t')\rangle =& \gamma T \tau_\phi (B\sin\theta^*)^2 \mathrm{e}^{-\frac{\omega_{\mathrm{d}}|t-t'|}{2}} \times \\ & \left[\cos(\omega|t-t'|) + \frac{\omega_{\mathrm{d}}}{2\omega}\sin(\omega|t-t'|)\right] \end{aligned} \tag{E.22}$$

where $\omega = \sqrt{\frac{\omega_{\mathrm{d}}}{\tau_\phi}\left(1 - \frac{\omega_{\mathrm{d}}\tau_\phi}{4}\right)}$ characterises the oscillation frequency of the correlations. These fast oscillations can be seen in Figure 3.7c.

As expected on time-scales much longer that $1/\omega_{\mathrm{d}}$ the covariance has the same value as with the previous cases

$$\begin{aligned} \langle \eta'(t)\eta'(t')\rangle \approx& 2\gamma T (B\tau_\phi \sin\theta^*)^2 \delta(t-t'), \\ =& \frac{2T}{\gamma(s\sin\theta)^2}\delta(t-t'). \end{aligned} \tag{E.23}$$

thus on time-scales much greater than the inverse bath frequency we recover the Markovian case (eqn (E.16)) and the $\theta$ dynamics of eqn (3.55) .

## E.4 Ensemble dynamics

In this appendix we study the dynamics of an ensemble of non-interacting to show the appearance of the Markovian anisotropic dynamics at ensemble level. The ensemble dynamics are captured by a Fokker-Planck equation which is found to have similarly anisotropic dynamics, which can in turn be related to Metropolis Hastings dynamics.

We show that in the simplest case of a non-interacting spins the ensemble dynamics do not

agree with the Bloch equations, this is clear as the anisotropic nature of the dynamics persists even after the ensemble averaging. This result is perhaps surprising so we provide an explicit derivation from the Fokker–Planck equation.

Within the first moment approximation the ensemble is described by the probability distribution

$$p(\boldsymbol{s},t)=\frac{1}{Z}\mathrm{e}^{\boldsymbol{\xi}(t)\cdot\boldsymbol{s}},\qquad Z=\frac{4\pi}{\xi}\sinh\left(\xi s\right). \tag{E.24}$$

The first moment approximation in not appropriate when considering systems of interacting spins as correlations between the trajectories of different spins cannot be neglected. Thus for the purpose of deriving ensemble dynamics, we consider a system of many spins, without interactions between them, each acting under the influence of an external field $\boldsymbol{B}$ and coupled anisotropically, along the $\hat{\boldsymbol{z}}$-direction only, to an ohmic bath.

For a specific realisation of the history of the bath, the dynamics are given by the equation (3.48b). When we sum over the histories of the bath, the dynamics are described by the evolution of the probability distribution (E.24).

Following the approach of Refs [116, 119]—in which an analogous calculation is performed for an isotropic bath coupling, i.e. microscopic dynamics corresponding to equation (3.9b)—we find that the evolution of $p(\boldsymbol{s},t)$is described by the Fokker-Planck equation

$$\dot{p}=\nabla_{\boldsymbol{s}}\cdot\left[\boldsymbol{s}\times\boldsymbol{B}+\gamma\boldsymbol{s}\times\hat{\boldsymbol{z}}\left(\hat{\boldsymbol{z}}\cdot\left[\boldsymbol{s}\times\left(\boldsymbol{B}-T\nabla_{\boldsymbol{s}}\right)\right]\right)\right]p. \tag{E.25}$$

By substituting equation (E.24) into equation (E.25) and integrating over $\boldsymbol{s}$, the dynamics of the parameter $\boldsymbol{\xi}=\xi\hat{\boldsymbol{\xi}}$ are found to be governed by the equation

$$\dot{\boldsymbol{\xi}}+\boldsymbol{\xi}\times\boldsymbol{B}+\gamma s^2\left(\frac{s}{\sigma}-\frac{3}{\xi s}\right)\boldsymbol{\xi}\times\hat{\boldsymbol{z}}\left[\hat{\boldsymbol{z}}\cdot\left(\boldsymbol{\xi}\times\boldsymbol{B}\right)\right]+\gamma T\left[\left(\frac{\sigma}{\xi\sigma'}\hat{\boldsymbol{\xi}}\hat{\boldsymbol{\xi}}^T\right)+\left(\mathbf{1}-\hat{\boldsymbol{\xi}}\hat{\boldsymbol{\xi}}^T\right)\right]\left(\mathbf{1}-\hat{\boldsymbol{z}}\hat{\boldsymbol{z}}^T\right)\left(\boldsymbol{\xi}-\boldsymbol{\xi}_0\right)=0. \tag{E.26}$$

The fixed point of the dynamics is given by $\boldsymbol{\xi}_0=\boldsymbol{B}/T$, which corresponds to the Boltzmann distribution. The mean polarisation is described by the magnetisation $\boldsymbol{m}=\langle\boldsymbol{s}\rangle$ with norm $m=\frac{1}{Z}\frac{\mathrm{d}Z}{\mathrm{d}\xi}=s\left(\coth\left(\xi s\right)-\frac{1}{\xi s}\right)$ and $m'=\frac{\mathrm{d}\sigma}{\mathrm{d}\xi}$ its derivative.

The physical origins of the first three terms are clear, as they correspond to the respective terms of equation (3.48b). The last term corresponds to longitudinal relaxation with a rate $\Gamma_1=\gamma T$ and transverse relaxation with a rate $\Gamma_2=\frac{\gamma T\langle s\rangle}{\xi\langle s\rangle'}$. It should be noted, however, that the dynamics described by these terms differs from the usual isotropic case due to the projecting out of the component in the $\hat{\boldsymbol{z}}$ direction, this reflects the underlying anisotropy of the coupling.

It is possible to re-write equation (E.26) to give the dynamics of the ensemble polarisation $\boldsymbol{\sigma}$, where $\xi$ is defined implicitly by the form of $\sigma(\xi)$. Doing so, one obtains

$$\dot{\boldsymbol{m}}=\boldsymbol{m}\times\boldsymbol{B}+\gamma\frac{s^2}{m^2}\left(1-\frac{3m}{\xi s^2}\right)\boldsymbol{m}\times\hat{\boldsymbol{z}}\left[\hat{\boldsymbol{z}}\cdot\left(\boldsymbol{m}\times\boldsymbol{B}\right)\right]+\gamma T\left(\mathbf{1}-\hat{\boldsymbol{z}}\hat{\boldsymbol{z}}^T\right)\left(\boldsymbol{m}-\frac{m}{\xi T}\boldsymbol{B}\right). \tag{E.27}$$

For a highly polarised ensemble, $m\approx s$, at low temperatures, the ensemble dynamics converge on the microscopic dynamics of equation (3.48b) showing that the unique behaviours described in chapter 3 persist in the ensemble dynamics of the system. These ensemble dynamics are shown in Figure 3.6 where they are obtained from sampling the stochastic sampling of the trajectories defined by equation 3.48, a sample of these trajectories is shown in Figure 3.7. In the main text we discuss the similarity between these dynamics and the Metropolis-Hastings dynamics of refs. [52, 53]. This similarity is most evident in their confinement to dynamics on an O(2) manifold, but is clear also in the similarity between their dynamics, both of which are overdamped and dissipative, as shown in Figure E.1. The existence of such a relationship between overdamped spin

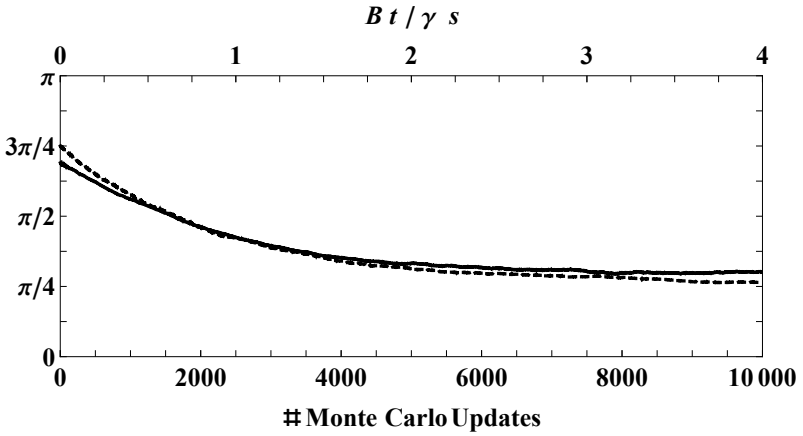


Figure E.1: *Comparison of Metropolis Hastings and anisotropic LLG dynamics.* The ensemble averaged value $\langle\theta\rangle$ of Metropolis Hastings (dashed) dynamics is compared with the anistropic LLG dynamics (solid) data from Figure 3.6. The LLG dynamics have small oscillations (see Figure 3.7 for further detail), thus we plot the ensemble averaged mid-point of these small oscillations, $\langle\theta_M\rangle$, as previously in Figure 3.6. Both simulation were performed using an ensemble of 1000 spins ($s = 1/2$) initialised at $\theta = 3\pi/4$, evolving in a magnetic field in the $\theta^* = \pi/4$, $\phi^* = 0$ direction, and a temperature $T = B/10$. For the LLG dynamics the coupling is $\gamma = 5 \times 10^3$, with energy scales $B = 10T = 100\omega_{\mathrm{d}}$, satisfying $B \gg T \gg \omega_{\mathrm{d}} \gg B/\gamma s$.

dynamics and the Metropolis Hastings algorithm has been previously established [146–148].

# F | Quantum-Classical Dimer

## F.1 Derivation of interpolated equations of motion

We know the dynamics of a single spin-1/2 in an external field, given by the Hamiltonian

$$H = -\frac{1}{2}\boldsymbol{\sigma}\cdot\boldsymbol{B} \tag{F.1}$$

evolve according to

$$\langle\dot{\boldsymbol{\sigma}}\rangle = \langle \mathrm{i}\,[H,\boldsymbol{\sigma}]\rangle = \langle\boldsymbol{\sigma}\rangle\times\boldsymbol{B} \tag{F.2}$$

Similarly, it is easily shown that when we generalise slightly to a two-site Hamiltonian

$$H = -\frac{1}{2}\boldsymbol{\sigma}_1\cdot\boldsymbol{B}_1 - \frac{1}{2}\boldsymbol{\sigma}_2\cdot\boldsymbol{B}_2 - \frac{J}{2}\boldsymbol{\sigma}_1\cdot\boldsymbol{\sigma}_1 \tag{F.3}$$

that the single site expectation value evolves as

$$\langle\dot{\boldsymbol{\sigma}_1}\rangle = \langle \mathrm{i}\,[H,\boldsymbol{\sigma}_1]\rangle = \langle\boldsymbol{\sigma}_1\rangle\times\boldsymbol{B}_1 + J\,\langle\boldsymbol{\sigma}_1\times\boldsymbol{\sigma}_2\rangle \tag{F.4}$$

We can seperate out the dynamics classical parts (local rotations) and entangling parts (mixing across sites). The classical part is found by applying a variational ansatz for the time evolved wavefunction of the form

$$|\dot{\psi}\rangle = -\frac{\mathrm{i}}{2}\left(\dot{\boldsymbol{x}}_1\cdot\boldsymbol{\sigma}_1 + \dot{\boldsymbol{x}}_2\cdot\boldsymbol{\sigma}_2\right)|\psi\rangle \tag{F.5}$$

By maximising the overlap with the exact update (as outlined in Section 2.1) given by $-\mathrm{i}H\,|\psi\rangle$. This yields an equation for $\dot{\boldsymbol{x}}_1$

$$\langle\boldsymbol{\sigma}_1\rangle\times\dot{\boldsymbol{x}}_1 = \langle \mathrm{i}\,[H,\boldsymbol{\sigma}_1]\rangle \tag{F.6}$$

without loss of generality we assume $\boldsymbol{x}$ and $\langle\boldsymbol{\sigma}\rangle$ are perpendicular[②] allowing $\boldsymbol{x}_1$ to be uniquely obtained

$$\dot{\boldsymbol{x}}_1 = -\frac{\langle\boldsymbol{\sigma}_1\rangle\times\langle \mathrm{i}\,[H,\boldsymbol{\sigma}_1]\rangle}{\langle\boldsymbol{\sigma}_1\rangle\cdot\langle\boldsymbol{\sigma}_1\rangle} \tag{F.7}$$

We can then write an effective Hamiltonian that generates these dynamics

$$H_{\mathrm{c}} = -\frac{1}{2}\left(\dot{\boldsymbol{x}}_1\cdot\boldsymbol{\sigma}_1 + \dot{\boldsymbol{x}}_2\cdot\boldsymbol{\sigma}_2\right) = \frac{1}{2}\left(\frac{\boldsymbol{\sigma}_1\cdot\langle\boldsymbol{\sigma}_1\rangle\times\langle \mathrm{i}\,[H,\boldsymbol{\sigma}_1]\rangle}{\langle\boldsymbol{\sigma}_1\rangle\cdot\langle\boldsymbol{\sigma}_1\rangle} + \frac{\boldsymbol{\sigma}_2\cdot\langle\boldsymbol{\sigma}_2\rangle\times\langle \mathrm{i}\,[H,\boldsymbol{\sigma}_2]\rangle}{\langle\boldsymbol{\sigma}_2\rangle\cdot\langle\boldsymbol{\sigma}_2\rangle}\right) \tag{F.8}$$

[②] this amounts to making a gauge choice of the global phase gauge symmetry of quantum mechanics

The dynamics of the single site expectation values under $H_{\mathrm{c}}$ is then

$$\begin{aligned}\langle\dot{\boldsymbol{\sigma}}_1\rangle &= -\frac{\langle\boldsymbol{\sigma}_1\rangle\times(\langle\boldsymbol{\sigma}_1\rangle\times\langle \mathrm{i}\,[H,\boldsymbol{\sigma}_1]\rangle)}{\langle\boldsymbol{\sigma}_1\rangle\cdot\langle\boldsymbol{\sigma}_1\rangle}\\ &= \langle \mathrm{i}\,[H,\boldsymbol{\sigma}_1]\rangle - \langle\boldsymbol{\sigma}_1\rangle\left(\frac{\langle\boldsymbol{\sigma}_1\rangle\cdot\langle \mathrm{i}\,[H,\boldsymbol{\sigma}_1]\rangle}{\langle\boldsymbol{\sigma}_1\rangle\cdot\langle\boldsymbol{\sigma}_1\rangle}\right)\\ &= \langle\boldsymbol{\sigma}_1\rangle\times\boldsymbol{B}_1 + J\langle\boldsymbol{\sigma}_1\times\boldsymbol{\sigma}_2\rangle - J\langle\boldsymbol{\sigma}_1\rangle\left(\frac{\langle\boldsymbol{\sigma}_1\rangle\cdot\langle\boldsymbol{\sigma}_1\times\boldsymbol{\sigma}_2\rangle}{\langle\boldsymbol{\sigma}_1\rangle\cdot\langle\boldsymbol{\sigma}_1\rangle}\right)\end{aligned} \tag{F.9}$$

We now consider the Hamiltonian $H' = (1-\epsilon)H + \epsilon H_{\mathrm{c}}$ interpolates between the full Hamiltonian at $\epsilon = 0$ and $H_{\mathrm{c}}$ at $\epsilon = 1$ which generates only local (i.e. classical) dynamics.

If we decompose $H = H_{\mathrm{c}} + H_{\mathrm{q}}$ (which we takes as the definition of $H_{\mathrm{q}}$), where $H_{\mathrm{c}}$ generates the classical dynamics, and $H_{\mathrm{q}}$ the remaining quantum dynamics, we can see that

$$H' = (1-\epsilon)H_{\mathrm{q}} + H_{\mathrm{c}} \tag{F.10}$$

and that the $q$ parameter tunes the degree of quantum dynamics.

The single site expectation dynamics generated by $H'$ are given by

$$\langle\dot{\boldsymbol{\sigma}}_1\rangle = \langle\boldsymbol{\sigma}_1\rangle\times\boldsymbol{B}_1 + J\langle\boldsymbol{\sigma}_1\times\boldsymbol{\sigma}_2\rangle - J\epsilon\langle\boldsymbol{\sigma}_1\rangle\left(\frac{\langle\boldsymbol{\sigma}_1\rangle\cdot\langle\boldsymbol{\sigma}_1\times\boldsymbol{\sigma}_2\rangle}{\langle\boldsymbol{\sigma}_1\rangle\cdot\langle\boldsymbol{\sigma}_1\rangle}\right) \tag{F.11}$$

.

## F.2 Classical and quantum degrees of freedom

The meaning of this can be more easily seen by writing the dynamics as

$$\langle\dot{\boldsymbol{\sigma}}_1\rangle = \langle \mathrm{i}\,[H',\boldsymbol{\sigma}_1]\rangle = (qQ+P)\langle \mathrm{i}\,[H,\boldsymbol{\sigma}_1]\rangle \tag{F.12}$$

where $Q$ is the $3\times 3$ projector given by $Q_{ij} = \left\langle\sigma_1^i\right\rangle\left\langle\sigma_1^j\right\rangle / \langle\boldsymbol{\sigma}_1\rangle\cdot\langle\boldsymbol{\sigma}_1\rangle$ which projects onto the direction $\boldsymbol{\sigma_1}$,and $P$ is the complement projector to $Q$ such that the two projectors sum to the identity $P+Q=\mathbf{1}$.

Thus we see tuning up the parameter $\epsilon$ slows the dynamics of $\langle\boldsymbol{\sigma_1}\rangle$ exclusively along its axis leaving the perpendicular part (which generates rotations) unaffected. That tuning down that dynamics of quantum degrees of freedom slows changes in the length of a local polarisation vector $\langle\boldsymbol{\sigma}\rangle$ agrees with our understanding of this quantity as corresponding to entanglement.

There are though two independent degrees of freedom which exist in the fully quantum model that do not have classical analogue. Only one of which, the entanglement entropy is accessible through local expectation values, the other, the phase angle between the superposed states, requires a global measurement. So has this degree of freedom been slowed in the analogous way?

This question is more complex to show formally in generality. Instead we consider an example: let $H = -\frac{1}{2}\boldsymbol{\sigma}_1\cdot\boldsymbol{B}_1$. Putting this into equation F.8 it is clear that this Hamiltonian is equal to its classical part, i.e. that $H_{\mathrm{c}} = H$ and $H_{\mathrm{q}} = 0$. However if we let $\boldsymbol{B}_1 = B_1\hat{\boldsymbol{z}}$ and consider the evolution of the state $|\psi_0\rangle = (|\uparrow\uparrow\rangle + |\downarrow\downarrow\rangle)/\sqrt{2}$. we see that the time evolution of this state is given by

$$|\psi(t)\rangle = \frac{1}{\sqrt{2}}\left(\mathrm{e}^{-\mathrm{i}B_1t/2}|\uparrow\uparrow\rangle + \mathrm{e}^{\mathrm{i}B_1t/2}|\downarrow\downarrow\rangle\right) \tag{F.13}$$

which is indeed the full quantum evolution, showing that in this case degree of freedom is not slowed by altering $\epsilon$.

In this case the phase between the two branches of a cat state evolves as the difference between their expected energies. This is not a general property, but is true for all maximally entangled

states. If we consider this observation with a more general Hamiltonian decomposed as $H' = (1-\epsilon)H_{\mathrm{q}} + H_{\mathrm{c}}$ we see that this energy difference will have generally have contributions generated by $H_{\mathrm{c}}$ and $H_{\mathrm{q}}$. This shows that even in the restricted case of maximally entangled states case the contributions to this phase cannot be easily decomposed as classical and quantum.

# G | Adiabatic quantum computation

## G.1 Universality of adiabatic quantum computation

Universal quantum computation is understood in terms of the gate model. In the gate model we initialise some state $|\psi_0\rangle = \left|0^N\right\rangle$ on $N$ qubits. A series of unitary gates $U_1, U_2, \cdots U_M$ are then applied, after the $m$th gate we are in the state $|\psi_m\rangle = U_m U_{m-1} \cdots U_1 |\psi_0\rangle$. The outcome of the computation is the state $|\psi_M\rangle$, which is not known *a priori*. Here we discuss how it can be shown that a universal computation defined by a set of local gates maybe be implemented as a set a local Hamiltonians in the Adiabatic protocol.

In complexity two computational resources are equivalent if they can solve problems with the same asymptotic resource scaling up to a polynomial scaling. If we want to show adiabatic computation to be equivalent to this universal computation, we then run into a problem: How can we write down a local Hamiltonian $H_{\text{target}}$ whose ground state is $|\psi_M\rangle$, a state we do not now?

This is possible due to a construction due to Kitaev [332] of in which we extend our Hilbert space so that our state is now defined on a $N$ qubits, and an $M$ state register $|m\rangle_{\text{c}}$ known as the clock (which is often written is $M$ qubits) to give an extended state $|\psi'_m\rangle = |\psi_m\rangle |m\rangle_{\text{c}}$ after the $m$th gate. If we then take $H_{\text{start}}$ to be some trivial hamiltonian for which he ground state is $|\psi_0\rangle = |0\rangle |0\rangle_{\text{c}}$ and the final Hamiltonian

$$H_{\text{target}} = \sum_{m=0}^{M} \omega_m \mathbf{1} \otimes |m\rangle \langle m|_{\text{c}} - \sum_{m=1}^{M} \left(U_m \otimes |m\rangle \langle m-1|_{\text{c}} + \text{h.c.}\right). \tag{G.1}$$

the clock can always be implemented with local operations, hence the locality of this Hamiltonian is inherited from the locality of the $U_m$. The $\omega_m$ are then energy penalties for the clock state being in an undesired intermediate state. This Hamiltonian can be written in the basis of $|\psi'_m\rangle$ as the $(M+1) \times (M+1)$ tridiagonal matrix

$$H_{\text{target}} = \begin{pmatrix} \omega_0 & -1 & & & & \\ -1 & \omega_1 & -1 & & & \\ & -1 & \omega_2 & -1 & & \\ & & \ddots & \ddots & \ddots & \\ & & & -1 & \omega_{M-1} & -1 \\ & & & & -1 & \omega_M \end{pmatrix}. \tag{G.2}$$

With finite $\omega_m$ the ground state cannot be chosen to be $|\psi_M\rangle$. However they can easily be chosen to have $\text{O}(1/\text{poly}(M))$ overlap. Then post-selecting on the clock being in the state $|M\rangle$ we change the resource scaling a tolerable factor. The proof that universal quantum computation can be implemented adiabatically is then completed in ref [202] by showing that the time-scale for the evolution, given by equation (5.4), is at most polynomial in $M$.

# H | Derivation of Wegner Flow

## H.1 Flow of eigenstates

The cost function is

$$\Delta(\psi) = \langle\psi|H^2|\psi\rangle - \langle\psi|H|\psi\rangle^2 = \left\langle H^2\right\rangle - \langle H\rangle^2 \tag{H.1}$$

which we re-write as

$$\Delta = -\mathrm{tr}\left[[H,P][H,P]\right] \tag{H.2}$$

where $P = |\psi\rangle\langle\psi|$. Thus

$$\frac{\mathrm{d}\Delta}{\mathrm{d}s} = -2\mathrm{tr}\left[[H,P]\left[H,\frac{\mathrm{d}P}{\mathrm{d}s}\right]\right] = -2\mathrm{tr}\left[\frac{\mathrm{d}P}{\mathrm{d}s}\left[[H,P],H\right]\right]. \tag{H.3}$$

Since we are considering only unitary rotations we know that $\frac{\mathrm{d}P}{\mathrm{d}s} = [A,P]$ for anti-hermitian $A$,

$$\frac{\mathrm{d}\Delta}{\mathrm{d}s} = -2\mathrm{tr}\left[[A,P]\left[[H,P],H\right]\right] = -2\mathrm{tr}\left[A\left[P,[H,[P,H]]\right]\right]. \tag{H.4}$$

For steepest descent we choose $A$ from the set of anti hermitian matrices such that the RHS is as negative as possible. Since the RHS is of the form of an inner product $-2(A,[P,[H,[P,H]]])$, where $(X,Y) = \mathrm{tr}\left[X^\dagger Y\right]$, it is clear that it is maximally negative when $A = [P,[H,[P,H]]]$. Thus we obtain the flow equation for eigenstates

$$\begin{aligned}\frac{\mathrm{d}\,|\psi\rangle}{\mathrm{d}s} &= A\,|\psi\rangle \\ &= [P,[H,[P,H]]]\,|\psi\rangle \\ &= \left(\left\langle(H-\langle H\rangle)^2\right\rangle - (H-\langle H\rangle)^2\right)|\psi\rangle\,.\end{aligned} \tag{H.5}$$

With minor adjustments the same principle can be used to derive flow equations for $\tau^z$ as discussed in the main text.

# I | Perturbation theory in the East model

In this appendix we obtain the matrix elements of the effective Hamiltonian of the Quantum East Model (QEM) (6.52) which is defined only on a sector of the Hilbert space in which the global magnetisation does not change. The methodology follows the approach of Section 6.5.2 in which the effective Hamiltonian is calculated according to 6.59. The $J_{\text{eff}}$ are the matrix elements of the effective Hamiltonian defined on the reduced Hilbert space of a single magnetisation sector

$$\begin{aligned} H_{\text{eff}} &= H_{aa} + H_{ab}\frac{1}{Mh - H_{bb}}H_{ba} \\ &= P_a H_0 P_a + \sum_{n=0}^{\infty} P_a \left[ V P_b \frac{1}{Mh - H_0} P_b \right]^n V P_a \end{aligned} \tag{I.1}$$

where $M$ denotes the total magnetisation of the relevant sector $a$, and $b$ denotes *all other sectors*. This is the usual method (of e.g.refs [310, 311]) where $H_{\text{eff}}$ is found by projecting the resolvent

$$R_{\text{eff}}(z) = \frac{1}{z - H_{\text{eff}}} = P_a R(z) P_a = P_a \frac{1}{z - H} P_a \tag{I.2}$$

Solving for $H_{\text{eff}}$ yields I.1. This yields an effective Hamiltonian with the correct spectrum to good approximation.

## I.1 Leading order perturbation theory

### I.1.1 Leading order 2-spin process

The leading order process by which the transition

$$|\cdots\uparrow \underbrace{\downarrow\cdots\downarrow\downarrow\uparrow}_{\substack{d \text{ spin} \\ \text{domain}}}\cdots\rangle \to |\cdots\uparrow \underbrace{\downarrow\cdots\downarrow\uparrow}_{\substack{d-1 \text{ spin} \\ \text{domain}}} \downarrow\cdots\rangle, \tag{I.3}$$

which we denote by $J_{\text{eff}}^{d\to d-1}$, occurs to leading order as $J_{\text{eff}}^{d\to d-1} = J\frac{(J/h)^{2d-3}}{(d-2)!^2} + \cdots$. To see this we tabulate one such series $\mathrm{O}(J)$ of processes by which it occurs for $d = 5$:

| Order | Configuration | $E$ off shell |
|---|---|---|
| 0 | 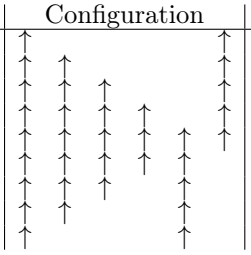 | |
| 1 | | $h$ |
| 2 | | $2h$ |
| 3 | | $3h$ |
| 4 | | $4h$ |
| 5 | | $3h$ |
| 6 | | $2h$ |
| 7 | | $h$ |
| 8 | | |

(I.4)

for clarity we have not denoted $\downarrow$ spins. For each transition we gain a factor $J$ and each intermediate configuration we gain a factor $(E \text{ off shell})^{-1}$. This yields

$$J\frac{1}{h}J\frac{1}{2h}J\frac{1}{3h}J\frac{1}{4h}J\frac{1}{3h}J\frac{1}{2h}J\frac{1}{1h}J = \frac{J}{4!3!}\left(\frac{J}{h}\right)^7 = \frac{J}{(5-1)!(5-2)!}\left(\frac{J}{h}\right)^{2\cdot 5-3}. \tag{I.5}$$

However there are other leading order processes, such as

| Order | Configuration | $E$ off shell |
|---|---|---|
| 0 | 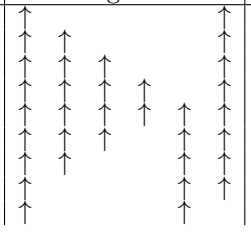 | |
| 1 | | $h$ |
| 2 | | $2h$ |
| 3 | | $3h$ |
| 4 | | $4h$ |
| 5 | | $3h$ |
| 6 | | $2h$ |
| 7 | | $h$ |
| 8 | | |

(I.6)

which is distinguished from (I.4) only by at which order in the process the final spin is flipped. The final spin could have been flipped at order 5, 6, 7, or 8. This process has the same energy associated with it. Thus the leading order contribution is given by

$$J_{\text{eff}}^{5\to 5-1} = 4\frac{J}{4!3!}\left(\frac{J}{h}\right)^7 = \frac{J}{(5-2)!(5-2)!}\left(\frac{J}{h}\right)^{2\cdot 5-3} \tag{I.7}$$

and in general by

$$J_{\text{eff}}^{d\to d-1} = J\frac{(J/h)^{2d-3}}{(d-2)!^2} + \cdots. \tag{I.8}$$

When we consider process that move a domain wall by two sites, instead of a single site, there are now two trailing spins to be flipped on the right hand end of the configuration. These can again be flipped at any point in the process once there are up spins to their left to facilitate this process. Thus though there were $d-1$ contributions when we moved a domain wall by a single site, there are $\binom{d-1}{2}$ contributions when we moved by two sites, eg

| Order | Configuration | $E$ off shell |
|---|---|---|
| 0 | 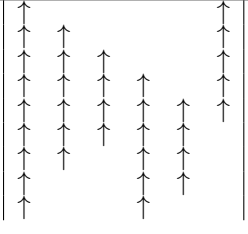 | |
| 1 | | $h$ |
| 2 | | $2h$ |
| 3 | | $3h$ |
| 4 | | $4h$ |
| 5 | | $3h$ |
| 6 | | $2h$ |
| 7 | | $h$ |
| 8 | | |

(I.9)

extending this argument we find a factor $\binom{d-1}{d'-1}$ when we move the domain from length $d$ to $d'$, where we assume without loss of generality that $d > d'$. Thus in general

$$J_{\text{eff}}^{d\to d'} = \binom{d-1}{d'-1}\frac{J(J/h)^{2d-3}}{(d-1)!(d-2)!} + \cdots \tag{I.10}$$

to get the scaling behaviour of this term we note that $\binom{d-1}{d'-1} \sim 2^{d-1}$ which yields

$$J_{\text{eff}}^{d\to d'} = \frac{2^{d-1}J(J/h)^{2d-3}}{(d-1)!(d-2)!} + \cdots \tag{I.11}$$

### I.1.2 Leading order 3-spin process

Here we consider processes which simultaneously rearrange several domains, such as the 3-spin process

| Order | Configuration | $E$ off shell |
|---|---|---|
| 0 | 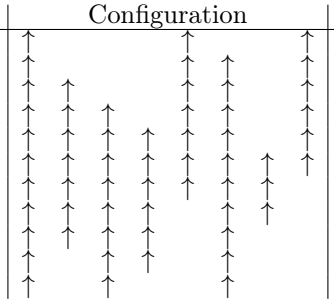 | |
| 1 | | $1h$ |
| 2 | | $2h$ |
| 3 | | $3h$ |
| 4 | | $4h$ |
| 5 | | $5h$ |
| 6 | | $4h$ |
| 7 | | $3h$ |
| 8 | | $2h$ |
| 9 | | $1h$ |
| 10 | | |

(I.12)

in which the domains $d_1 = 4$ and $d_2 = 3$ transition to $d_1' = 2$ and $d_2' = 3$. This process is very similar to the 2-spin process $d = d_1 + d_2 - 1 \to d' = d_1' + d_2' - 1$. The initial and final state of the 2-spin process are related to the above process by inserting extra mid-domain ↑-spins. The effect of these extra spins is to introduce combinatoric factors, $\binom{d_1+d_2-2}{d_1-1}$ corresponding to the different orders of spin flips which for the steps 0 to 5 and a factor $\binom{d_1'+d_2'-2}{d_1'-1}$ corresponding to the steps 5 to 10. This yields

$$J_{\text{eff}}^{d_1,d_2\to d_1',d_2'} = \binom{d_1+d_2-2}{d_1-1}\binom{d_1'+d_2'-2}{d_1'-1}\binom{d_1+d_2-2}{d_1'+d_2'-2}\frac{J(J/h)^{2(d_1+d_2)-5}}{(d_1+d_2-2)!(d_1+d_2-3)!} \tag{I.13}$$

for $d_1 \approx d_2 \approx d_1' \approx d_2' \approx d$ we use that $\binom{d_1+d_2-2}{d_1-1} \sim 2^{2d}$ and $\binom{d_1'+d_2'-2}{d_1'-1}\binom{d_1+d_2-2}{d_1'+d_2'-2} \sim 3^{2d}$ this becomes

$$J_{\text{eff}}^{d_1,d_2\to d_1',d_2'} \sim 2^{2d}3^{2d}\frac{J(J/h)^{4d-5}}{(2d-2)!(2d-3)!} \tag{I.14}$$

Thus if we are considering particles with a typical spacing $d$ we see that this 3-spin process (I.14) is much smaller than the two-spin process (I.11).

### I.1.3 Leading order $p$-spin process

We now generalise the above to process involving the movement of arbitrary numbers of domain walls. Following the arguments presented in the previous two sections we expect a combinatoric factor given by the product of multinomials

$$\binom{d_1+d_2+d_3\cdots d_p}{d_1,d_2,d_3,\cdots,d_p}\binom{d_1+d_2+d_3\cdots d_p}{d_1',d_2',d_3',\cdots d_p',\Delta d} \sim (p(p+1))^{pd} \tag{I.15}$$

where $\Delta d = \sum_i (d_i - d_i')$. Thus, for $d_i \approx d_i' \approx d$ such a process goes as

$$J_{\text{eff}}^{d_1,d_2,d_3,\cdots,d_p\to d_1',d_2',d_3'\cdots,d_p'} \sim (p(p+1))^{pd}\frac{J(J/h)^{(2d-p-2)p}}{(pd)!^2} \sim \frac{J(J/h)^{(2d-p-2)p}}{d!^2} \tag{I.16}$$

which, when $J < h$, is exponentially small with $p$ compared to the leading order process in equation (I.11). The power $(2d-p-2)p = (2d-3)+(2(d-1)-3)+(2(d-2)-3)+\cdots+(2(d-p)-3)$.

## I.2 Higher order perturbation theory

### I.2.1 First order sub-leading term to two-spin process

The leading order term in perturbation theory is the one in which a whole domain is flipped, allowing the right hand boundary to then be mobilised. The major contribution to the sub-leading terms is when spins are flipped temporarily back down, bringing the system closer to being on shell again. For example, a higher order contribution to (I.4)

| Order | Configuration | $E$ off shell |
|---|---|---|
| 0 | 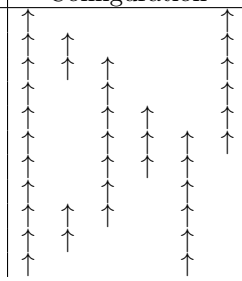 | |
| 1 | | $h$ |
| 2 | | $2h$ |
| 3 | | $h$ |
| 4 | | $2h$ |
| 5 | | $3h$ |
| 6 | | $2h$ |
| 7 | | $h$ |
| 8 | | $2h$ |
| 9 | | $h$ |
| 10 | | |

(I.17)

which is two orders higher in magnitude, but goes $h$ less off shell. To represent these processes we will write (I.4) as

$$\rightarrow \quad 1 \quad \rightarrow \quad 2 \quad \rightarrow \quad 3 \quad \rightarrow \quad 4 \quad \rightarrow \quad 3 \quad \rightarrow \quad 2 \quad \rightarrow \quad 1 \quad \rightarrow \tag{I.18}$$

where each arrow introduces a factor $J$ and each node $n$ which the path passes through introduces a factor $1/nh$. In this notation the higher order process (I.17) is written

$$\begin{array}{ccccccccccccccc} & & & & 1 & \rightarrow & 2 & \rightarrow & 3 & \rightarrow & 2 & \rightarrow & 1 & & \\ & & & & \uparrow & & & & & & & & \downarrow & & \\ \rightarrow & 1 & \rightarrow & 2 & & & 3 & & 4 & & 3 & & 2 & \rightarrow & 1 & \rightarrow \end{array} \tag{I.19}$$

where the vertical displacement indicates that there is a $\downarrow$ spin in the domain which is all $\uparrow$ spins in the leading order process. To return to being on-shell this $\downarrow$ spin must be flipped $\uparrow$ again, as shown in (I.17), and as indicated by the path stepping back down again. The sub-leading process is by summing all of the contributions from all unique paths across the array of numbers (moving in all 4 directions at any step) in (I.19). The contribution from each path is evaluated by the following rules (which are as before with some additional counting factors):

1. Factor $J$ for every arrow. This accounts for the energy of the process.
2. Factor $1/nh$ for every node $n$. This accounts for the cost of being off-shell.
3. Factor $m$ for the vertical $\uparrow$, $\downarrow$ arrows (the pair of which are considered as a unit) where $m$ is the lowest value of any of the nodes joined by the vertical arrows. This accounts for the multiplicity of the spins which could be flipped to bring us closer to being on shell.

The dominant contributions to this come from the baths which avoid the largest node on the diagram. Given that the leading order term (corresponding to the shortest path, and given in equation (I.18)), is given by $\left[J_{\text{eff}}^{d\to d-1}\right]_{(0)}$. Then the first-sub-leading term is given by

$$\left[J_{\text{eff}}^{d\to d-1}\right]_{(1)} = \left[J_{\text{eff}}^{d\to d-1}\right]_{(0)} \left[\left(\frac{J}{h}\right)^2 \sum_{i=2}^{d-1}\sum_{j=2}^{d-1} \frac{(d-1)(d-2)m(i,j)}{i(i-1)j(j-1)}\right] \tag{I.20}$$

where $i$ is the value on the lower row of the array at the position of the $\uparrow$ arrow, $j$ is the value on the lower row of the array at the position of the $\downarrow$ arrow, and hence $m(i,j) = \min(i-1, j-1)$. This sum evaluates to

$$\left[J_{\text{eff}}^{d\to d-1}\right]_{(1)} = \left[J_{\text{eff}}^{d\to d-1}\right]_{(0)} \left[2\left(\frac{J}{h}\right)^2 ((d-1)(d-2) - (d-1)H_{d-2})\right] \tag{I.21}$$

where $H_n \sim \log n$ is the $n$th harmonic number. Thus, keeping only leading order terms in $d$, to sub-leading order in perturbation theory we have

$$J_{\text{eff}}^{d\to d'} = \binom{d-1}{d'-1}\left(\frac{J(J/h)^{2d-3}}{(d-1)!(d-2)!} + \frac{2J(J/h)^{2d-1}}{(d-2)!(d-3)!} + \cdots\right) \tag{I.22}$$

### I.2.2 Higher order sub-leading term to two-spin process

Analogous to how we represented (I.17) with the diagram (I.19) we do the same for higher order processes. E.g.

| Order | Configuration | $E$ off shell |
|---|---|---|
| 0 | 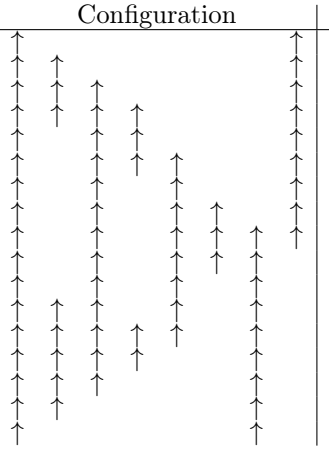 | |
| 1 | | $h$ |
| 2 | | $2h$ |
| 3 | | $3h$ |
| 4 | | $2h$ |
| 5 | | $3h$ |
| 6 | | $2h$ |
| 7 | | $3h$ |
| 8 | | $4h$ |
| 9 | | $3h$ |
| 10 | | $2h$ |
| 11 | | $3h$ |
| 12 | | $4h$ |
| 13 | | $3h$ |
| 14 | | $2h$ |
| 15 | | $h$ |
| 16 | | |

(I.23)

which is represented

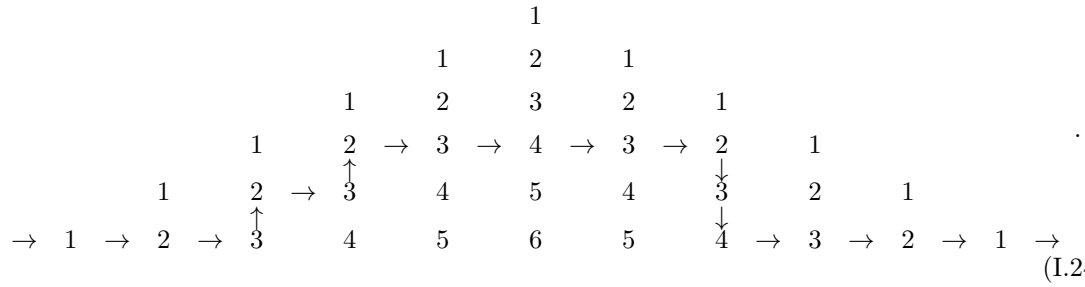

(I.24)

Following the progress of the previous section, it may seem that we can then evaluate all the higher order diagrams by summing over the paths across this array. This is not the case, as this neglects to consider that, for the East model, a spin can only flip if its left neighbour is in the up position. For example in (I.24) the two down flips could not have been direct neighbours. This can be accounted for by careful evaluation of the factor $m$ associated with the vertical arrows, which can no longer be evaluated independently for each vertical pair, but become collectively inter-dependent. Rather than go into this in detail, we make the approximation that for order $n \ll d$ almost all of the spins will not be double-flipped and so we can discount this effect to leading order in $d$.

Taking this approach we find

$$\begin{aligned}\left[J_{\text{eff}}^{d\to d'}\right]_{(2)} &= \left[J_{\text{eff}}^{d\to d'}\right]_{(0)}\left[\left(\frac{J}{h}\right)^4\left(\sum_{i=2}^{d-1}\sum_{j=2}^{d-1}\frac{(d-1)(d-2)m(i,j)}{i(i-1)j(j-1)}\right)\left(\sum_{i=2}^{d-1}\sum_{j=2}^{d-1}\frac{(d-2)(d-3)m(i,j)}{i(i-1)j(j-1)}\right)\right]\\ &= \left[J_{\text{eff}}^{d\to d'}\right]_{(0)} 4\left(\frac{J}{h}\right)^4\left[(d-1)(d-2)^2(d-3)+\mathrm{O}(d^3\log d)\right].\end{aligned} \tag{I.25}$$

In general at higher order in the two spin process, for $n \ll d$, and making the same approximations as above

$$\left[J_{\text{eff}}^{d\to d'}\right]_{(n)} = \left[J_{\text{eff}}^{d\to d'}\right]_{(0)} 2^n\left(\frac{J}{h}\right)^{2n}\frac{(d-1)!(d-2)!}{(d-n-1)!(d-n-2)!} \tag{I.26}$$

which yields for $m \ll d$

$$J_{\text{eff}}^{d\to d'} = \binom{d-1}{d'-1}\sum_{n=0}^{m}\frac{J2^n(J/h)^{2d+2n-3}}{(d-n-1)!(d-n-2)!} + \mathrm{O}(J/h)^{2(d+n+1)} \tag{I.27}$$

whereas at higher orders this becomes an over-estimate.

### I.2.3 Evaluation of equation (I.27)

$J_{\text{eff}}$ is given by

$$J_{\text{eff}}^{d\to d'} = \binom{d-1}{d'-1}\sum_{n=0}^{m}\frac{J2^n(J/h)^{2d+2n-3}}{(d-n-1)!(d-n-2)!} + \mathrm{O}(J/h)^{2(d+m+1)} \tag{I.28}$$

For $0 < d-1-h/(\sqrt{2}J) < m$ and $\sqrt{2}J < h$ this sum can be approximately evaluated. For brevity we write it as

$$J_{\text{eff}}^{d\to d'} = c\sum_{n=0}^{m}\frac{\lambda^{2n}}{(x-n)!(x-n-1)!} \tag{I.29}$$

with $c = \binom{d-1}{d'-1}J(J/h)^{2d-3}$, $x = d-1$ and $\lambda = \sqrt{2}(J/h)$. The summand is sharply peaked at $n_0 \approx x - 1/\lambda$ and thus, providing $0 < n_0 < m$, the sum can then be approximated using the Saddle point approximation. This yields

$$J_{\text{eff}}^{d\to d'} = c\sum_{n=0}^{m}\mathrm{e}^{g(n)} \approx c\int_{-\infty}^{\infty}\mathrm{d}n\,\mathrm{e}^{g(n_0)+g''(n_0)(n-n_0)^2/2} = c\mathrm{e}^{g(n_0)}\sqrt{\frac{2\pi}{|g''(n_0)|}} \tag{I.30}$$

where

$$\mathrm{e}^{g(n_0)} \approx \frac{\lambda^{2(x+1-1/\lambda)}}{\Gamma(\frac{1}{\lambda})^2} \tag{I.31}$$

$$g''(n_0) \approx -2\lambda. \tag{I.32}$$

This yields

$$J_{\text{eff}}^{d\to d'} = \sqrt{\frac{h\pi}{\sqrt{2}J}}\binom{d-1}{d'-1}J(J/h)^{2d-3}\frac{(\sqrt{2}J/h)^{2d-\sqrt{2}h/J}}{\Gamma(\frac{h}{\sqrt{2}J})^2} \tag{I.33}$$

which scales as

$$J_{\text{eff}}^{d\to d'} \sim \sqrt{Jh}\frac{(\sqrt{2}J/h)^{(4d-\sqrt{2}h/J-3)}}{\Gamma(\frac{h}{\sqrt{2}J})^2} \tag{I.34}$$

# Bibliography


[1] Max Born, Albert Einstein, and Irene Born. The Born Einstein Letters: correspondence between Albert Einstein and Max and Hedwig Born from 1916 to 1955 with commentaries by Max Born. Translated by Irene Born. Basingstoke, Macmillan Press, 1971.

[2] John Stewart Bell. Speakable and unspeakable in quantum mechanics: Collected papers on quantum philosophy. Cambridge university press, 2004.

[3] John S Bell. On the einstein podolsky rosen paradox, 1964.

[4] Nicolas Brunner, Daniel Cavalcanti, Stefano Pironio, Valerio Scarani, and Stephanie Wehner. Bell nonlocality. Reviews of Modern Physics, 86(2):419, 2014.

[5] Albert Einstein, Boris Podolsky, and Nathan Rosen. Can quantum-mechanical description of physical reality be considered complete? Physical review, 47(10):777, 1935.

[6] John F Clauser, Michael A Horne, Abner Shimony, and Richard A Holt. Proposed experiment to test local hidden-variable theories. Physical review letters, 23(15):880, 1969.

[7] Bernien Hensen, H Bernien, AE Dréau, A Reiserer, N Kalb, MS Blok, J Ruitenberg, RFL Vermeulen, RN Schouten, C Abellán, et al. Experimental loophole-free violation of a bell inequality using entangled electron spins separated by 1.3 km. arXiv preprint arXiv:1508.05949, 2015.

[8] David Deutsch. Quantum theory, the church-turing principle and the universal quantum computer. In Proceedings of the Royal Society of London A: Mathematical, Physical and Engineering Sciences, volume 400, pages 97–117. The Royal Society, 1985.

[9] Seth Lloyd. Computational capacity of the universe. Physical Review Letters, 88(23):237901, 2002.

[10] Jacob D Bekenstein. Universal upper bound on the entropy-to-energy ratio for bounded systems. Physical Review D, 23(2):287, 1981.

[11] Jacob D Bekenstein. Black holes and information theory. Contemporary Physics, 45(1):31–43, 2004.

[12] Matthew F Pusey, Jonathan Barrett, and Terry Rudolph. On the reality of the quantum state. Nature Physics, 8(6):475–478, 2012.

[13] Walter Kohn. Nobel lecture: Electronic structure of matterâĂŤwave functions and density functionals. Reviews of Modern Physics, 71(5):1253, 1999.

[14] Michael M Wolf, Frank Verstraete, Matthew B Hastings, and J Ignacio Cirac. Area laws in quantum systems: mutual information and correlations. Physical review letters, 100(7):070502, 2008.

[15] MB Plenio, J Eisert, J Dreissig, and M Cramer. Entropy, entanglement, and area: analytical results for harmonic lattice systems. Physical review letters, 94(6):060503, 2005.

[16] Mark Srednicki. Entropy and area. Physical Review Letters, 71(5):666, 1993.

[17] Jens Eisert, Marcus Cramer, and Martin B Plenio. Colloquium: Area laws for the entanglement entropy. Reviews of Modern Physics, 82(1):277, 2010.

[18] Fernando GSL Brandão and Michał Horodecki. An area law for entanglement from exponential decay of correlations. Nature Physics, 9(11):721–726, 2013.

[19] Fernando GSL Brandão and Michał Horodecki. Exponential decay of correlations implies area law. Communications in mathematical physics, 333(2):761–798, 2015.

[20] Patrick Hayden, Debbie W Leung, and Andreas Winter. Aspects of generic entanglement. Communications in Mathematical Physics, 265(1):95–117, 2006.

[21] Michael M Wolf. Violation of the entropic area law for fermions. Physical review letters, 96(1):010404, 2006.

[22] Marcus Cramer, Jens Eisert, and MB Plenio. Statistics dependence of the entanglement entropy. Physical review letters, 98(22):220603, 2007.

[23] Pasquale Calabrese and John Cardy. Entanglement entropy and quantum field theory. Journal of Statistical Mechanics: Theory and Experiment, 2004(06):P06002, 2004.

[24] Guifre Vidal, Jose I Latorre, Enrique Rico, and Alexei Kitaev. Entanglement in quantum critical phenomena. Physical review letters, 90(22):227902, 2003.

[25] Christoph Holzhey, Finn Larsen, and Frank Wilczek. Geometric and renormalized entropy in conformal field theory. Nuclear Physics B, 424(3):443–467, 1994.

[26] David Poulin, Angie Qarry, Rolando Somma, and Frank Verstraete. Quantum simulation of time-dependent hamiltonians and the convenient illusion of hilbert space. Physical review letters, 106(17):170501, 2011.

[27] Román Orús. A practical introduction to tensor networks: Matrix product states and projected entangled pair states. Annals of Physics, 349:117–158, 2014.

[28] Román Orús. Advances on tensor network theory: symmetries, fermions, entanglement, and holography. The European Physical Journal B, 87(11):1–18, 2014.

[29] Carl Eckart and Gale Young. The approximation of one matrix by another of lower rank. Psychometrika, 1(3):211–218, 1936.

[30] Alexei Gilchrist, Nathan K Langford, and Michael A Nielsen. Distance measures to compare real and ideal quantum processes. Physical Review A, 71(6):062310, 2005.

[31] Stellan Östlund and Stefan Rommer. Thermodynamic limit of density matrix renormalization. Physical review letters, 75(19):3537, 1995.

[32] Jorge Dukelsky, Miguel A Martín-Delgado, Tomotoshi Nishino, and Germán Sierra. Equivalence of the variational matrix product method and the density matrix renormalization group applied to spin chains. EPL (Europhysics Letters), 43(4):457, 1998.

[33] Guifré Vidal. Efficient classical simulation of slightly entangled quantum computations. Physical Review Letters, 91(14):147902, 2003.

[34] AJ Daley, C Kollath, U Schollwöck, and G Vidal. Time-dependent density-matrix renormalization-group using adaptive effective hilbert spaces. Journal of Statistical Mechanics: Theory and Experiment, 2004(04):P04005, 2004.

[35] Frank Verstraete, Diego Porras, and J Ignacio Cirac. Density matrix renormalization group and periodic boundary conditions: a quantum information perspective. Physical review letters, 93(22):227205, 2004.

[36] Guifré Vidal. Efficient simulation of one-dimensional quantum many-body systems. Physical review letters, 93(4):040502, 2004.

[37] J Ignacio Cirac and Frank Verstraete. Renormalization and tensor product states in spin chains and lattices. Journal of Physics A: Mathematical and Theoretical, 42(50):504004, 2009.

[38] D Perez-Garcia, F Verstraete, MM Wolf, and JI Cirac. Matrix product state representations. Quantum Information & Computation, 7(5):401–430, 2007.

[39] Glen Evenbly and Guifré Vidal. Tensor network states and geometry. Journal of Statistical Physics, 145(4):891–918, 2011.

[40] Brian Swingle. Entanglement renormalization and holography. Physical Review D, 86(6):065007, 2012.

[41] Richard P Feynman. Simulating physics with computers. International journal of theoretical physics, 21(6):467–488, 1982.

[42] Eleanor Rieffel and Wolfgang Polak. An introduction to quantum computing for non-physicists. ACM Computing surveys, 32(3):300–335, 2000.

[43] Andrew Steane. Quantum computing. Reports on Progress in Physics, 61(2):117, 1998.

[44] Y-Y Shi, L-M Duan, and Guifre Vidal. Classical simulation of quantum many-body systems with a tree tensor network. Physical review a, 74(2):022320, 2006.

[45] Guifré Vidal. Class of quantum many-body states that can be efficiently simulated. Physical review letters, 101(11):110501, 2008.

[46] Guifre Vidal. Entanglement renormalization. Physical review letters, 99(22):220405, 2007.

[47] IM Georgescu, S Ashhab, and Franco Nori. Quantum simulation. Reviews of Modern Physics, 86(1):153, 2014.

[48] Anatoli Polkovnikov, Krishnendu Sengupta, Alessandro Silva, and Mukund Vengalattore. Colloquium: Nonequilibrium dynamics of closed interacting quantum systems. Reviews of Modern Physics, 83(3):863, 2011.

[49] Francisco Barahona. On the computational complexity of ising spin glass models. Journal of Physics A: Mathematical and General, 15(10):3241, 1982.

[50] Troels F Rønnow, Zhihui Wang, Joshua Job, Sergio Boixo, Sergei V Isakov, David Wecker, John M Martinis, Daniel A Lidar, and Matthias Troyer. Defining and detecting quantum speedup. Science, 345(6195):420–424, 2014.

[51] John A Smolin and Graeme Smith. Classical signature of quantum annealing. arXiv preprint arXiv:1305.4904, 2013.

[52] Seung Woo Shin, Graeme Smith, John A Smolin, and Umesh Vazirani. How" quantum" is the d-wave machine? arXiv preprint arXiv:1401.7087, 2014.

[53] Seung Woo Shin, Graeme Smith, John A Smolin, and Umesh Vazirani. Comment on" distinguishing classical and quantum models for the d-wave device". arXiv preprint arXiv:1404.6499, 2014.

[54] AN Kolmogorov. On preservation of conditionally periodic motions under a small change in the hamiltonian function. In Dokl. Akad. Nauk SSSR, volume 98, pages 527–530, 1954.

[55] Vladimir I Arnol'd. Proof of a theorem of an kolmogorov on the invariance of quasi-periodic motions under small perturbations of the hamiltonian. Russian Mathematical Surveys, 18(5):9–36, 1963.

[56] Jürgen Moser. On invariant curves of area-preserving mappings of an annulus. Vandenhoeck & Ruprecht, 1962.

[57] Leonid Abramovich Bunimovich. On ergodic properties of certain billiards. Functional Analysis and Its Applications, 8(3):254–255, 1974.

[58] Michael V Berry. The bakerian lecture, 1987: quantum chaology. In Proceedings of the Royal Society of London A: Mathematical, Physical and Engineering Sciences, volume 413, pages 183–198. The Royal Society, 1987.

[59] Michael Courtney. Rydberg atoms in strong fields: a testing ground for quantum chaos. 1995.

[60] Michael V Berry and Michael Tabor. Level clustering in the regular spectrum. In Proceedings of the Royal Society of London A: Mathematical, Physical and Engineering Sciences, volume 356, pages 375–394. The Royal Society, 1977.

[61] JM Deutsch. Quantum statistical mechanics in a closed system. Physical Review A, 43(4):2046, 1991.

[62] Mark Srednicki. Chaos and quantum thermalization. Physical Review E, 50(2):888, 1994.

[63] Hal Tasaki. From quantum dynamics to the canonical distribution: general picture and a rigorous example. Physical review letters, 80(7):1373, 1998.

[64] Marcos Rigol, Vanja Dunjko, and Maxim Olshanii. Thermalization and its mechanism for generic isolated quantum systems. Nature, 452(7189):854–858, 2008.

[65] Rahul Nandkishore and David A Huse. Many-body localization and thermalization in quantum statistical mechanics. Annu. Rev. Condens. Matter Phys., 6(1):15–38, 2015.

[66] Philip W Anderson. Absence of diffusion in certain random lattices. Physical review, 109(5):1492, 1958.

[67] Vid Stojevic, Philip Crowley, Tanja Đurić, Callum Grey, and Andrew G. Green. Time evolution and deterministic optimization of correlator product states. Physical Review B, 94(16):165135, 2016.

[68] Norbert Schuch, Michael M Wolf, Frank Verstraete, and J Ignacio Cirac. Computational complexity of projected entangled pair states. Physical review letters, 98(14):140506, 2007.

[69] Hitesh J Changlani, Jesse M Kinder, Cyrus J Umrigar, and Garnet Kin-Lic Chan. Approximating strongly correlated wave functions with correlator product states. Physical Review B, 80(24):245116, 2009.

[70] Daniel Gottesman. Stabilizer codes and quantum error correction. arXiv preprint quant-ph/9705052, 1997.

[71] A Yu Kitaev. Fault-tolerant quantum computation by anyons. Annals of Physics, 303(1):2–30, 2003.

[72] David A Huse and Veit Elser. Simple variational wave functions for two-dimensional heisenberg spin-1/2 antiferromagnets. Physical review letters, 60(24):2531, 1988.

[73] Robert B Laughlin. Anomalous quantum hall effect: an incompressible quantum fluid with fractionally charged excitations. Physical Review Letters, 50(18):1395, 1983.

[74] S Liang, B Doucot, and PW Anderson. Some new variational resonating-valence-bond-type wave functions for the spin-1/2 antiferromagnetic heisenberg model on a square lattice. Physical review letters, 61(3):365, 1988.

[75] MP Nightingale and HWJ Blöte. Gap of the linear spin-1 heisenberg antiferromagnet: A monte carlo calculation. Physical Review B, 33(1):659, 1986.

[76] Andrej Gendiar and Tomotoshi Nishino. Latent heat calculation of the three-dimensional q= 3, 4, and 5 potts models by the tensor product variational approach. Physical Review E, 65(4):046702, 2002.

[77] Fabio Mezzacapo, Norbert Schuch, Massimo Boninsegni, and J Ignacio Cirac. Ground-state properties of quantum many-body systems: entangled-plaquette states and variational monte carlo. New Journal of Physics, 11(8):083026, 2009.

[78] Fabio Mezzacapo and J Ignacio Cirac. Ground-state properties of the spin-antiferromagnetic heisenberg model on the triangular lattice: a variational study based on entangled-plaquette states. New Journal of Physics, 12(10):103039, 2010.

[79] S Al-Assam, SR Clark, CJ Foot, and D Jaksch. Capturing long range correlations in two-dimensional quantum lattice systems using correlator product states. Physical Review B, 84(20):205108, 2011.

[80] Eric Neuscamman, Hitesh Changlani, Jesse Kinder, and Garnet Kin-Lic Chan. Nonstochastic algorithms for jastrow-slater and correlator product state wave functions. Physical Review B, 84(20):205132, 2011.

[81] Eric Neuscamman and Garnet Kin-Lic Chan. Correlator product state study of molecular magnetism in the giant keplerate mo 72 fe 30. Physical Review B, 86(6):064402, 2012.

[82] R Darradi, O Derzhko, R Zinke, J Schulenburg, SE Krüger, and J Richter. Ground state phases of the spin-1/2 j 1–j 2 heisenberg antiferromagnet on the square lattice: A high-order coupled cluster treatment. Physical Review B, 78(21):214415, 2008.

[83] Ehud Altman and Assa Auerbach. Plaquette boson-fermion model of cuprates. Physical Review B, 65(10):104508, 2002.

[84] Leonid Isaev, Gerardo Ortiz, and Jorge Dukelsky. Hierarchical mean-field approach to the j 1- j 2 heisenberg model on a square lattice. Physical Review B, 79(2):024409, 2009.

[85] Tanja Đurić, Nicholas Chancellor, Philip JD Crowley, Pierfrancesco Di Cintio, and Andrew G Green. Pfaffian-like ground states for bosonic atoms and molecules in one-dimensional optical lattices. Physical Review B, 93(8):085143, 2016.

[86] P Kramer and M Saraceno. Geometry of the time-dependent variational principle in quantum mechanics. In Group Theoretical Methods in Physics, pages 112–121. Springer, 1980.

[87] Abhay Ashtekar and Troy A Schilling. Geometrical formulation of quantum mechanics. arXiv preprint gr-qc/9706069, 1997.

[88] PW Langhoff, ST Epstein, and M Karplus. Aspects of time-dependent perturbation theory. Reviews of Modern Physics, 44(3):602, 1972.

[89] Paul Adrien Maurice Dirac. The principles of quantum mechanics. Number 27. Oxford university press, 1981.

[90] Paul AM Dirac. Note on exchange phenomena in the thomas atom. In Mathematical Proceedings of the Cambridge Philosophical Society, volume 26, pages 376–385. Cambridge Univ Press, 1930.

[91] J Frenkel. Wave mechanics, advanced general theory. Oxford, 1934.

[92] AD McLachlan. A variational solution of the time-dependent schrodinger equation. Molecular Physics, 8(1):39–44, 1964.

[93] J Broeckhove, L Lathouwers, E Kesteloot, and P Van Leuven. On the equivalence of time-dependent variational principles. Chemical physics letters, 149(5-6):547–550, 1988.

[94] Jutho Haegeman, J Ignacio Cirac, Tobias J Osborne, Iztok Pižorn, Henri Verschelde, and Frank Verstraete. Time-dependent variational principle for quantum lattices. Physical review letters, 107(7):070601, 2011.

[95] Kit-Keung Kan. Gauge invariant periodic quantization method. Physical Review C, 24(1):279, 1981.

[96] Kit-Keung Kan. Equivalence of time-dependent variational descriptions of quantum systems and hamilton's mechanics. Physical Review A, 24(5):2831, 1981.

[97] K-K Kan, JJ Griffin, TW Atwater, and M Dworzecka. Gauge-invariant periodic solutions of the exact time-dependent schrödinger equation and their time averages. Physical Review A, 27(1):12, 1983.

[98] AG Green, CA Hooley, J Keeling, and SH Simon. Feynman path integrals over entangled states. arXiv preprint arXiv:1607.01778, 2016.

[99] Philip Pearle. Toward a relativistic theory of statevector reduction. In Sixty-two years of uncertainty, pages 193–214. Springer, 1990.

[100] Norbert Schuch, Michael M Wolf, Frank Verstraete, and J Ignacio Cirac. Simulation of quantum many-body systems with strings of operators and monte carlo tensor contractions. Physical review letters, 100(4):040501, 2008.

[101] L Tagliacozzo, Thiago R de Oliveira, S Iblisdir, and JI Latorre. Scaling of entanglement support for matrix product states. Physical review b, 78(2):024410, 2008.

[102] Frank Pollmann, Subroto Mukerjee, Ari M Turner, and Joel E Moore. Theory of finite-entanglement scaling at one-dimensional quantum critical points. Physical review letters, 102(25):255701, 2009.

[103] B Pirvu, G Vidal, F Verstraete, and L Tagliacozzo. Matrix product states for critical spin chains: Finite-size versus finite-entanglement scaling. Physical review b, 86(7):075117, 2012.

[104] Vid Stojevic, Jutho Haegeman, IP McCulloch, Luca Tagliacozzo, and Frank Verstraete. Conformal data from finite entanglement scaling. Physical Review B, 91(3):035120, 2015.

[105] Pasquale Calabrese and John Cardy. Entanglement entropy and quantum field theory: a non-technical introduction. International Journal of Quantum Information, 4(03):429–438, 2006.

[106] Alessandro Silva. Statistics of the work done on a quantum critical system by quenching a control parameter. Physical review letters, 101(12):120603, 2008.

[107] F Andraschko and J Sirker. Dynamical quantum phase transitions and the loschmidt echo: A transfer matrix approach. Physical Review B, 89(12):125120, 2014.

[108] Markus Heyl, Anatoli Polkovnikov, and Stefan Kehrein. Dynamical quantum phase transitions in the transverse-field ising model. Physical review letters, 110(13):135704, 2013.

[109] C Karrasch and D Schuricht. Dynamical phase transitions after quenches in nonintegrable models. Physical Review B, 87(19):195104, 2013.

[110] Philip JD Crowley and AG Green. Anisotropic landau-lifshitz-gilbert models of dissipation in qubits. Phys Rev A, 94:062106, Dec 2016.

[111] A Kamenev. Field theory of non-equilibrium systems. Cambridge University Press, 2011.

[112] A J Leggett, S Chakravarty, A T Dorsey, M P A Fisher, A Garg, and W Zwerger. Dynamics of the dissipative two-state system. Reviews of Modern Physics, 59(1):1, 1987.

[113] Ryogo Kubo and Natsuki Hashitsume. Brownian motion of spins. Progress of Theoretical Physics Supplement, 46:210–220, 1970.

[114] Pierre C Hohenberg and Bertrand I Halperin. Theory of dynamic critical phenomena. Reviews of Modern Physics, 49(3):435, 1977.

[115] A M Jayannavar. Brownian motion of spins; generalized spin langevin equation. Zeitschrift für Physik B Condensed Matter, 82(1):153–156, 1991.

[116] D A Garanin, V V Ishchenko, and LV Panina. Dynamics of an ensemble of single-domain magnetic particles. Theoretical and Mathematical Physics, 82(2):169–179, 1990.

[117] D A_ Garanin. Generalized equation of motion for a ferromagnet. Physica A: Statistical Mechanics and its Applications, 172(3):470–491, 1991.

[118] T Plefka. Nonlinear damping in spin systems: long range spin-spin interactions. Zeitschrift für Physik B Condensed Matter, 90(4):447–454, 1993.

[119] DA Garanin. Fokker-planck and Landau-Lifshitz-Bloch equations for classical ferromagnets. Physical Review B, 55(5):3050, 1997.

[120] Z Nussinov, A Shnirman, D P Arovas, A V Balatsky, and J X Zhu. Spin and spin-wave dynamics in josephson junctions. Phys. Rev. B, 71:214520, Jun 2005.

[121] H Katsura, A V Balatsky, Z Nussinov, and N Nagaosa. Voltage dependence of Landau-Lifshitz-Gilbert damping of spin in a current-driven tunnel junction. Phys. Rev. B, 73:212501, Jun 2006.

[122] E M Chudnovsky, D A Garanin, and M F O'Keeffe. Conservation of angular momentum in a flux qubit. Journal of Superconductivity and Novel Magnetism, 25(4):1007–1016, 2012.

[123] Albert Schmid. On a quasiclassical langevin equation. Journal of Low Temperature Physics, 49(5-6):609–626, 1982.

[124] H Kleinert and SV Shabanov. Quantum langevin equation from forward-backward path integral. Physics Letters A, 200(3):224–232, 1995.

[125] Ulrich Weiss. Quantum dissipative systems, volume 10. World Scientific, 1999.

[126] Sergio Boixo, Troels F Rønnow, Sergei V Isakov, Zhihui Wang, David Wecker, Daniel A Lidar, John M Martinis, and Matthias Troyer. Evidence for quantum annealing with more than one hundred qubits. Nature Physics, 10(3):218–224, 2014.

[127] Lei Wang, Troels F Rønnow, Sergio Boixo, Sergei V Isakov, Zhihui Wang, David Wecker, Daniel A Lidar, John M Martinis, and Matthias Troyer. Comment on:" classical signature of quantum annealing". arXiv preprint arXiv:1305.5837, 2013.

[128] Tameem Albash, Walter Vinci, Anurag Mishra, Paul A Warburton, and Daniel A Lidar. Consistency tests of classical and quantum models for a quantum annealer. Physical Review A, 91(4):042314, 2015.

[129] PJD Crowley, T Đurić, W Vinci, PA Warburton, and AG Green. Quantum and classical dynamics in adiabatic computation. Physical Review A, 90(4):042317, 2014.

[130] Bela Bauer, Lei Wang, Iztok Pižorn, and Matthias Troyer. Entanglement as a resource in adiabatic quantum optimization. arXiv preprint arXiv:1501.06914, 2015.

[131] R Harris, J Johansson, AJ Berkley, MW Johnson, T Lanting, Siyuan Han, P Bunyk, E Ladizinsky, T Oh, I Perminov, et al. Experimental demonstration of a robust and scalable flux qubit. Physical Review B, 81(13):134510, 2010.

[132] Lev D Landau and Es Lifshitz. On the theory of the dispersion of magnetic permeability in ferromagnetic bodies. Phys. Z. Sowjetunion, 8(153):101–114, 1935.

[133] Thomas L Gilbert. A phenomenological theory of damping in ferromagnetic materials. IEEE Transactions on Magnetics, 40(6):3443–3449, 2004.

[134] John C Mallinson. Damped gyromagnetic switching. IEEE transactions on magnetics, 36(4):1976–1981, 2000.

[135] Ryoichi Kikuchi. On the minimum of magnetization reversal time. Journal of Applied Physics, 27(11):1352–1357, 1956.

[136] Albert Einstein. The theory of the brownian movement. Ann. der Physik, 17:549, 1905.

[137] Gustav Kirchhoff. Ueber das verhältniss zwischen dem emissionsvermögen und dem absorptionsvermögen der körper für wärme und licht. Annalen der Physik, 185(2):275–301, 1860.

[138] John Bertrand Johnson. Thermal agitation of electricity in conductors. Physical review, 32(1):97, 1928.

[139] Harry Nyquist. Thermal agitation of electric charge in conductors. Physical review, 32(1):110, 1928.

[140] Gilbert N Lewis. A new principle of equilibrium. Proceedings of the National Academy of Sciences, 11(3):179–183, 1925.

[141] Fernando Casas, Ander Murua, and Mladen Nadinic. Efficient computation of the zassenhaus formula. Computer Physics Communications, 183(11):2386–2391, 2012.

[142] Justin H Wilson and Victor Galitski. Breakdown of the coherent state path integral: two simple examples. Physical review letters, 106(11):110401, 2011.

[143] A Kamenev. Keldysh and Doi-Peliti techniques for out-of-equilibrium systems. In Strongly Correlated Fermions and Bosons in Low-Dimensional Disordered Systems, pages 313–340. Springer, 2002.

[144] E Minguzzi. Rayleigh's dissipation function at work. European Journal of Physics, 36(3):035014, 2015.

[145] Juan P Garrahan, Robert L Jack, Vivien Lecomte, Estelle Pitard, Kristina van Duijvendijk, and Frédéric van Wijland. First-order dynamical phase transition in models of glasses: an approach based on ensembles of histories. Journal of Physics A: Mathematical and Theoretical, 42(7):075007, 2009.

[146] K Kikuchi, M Yoshida, T Maekawa, and H Watanabe. Metropolis monte carlo method as a numerical technique to solve the fokkerâĂŤplanck equation. Chemical Physics Letters, 185(3-4):335–338, 1991.

[147] Ulrich Nowak, Roy W Chantrell, and EC Kennedy. Monte carlo simulation with time step quantification in terms of langevin dynamics. Physical review letters, 84(1):163, 2000.

[148] XZ Cheng, MBA Jalil, Hwee Kuan Lee, and Yutaka Okabe. Mapping the monte carlo scheme to Langevin dynamics: a fokker-planck approach. Physical review letters, 96(6):067208, 2006.

[149] David P DiVincenzo et al. The physical implementation of quantum computation. arXiv preprint quant-ph/0002077, 2000.

[150] M Dubé and PCE Stamp. Mechanisms of decoherence at low temperatures. Chemical Physics, 268(1):257–272, 2001.

[151] NV Prokof'ev and PCE Stamp. Theory of the spin bath. Reports on Progress in Physics, 63(4):669, 2000.

[152] MW Johnson, MHS Amin, S Gildert, T Lanting, F Hamze, N Dickson, R Harris, AJ Berkley, J Johansson, P Bunyk, et al. Quantum annealing with manufactured spins. Nature, 473(7346):194–198, 2011.

[153] Sergio Boixo, Tameem Albash, Federico M Spedalieri, Nicholas Chancellor, and Daniel A Lidar. Experimental signature of programmable quantum annealing. Nature communications, 4, 2013.

[154] Tameem Albash, Troels F Rønnow, Matthias Troyer, and Daniel A Lidar. Reexamining classical and quantum models for the d-wave one processor. The European Physical Journal Special Topics, 224(1):111–129, 2015.

[155] T Lanting, MHS Amin, MW Johnson, F Altomare, AJ Berkley, S Gildert, R Harris, J Johansson, P Bunyk, E Ladizinsky, et al. Probing high-frequency noise with macroscopic resonant tunneling. Physical Review B, 83(18):180502, 2011.

[156] HJ Carmichael. Stochastic schrödinger equations: What they. In Coherence and Quantum Optics VII: Proceedings of the Seventh Rochester Conference on Coherence and Quantum Optics, held at the University of Rochester, June 7–10, 1995, page 177. Springer Science & Business Media, 2013.

[157] Howard Carmichael. An open systems approach to quantum optics: lectures presented at the Université Libre de Bruxelles, October 28 to November 4, 1991, volume 18. Springer Science & Business Media, 2009.

[158] Joseph H Eberly, Leonard Mandel, and Emil Wolf. Coherence and Quantum Optics VII: Proceedings of the Seventh Rochester Conference on Coherence and Quantum Optics, held at the University of Rochester, June 7–10, 1995. Springer Science & Business Media, 2013.

[159] MB Plenio and PL Knight. The quantum-jump approach to dissipative dynamics in quantum optics. Reviews of Modern Physics, 70(1):101, 1998.

[160] Nicolas Gisin. Quantum measurements and stochastic processes. Physical Review Letters, 52(19):1657, 1984.

[161] Nicolas Gisin and Ian C Percival. The quantum-state diffusion model applied to open systems. Journal of Physics A: Mathematical and General, 25(21):5677, 1992.

[162] Niels Bohr. Über die serienspektra der elemente. Zeitschrift für Physik A Hadrons and Nuclei, 2(5):423–469, 1920.

[163] Niraj Srivastava, Charles Kaufman, Gerhard Müller, R Weber, and H Thomas. Regular and chaotic dynamics of classical spin systems. In Magnetic Excitations and Fluctuations II, pages 70–74. Springer, 1987.

[164] SM Rezende and FM De Aguiar. Chaotic dynamics of two coupled classical spins. Physics Letters A, 208(4):286–292, 1995.

[165] B Rumpf and H Sauermann. Bifurcations of two coupled classical spin oscillators. Physics Letters A, 185(5-6):461–468, 1994.

[166] Iztok Fister Jr, Xin-She Yang, Iztok Fister, Janez Brest, and Dušan Fister. A brief review of nature-inspired algorithms for optimization. arXiv preprint arXiv:1307.4186, 2013.

[167] Raymond Chiong. Nature-inspired algorithms for optimisation, volume 193. Springer, 2009.

[168] John H Holland. Adaptation in natural and artificial systems: an introductory analysis with applications to biology, control, and artificial intelligence. U Michigan Press, 1975.

[169] John J Hopfield. Neural networks and physical systems with emergent collective computational abilities. Proceedings of the national academy of sciences, 79(8):2554–2558, 1982.

[170] Scott Kirkpatrick. Optimization by simulated annealing: Quantitative studies. Journal of statistical physics, 34(5-6):975–986, 1984.

[171] Tadashi Kadowaki and Hidetoshi Nishimori. Quantum annealing in the transverse ising model. Physical Review E, 58(5):5355, 1998.

[172] J Brooke, D Bitko, G Aeppli, et al. Quantum annealing of a disordered magnet. Science, 284(5415):779–781, 1999.

[173] Edward Farhi, Jeffrey Goldstone, Sam Gutmann, Joshua Lapan, Andrew Lundgren, and Daniel Preda. A quantum adiabatic evolution algorithm applied to random instances of an np-complete problem. Science, 292(5516):472–475, 2001.

[174] Giuseppe E Santoro, Roman Martoňák, Erio Tosatti, and Roberto Car. Theory of quantum annealing of an ising spin glass. Science, 295(5564):2427–2430, 2002.

[175] Arnab Das and Bikas K Chakrabarti. Colloquium: Quantum annealing and analog quantum computation. Reviews of Modern Physics, 80(3):1061, 2008.

[176] Matthew B Hastings. Quantum adiabatic computation with a constant gap is not useful in one dimension. Physical review letters, 103(5):050502, 2009.

[177] Matthew B Hastings. Obstructions to classically simulating the quantum adiabatic algorithm. Quantum Information & Computation, 13(11-12):1038–1076, 2013.

[178] T Lanting, AJ Przybysz, A Yu Smirnov, FM Spedalieri, MH Amin, AJ Berkley, R Harris, F Altomare, S Boixo, P Bunyk, et al. Entanglement in a quantum annealing processor. Physical Review X, 4(2):021041, 2014.

[179] Mario P Vecchi and Scott Kirkpatrick. Global wiring by simulated annealing. IEEE transactions on computer-aided design of integrated circuits and systems, (4):215–222, 1983.

[180] Stuart Geman and Donald Geman. Stochastic relaxation, gibbs distributions, and the bayesian restoration of images. IEEE Transactions on pattern analysis and machine intelligence, (6):721–741, 1984.

[181] Sudip Mukherjee and Bikas K Chakrabarti. Multivariable optimization: Quantum annealing and computation. The European Physical Journal Special Topics, 224(1):17–24, 2015.

[182] Jérémie Roland and Nicolas J Cerf. Quantum search by local adiabatic evolution. Physical Review A, 65(4):042308, 2002.

[183] Lov K Grover. A fast quantum mechanical algorithm for database search. In Proceedings of the twenty-eighth annual ACM symposium on Theory of computing, pages 212–219. ACM, 1996.

[184] Lov K Grover. Quantum mechanics helps in searching for a needle in a haystack. Physical review letters, 79(2):325, 1997.

[185] Charles H Bennett, Ethan Bernstein, Gilles Brassard, and Umesh Vazirani. Strengths and weaknesses of quantum computing. SIAM journal on Computing, 26(5):1510–1523, 1997.

[186] Christof Zalka. GroverâĂŹs quantum searching algorithm is optimal. Physical Review A, 60(4):2746, 1999.

[187] Bahram Alidaee, Gary A Kochenberger, and Ahmad Ahmadian. 0-1 quadratic programming approach for optimum solutions of two scheduling problems. International Journal of Systems Science, 25(2):401–408, 1994.

[188] Giorgio Gallo, Peter L Hammer, and Bruno Simeone. Quadratic knapsack problems. In Combinatorial Optimization, pages 132–149. Springer, 1980.

[189] Jakob Krarup and Peter Mark Pruzan. Computer-aided layout design. In Mathematical programming in use, pages 75–94. Springer, 1978.

[190] RD McBride and JS Yormark. An implicit enumeration algorithm for quadratic integer programming. Management Science, 26(3):282–296, 1980.

[191] AT Phillips and JB Rosen. A quadratic assignment formulation of the molecular conformation problem. Journal of Global Optimization, 4(2):229–241, 1994.

[192] Andrew Lucas. Ising formulations of many NP problems. arXiv preprint arXiv:1302.5843, 2013.

[193] Ben W Reichardt. The quantum adiabatic optimization algorithm and local minima. In Proceedings of the thirty-sixth annual ACM symposium on Theory of computing, pages 502–510. ACM, 2004.

[194] Tosio Kato. On the adiabatic theorem of quantum mechanics. Journal of the Physical Society of Japan, 5(6):435–439, 1950.

[195] Alexander Elgart and George A Hagedorn. A note on the switching adiabatic theorem. Journal of Mathematical Physics, 53(10):102202, 2012.

[196] Sabine Jansen, Mary-Beth Ruskai, and Ruedi Seiler. Bounds for the adiabatic approximation with applications to quantum computation. arXiv preprint quant-ph/0603175, 2006.

[197] Andris Ambainis and Oded Regev. An elementary proof of the quantum adiabatic theorem. arXiv preprint quant-ph/0411152, 2004.

[198] Karl-Peter Marzlin and Barry C Sanders. Inconsistency in the application of the adiabatic theorem. Physical review letters, 93(16):160408, 2004.

[199] DM Tong, K Singh, Leong Chuan Kwek, and Choo Hiap Oh. Quantitative conditions do not guarantee the validity of the adiabatic approximation. Physical review letters, 95(11):110407, 2005.

[200] Henry L Haselgrove, Michael A Nielsen, and Tobias J Osborne. Quantum states far from the energy eigenstates of any local hamiltonian. Physical review letters, 91(21):210401, 2003.

[201] Ari Mizel, Daniel A Lidar, and Morgan Mitchell. Simple proof of equivalence between adiabatic quantum computation and the circuit model. Physical review letters, 99(7):070502, 2007.

[202] Dorit Aharonov, Wim Van Dam, Julia Kempe, Zeph Landau, Seth Lloyd, and Oded Regev. Adiabatic quantum computation is equivalent to standard quantum computation. SIAM review, 50(4):755–787, 2008.

[203] Vasil S. Denchev, Sergio Boixo, Sergei V. Isakov, Nan Ding, Ryan Babbush, Vadim Smelyanskiy, John Martinis, and Hartmut Neven. What is the computational value of finite-range tunneling? Phys. Rev. X, 6:031015, Aug 2016.

[204] Stephen P Jordan, Edward Farhi, and Peter W Shor. Error-correcting codes for adiabatic quantum computation. Physical Review A, 74(5):052322, 2006.

[205] Kevin C Young, Mohan Sarovar, and Robin Blume-Kohout. Error suppression and error correction in adiabatic quantum computation: Techniques and challenges. Physical Review X, 3(4):041013, 2013.

[206] Peter P Orth, Adilet Imambekov, and Karyn Le Hur. Universality in dissipative landau-zener transitions. Physical Review A, 82(3):032118, 2010.

[207] Scott Aaronson. D-wave: Truth finally starts to emerge, 2013. http://www.scottaaronson.com/blog/?p=1400.

[208] Helmut G Katzgraber, Firas Hamze, Zheng Zhu, Andrew J Ochoa, and H Munoz-Bauza. Seeking quantum speedup through spin glasses: The good, the bad, and the ugly. Physical Review X, 5(3):031026, 2015.

[209] AJ Berkley, AJ Przybysz, T Lanting, R Harris, N Dickson, F Altomare, MH Amin, P Bunyk, C Enderud, E Hoskinson, et al. Tunneling spectroscopy using a probe qubit. Physical Review B, 87(2):020502, 2013.

[210] Tameem Albash, Itay Hen, Federico M Spedalieri, and Daniel A Lidar. Reexamination of the evidence for entanglement in a quantum annealer. Physical Review A, 92(6):062328, 2015.

[211] MHS Amin, Peter J Love, and CJS Truncik. Thermally assisted adiabatic quantum computation. Physical review letters, 100(6):060503, 2008.

[212] Scott Aaronson. Google, D-wave, and the case of the factor-$10^8$ speedup for what?, 2016. http://www.scottaaronson.com/blog/?p=2555.

[213] Firas Hamze and Nando de Freitas. From fields to trees. In Proceedings of the 20th conference on Uncertainty in artificial intelligence, pages 243–250. AUAI Press, 2004.

[214] Alex Selby. Efficient subgraph-based sampling of ising-type models with frustration. arXiv preprint arXiv:1409.3934, 2014.

[215] Ilia Zintchenko, Matthew B Hastings, and Matthias Troyer. From local to global ground states in ising spin glasses. Physical Review B, 91(2):024201, 2015.

[216] Nevill F Mott and WD Twose. The theory of impurity conduction. Advances in Physics, 10(38):107–163, 1961.

[217] Elihu Abrahams, PW Anderson, DC Licciardello, and TV Ramakrishnan. Scaling theory of localization: Absence of quantum diffusion in two dimensions. Physical Review Letters, 42(10):673, 1979.

[218] Patrick A Lee and Daniel S Fisher. Anderson localization in two dimensions. Physical Review Letters, 47(12):882, 1981.

[219] DM Basko, IL Aleiner, and BL Altshuler. Metal–insulator transition in a weakly interacting many-electron system with localized single-particle states. Annals of physics, 321(5):1126–1205, 2006.

[220] DM Basko, LI Aleiner, and BL Altshuler. On the problem of many-body localization. Problems of Condensed Matter Physics, pages 50–70, 2006.

[221] John Z Imbrie. On many-body localization for quantum spin chains. Journal of Statistical Physics, 163(5):998–1048, 2016.

[222] Vadim Oganesyan and David A Huse. Localization of interacting fermions at high temperature. Physical Review B, 75(15):155111, 2007.

[223] Geneviève Fleury and Xavier Waintal. Numerical finite size scaling approach to many-body localization. Physical review letters, 100(7):076602, 2008.

[224] Marko Žnidarič, Tomaž Prosen, and Peter Prelovšek. Many-body localization in the heisenberg x x z magnet in a random field. Physical Review B, 77(6):064426, 2008.

[225] Timothy C Berkelbach and David R Reichman. Conductivity of disordered quantum lattice models at infinite temperature: Many-body localization. Physical Review B, 81(22):224429, 2010.

[226] Arijeet Pal and David A Huse. Many-body localization phase transition. Physical review b, 82(17):174411, 2010.

[227] Michael Schreiber, Sean S Hodgman, Pranjal Bordia, Henrik P Lüschen, Mark H Fischer, Ronen Vosk, Ehud Altman, Ulrich Schneider, and Immanuel Bloch. Observation of many-body localization of interacting fermions in a quasirandom optical lattice. Science, 349(6250):842–845, 2015.

[228] Bernhard Kramer and Angus MacKinnon. Localization: theory and experiment. Reports on Progress in Physics, 56(12):1469, 1993.

[229] Ferdinand Evers and Alexander D Mirlin. Anderson transitions. Reviews of Modern Physics, 80(4):1355, 2008.

[230] Jürg Fröhlich, Fabio Martinelli, Elisabetta Scoppola, and Thomas Spencer. Constructive proof of localization in the anderson tight binding model. Communications in Mathematical Physics, 101(1):21–46, 1985.

[231] John Z Imbrie. Multi-scale jacobi method for anderson localization. Communications in Mathematical Physics, 341(2):491–521, 2016.

[232] A Chandran, CR Laumann, and V Oganesyan. Finite size scaling bounds on many-body localized phase transitions. arXiv preprint arXiv:1509.04285, 2015.

[233] N. F. Mott. Conduction in non-crystalline systems. Philosophical Magazine, 17(150):1259–1268, 1968.

[234] Neville Francis Mott and Edward A Davis. Electronic processes in non-crystalline materials. Oxford University Press, 1979.

[235] AL Efros and BI Shklovskii. Coulomb gap and low temperature conductivity of disordered systems. Journal of Physics C: Solid State Physics, 8(4):L49, 1975.

[236] K Życzkowski, M Lewenstein, M Kuś, and F Izrailev. Eigenvector statistics of random band matrices. Physical Review A, 45(2):811, 1992.

[237] F Evers and AD Mirlin. Fluctuations of the inverse participation ratio at the anderson transition. Physical review letters, 84(16):3690, 2000.

[238] John M Ziman. Models of disorder: the theoretical physics of homogeneously disordered systems. CUP Archive, 1979.

[239] CE Porter and RG Thomas. Fluctuations of nuclear reaction widths. Physical Review, 104(2):483, 1956.

[240] Eugene P Wigner. Random matrices in physics. SIAM review, 9(1):1–23, 1967.

[241] Freeman J Dyson. Statistical theory of the energy levels of complex systems. i. Journal of Mathematical Physics, 3(1):140–156, 1962.

[242] Freeman J Dyson. Statistical theory of the energy levels of complex systems. ii. Journal of Mathematical Physics, 3(1):157–165, 1962.

[243] Freeman J Dyson. Statistical theory of the energy levels of complex systems. iii. Journal of Mathematical Physics, 3(1):166–175, 1962.

[244] Freeman J Dyson and Madan Lal Mehta. Statistical theory of the energy levels of complex systems. iv. Journal of Mathematical Physics, 4(5):701–712, 1963.

[245] Madan Lal Mehta and Freeman J Dyson. Statistical theory of the energy levels of complex systems. v. Journal of Mathematical Physics, 4(5):713–719, 1963.

[246] Madan Lal Mehta. Random matrices, 3rd edition, volume 142. Academic press, 2004.

[247] O Bohigas, RU Haq, and A Pandey. Fluctuation properties of nuclear energy levels and widths: comparison of theory with experiment. In Nuclear data for science and technology, pages 809–813. Springer, 1983.

[248] YY Atas, E Bogomolny, O Giraud, and G Roux. Distribution of the ratio of consecutive level spacings in random matrix ensembles. Physical review letters, 110(8):084101, 2013.

[249] Luca D'Alessio, Yariv Kafri, Anatoli Polkovnikov, and Marcos Rigol. From quantum chaos and eigenstate thermalization to statistical mechanics and thermodynamics. arXiv preprint arXiv:1509.06411, 2015.

[250] Marcos Rigol. Breakdown of thermalization in finite one-dimensional systems. Physical review letters, 103(10):100403, 2009.

[251] Marcos Rigol and Lea F Santos. Quantum chaos and thermalization in gapped systems. Physical Review A, 82(1):011604, 2010.

[252] Tatsuhiko N Ikeda, Yu Watanabe, and Masahito Ueda. Finite-size scaling analysis of the eigenstate thermalization hypothesis in a one-dimensional interacting bose gas. Physical Review E, 87(1):012125, 2013.

[253] Marcos Rigol and Mark Srednicki. Alternatives to eigenstate thermalization. Physical review letters, 108(11):110601, 2012.

[254] Hyungwon Kim, Tatsuhiko N Ikeda, and David A Huse. Testing whether all eigenstates obey the eigenstate thermalization hypothesis. Physical Review E, 90(5):052105, 2014.

[255] L Fleishman, DC Licciardello, and PW Anderson. Elementary excitations in the fermi glass. Physical Review Letters, 40(20):1340, 1978.

[256] L Fleishman and PW Anderson. Interactions and the anderson transition. Physical Review B, 21(6):2366, 1980.

[257] David A Huse, Rahul Nandkishore, and Vadim Oganesyan. Phenomenology of fully many-body-localized systems. Physical Review B, 90(17):174202, 2014.

[258] Maksym Serbyn, Z Papić, and Dmitry A Abanin. Local conservation laws and the structure of the many-body localized states. Physical review letters, 111(12):127201, 2013.

[259] Maksym Serbyn, Z Papić, and Dmitry A Abanin. Universal slow growth of entanglement in interacting strongly disordered systems. Physical review letters, 110(26):260601, 2013.

[260] David Pekker and Bryan K Clark. Encoding the structure of many-body localization with matrix product operators. arXiv preprint arXiv:1410.2224, 2014.

[261] Vedika Khemani, Frank Pollmann, and SL Sondhi. Obtaining highly-excited eigenstates of many-body localized hamiltonians by the density matrix renormalization group. arXiv preprint arXiv:1509.00483, 2015.

[262] David J Luitz, Nicolas Laflorencie, and Fabien Alet. Many-body localization edge in the random-field heisenberg chain. Physical Review B, 91(8):081103, 2015.

[263] Mathis Friesdorf, AH Werner, W Brown, VB Scholz, and Jens Eisert. Many-body localization implies that eigenvectors are matrix-product states. Physical review letters, 114(17):170505, 2015.

[264] David J Luitz, Nicolas Laflorencie, and Fabien Alet. Extended slow dynamical regime close to the many-body localization transition. Physical Review B, 93(6):060201, 2016.

[265] Elena Canovi, Davide Rossini, Rosario Fazio, Giuseppe E Santoro, and Alessandro Silva. Many-body localization and thermalization in the full probability distribution function of observables. New Journal of Physics, 14(9):095020, 2012.

[266] Andrew C Potter, Romain Vasseur, and SA Parameswaran. Universal properties of many-body delocalization transitions. Physical Review X, 5(3):031033, 2015.

[267] Sarang Gopalakrishnan, Markus Müller, Vedika Khemani, Michael Knap, Eugene Demler, and David A Huse. Low-frequency conductivity in many-body localized systems. Physical Review B, 92(10):104202, 2015.

[268] Maksym Serbyn, Z Papić, and Dmitry A Abanin. Criterion for many-body localization-delocalization phase transition. Physical Review X, 5(4):041047, 2015.

[269] Shankar Iyer, Vadim Oganesyan, Gil Refael, and David A Huse. Many-body localization in a quasiperiodic system. Physical Review B, 87(13):134202, 2013.

[270] Wojciech De Roeck, Francois Huveneers, Markus Müller, and Mauro Schiulaz. Absence of many-body mobility edges. Physical Review B, 93(1):014203, 2016.

[271] EJ Torres-Herrera and Lea F Santos. Dynamics at the many-body localization transition. Physical Review B, 92(1):014208, 2015.

[272] Merlijn van Horssen, Emanuele Levi, and Juan P Garrahan. Dynamics of many-body localization in a translation-invariant quantum glass model. Physical Review B, 92(10):100305, 2015.

[273] V Ros, M Müller, and A Scardicchio. Integrals of motion in the many-body localized phase. Nuclear Physics B, 891:420–465, 2015.

[274] John Z Imbrie, Valentina Ros, and Antonello Scardicchio. Review: Local integrals of motion in many-body localized systems. arXiv preprint arXiv:1609.08076, 2016.

[275] Anushya Chandran, Isaac H Kim, Guifre Vidal, and Dmitry A Abanin. Constructing local integrals of motion in the many-body localized phase. Physical Review B, 91(8):085425, 2015.

[276] David Pekker, Bryan K Clark, Vadim Oganesyan, and Gil Refael. Fixed points of wegner-wilson flows and many-body localization. arXiv preprint arXiv:1607.07884, 2016.

[277] Bela Bauer and Chetan Nayak. Area laws in a many-body localized state and its implications for topological order. Journal of Statistical Mechanics: Theory and Experiment, 2013(09):P09005, 2013.

[278] Jonas A Kjäll, Jens H Bardarson, and Frank Pollmann. Many-body localization in a disordered quantum ising chain. Physical review letters, 113(10):107204, 2014.

[279] Xiongjie Yu, David Pekker, and Bryan K Clark. Finding matrix product state representations of highly-excited eigenstates of many-body localized hamiltonians. arXiv preprint arXiv:1509.01244, 2015.

[280] Christian K Burrell and Tobias J Osborne. Bounds on the speed of information propagation in disordered quantum spin chains. Physical review letters, 99(16):167201, 2007.

[281] Isaac H Kim, Anushya Chandran, and Dmitry A Abanin. Local integrals of motion and the logarithmic lightcone in many-body localized systems. arXiv preprint arXiv:1412.3073, 2014.

[282] Dong-Ling Deng, Xiaopeng Li, JH Pixley, Yang-Le Wu, and S Das Sarma. Logarithmic entanglement lightcone in many-body localized systems. arXiv preprint arXiv:1607.08611, 2016.

[283] Jens H Bardarson, Frank Pollmann, and Joel E Moore. Unbounded growth of entanglement in models of many-body localization. Physical review letters, 109(1):017202, 2012.

[284] G Torlai, L Tagliacozzo, and G De Chiara. Dynamics of the entanglement spectrum in spin chains. Journal of Statistical Mechanics: Theory and Experiment, 2014(6):P06001, 2014.

[285] NY Yao, CR Laumann, J Ignacio Cirac, MD Lukin, and JE Moore. Quasi many-body localization in translation invariant systems. arXiv preprint arXiv:1410.7407, 2014.

[286] Giuseppe Carleo, Federico Becca, Marco Schiró, and Michele Fabrizio. Localization and glassy dynamics of many-body quantum systems. Scientific reports, 2, 2012.

[287] Yevgeny Bar Lev and David R Reichman. Dynamics of many-body localization. Physical Review B, 89(22):220201, 2014.

[288] R Vasseur, SA Parameswaran, and JE Moore. Quantum revivals and many-body localization. Physical Review B, 91(14):140202, 2015.

[289] Maurizio Fagotti. Conservation laws for a class of generic hamiltonians. arXiv preprint arXiv:1408.1950, 2014.

[290] Vedika Khemani, Rahul Nandkishore, and Shivaji L Sondhi. Nonlocal adiabatic response of a localized system to local manipulations. Nature Physics, 11(7):560–565, 2015.

[291] Franz Wegner. Flow-equations for hamiltonians. Annalen der physik, 506(2):77–91, 1994.

[292] Franz Wegner. Flow equations of hamiltonians. Philosophical Magazine B, 77(5):1249–1253, 1998.

[293] Franz J Wegner. Flow equations for hamiltonians. Physics Reports, 348(1):77–89, 2001.

[294] A Hackl and S Kehrein. Real time evolution in quantum many-body systems with unitary perturbation theory. Physical Review B, 78(9):092303, 2008.

[295] A Hackl and S Kehrein. A unitary perturbation theory approach to real-time evolution problems. Journal of Physics: Condensed Matter, 21(1):015601, 2008.

[296] DH Dunlap and VM Kenkre. Dynamic localization of a charged particle moving under the influence of an electric field. Physical Review B, 34(6):3625, 1986.

[297] C Cedzich, T Rybár, AH Werner, A Alberti, M Genske, and RF Werner. Propagation of quantum walks in electric fields. Physical review letters, 111(16):160601, 2013.

[298] Salvador Elías Venegas-Andraca. Quantum walks: a comprehensive review. Quantum Information Processing, 11(5):1015–1106, 2012.

[299] Manuel Pino, Lev B Ioffe, and Boris L Altshuler. Nonergodic metallic and insulating phases of josephson junction chains. Proceedings of the National Academy of Sciences, 113(3):536–541, 2016.

[300] Mauro Schiulaz, Alessandro Silva, and Markus Müller. Dynamics in many-body localized quantum systems without disorder. Physical Review B, 91(18):184202, 2015.

[301] Mauro Schiulaz and M Müller. Ideal quantum glass transitions: many-body localization without quenched disorder. arXiv preprint arXiv:1309.1082, 2013.

[302] Tarun Grover and Matthew PA Fisher. Quantum disentangled liquids. Journal of Statistical Mechanics: Theory and Experiment, 2014(10):P10010, 2014.

[303] Z Papić, E Miles Stoudenmire, and Dmitry A Abanin. Many-body localization in disorder-free systems: The importance of finite-size constraints. Annals of Physics, 362:714–725, 2015.

[304] Wojciech De Roeck and François Huveneers. Scenario for delocalization in translation-invariant systems. Physical Review B, 90(16):165137, 2014.

[305] James M Hickey, Sam Genway, and Juan P Garrahan. Signatures of many-body localisation in a system without disorder and the relation to a glass transition. Journal of Statistical Mechanics: Theory and Experiment, 2016(5):054047, 2016.

[306] P Sollich and MR Evans. Glassy dynamics in the asymmetrically constrained kinetic ising chain. Physical Review E, 68(3):031504, 2003.

[307] Juan P Garrahan, Peter Sollich, and Cristina Toninelli. Kinetically constrained models. Dynamical heterogeneities in glasses, colloids, and granular media, 150:111–137, 2011.

[308] Alessandra Faggionato, F Martinelli, Cyril Roberto, and C Toninelli. Aging through hierarchical coalescence in the east model. Communications in Mathematical Physics, 309(2):459–495, 2012.

[309] Alessandra Faggionato, Fabio Martinelli, Cyril Roberto, and Cristina Toninelli. The east model: recent results and new progresses. arXiv preprint arXiv:1205.1607, 2012.

[310] Alexander L Fetter and John Dirk Walecka. Quantum theory of many-particle systems. Quantum theory of many-particle systems, by Fetter, Alexander L.; Walecka, John Dirk. San Francisco, McGraw-Hill [c1971]. International series in pure and applied physics, 1, 1971.

[311] Julia Kempe, Alexei Kitaev, and Oded Regev. The complexity of the local hamiltonian problem. SIAM Journal on Computing, 35(5):1070–1097, 2006.

[312] Yu Kagan and LA Maksimov. Localization in a system of interacting particles diffusing in a regular crystal. Zh. Eksp. Teor. Fiz, 87:348–365, 1984.

[313] Markus P Müller, Emily Adlam, Lluís Masanes, and Nathan Wiebe. Thermalization and canonical typicality in translation-invariant quantum lattice systems. Communications in Mathematical Physics, 340(2):499–561, 2015.

[314] Eliot Kapit. Universal two-qubit interactions, measurement, and cooling for quantum simulation and computing. Physical Review A, 92(1):012302, 2015.

[315] RJ Baxter. Corner transfer matrices. Physica A: Statistical Mechanics and its Applications, 106(1):18–27, 1981.

[316] Daniel A Lidar, Isaac L Chuang, and K Birgitta Whaley. Decoherence-free subspaces for quantum computation. Physical Review Letters, 81(12):2594, 1998.

[317] Almut Beige, Daniel Braun, Ben Tregenna, and Peter L Knight. Quantum computing using dissipation to remain in a decoherence-free subspace. Physical Review Letters, 85(8):1762, 2000.

[318] Alireza Shabani and Daniel A Lidar. Theory of initialization-free decoherence-free subspaces and subsystems. Physical Review A, 72(4):042303, 2005.

[319] D Bacon. Decoherence, control, and symmetry in quantum computers. arXiv preprint quant-ph/0305025, 2003.

[320] Martin B Plenio, Vlatko Vedral, and Peter L Knight. Quantum error correction in the presence of spontaneous emission. Physical Review A, 55(1):67, 1997.

[321] Daniel A Lidar and K Birgitta Whaley. Decoherence-free subspaces and subsystems. In Irreversible Quantum Dynamics, pages 83–120. Springer, 2003.

[322] Victor L Quito, Paraj Titum, David Pekker, and Gil Refael. Localization transition in one dimension using wegner flow equations. Physical Review B, 94(10):104202, 2016.

[323] Wojciech De Roeck and François Huveneers. Asymptotic localization of energy in nondisordered oscillator chains. Communications on Pure and Applied Mathematics, 68(9):1532–1568, 2015.

[324] Balázs Pozsgay, Willem-Victor van Gerven Oei, and Márton Kormos. On form factors in nested bethe ansatz systems. Journal of Physics A: Mathematical and Theoretical, 45(46):465007, 2012.

[325] Ulrich Schollwöck. The density-matrix renormalization group. Reviews of modern physics, 77(1):259, 2005.

[326] Steven R White and Adrian E Feiguin. Real-time evolution using the density matrix renormalization group. Physical review letters, 93(7):076401, 2004.

[327] Ping Sheng. Introduction to wave scattering, localization and mesoscopic phenomena, volume 88. Springer Science & Business Media, 2006.

[328] Vadim Oganesyan, Arijeet Pal, and David A Huse. Energy transport in disordered classical spin chains. Physical Review B, 80(11):115104, 2009.

[329] Jutho Haegeman, Tobias J Osborne, and Frank Verstraete. Post-matrix product state methods: To tangent space and beyond. Physical Review B, 88(7):075133, 2013.

[330] Jutho Haegeman, Michaël Mariën, Tobias J Osborne, and Frank Verstraete. Geometry of matrix product states: Metric, parallel transport, and curvature. Journal of Mathematical Physics, 55(2):021902, 2014.

[331] Pierre Meystre and Murray Sargent. Elements of quantum optics. Springer Science & Business Media, 2013.

[332] Alexei Yu Kitaev, Alexander Shen, and Mikhail N Vyalyi. Classical and Quantum Computation. Number 47. American Mathematical Soc., 2002.